Stochastic analysis, simulation and identification of hyperelastic constitutive equations

Brian Staber

Université Paris-Est Marne-la-Vallée
École doctorale Sciences, Ingénierie et Environnement

THÈSE

présentée et soutenue publiquement le 29 juin 2018

pour l'obtention du

Doctorat de l'Université Paris-Est Marne-la-Vallée

Discipline: mécanique

par

Brian Staber

Stochastic analysis, simulation and identification of hyperelastic constitutive equations

Composition du jury

Président :	Didier Clouteau	Professor – École Centrale Supélec Paris
Rapporteurs :	Stéphane Bordas	Professor – Université du Luxembourg
	Roger Ghanem	Professor – University of Southern California
Examinateurs :	Maarten Arnst	Assistant Professor – Université de Liège
	Frédéric Legoll	Professor – École Nationale des Ponts et Chaussées
	Christian Soize	Professor – Université Paris-Est
Directeur de thèse :	Johann Guilleminot	Assistant Professor – Duke University

---

Laboratoire de Modélisation et Simulation Multi-Echelle — UMR 8208 CNRS

Mis en page avec la classe thesul.

Acknowledgment

First of all, I would like to deeply thank my PhD advisor, Professor Johann Guilleminot, for all the time he has dedicated to me and for all the things I have learnt under his supervision. His devotion to his research has always given me a lot of motivation. We spent many hours working together, and it has really been an amazing experience.

I would like to thank Professor Stéphane Bordas and Professor Roger Ghanem for accepting to review the present thesis. I also express my gratitude to Professor Maarten Arnst, Professor Didier Clouteau, Professor Frédéric Legoll and Professor Christian Soize for accepting to evaluate this work.

Special thanks to all the colleagues I had great times with. The list would actually be quite long, and I apologize if I forgot someone. To name a few: Quentin, Anthony H. and Anthony P., for all the nice (lunch) breaks and other good times we shared; Florent, for always being available and helping me with coding and other geek stuffs; Quentin for his kindness, for feeding me, and even for his platonic massages; Anthony H. for picking me up some mornings and reading this thesis; Anthony P. for all the sweets I stole from you and the funny jokes; Luo Yun Mei for all the wasabi greenpeas. I also would like to mention N.F., Gong Yanghao, Liao Meng, Chen Zhou, Wu Shuchao, Cai Yu Ting and Lei Lei, Kossi-Mensah Kodjo, amongst others.

I acknowledge the financial support from the Université Paris-Est Marne-la-Vallée. I also acknowledge the financial support of the Graduate School at Duke University. This work was partially funded by the National Science Foundation under grant CMMI-1726403 during my stay at Duke University.

Last but not least, I thank my family and Roxane for believing in me and supporting me during all these years.

Contents

Chapter 1

General Introduction

Contents

1.1 Research positioning

Uncertainty quantification has now become a predominant ingredient of predictive science and engineering. Since the seminal work from Ghanem and Spanos [1], many developments were proposed regarding the mathematical representation, identification and propagation of model-form and parametric uncertainties in computational models (see [2] for state-of-the-art reviews; see also [3, 4, 5]). All these aspects of uncertainty quantification are deeply intertwined and are of paramount importance in the development of numerical tools for robust design and high-fidelity simulations.

This thesis is specifically focused on the construction, identification and simulation of new mathematical models for stochastic nonlinear constitutive laws in computational mechanics and mechanics of materials. The complementary issue of devising efficient solvers for the propagation of uncertainties in this setup will not be addressed, and the interested reader is referred to the extensive literature available on this topic [2]. Here, the class of hyperelastic models is considered, with the aim to address a wide span of materials ranging from engineered polymeric composites to soft biological tissues. The variability exhibited by these media is very well documented. In the case of biological materials for instance, aleatoric uncertainties are raised by various factors such as microstructural complexity and randomness, potential disease and subject-to-subject variability. In practice, they offer great challenges for the development and widespread adoption of, *e.g.*, computational assisted diagnosis and surgery, as well as for the development of compatible artificial substitutes. Experimental evidences of such variability can be found in, *e.g.*, [6, 7, 8, 9, 10, 11, 12, 13, 14, 15, 16, 17] for brain and liver tissues, spinal cord white matter and abdominal organs. As an illustration, stress responses of thirteen samples for the three layers constituting arterial walls are shown in Fig. 1.1. The fluctuations in the mechanical responses are significant and advocate the development of a stochastic modeling framework (see [19] and the references therein for applications to the cardiovascular system).

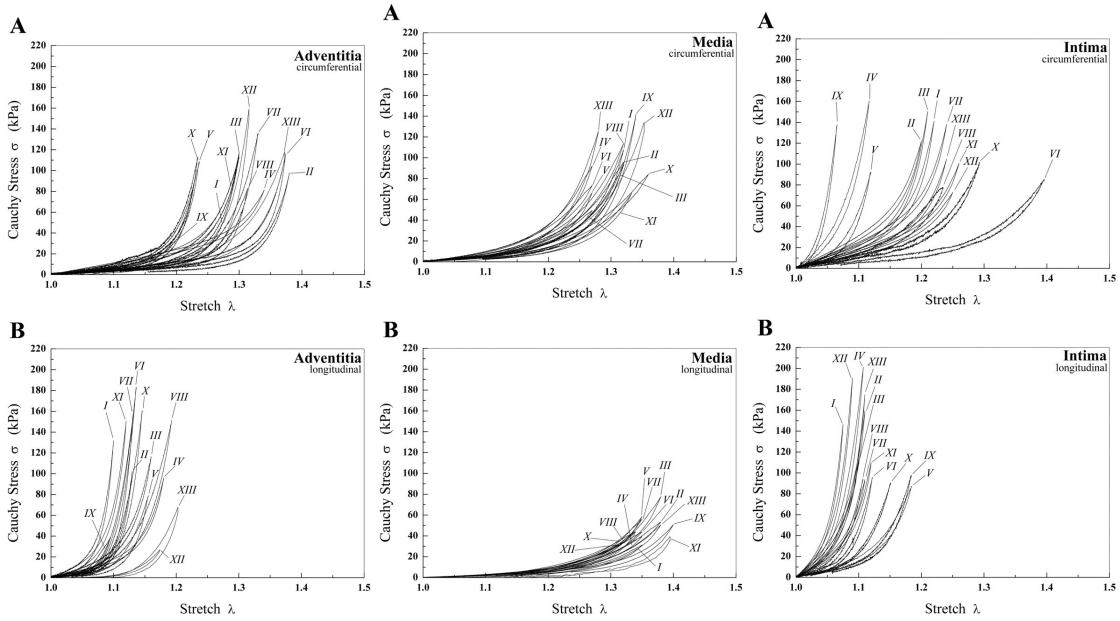

Figure 1.1 – Stretch-stress responses for thirteen samples of the three layers composing an artery wall (from left to right: *adventitia*, *media* and *intima*). A uniaxial tensile test is considered [18].

In contrast to the modeling of scalar- and tensor-valued coefficients for stochastic linear elliptic operators, which was quite extensively investigated during the past decade (see, *e.g.*, [20, 21, 22, 23, 24, 25, 26, 27, 28, 29, 30, 31, 32, 33, 34, 35, 36], the proper *modeling* of constitutive equations in finite elasticity has received little attention to date. Note first that randomness in nonlinear constitutive models can be defined in a multiscale setup where some morphological parameters, such as fiber length and orientation for fibrous tissues, are made random; see, *e.g.*, [37, 38] for the case of two-dimensional engineered composites. In this context, the problem of representing the stochastic stored energy function can be approached by relying on a polynomial chaos expansion, the coefficients of which can be evaluated using an appropriate stochastic solver. An early attempt to randomize the parameters defining a particular isotropic stored energy function can be found in [39], where information theory was invoked to derive a model that is consistent with the knowledge of the support for the random variables (see [40] for an extension to the anisotropic case). Other studies involving Gaussian models (which will be seen to be non-admissible) can be found in, *e.g.*, [41, 42]. In [43] (see also [44]), a Bayesian approach accounting for both spatial variability and non-simplified domains was proposed for isotropic hyperelastic materials.

The main objective of this work is to provide an integrated modeling approach for a variety of situations that were independently and/or partially considered so far, focusing on one of the most widely used class of stored energy functions, and including the case of

(i) compressible and incompressible media;

(ii) isotropic and anisotropic materials;

(iii) homogeneous and spatially varying behaviors.

The framework will be developed by accounting for two types of constraints. First, mathematical constraints related to the analysis of the nonlinear boundary value problems will be *systematically* incorporated, hence making the propagation of the model(s) through nonlinear operators a well-posed problem. Second, it will be assumed that the data available for model calibration are

limited in terms of both the nature of the experiments and the number of tested samples. The latter constraint prevents, in particular, to resort to a pure statistical approach. Some results of this thesis were published in the series of papers [45, 46, 47, 48] that have inspired the recent works [49] and [50], in which a Bayesian identification procedure and a specific statistical treatment of (virtually generated) dependencies between the parameters were introduced, respectively. Note finally that the results presented in this document constitute a theoretically sound basis for the integration of time-dependency (that is, for developing stochastic nonlinear viscoelastic models for hyperelastic media), which is not discussed hereinafter.

1.2 Organization of the dissertation

This dissertation is organized as follows. The theoretical background related to the theory of finite elasticity is recalled in Section 1.4. The nonlinear boundary value problem is introduced, and the mathematical constraints under which the existence of solutions is ensured are detailed. **Chapters 2**, **3** and **4** are concerned with the stochastic modeling and functional approximation of homogeneous, isotropic stored energy functions for incompressible and compressible hyperelastic media. **Chapters 5** and **6** investigate the extension of such probabilistic models to spatially dependent, anisotropic hyperelastic media at small and finite strains. These chapters are described in detail below.

- **Chapter 2** is focused on the modeling of *isotropic*, *incompressible* hyperelastic materials. The class of Ogden-type stored energy functions is specifically considered and extended to a stochastic framework. The modeling capabilities offered by the proposed probabilistic model are next assessed by performing Monte Carlo simulations. An inverse identification strategy is then discussed and benchmarked for various soft biological tissues at given strain rates.

- In **Chapter 3**, the case of *isotropic*, *compressible* hyperelastic media is considered. The class of Ogden's potentials is investigated, and explicit results for Neo-Hookean and Mooney-Rivlin materials are specified. As an illustration, the propagation of material uncertainties through a multiscale operator is addressed, using a polynomial chaos expansion for the homogenized stored energy function.

- In **Chapter 4**, the construction of functional approximations for nonlinear multiscale solution maps is tackled. This chapter is independent from the rest of the thesis. Here, the homogenized potential is approximated by a polynomial series, and the accuracy of the surrogate model is then assessed on selected two-dimensional microstructures. The definition of *closest approximations* into appropriate sets of stored energy functions is subsequently proposed and benchmarked using a FE^2-type approach.

- **Chapter 5** is concerned with *spatially dependent, anisotropic* and nearly-incompressible stored energy functions. A prototypical stored energy function is purposely selected and used to develop the modeling approach, and the simulation of the random field model on complex geometries is addressed. The framework is then deployed to perform uncertainty quantification on arterial walls using a real, patient-specific geometry.

- **Chapter 6** presents a probabilistic model for non-Gaussian random fields of elasticity tensors with values in any material symmetry class. The approach exploits the underlying structure of the state space and combines a tensor decomposition with a random matrix formulation. Monte-Carlo simulations of spatially dependent transversely isotropic and orthotropic tensors are finally conducted on curved geometries.

1.3 Notation

- *Matrix sets.* In what follows, $\mathbb{M}^n$ denotes the set of real square matrices $[A]$ of size n, $\mathbb{S}^n \subset \mathbb{M}^n$ is the subset of symmetric matrices, $\mathbb{M}^n_+ \subset \mathbb{M}^n$ is the subset of matrices with strictly positive determinants and $\mathbb{S}^n_+ \subset \mathbb{S}^n$ is the subset of symmetric and positive definite matrices. In addition, let $\mathbb{S}^n_{\text{sym}} \subset \mathbb{S}^n$ be the set of symmetric and positive-definite matrices $[A]$ such that $[Q][A][Q]^T = [A]$ for all $[Q] \in \mathscr{G}_{\text{sym}}$, where $\mathscr{G}_{\text{sym}} \subset \text{SO}(n)$ is a symmetry goup. The superscript "sym" corresponds to the symmetry class under consideration such as isotropy (iso), transverse isotropy (ti) or triclinic materials (tric). Finally, $[I_n]$ denotes the $(n \times n)$ identity matrix.

- *Random variables and random fields.* Deterministic scalar, vectors in $\mathbb{R}^n$ and matrices in $\mathbb{M}^n$ are denoted by a, $\mathbf{a}$ and $[A]$, respectively. The entries in the canonical bases $\{\mathbf{e}_i\}_{i=1}^n$ and $\{\mathbf{e}_i \otimes \mathbf{e}_j\}_{i=1,j=1}^n$ are denoted by $\{a_i\}_{i=1}^n$ and $\{A_{ij}\}_{i=1,j=1}^n$. Random scalars, vectors and matrices, defined on a probability space $(\Theta, \mathscr{T}, \mathbb{P})$, will be denoted by A, $\mathbf{A}$ and $[\mathbf{A}]$. A family of random variables indexed by a set $\mathcal{S} \subseteq \mathbb{R}^n$ are referred to as random fields and denoted by $\{A(\mathbf{x}), \mathbf{x} \in \mathcal{S}\}$, $\{\mathbf{A}(\mathbf{x}), \mathbf{x} \in \mathcal{S}\}$ and $\{[\mathbf{A}(\mathbf{x})], \mathbf{x} \in \mathcal{S}\}$, depending on the nature of the state space. For any $\mathbf{x}$ fixed in the subset $\mathcal{S}$, $A(\mathbf{x})$, $\mathbf{A}(\mathbf{x})$ and $[\mathbf{A}(\mathbf{x})]$ are random variables defined on the probability space $(\Theta, \mathscr{T}, \mathbb{P})$. For any fixed $\theta \in \Theta$, $a(\theta)$, $\mathbf{a}(\theta)$ and $[A(\theta)]$ are realizations of the random variables A, $\mathbf{A}$ and $[\mathbf{A}]$. Similarly, $\mathbf{x} \mapsto a(\mathbf{x}; \theta)$, $\mathbf{x} \mapsto \mathbf{a}(\mathbf{x}; \theta)$ and $\mathbf{x} \mapsto [A(\mathbf{x}; \theta)]$ are realizations of the random fields $\{A(\mathbf{x}), \mathbf{x} \in \mathcal{S}\}$, $\{\mathbf{A}(\mathbf{x}), \mathbf{x} \in \mathcal{S}\}$ and $\{[\mathbf{A}(\mathbf{x})], \mathbf{x} \in \mathcal{S}\}$. Finally, k_0 denotes the normalization constant in probability density functions. The value of k_0 may therefore change from line to line.

- *Inner products and norms.* For any $\mathbf{a}$ and $\mathbf{b}$ in $\mathbb{R}^n$, the inner product is given by $\langle \mathbf{a}, \mathbf{b} \rangle = \sum_{i=1}^n a_i b_i$ and the associated norm writes $\|\mathbf{a}\|^2 = \langle \mathbf{a}, \mathbf{a} \rangle$. More generally, the p-norm $\|\mathbf{a}\|_p$ is given by $\|\mathbf{a}\|_p = (\sum_{i=1}^n |a_i|^p)^{1/p}$. For any $[A]$ and $[B]$ in $\mathbb{M}^n$, the inner product $\langle [A], [B] \rangle_F = \text{Tr}([A]^T[B])$ and the associated Frobenius norm $\|[A]\|_F$ of $[A]$ reads as $\|[A]\|_F^2 = \langle [A], [A] \rangle_F$.

1.4 Background in continuum mechanics

In this section, we briefly recall the framework of continuum mechanics that will be used throughout this work. The exposure is borrowed from classical textbooks in finite elasticity; see, *e.g.*, [51, 52, 53] and [54, 55].

1.4.1 Kinematics

Let $\mathscr{P}$ be a body consisting of a continuous collection of material points. At some time $t = t_0$, this body occupies a reference configuration $\overline{\mathscr{B}} \subset \mathbb{R}^3$ whose particles are identified by their position $\mathbf{x} = (x_1, x_2, x_3)$. The reference configuration $\overline{\mathscr{B}}$ is understood as the closure of an open connected set $\mathscr{B}$ with boundary $\partial\mathscr{B}$. For some time $t > t_0$, the body of interest occupies a new configuration $\overline{\mathscr{B}}^{\boldsymbol{\varphi}}$ referred to as the deformed or actual configuration. For any material point $\mathbf{x} \in \overline{\mathscr{B}}$, the position $\mathbf{x}^{\boldsymbol{\varphi}}$ in the deformed configuration is given by $\mathbf{x}^{\boldsymbol{\varphi}} = \boldsymbol{\varphi}(\mathbf{x})$ where the so-called deformation map $\boldsymbol{\varphi} : \overline{\mathscr{B}} \to \overline{\mathscr{B}}^{\boldsymbol{\varphi}}$ is injective, except on the boundaries where there is self-contact, and orientation-preserving. For any $\mathbf{x} \in \mathscr{B}$, the deformation gradient $[F_{\boldsymbol{\varphi}}]$ is a second-order tensor defined as

$$[F_{\boldsymbol{\varphi}}(\mathbf{x})] = \sum_{k=1}^{3} \sum_{\ell=1}^{3} \frac{\partial \varphi_k(\mathbf{x})}{\partial x_\ell} \, \mathbf{e}_k \otimes \mathbf{e}_\ell \,, \tag{1.1}$$

where $\{\mathbf{e}_i\}_{i=1}^3$ denotes the canonical basis of the Euclidean space $\mathbb{R}^3$ and $\otimes$ is the dyadic product such that $(\mathbf{a}\otimes\mathbf{b})_{ij} = a_i b_j$, $1 \leqslant i,j \leqslant n$ for any $\mathbf{a},\mathbf{b}$ in $\mathbb{R}^n$. The deformation gradient satisfies the orientation-preserving condition:

$$\det([F_\varphi(\mathbf{x})]) > 0\,, \quad \forall \mathbf{x} \in \mathscr{B}\,. \tag{1.2}$$

The vector-valued fields $\mathbf{u} : \mathscr{B} \to \mathbb{R}^3$ and $\mathbf{u}^\varphi : \mathscr{B}^\varphi \to \mathbb{R}^3$ defined as $\mathbf{u}(\mathbf{x}) = \boldsymbol{\varphi}(\mathbf{x}) - \mathbf{x}$ and $\mathbf{u}^\varphi(\mathbf{x}^\varphi) = \mathbf{x}^\varphi - \boldsymbol{\varphi}^{-1}(\mathbf{x}^\varphi)$ correspond to the displacement fields in the Lagrangian and Eulerian description, respectively. For all $\mathbf{x} \in \mathscr{B}$, the deformation gradient is related to the displacement field by the relation $[F_\varphi(\mathbf{x})] = [I_3] + [\nabla\mathbf{u}(\mathbf{x})]$ where

$$[\nabla\mathbf{u}(\mathbf{x})] = \sum_{k=1}^{3}\sum_{\ell=1}^{3} \frac{\partial u_k(\mathbf{x})}{\partial x_\ell}\, \mathbf{e}_k \otimes \mathbf{e}_\ell\,, \tag{1.3}$$

is the Lagrangian gradient of the displacement field. The symmetric second-order tensor $[C_\varphi(\mathbf{x})]$ is known as the right Cauchy-Green deformation tensor and defined as $[C_\varphi(\mathbf{x})] = [F_\varphi(\mathbf{x})]^T[F_\varphi(\mathbf{x})]$. Due to the orientation-preserving property of the deformation gradient, it can be deduced that the right Cauchy-Green tensor is positive-definite

1.4.2 Quasi-static boundary value problem of finite elasticity

In what follows, we restrict our attention to materials that exhibit an elastic behavior. In this case, the constitutive equations are entirely determined by the current deformation gradient field $\mathbf{x} \mapsto [F_\varphi(\mathbf{x})]$. The continuum body is submitted to surface forces on a portion of its boundary $\partial\mathscr{B}^\varphi$ and to body forces in its interior. We then denote by $\mathbf{g}^\varphi : \Gamma_N^\varphi \to \mathbb{R}^3$ and $\mathbf{b}^\varphi : \mathscr{B}^\varphi \to \mathbb{R}^3$ the applied surfaces and body forces, respectively, where $\Gamma_N^\varphi \subset \partial\mathscr{B}^\varphi$ is the portion of the deformed configuration submitted to the natural boundary conditions. According to the stress principle, there exists a vector field $\mathbf{t}^\varphi : \mathscr{B}^\varphi \times \mathcal{S} \to \mathbb{R}^3$ such that $\mathbf{t}^\varphi(\mathbf{x}^\varphi, \mathbf{n}^\varphi) = \mathbf{g}^\varphi(\mathbf{x}^\varphi)$, where $\mathbf{n}^\varphi$ is the outer unit normal of the boundary Γ_N^φ and $\mathcal{S}$ is the unit sphere. Cauchy's theorem then states that there exists a unique and symmetric second-order tensor $[\sigma] : \mathscr{B}^\varphi \times \mathbb{M}^3_+ \to \mathbb{S}^3$ such that

$$\mathbf{t}^\varphi(\mathbf{x}^\varphi, \mathbf{n}^\varphi) = [\sigma(\mathbf{x}^\varphi, [F_\varphi])]\mathbf{n}^\varphi\,, \tag{1.4}$$

and

$$\begin{aligned} -\mathbf{div}^\varphi([\sigma(\mathbf{x}^\varphi, [F_\varphi])]) &= \mathbf{b}^\varphi(\mathbf{x}^\varphi)\,, \quad \mathbf{x}^\varphi \in \mathscr{B}^\varphi\,, \\ \mathbf{t}^\varphi(\mathbf{x}^\varphi, \mathbf{n}^\varphi) &= \mathbf{g}^\varphi(\mathbf{x}^\varphi)\,, \quad \mathbf{x}^\varphi \in \Gamma_N^\varphi\,, \end{aligned} \tag{1.5}$$

where $\mathbf{div}^\varphi$ is the divergence operator with respect to the actual coordinates $\mathbf{x}^\varphi$. This boundary value problem is supplemented with essential boundary conditions of the form $\mathbf{u}^\varphi(\mathbf{x}^\varphi) = \mathbf{u}_d^\varphi(\mathbf{x}^\varphi)$ on a portion Γ_D^φ such that $\Gamma_D^\varphi \bigcap \Gamma_N^\varphi = \{0\}$. In addition, it can be expressed in terms of the reference configuration by having recourse to the so-called Piola transforms. More precisely, the first Piola-Kirchhoff stress tensor $[P] : \mathscr{B} \times \mathbb{M}^3_+ \to \mathbb{M}^3$ is defined as

$$[P(\mathbf{x}, [F_\varphi])] = \det([F_\varphi(\mathbf{x})])[\sigma(\mathbf{x}^\varphi, [F_\varphi])][F_\varphi(\mathbf{x})]^{-T}\,, \quad \mathbf{x}^\varphi = \boldsymbol{\varphi}(\mathbf{x})\,. \tag{1.6}$$

Given a location $\mathbf{x}$ in the reference configuration, the first Piola-Kirchhoff stress tensor allows for computing the stress associated in the deformed configuration. Let then $\mathbf{b} : \mathscr{B} \to \mathbb{R}^3$ be the applied body forces in the reference configuration such that $\mathbf{b}(\mathbf{x})\mathrm{d}v = \mathbf{b}^\varphi(\mathbf{x}^\varphi)\mathrm{d}v_\varphi$ where $\mathrm{d}v_\varphi$ and $\mathrm{d}v$ are infinitesimal volume elements in the deformed and reference configurations. The applied body force in the reference configuration can then be written as

$$\mathbf{b}(\mathbf{x}) = \det([F_\varphi(\mathbf{x})])\mathbf{b}^\varphi(\mathbf{x}^\varphi)\,, \quad \mathbf{x}^\varphi = \boldsymbol{\varphi}(\mathbf{x})\,. \tag{1.7}$$

Similarly, via the so-called Nanson's formula [53] and the equivalence $\mathbf{g}(\mathbf{x})\mathrm{d}a = \mathbf{g}^{\varphi}(\mathbf{x}^{\varphi})\mathrm{d}a_{\varphi}$, it is found that the surface forces $\mathbf{g} : \Gamma_N \to \mathbb{R}^3$ applied on the portion $\Gamma_N \subset \partial\mathscr{B}$ reads as

$$\mathbf{g}(\mathbf{x}) = \det([F_{\varphi}(\mathbf{x})])\|[F_{\varphi}(\mathbf{x})]^{-T}\mathbf{n}\|\mathbf{g}^{\varphi}(\mathbf{x}^{\varphi})\,, \quad \mathbf{x}^{\varphi} = \boldsymbol{\varphi}(\mathbf{x})\,. \tag{1.8}$$

Using the properties of the divergence operator and the expressions of the applied forces given by Eqs. (1.7) and (1.8), the boundary value problem in the undeformed configuration is given by

$$\begin{array}{rcll} -\mathbf{div}([P(\mathbf{x},[F_{\varphi}])]) & = & \mathbf{b}(\mathbf{x})\,, & \mathbf{x} \in \mathscr{B}\,, \\ \mathbf{t}(\mathbf{x},\mathbf{n}) & = & \mathbf{g}(\mathbf{x})\,, & \mathbf{x} \in \Gamma_N\,, \end{array} \tag{1.9}$$

where **div** is the divergence operator with to the coordinates $\mathbf{x}$. The above boundary value problem is supplemented with additional essential boundary conditions $\mathbf{u}(\mathbf{x}) = \mathbf{u}_d(\mathbf{x})$ on Γ_D, with $\Gamma_D \bigcap \Gamma_N = \{0\}$.

1.4.3 The constitutive equations of hyperelasticity

This work is focused on the modeling of hyperelastic media. In this case, there exists a so-called stored energy function $w : \mathscr{B} \times \mathbb{M}^3_+ \to \mathbb{R}$ such that the first Piola-Kirchhoff stress tensor reads as

$$[P(\mathbf{x},[F])] = \sum_{k=1}^{3}\sum_{\ell=1}^{3} \frac{\partial w(\mathbf{x},[F])}{\partial F_{k\ell}}\, \mathbf{e}_k \otimes \mathbf{e}_{\ell}\,, \quad \forall\, \mathbf{x} \in \mathscr{B}\,, \quad \forall [F] \in \mathbb{M}^3_+\,. \tag{1.10}$$

The hyperelastic material is said to be homogeneous if the stored energy function depends on the location $\mathbf{x}$ only through the deformation gradient. We consider a stored energy function that fulfills the principle of frame-invariance (see [56, 57] or, *e.g.*, [51]) which states that the response of the material and any observable physical quantity must be invariant under changes of the frame of reference. This implies that the stored energy function must satisfy the invariance condition

$$w(\mathbf{x},[F]) = w(\mathbf{x},[Q][F])\,, \quad \forall [Q] \in \mathrm{SO}(3)\,, \tag{1.11}$$

for all $\mathbf{x} \in \mathscr{B}$ and $[F] \in \mathbb{M}^3_+$. It can be deduced that for any $[F] \in \mathbb{M}^3_+$, the constitutive equations in the reference configuration can be written in terms of the associated right Cauchy-Green tensor [53]. More precisely, there exists a stored energy function $\widetilde{w} : \mathscr{B} \times \mathbb{S}^3_+ \to \mathbb{R}$ such that

$$w(\mathbf{x},[F]) = \widetilde{w}(\mathbf{x},[C])\,, \quad [C] = [F]^T[F]\,, \tag{1.12}$$

for all $[F] \in \mathbb{M}^3_+$. In order to obtain simpler constitutive equations in the reference configuration, the symmetric second Piola-Kirchhoff stress tensor $[S] : \mathscr{B} \times \mathbb{S}^3_+ \to \mathbb{S}^3$ is introduced and defined as

$$[S(\mathbf{x},[C])] = [F]^{-1}[P(\mathbf{x},[F])]\,, \quad [C] = [F]^T[F]\,, \tag{1.13}$$

for any $[F]$ fixed in $\mathbb{M}^3_+$. Using the constitutive equation for hyperelastic materials given by Eq. (1.10) together with Eqs. (1.12)-(1.13), it is deduced that the second Piola-Kirchhoff stress tensor can be written as

$$[S(\mathbf{x},[C])] = \sum_{k=1}^{3}\sum_{\ell=1}^{3} 2\frac{\partial \widetilde{w}(\mathbf{x},[C])}{\partial C_{k\ell}}\, \mathbf{e}_k \otimes \mathbf{e}_{\ell}\,. \tag{1.14}$$

The stored energy function satisfies additional invariance conditions related to the symmetry properties of the material under consideration. For instance, a material is said to be isotropic

if its mechanical response is invariant under any rotation of its reference configuration. More generally, an anisotropic material is characterized by the property that a rotation $[Q]$ of its reference configuration modifies the constitutive equations except if $[Q]$ belongs to a specific group of orthogonal transformations, referred to as the symmetry group $\mathscr{G}$ and such that, for all $\mathbf{x} \in \mathscr{B}$ and for all $[F] \in \mathbb{M}^3_+$,

$$w(\mathbf{x}, [F]) = w(\mathbf{x}, [F][Q]) \,, \quad \forall\, [Q] \in \mathscr{G} \,, \tag{1.15}$$

or equivalently, for all $[C] \in \mathbb{S}^3_+$,

$$\widetilde{w}(\mathbf{x}, [C]) = \widetilde{w}(\mathbf{x}, [Q]^T [C][Q]) \,, \quad \forall\, [Q] \in \mathscr{G} \,. \tag{1.16}$$

For a given symmetry class, the invariance condition given by Eq. (1.16) imposes restrictions on the functional forms of the stored energy function $\widetilde{w}(\mathbf{x}, \cdot) : \mathbb{S}^3_+ \to \mathbb{R}$. In practice, isotropic and anisotropic models are constructed by invoking representation theorems, such as the Rivlin-Ericksen theorem [58, 51] and by introducing additional second-order tensors that reflect the symmetry properties of the material of interest [59, 60].

1.4.4 Existence of solutions in finite elasticity

In the context of hyperelasticity, solving the boundary value problem given by Eq. (1.9) is equivalent to minimizing the energy functional $\mathcal{I} : \mathcal{X}^{1,p} \to \mathbb{R}$ defined as [53, 55]

$$\mathcal{I}(\boldsymbol{\varphi}) = \int_{\mathscr{B}} w(\mathbf{x}, [F_\varphi(\mathbf{x})])\, d\mathbf{x} - \int_{\Gamma_N} \langle \mathbf{g}(\mathbf{x}), \boldsymbol{\varphi}(\mathbf{x}) \rangle\, d\mathbf{a} - \int_{\mathscr{B}} \langle \mathbf{f}(\mathbf{x}), \boldsymbol{\varphi}(\mathbf{x}) \rangle\, d\mathbf{x} \,, \tag{1.17}$$

where $\mathcal{X}^{1,p}$, $p \geqslant 1$, is a functional space of the form

$$\mathcal{X}^{1,p} = \{ \boldsymbol{\varphi} \in W^{1,p}(\mathscr{B}, \mathbb{R}^3) \,:\, \mathcal{I}(\boldsymbol{\varphi}) < +\infty \,,\, \boldsymbol{\varphi} = \boldsymbol{\varphi}^d|_{\Gamma_D} \} \,, \tag{1.18}$$

with $W^{1,p}(\mathscr{B}, \mathbb{R})$ the Sobolev space of functions in $L^p(\mathscr{B}, \mathbb{R}^3)$ with partial derivatives in $L^p(\mathscr{B}, \mathbb{R}^3)$ [61]. By computing the first Gateaux derivative of the energy function given by Eq. (1.17), one has

$$\frac{d}{\mathrm{d}\epsilon}\, \mathcal{I}(\boldsymbol{\varphi} + \epsilon \mathbf{v})|_{\epsilon=0} = \int_{\mathscr{B}} \frac{\partial w(\mathbf{x}, [F_\varphi(\mathbf{x})])}{\partial F_{k\ell}} \frac{\partial v_k(\mathbf{x})}{\partial x_\ell}\, d\mathbf{x} - \int_{\Gamma_N} \langle \mathbf{g}(\mathbf{x}), \mathbf{v}(\mathbf{x}) \rangle\, d\mathbf{a} - \int_{\mathscr{B}} \langle \mathbf{f}(\mathbf{x}), \mathbf{v}(\mathbf{x}) \rangle\, d\mathbf{x} \,, \tag{1.19}$$

which leads to the weak formulation of the boundary value problem given by (1.9), *i.e.*, find $\boldsymbol{\varphi} \in \mathcal{X}^{1,p}$ such that

$$\int_{\mathscr{B}} \langle [P(\mathbf{x}, [F_\varphi(\mathbf{x})])], [\nabla \mathbf{v}(\mathbf{x})] \rangle_F\, d\mathbf{x} = \int_{\Gamma_N} \langle \mathbf{g}(\mathbf{x}), \mathbf{v}(\mathbf{x}) \rangle\, d\mathbf{a} + \int_{\mathscr{B}} \langle \mathbf{f}(\mathbf{x}), \mathbf{v}(\mathbf{x}) \rangle\, d\mathbf{x} \,, \quad \forall \mathbf{v} \in \mathcal{X}^{1,p}_0 \,, \tag{1.20}$$

with $\mathcal{X}^{1,p}_0$ the space of functions in $\mathcal{X}$ that vanish on the boundary Γ_D where essential boundary conditions are applied, that is,

$$\mathcal{X}^{1,p}_0 = \{ \boldsymbol{\varphi} \in W^{1,p}(\mathscr{B}, \mathbb{R}^3) \,:\, \mathcal{I}(\boldsymbol{\varphi}) < +\infty \,,\, \boldsymbol{\varphi} = \mathbf{0}|_{\Gamma_D} \} \,. \tag{1.21}$$

Existence theorems in finite elasticity are based on the minimization of the energy functional and the method of direct calculus of variations [62, 63]. The existence of minimizers is ensured if the energy functional is sequentially weakly lower semicontinuous and coercive [62]. In practice, this property is imposed by constructing stored energy functions that satisfy generalized convexity

and growth conditions, also referred to as coercivity. While a convex stored energy function with respect to the deformation gradient leads to sequentially weakly lower semicontinuity, it is well-known that it conflicts with physical restrictions such as frame-invariance and non-uniqueness [53]. As an alternative, the concept of quasiconvexity was proposed by Morrey [64]. It is a non-local convexity condition which is rather complicated to verify in practice and the growth conditions are incompatible with physical requirements. In order to circumvent these issues, the condition of polyconvexity is widely used nowadays as it does not conflict with physical restrictions, and leads to a sequentially weakly lower semicontinuous energy functional.

Definition 1.4.1 (Polyconvexity)**.** *In three-dimensional elasticity, a function f is said to be polyconvex if there exists a convex function $f^\star$ such that [65, 62]*

$$f([F]) = f^\star([F], \mathrm{Cof}([F]), \det([F])) \tag{1.22}$$

where $\mathrm{Cof}([F]) = \det([F])[F]^{-T}$.

Example. *For any constants $a > 0$, $b > 0$, $c > 0$ and $d > 0$, let f be the function defined as*

$$f([F]) = a\|[F]\|_F^2 + b\|\mathrm{Cof}([F])\|_F^2 + c(\det([F]))^2 - d\log(\det([F]))\,, \quad \forall\, [F] \in \mathbb{M}^3\,. \tag{1.23}$$

The functions $[F] \mapsto a\|[F]\|_F^2$ and $\delta \mapsto c\delta^2 - d\log(\delta)$ are both strictly convex. Hence, the function $f^\star$ can be defined as

$$f^\star([F], [H], \delta) = a\|[F]\|_F^2 + b\|[H]\|_F^2 + c\delta^2 - d\log(\delta)\,. \tag{1.24}$$

It is worth pointing out that the definition of $f^\star$ is not necessarily unique.

Polyconvexity implies that the function f is also rank-one convex, which is another important convex condition defined below.

Definition 1.4.2 (Rank-one convexity)**.** *A function f is said to be rank-one convex if [62]*

$$f(\lambda[F_1] + (1-\lambda)[F_2]) \leqslant \lambda f([F_1]) + (1-\lambda) f([F_2])\,, \tag{1.25}$$

for every $\lambda \in [0,1]$ and $[F_1]$, $[F_2]$ with $\mathrm{rank}\{[F_1] - [F_2]\} \leqslant 1$. Let then $\boldsymbol{\xi}$ and $\boldsymbol{\eta}$ be two vectors in $\mathbb{R}^3$ such that $[F_1] - [F_2] = \boldsymbol{\xi} \otimes \boldsymbol{\eta}$, then rank-one convexity can be rewritten as

$$f([F_2] + (1-\mu)\boldsymbol{\xi} \otimes \boldsymbol{\eta}) \leqslant \mu f([F_2]) + (1-\mu) f([F_2] + \boldsymbol{\xi} \otimes \boldsymbol{\eta})\,, \tag{1.26}$$

for all $\mu \in [0,1]$.

If in addition the function f is twice differentiable, *i.e.*, $f \in \mathcal{C}^2(\mathbb{M}^3)$, then rank-one convexity is equivalent to the ellipticity condition

$$\sum_{i,j,k,\ell=1}^{3} \frac{\partial^2 f([F])}{\partial F_{ij} \partial F_{k\ell}} \xi_i \eta_j \xi_k \eta_\ell \geqslant 0\,, \quad \forall\, \boldsymbol{\xi}, \boldsymbol{\eta} \in \mathbb{R}^3\,, \tag{1.27}$$

which is also referred to as the Legendre-Hadamard condition. For brevity, quasiconvexity is not discussed herein and the interested reader is referred to, *e.g.*, [62]. We finally note that these generalized convexity conditions are related as follows:

$$\text{convexity} \;\Rightarrow\; \text{polyconvexity} \;\Rightarrow\; \text{quasiconvexity} \;\Rightarrow\; \text{rank-one convexity}. \tag{1.28}$$

We are now in position to state Ball's existence theorem in nonlinear elasticity [65]. This theorem is based on the assumptions of polyconvexity and suitable growth conditions which express the physical requirement that extreme strains lead to infinite stress. Let w be a stored energy function that satisfies the following properties:

(i) *Polyconvexity.* There exists a convex function $w^\star$ such that

$$w(\mathbf{x},[F]) = w^\star(\mathbf{x},[F],\mathrm{Cof}([F]),\det([F]))\,, \tag{1.29}$$

for all $\mathbf{x}\in\mathscr{B}$.

(ii) *Coercivity.* There exist constants $c_0>0$, $c_1\in\mathbb{R}$, $p\geqslant 2$, $q\geqslant 3/2$, such that

$$w(\mathbf{x},[F]) \geqslant c_0(\|[F]\|_F^p + \|\mathrm{Cof}([F])\|_F^q) - c_1\,, \tag{1.30}$$

for all $\mathbf{x}\in\mathscr{B}$ and for all $[F]\in\mathbb{M}^3_+$.

(iii) *Limit behavior.* The limit of the stored energy function as $\det([F])\downarrow 0$ is infinity, *i.e.*

$$\lim_{\det([F])\downarrow 0} w(\mathbf{x},[F]) = +\infty\,. \tag{1.31}$$

In this setting, it can be shown that there exists at least one minimizer of the energy functional in the space

$$\mathcal{X}^{1,1} = \{\boldsymbol{\varphi}\in W^{1,1}(\mathscr{B},\mathbb{R}^3)\,:\,\mathcal{I}(\boldsymbol{\varphi})<+\infty\,,\,\boldsymbol{\varphi}=\boldsymbol{\varphi}^d|_{\Gamma_D}\}\,. \tag{1.32}$$

The above existence result is due to Müller et al. [66] and is a refinement of Ball's existence theorem with weaker growth conditions (see also, *e.g.*, [67, 68]). As an illustration, let us consider the isotropic and homogeneous stored energy function defined as

$$w([F]) = a\|[F]\|_F^2 + b\|\mathrm{Cof}([F])\|_F^2 + c(\det([F]))^2 - d\log(\det([F]))\,. \tag{1.33}$$

Under the assumptions that $a>0$, $b>0$, $c>0$ and $d>0$, the above stored energy function is polyconvex, satisfies the coercivity property with $p=q=2$, and the limit behavior given by Eq. (1.31). This constitutive model has been proposed in [69] (see also [53]) and corresponds to a Mooney-Rivlin type model [54]. It should be noted that the above existence results hold for compressible and incompressible materials. In the particular case of near/weak incompressibility, extended existence results can be found [70].

1.4.5 The boundary value problem of linearized elasticity

In this last section, we consider the particular case of linearized elasticity. A first-order approximation of the boundary value problem given by Eq. (1.9) leads to the boundary value problem of linearized elasticity [58, 53], that is,

$$\begin{aligned} -\mathbf{div}([\sigma(\mathbf{u})]) &= \mathbf{b}(\mathbf{x})\,,\quad \mathbf{x}\in\mathscr{B}\,,\\ [\sigma(\mathbf{u})]\mathbf{n} &= \mathbf{g}(\mathbf{x})\,,\quad \mathbf{x}\in\Gamma_N\,, \end{aligned} \tag{1.34}$$

where for any displacement field $\mathbf{x}\mapsto\mathbf{u}(\mathbf{x})$, the linearized stress tensor $[\sigma(\mathbf{u})]$ and the deformation tensor at small strains $[\varepsilon(\mathbf{u})]$ are defined as

$$\sigma_{ij}(\mathbf{u}) = A_{ijk\ell}(\mathbf{x})\varepsilon_{k\ell}(\mathbf{u})\,,\quad 1\leqslant i,j,k,\ell\leqslant 3\,, \tag{1.35}$$

with summation over repeated indices and

$$[\varepsilon(\mathbf{u})] = \frac{1}{2}([\nabla\mathbf{u}(\mathbf{x})] + [\nabla\mathbf{u}(\mathbf{x})]^T)\,. \tag{1.36}$$

In Eq. (1.35), the fourth-order elasticity tensor $[\![A]\!]$ is given by

$$A_{ijk\ell}(\mathbf{x}) = \left.\frac{\partial^2 \widetilde{w}(\mathbf{x},[C])}{\partial C_{ij} C_{k\ell}}\right|_{[C]=[I_3]}, \quad \forall\, \mathbf{x} \in \mathscr{B}\,, \tag{1.37}$$

and has the minor and major symmetry properties

$$A_{ijk\ell}(\mathbf{x}) = A_{jik\ell}(\mathbf{x}) = A_{ij\ell k}(\mathbf{x})\,, \quad A_{ijk\ell}(\mathbf{x}) = A_{k\ell ij}(\mathbf{x})\,, \quad 1 \leqslant i,j,k,\ell \leqslant 3\,. \tag{1.38}$$

In addition, from the material symmetry properties of stored energy function (see Eq. (1.16)), it can be deduced that the elasticity tensor also satisfies the invariance condition

$$A_{ijk\ell}(\mathbf{x}) = \sum_{p=1}^{3}\sum_{q=1}^{3}\sum_{r=1}^{3}\sum_{s=1}^{3} Q_{ip}Q_{jq}Q_{kr}Q_{\ell s}A_{pqrs}(\mathbf{x})\,, \quad \forall\,[Q] \in \mathscr{G}\,. \tag{1.39}$$

Depending on the material symmetry group $\mathscr{G}$, the number of independent coefficients of the elasticity tensor ranges from 2 for isotropic materials to 21 for triclinic materials. Following [71], the elasticity tensor can be decomposed as

$$[\![A(\mathbf{x})]\!] = \sum_{i=1}^{N} c_i(\mathbf{x})[\![E_i]\!]\,, \tag{1.40}$$

where $\{[\![E_i]\!]\}_{i=1}^{N}$ is a set of fourth-elasticity tensors whose expressions depend on the symmetry group $\mathscr{G}$ under consideration. For instance, in the case of isotropic materials, the elasticity tensor depends on only two independent coefficients and can be written as

$$[\![A(\mathbf{x})]\!] = 3c_1(\mathbf{x})[\![E_1]\!] + 2c_2(\mathbf{x})[\![E_2]\!]\,, \tag{1.41}$$

where $[\![E_1]\!]$ and $[\![E_2]\!]$ are two mutually orthogonal projectors defined as

$$E_{1ijk\ell} = \frac{1}{3}\delta_{ij}\delta_{k\ell}\,, \quad E_{2ijk\ell} = \frac{1}{2}(\delta_{ik}\delta_{j\ell} + \delta_{i\ell}\delta_{jk}) - E_{1ijk\ell}\,, \quad 1 \leqslant i,j,k,\ell \leqslant 3\,, \tag{1.42}$$

and the parameters $c_1(\mathbf{x})$ and $c_2(\mathbf{x})$ correspond to the bulk and shear moduli at small strains. In contrast, in the case of triclinic materials the set of tensors $\{[\![E_i]\!]\}_{i=1}^{21}$ is given by the canonical basis of $\mathbb{S}^6$, and the elasticity tensor depends on 21 independent coefficients. Other important symmetry classes that cover a wide range of applications are, for instance, transverse isotropy and orthotropy.

1.4.5.1 Existence of a weak solution

Let $\mathcal{V}$ be the Sobolev space $\mathbf{H}^1_0(\mathscr{B},\mathbb{R}^3)$. For the boundary value problem of linearized elasticity, the weak formulation writes: find $\mathbf{w} = \mathbf{u} - \mathbf{u}_d \in \mathcal{V}$ such that

$$a(\mathbf{v},\mathbf{w}) = \ell(\mathbf{v}) - a(\mathbf{v},\mathbf{u}_d)\,, \quad \forall \mathbf{v} \in \mathcal{V}\,, \tag{1.43}$$

where the symmetric bilinear form $a : \mathcal{V}\times\mathcal{V} \to \mathbb{R}$ and the linear form $\ell : \mathcal{V} \to \mathbb{R}$ are given by

$$a(\mathbf{v},\mathbf{w}) = \int_{\mathscr{B}} [\varepsilon(\mathbf{v})] : [\![A(\mathbf{x})]\!] : [\varepsilon(\mathbf{w})]\,\mathrm{d}\mathbf{x}\,, \tag{1.44}$$

where the double inner product represents the double contraction and

$$\ell(\mathbf{v}) = \int_{\mathscr{B}} \langle \mathbf{f}(\mathbf{x}), \mathbf{v}(\mathbf{x})\rangle\,\mathrm{d}\mathbf{x} + \int_{\Gamma_N} \langle \mathbf{h}(\mathbf{x}), \mathbf{v}(\mathbf{x})\rangle\,\mathrm{d}\mathbf{a}\,. \tag{1.45}$$

If the linear form $\ell : \mathcal{V} \to \mathbb{R}$ is continuous, and the bilinear form $a : \mathcal{V}\times\mathcal{V} \to \mathbb{R}$ is continuous and elliptic then according to Lax-Milgram's theorem, there exists a unique solution to the weak formulation given by Eq. (1.43) (see, *e.g.*, [52, 53, 72] and the references therein).

1.4.5.2 Voigt's modified notation

For calculations and numerical purposes, a matrix representation of the elasticity tensor is generally introduced using Voigt's modified notation [73]. Let then $\boldsymbol{\varepsilon}(\mathbf{u})$ and $\boldsymbol{\sigma}(\mathbf{u})$ be the vectors in $\mathbb{R}^6$ defined as

$$\boldsymbol{\varepsilon}(\mathbf{u}) = (\epsilon_{11}(\mathbf{u}), \epsilon_{22}(\mathbf{u}), \epsilon_{33}(\mathbf{u}), \sqrt{2}\epsilon_{23}(\mathbf{u}), \sqrt{2}\epsilon_{13}(\mathbf{u}), \sqrt{2}\epsilon_{12}(\mathbf{u}))\,, \tag{1.46}$$

and

$$\boldsymbol{\sigma}(\mathbf{u}) = (\sigma_{11}(\mathbf{u}), \sigma_{22}(\mathbf{u}), \sigma_{33}(\mathbf{u}), \sqrt{2}\sigma_{23}(\mathbf{u}), \sqrt{2}\sigma_{13}(\mathbf{u}), \sqrt{2}\sigma_{12}(\mathbf{u}))\,, \tag{1.47}$$

The constitutive equations of linearized elasticity (see Eq. (1.35)) can then be rewritten as $\boldsymbol{\sigma}(\mathbf{u}) = [A(\mathbf{x})]\boldsymbol{\varepsilon}(\mathbf{u})$ where the second-order elasticity tensor $[A(\mathbf{x})]$ is given by

$$[A(\mathbf{x})] = \begin{bmatrix} A_{1111}(\mathbf{x}) & A_{1122}(\mathbf{x}) & A_{1133}(\mathbf{x}) & \sqrt{2}A_{1123}(\mathbf{x}) & \sqrt{2}A_{1113}(\mathbf{x}) & \sqrt{2}A_{1112}(\mathbf{x}) \\ A_{2211}(\mathbf{x}) & A_{2222}(\mathbf{x}) & A_{2233}(\mathbf{x}) & \sqrt{2}A_{2223}(\mathbf{x}) & \sqrt{2}A_{2213}(\mathbf{x}) & \sqrt{2}A_{2212}(\mathbf{x}) \\ A_{3311}(\mathbf{x}) & A_{3322}(\mathbf{x}) & A_{3333}(\mathbf{x}) & \sqrt{2}A_{3323}(\mathbf{x}) & \sqrt{2}A_{3313}(\mathbf{x}) & \sqrt{2}A_{3312}(\mathbf{x}) \\ \sqrt{2}A_{2311}(\mathbf{x}) & \sqrt{2}A_{2322}(\mathbf{x}) & \sqrt{2}A_{2333}(\mathbf{x}) & 2A_{2323}(\mathbf{x}) & 2A_{2313}(\mathbf{x}) & 2A_{2312}(\mathbf{x}) \\ \sqrt{2}A_{1311}(\mathbf{x}) & \sqrt{2}A_{1322}(\mathbf{x}) & \sqrt{2}A_{1333}(\mathbf{x}) & 2A_{1323}(\mathbf{x}) & 2A_{1313}(\mathbf{x}) & 2A_{1312}(\mathbf{x}) \\ \sqrt{2}A_{1211}(\mathbf{x}) & \sqrt{2}A_{1222}(\mathbf{x}) & \sqrt{2}A_{1233}(\mathbf{x}) & 2A_{1223}(\mathbf{x}) & 2A_{1213}(\mathbf{x}) & 2A_{1212}(\mathbf{x}) \end{bmatrix}.$$

For instance, in the case of isotropic materials, the modified Voigt notation of the projectors $[\![E_1]\!]$ and $[\![E_2]\!]$ are given by (see Eq. (1.41))

$$[E_1] = \begin{bmatrix} 1/3 & 1/3 & 1/3 & 0 & 0 & 0 \\ 1/3 & 1/3 & 1/3 & 0 & 0 & 0 \\ 1/3 & 1/3 & 1/3 & 0 & 0 & 0 \\ 0 & 0 & 0 & 0 & 0 & 0 \\ 0 & 0 & 0 & 0 & 0 & 0 \\ 0 & 0 & 0 & 0 & 0 & 0 \end{bmatrix}, \quad [E_2] = \begin{bmatrix} 2/3 & 2/3 & 2/3 & 0 & 0 & 0 \\ 2/3 & 2/3 & 2/3 & 0 & 0 & 0 \\ 2/3 & 2/3 & 2/3 & 0 & 0 & 0 \\ 0 & 0 & 0 & 1 & 0 & 0 \\ 0 & 0 & 0 & 0 & 1 & 0 \\ 0 & 0 & 0 & 0 & 0 & 1 \end{bmatrix}, \tag{1.48}$$

and the second-order elasticity tensor reduces to

$$[A(\mathbf{x})] = \begin{bmatrix} c_1(\mathbf{x}) + 2c_2(\mathbf{x})/3 & c_1(\mathbf{x}) - 2c_2(\mathbf{x})/3 & c_1(\mathbf{x}) - 2c_2(\mathbf{x})/3 & 0 & 0 & 0 \\ c_1(\mathbf{x}) - 2c_2(\mathbf{x})/3 & c_1(\mathbf{x}) + 2c_2(\mathbf{x})/3 & c_1(\mathbf{x}) - 2c_2(\mathbf{x})/3 & 0 & 0 & 0 \\ c_1(\mathbf{x}) - 2c_2(\mathbf{x})/3 & c_1(\mathbf{x}) - 2c_2(\mathbf{x})/3 & c_1(\mathbf{x}) + 2c_2(\mathbf{x})/3 & 0 & 0 & 0 \\ 0 & 0 & 0 & 2c_2(\mathbf{x}) & 0 & 0 \\ 0 & 0 & 0 & 0 & 2c_2(\mathbf{x}) & 0 \\ 0 & 0 & 0 & 0 & 0 & 2c_2(\mathbf{x}) \end{bmatrix}.$$

Chapter 2

Stochastic Modeling of Incompressible Isotropic Hyperelastic Materials

Contents

2.1 Introduction

In this chapter, we address the construction of a class of stochastic stored energy energy functions associated with incompressible, homogeneous and isotropic hyperelastic materials [45, 46]. The aim is twofold. The primary goal is to derive a methodology to construct probabilistic models for which samples are consistent with existence theorems in nonlinear elasticity. These models can be used, for instance, to regularize ill-posed statistical inverse problems, or as prior models in a Bayesian approach to model identification [74, 75]—in both deterministic and stochastic frameworks. A second investigated aspect is the identification of these new models using real experimental data on soft biological tissues. As pointed out in Chapter 1, the experimental responses of such materials are very prone to uncertainties, and thus constitute appropriate benchmarks for the stochastic constitutive models. Here, the attention is restricted to the class of Ogden's stored energy functions [76, 77], which is widely used within the engineering and scientific communities [78] to model polymeric materials and most soft biological tissues (see, *e.g.*, [79, 80]). The generalization to other types of stored energy functions can be addressed in a straightforward manner but may raise additional technicalities, depending on the retained

functional form for the nonlinear potential. Extensions to anisotropic and/or spatially dependent nonlinear behaviors will be addressed later on in this thesis.

This chapter is organized as follows. In Section 2.2, the deterministic hyperelastic model is first presented. The construction of a class of stochastic stored energy functions is then addressed in Sections 2.3–2.7. Monte Carlo simulations are performed in Section 2.8 in order to illustrate the model capabilities. Finally, in Section 2.9, an inverse identification procedure is presented and applied to experimental data bases for brain tissues, liver tissues and spinal cord white matter.

2.2 Deterministic background

In this section, the deterministic form of the stored energy function under consideration is introduced, and constraints on model parameters are detailed. These constraints will be specifically invoked in Section 2.3 to derive the stochastic version of the stored energy function.

Let w be the stored energy function of the homogeneous and incompressible hyperelastic medium. The incompressibility condition is taken into account by introducing a Lagrange multiplier κ (which is typically interpreted as an hydrostatic pressure) in the constitutive equations [54], that is, the first Piola-Kirchhoff stress tensor is given by

$$[P([F])] = \sum_{k=1}^{3}\sum_{\ell=1}^{3} \frac{\partial w([F])}{\partial F_{k\ell}} \mathbf{e}_k \otimes \mathbf{e}_\ell - \kappa [F]^{-T} . \tag{2.1}$$

A general-order Ogden-type stored energy function is defined as [76, 77]

$$w([F]) = \sum_{i=1}^{m} p_i (\mathrm{Tr}(([F]^T[F])^{\eta_i/2}) - 3) + \sum_{j=1}^{n} p_{j+m} (\mathrm{Tr}((\mathrm{Cof}([F]^T[F]))^{\eta_{j+m}/2}) - 3) , \quad \forall [F] \in \mathbb{M}^3_+ , \tag{2.2}$$

where $\{p_k\}_{k=1}^{m+n}$ and $\{\eta_k\}_{k=1}^{m+n}$ are two sets of model parameters. Let $\mathbf{p} = (p_1, \ldots, p_{m+n})$ and $\boldsymbol{\eta} = (\eta_1, \ldots, \eta_{m+n})$. The following assumptions regarding these parameters are next introduced:

$$p_k > 0 , \quad 1 \leqslant k \leqslant m+n , \tag{2.3}$$

and

$$\eta_1 \geqslant \cdots \geqslant \eta_m \geqslant 1 , \quad \eta_{m+1} \geqslant \cdots \geqslant \eta_{m+n} \geqslant 1 . \tag{2.4}$$

Under these assumptions, it can be shown that the stored energy function given by Eq. (2.2) is polyconvex; see, *e.g.*, [65, 53]. Since the hyperelastic material is incompressible throughout this chapter, the convexity statement does not involve the determinant of the deformation gradient anymore and thus, there exists a convex function $w^\star$ such that

$$w([F]) = w^\star([F], \mathrm{Cof}([F])) , \quad \forall [F] \in \mathbb{M}^3_+ . \tag{2.5}$$

If the inequalities in Eq. (2.4) are complemented by the following ones:

$$\eta_1 \geqslant 2 , \quad \eta_{m+1} \geqslant \frac{3}{2} , \tag{2.6}$$

then the growth conditions given by Eq. (1.30) are fulfilled and the existence of solutions to the associated nonlinear boundary value problem is ensured (see Section 1.4.4).

Upon expanding the stored energy function near the reference configuration, it can be deduced that the model parameters further satisfy the following consistency relation with linearized elasticity:

$$\sum_{k=1}^{m+n} p_k \eta_k^2 = 2\mu\,, \tag{2.7}$$

where μ is the shear modulus at small strains (recall that only isotropic, incompressible materials are considered at this stage); see [54, 55].

For $m = n = 1$ and $\eta_1 = \eta_2 = 2$, the potential (2.2) reduces to the Mooney-Rivlin model for incompressible materials:

$$w([F]) = p_1(\|[F]\|_F^2 - 3) + p_2(\|\mathrm{Cof}([F])\|_F^2 - 3)\,, \quad \forall [F] \in \mathbb{M}^3_+\,, \tag{2.8}$$

with $p_1 > 0$, $p_2 > 0$ and $4p_1 + 4p_2 = 2\mu$. Note that the single-term stored energy function of the form

$$w([F]) = p_1(\mathrm{Tr}(([F]^T[F])^{\eta_1/2}) - 3)\,, \quad \forall [F] \in \mathbb{M}^3_+\,, \tag{2.9}$$

satisfies the assumptions in Ball's existence theorem if $p_1 = 2\mu/\eta_1^2 > 0$ and $\eta_1 \geqslant 3$ [65].

Finally, the Neo-Hookean model for incompressible materials [81] can be obtained by taking $\eta_1 = 2$ in the above equation, that is,

$$w([F]) = \frac{\mu}{2}(\|[F]\|_F^2 - 3)\,, \quad \forall [F] \in \mathbb{M}^3_+\,. \tag{2.10}$$

Specific discussions on existence theorems for the Neo-Hookean model can be found in [65, 82].

2.3 Construction of the probabilistic model

Let $\mathcal{W}$ be the stochastic stored energy function corresponding to the probabilistic modeling of w, defined on a probability space $(\Theta, \mathcal{T}, \mathbb{P})$ and indexed by the matrix set $\mathbb{M}^3_+$.

In this work, the vector of exponents $\boldsymbol{\eta}$ is kept deterministic (hence, the coercivity property does not constraint the construction of the probabilistic model) and a few remarks related to this modeling choice are in order. It should be noticed first that proceeding with random exponents does not raise any technical issue while constructing the probabilistic formulation. However, this would lead to a high-dimensional parametrization that would make model identification hardly feasible, especially when the amount of data is limited. In addition, the consideration of random exponents amounts to modifying the space in which the nonlinear response is approximated from one sample to another, which is not justified in most applications. Finally, it will be seen at the end of this chapter that randomizing the vector $\mathbf{p}$ is sufficient to properly mimic the variability observed for a wide class of materials.

Let $\mathbf{P} = (P_1, \ldots, P_{m+n})$ be the random vector corresponding to the probabilistic modeling of $\mathbf{p}$, and define the stochastic Ogden-type stored energy function as

$$\mathcal{W}([F]) = \sum_{i=1}^{m} P_i(\mathrm{Tr}(([F]^T[F])^{\eta_i/2}) - 3) + \sum_{j=1}^{n} P_{j+m}(\mathrm{Tr}((\mathrm{Cof}([F]^T[F]))^{\eta_{j+m}/2}) - 3)\,, \quad \forall [F] \in \mathbb{M}^3_+\,. \tag{2.11}$$

The construction of a probabilistic model for the random variable $\mathbf{P}$ is performed by imposing that the stochastic stored energy function is polyconvex and consistent with linearized elasticity almost surely (a.s.). The first constraint imposes that

$$P_k > 0 \text{ a.s.}, \quad 1 \leqslant k \leqslant m+n\,, \tag{2.12}$$

while the second one yields the coupling equation (see Eq. (2.7))

$$\sum_{k=1}^{m+n} P_k \eta_k^2 = 2\mathbb{\mu} \text{ a.s.}, \tag{2.13}$$

where $\mathbb{\mu}$ is the random variable corresponding to the stochastic modeling of the shear modulus μ. In practice, imposing Eq. (2.13) can be achieved in two different ways. In a first approach, a probabilistic model can be constructed for the random vector $\mathbf{P}$ without taking into account the consistency relation. The probability distribution of the random shear modulus can then easily be determined by an appropriate measure transformation. While this choice leads to simpler derivations, it does not allow constraints on the elastic modulus to be accounted for, at least in a direct form. A second, two-step approach can be developed where a probabilistic model is first constructed for the random shear modulus $\mathbb{\mu}$, and a stochastic model for random variable $\mathbf{P}$ is subsequently derived through a conditioning on $\mathbb{\mu}$. In order to ensure that Eq. (2.13) holds a.s., an arbitrary component of $\mathbf{P}$, say P_{m+n}, must then be selected and defined afterwards as:

$$P_{m+n} = \frac{1}{\eta_{m+n}^2}\left(2\mathbb{\mu} - \sum_{k=1}^{m+n-1} P_k \eta_k^2\right). \tag{2.14}$$

In this case, the construction of the probabilistic model is achieved on the random variables $\mathbb{\mu}$ and $(P_1, \ldots, P_{m+n-1})$. More precisely, the joint probability density function $f_{\mathbb{\mu},P_1,\ldots,P_{m+n-1}}$ is written as

$$f_{\mathbb{\mu},P_1,\ldots,P_{m+n-1}}(\mu, p_1, \ldots, p_{m+n-1}) = f_{\mathbb{\mu}}(\mu) \times f_{P_1,\ldots,P_{m+n-1}|\mathbb{\mu}=\mu}(p_1, \ldots, p_{m+n-1}|\mu)\,, \tag{2.15}$$

where $f_{\mathbb{\mu}}$ is the probability density function of $\mathbb{\mu}$ and $f_{P_1,\ldots,P_{m+n-1}|\mathbb{\mu}=\mu}$ denotes the conditional probability density function of $(P_1, \ldots, P_{m+n-1})$ given $\mathbb{\mu} = \mu$. Note that the probabilistic model for $f_{\mathbb{\mu},P_1,\ldots,P_{m+n-1}}$ completely defines the system of marginal probability distributions for the stochastic process $\{\mathcal{W}([F]), [F] \in \mathbb{M}_+^3\}$.

In what follows, the second strategy is pursued. For technical convenience, we introduce the normalized random variable $\mathbf{U}$ defined as

$$U_k = \frac{\eta_k^2}{2\mathbb{\mu}} P_k\,, \quad 1 \leqslant k \leqslant m+n-1\,, \tag{2.16}$$

where $\mathbb{\mu} > 0$ a.s., by construction. By combining Eqs. (2.14) and (2.16), it can be deduced that the random variable $\mathbf{U}$ takes its values in the set $\mathcal{S}$ defined as

$$\mathcal{S} = \left\{\mathbf{u} \in (0,1)^{m+n-1} \,:\, 1 - \sum_{k=1}^{m+n-1} u_k > 0\right\} \tag{2.17}$$

and corresponding to the interior of a simplex. The conditional probability density function $f_{P_1,\ldots,P_{m+n-1}|\mathbb{\mu}}$ can then be written as

$$f_{P_1,\ldots,P_{m+n-1}|\mathbb{\mu}=\mu}(p_1, \ldots, p_{m+n-1}|\mu) = f_{\mathbf{U}}\left(\frac{\eta_1^2}{2\mu}p_1, \ldots, \frac{\eta_{m+n-1}^2}{2\mu}p_{m+n-1}\right) \times \prod_{k=1}^{m+n-1} \frac{\eta_k^2}{2\mu}\,, \tag{2.18}$$

where $f_{\mathbf{U}}$ is the probability density function of the random variable $\mathbf{U}$.

In this work, explicit forms for $f_{\mathbb{\mu}}$ and $f_{\mathbf{U}}$ are constructed within the framework of information theory, using the principle of maximum entropy. This important tool is briefly introduced using generic notations in the next section.

2.4 Maximum entropy principle

Let $\mathbf{X}$ be a vector-valued random variable defined by a probability distribution $f_{\mathbf{X}}(\mathbf{x})d\mathbf{x}$, the definition of which is sought. Assume that the probability density function $f_{\mathbf{X}}$ has a support denoted by $\mathscr{S}_{\mathbf{X}} \subseteq \mathbb{R}^n$ (hence, $f_{\mathbf{X}}(\mathbf{x}) = 0$ for $\mathbf{x} \notin \mathscr{S}_{\mathbf{X}}$), with $\mathscr{S}_{\mathbf{X}} \subseteq \mathbb{R}^n$. Additionally, it is assumed that some information related to $\mathbf{X}$ can be formulated in the form of a mathematical expectation:

$$\mathbb{E}\left\{\mathscr{H}\left(\mathbf{X}\right)\right\} = \mathbf{f}\,, \tag{2.19}$$

where $\mathscr{H}$ is a given measurable mapping from $\mathbb{R}^n$ into $\mathbb{R}^N$, with $N \geqslant 1$, and $\mathbf{f}$ is a given vector in $\mathbb{R}^N$. If $\mathscr{H}$ is the identity operator, then $\mathbf{f}$ corresponds to the mean value of $\mathbf{X}$ for instance. When $\mathscr{H}$ gathers several constraints, it is assumed that the latter are algebraically independent.

The Maximum Entropy (MaxEnt) principle then states that the most objective model given the above constraint (see Eq. (2.19)) is defined as [83, 84]

$$f_{\mathbf{X}} = \underset{f \in \mathscr{C}_{\mathbf{X}}}{\operatorname{argmax}}\ \mathscr{E}\{f\}\,, \tag{2.20}$$

where

$$\mathscr{E}\{f\} = -\int_{\mathscr{S}_{\mathbf{X}}} f(\mathbf{x}) \log\left(f(\mathbf{x})\right) d\mathbf{x} \tag{2.21}$$

denotes Shannon's entropy for the probability density function f [85], and $\mathscr{C}_{\mathbf{X}}$ is the set of all probability density functions supported over $\mathscr{S}_{\mathbf{X}}$ and satisfying the constraints defined by Eq. (2.19).

In order to solve the functional optimization problem defined by Eq. (2.20), a Lagrange multiplier $\boldsymbol{\tau}$ with values in $\mathbb{T} \subset \mathbb{R}^N$ and associated with Eq. (2.19) is introduced. Proceeding with the calculus of variation on the associated Lagrangian, the solution is found as

$$f_{\mathbf{X}}(\mathbf{x}) = \mathbb{1}_{\mathscr{S}_{\mathbf{X}}}(\mathbf{x})\, k_0\, \exp\left(-\langle \boldsymbol{\tau}, \mathscr{H}(\mathbf{x})\rangle\right)\,, \tag{2.22}$$

where $\mathbb{1}_{\mathscr{S}_{\mathbf{X}}}$ is the indicator function of $\mathscr{S}_{\mathbf{X}}$ and k_0 is the normalization constant.

In the sequel, the MaxEnt principle will be used to construct the probabilistic models for the random shear modulus $\mathbb{\mu}$ and the conditioned random vector $\mathbf{P}|_{\mathbb{\mu}}$. These models are detailed in Section 2.5 and Sections 2.6–2.7, respectively.

2.5 Stochastic modeling of the shear modulus

Following the previous section, assume that the constraints related to the available information on the stochastic shear modulus $\mathbb{\mu}$ are given by

$$\mathbb{E}\{\mathbb{\mu}\} = \underline{\mu}\,, \quad \underline{\mu} > 0\,, \tag{2.23a}$$

$$\mathbb{E}\{\log(\mathbb{\mu})\} = \nu\,, \quad |\nu| < +\infty\,. \tag{2.23b}$$

The first constraint given by Eq. (2.23a) is related to the mean value of $\mathbb{\mu}$, while the second one is a repulsive term near the origin implying that $\mathbb{\mu}$ and $\mathbb{\mu}^{-1}$ are second-order random variables [86], *i.e.*,

$$\mathbb{E}\{\mathbb{\mu}^2\} < +\infty\,, \quad \mathbb{E}\{\mathbb{\mu}^{-2}\} < +\infty\,. \tag{2.24}$$

Let $\rho_1 \in \mathbb{R}_*^+$ and $(1-\rho_2) \in (-\infty, 1)$ be the Lagrange multipliers associated with the constraints given by Eqs. (2.23a) and (2.23b), respectively. The probability density function $f_{\mathbb{\mu}}$ inferred from the MaxEnt principle then writes

$$f_{\mathbb{\mu}}(\mu) = \mathbb{1}_{\mathbb{R}_*^+}(\mu)\, k_0\, \mu^{\rho_2 - 1} \exp\left(-\rho_1 \mu \right) , \tag{2.25}$$

where $\mathbb{1}_{\mathbb{R}_*^+}$ is the indicator function of $\mathbb{R}_*^+$. It can be seen that the probability law $f_{\mathbb{\mu}}(\mu)d\mu$ thus defined corresponds to a Gamma probability measure with parameters (ρ_2, ρ_1^{-1}). Consequently, the Lagrange multipliers can be expressed in terms of the mean $\underline{\mu}$ and the coefficient of variation $\delta_{\mathbb{\mu}}$ of the random shear modulus, so that

$$f_{\mathbb{\mu}}(\mu) = \mathbb{1}_{\mathbb{R}_*^+}(\mu)\, k_0\, \mu^{\delta_{\mathbb{\mu}}^{-2} - 1} \exp\left(-\frac{\mu}{\underline{\mu}\delta_{\mathbb{\mu}}^2} \right) , \tag{2.26}$$

where

$$k_0 = \frac{1}{(\underline{\mu}\delta_{\mathbb{\mu}}^2)^{\delta_{\mathbb{\mu}}^{-2}} \Gamma(\delta_{\mathbb{\mu}}^{-2})} , \tag{2.27}$$

with Γ the Gamma function [87] defined as

$$\Gamma(z) = \int_0^{+\infty} t^{z-1} \exp(-t)\, dt , \quad \forall\, z > 0 . \tag{2.28}$$

2.6 Stochastic modeling accounting for polyconvexity and small strain consistency

2.6.1 General derivations

Let us now consider the modeling of the $\mathcal{S}$-valued random variable $\mathbf{U}$. As with the shear modulus, repulsive constraints at the boundaries of $\mathcal{S}$ are introduced as

$$\mathbb{E}\{\log(U_k)\} = \nu_k , \quad 1 \leqslant k \leqslant m+n-1 , \tag{2.29a}$$

$$\mathbb{E}\Big\{ \log\Big(1 - \sum_{k=1}^{m+n-1} U_k\Big)\Big\} = \nu_{m+n} , \tag{2.29b}$$

where $|\nu_k| < +\infty$ for $1 \leqslant k \leqslant m+n$. Let $(1-\lambda_1), \ldots, (1-\lambda_{m+n})$ be the associated $(m+n)$ Lagrange multipliers. By invoking the MaxEnt principle, it can then be deduced that the probability density function $f_{\mathbf{U}}$ writes

$$f_{\mathbf{U}}(\mathbf{u}) = \mathbb{1}_{\mathcal{S}}(\mathbf{u})\, k_0 \left(\prod_{k=1}^{m+n-1} u_k^{\lambda_k - 1} \right) \left(1 - \sum_{k=1}^{m+n-1} u_k \right)^{\lambda_{m+n}-1} . \tag{2.30}$$

The above equation shows that $\mathbf{U}$ is distributed according to a Dirichlet-type I probability law [88] with parameters $\lambda_1, \ldots, \lambda_{m+n}$, and the normalization constant then takes the form

$$k_0 = \frac{\Gamma(\sum_{k=1}^{m+n} \lambda_k)}{\prod_{k=1}^{m+n} \Gamma(\lambda_k)} . \tag{2.31}$$

The integrality of $f_{\mathbf{U}}$ requires the Lagrange multipliers to be all strictly positive. In what follows, the additional constraints $\lambda_k \geqslant 1$, $1 \leqslant k \leqslant m+n$, are considered to yield unimodal first-order marginal probability density functions. The admissible set $\mathbb{D}_{\boldsymbol{\lambda}}$ for the vector-valued Lagrange multiplier $\boldsymbol{\lambda} = (\lambda_1, \ldots, \lambda_{m+n})$ is chosen as

$$\mathbb{D}_{\boldsymbol{\lambda}} = \{\boldsymbol{\lambda} \in \mathbb{R}^{m+n} \, : \, \lambda_k \geqslant 1 \, , \quad 1 \leqslant k \leqslant m+n\} \, . \tag{2.32}$$

It should be noticed at this point that the selection of the random variable P_k, $1 \leqslant k \leqslant m+n$, in the consistency relation (see Eqs. (2.14) and (2.13)) is arbitrary, given the symmetry of the constraints given by Eqs. (2.29a)–(2.29b). From the proposed construction, we can now state the following proposition.

Proposition 2.1. *For $m \geqslant 1$ and $n \geqslant 1$, let $\mathcal{W}$ be the stochastic stored energy function defined as*

$$\mathcal{W}([F]) = \sum_{i=1}^{m} P_i(\mathrm{Tr}(([F]^T[F])^{\eta_i/2}) - 3) + \sum_{j=1}^{n} P_{j+m}(\mathrm{Tr}((\mathrm{Cof}([F]^T[F]))^{\eta_{j+m}/2}) - 3) \tag{2.33}$$

for all $[F]$ in $\mathbb{M}^3_+$, in which

(i) $\eta_1 \geqslant 2$, $\eta_{m+1} \geqslant 3/2$, $\eta_1 \geqslant \cdots \geqslant \eta_m \geqslant 1$, and $\eta_{m+1} \geqslant \ldots \eta_{m+n} \geqslant 1$;

(ii) the random shear modulus $\mathbb{\mu}$ is Gamma-distributed with parameters $(\delta_{\mathbb{\mu}}^{-2}, \underline{\mu}\delta_{\mathbb{\mu}}^2)$, where $\underline{\mu}$ and $\delta_{\mathbb{\mu}}$ are respectively the mean value and coefficient of variation of $\mathbb{\mu}$;

(iii) the random variables P_k, $1 \leqslant k \leqslant m+n$, are defined as

$$P_k = \frac{2\mathbb{\mu}}{\eta_k^2} U_k \, , \quad 1 \leqslant k \leqslant m+n-1 \, , \quad P_{m+n} = \frac{2\mathbb{\mu}}{\eta_{m+n}^2} \left(1 - \sum_{k=1}^{m+n-1} U_k\right) , \tag{2.34}$$

where the random variable $\mathbf{U} = (U_1, \ldots, U_{m+n-1})$ takes its values in

$$\mathcal{S} = \left\{ \mathbf{u} \in (0,1)^{m+n-1} \, : \, 1 - \sum_{k=1}^{m+n-1} u_k > 0 \right\} , \tag{2.35}$$

and follows a Dirichlet-type I distribution with a vector-valued parameter $\boldsymbol{\lambda}$ such that $\lambda_k \geqslant 1$ for $1 \leqslant k \leqslant m+n$.

Then the stored energy function $\mathcal{W}$ is polyconvex, coherent at small strains, and coercive almost surely.

The above proposition ensures the well-posedness of the nonlinear stochastic boundary value problem for any element in the class of stochastic stored energy functions.

Remark 2.6.1. *From a practical standpoint, realizations of $\mathbf{U}$ can easily be drawn as follows. If $Y_1, \ldots, Y_{m+n}$ are independent Gamma random variables with respective parameters $(\lambda_1, 1)$, …, $(\lambda_{m+n}, 1)$, then the random variable $\mathbf{U}$ can be defined component-wise as [89]*

$$U_i = Y_i \times \left(\sum_{k=1}^{m+n} Y_k \right)^{-1} , \quad 1 \leqslant i \leqslant m+n-1 \, . \tag{2.36}$$

Remark 2.6.2. *Explicit expressions of the probability density functions* $p \mapsto f_{P_k}(p)$ *for the random variables* $P_1, \ldots, P_{m+n}$ *can be readily obtained. In fact, given that the shear modulus is gamma distributed with parameters* (ρ_2, ρ_1^{-1}) *and that the marginal probability measures of* U_k *and* $(1 - \sum_{k=1}^{m+n-1} U_k)$ *are beta distributions with parameters* (λ_k, χ_k) *and* $(\lambda_{m+n}, \chi_{m+n})$ *respectively, it can be shown that [90]*

$$f_{P_k}(p) = \mathbb{1}_{\mathbb{R}_*^+}(p)\, k_0\, p^{\rho_2 - 1} \exp\left(-\frac{\eta_k^2 \rho_1}{2} p\right) \mathcal{U}\left(\chi_k, 1 + \rho_2 - \lambda_k, \frac{\eta_k^2 \rho_1}{2} p\right) , \quad 1 \leqslant k \leqslant m+n , \tag{2.37}$$

where $\mathcal{U}$ *corresponds to the Kummer function [87]*

$$\mathcal{U}(a, b; z) = \frac{1}{\Gamma(a)} \int_0^{+\infty} \exp(-zt) t^{a-1} (1+t)^{b-a-1}\, dt , \tag{2.38}$$

and

$$\chi_k = (\sum_{\ell=1}^{m+n} \lambda_\ell) - \lambda_k , \quad 1 \leqslant k \leqslant m+n . \tag{2.39}$$

The normalization constant k_0 *writes*

$$k_0 = \left(\frac{2}{\rho_1 \eta_k^2}\right)^{-\rho_2} \frac{\Gamma(\chi_k)}{\Gamma(\rho_2) \mathcal{B}(\lambda_k, \chi_k)} . \tag{2.40}$$

2.6.2 Case of Mooney-Rivlin materials

In the case of an incompressible isotropic Mooney-Rivlin model, for which $m = n = 1$ and $\eta_1 = \eta_2 = 2$, the stochastic stored energy function reduces to

$$\mathcal{W}([F]) = P_1(\|[F]\|_F^2 - 3) + P_2(\|\mathrm{Cof}([F])\|_F^2 - 3) , \quad \forall\, [F] \in \mathbb{M}_+^3 , \tag{2.41}$$

where the random coefficients are given by

$$P_1 = \frac{\mathbb{\mu}}{2} U , \quad P_2 = \frac{\mathbb{\mu}}{2}(1 - U) . \tag{2.42}$$

The random variable U follows a beta-type I distribution with parameters $\lambda_1 \geqslant 1$ and $\lambda_2 \geqslant 1$, that is

$$f_U(u) = \mathbb{1}_{(0,1)}(u) \{\mathcal{B}(\lambda_1, \lambda_2)\}^{-1} u^{\lambda_1 - 1} (1-u)^{\lambda_2 - 1} , \tag{2.43}$$

in which $\mathcal{B}$ is the beta function given by [87]

$$\mathcal{B}(x, y) = \int_0^1 t^{x-1} (1-t)^{y-1}\, dt . \tag{2.44}$$

2.6.3 Case of single-term Ogden stochastic stored energy functions

The stochastic stored energy function

$$\mathcal{W}([F]) = P_1(\mathrm{Tr}(([F]^T [F])^{\eta_1/2}) - 3) , \quad \forall\, [F] \in \mathbb{M}_+^3 , \tag{2.45}$$

is admissible (in the sense that the associated nonlinear stochastic boundary value problem is well posed) if $P_1 > 0$ almost surely, and $\eta_1 \geqslant 3$ (see [65]). Moreover, consistency with linearized elasticity yields $P_1 \eta_1^2 = 2\mathbb{\mu}$, so that the stochastic stored energy function can be rewritten as

$$\mathcal{W}([F]) = \frac{2\mathbb{\mu}}{\eta_1^2}(\mathrm{Tr}(([F]^T [F])^{\eta_1/2}) - 3) , \quad \forall\, [F] \in \mathbb{M}_+^3 . \tag{2.46}$$

The particular case $\eta_1 = 2$ leads to the Neo-Hookean model in three dimensional elasticity.

2.6.4 Computation of the Lagrange multipliers

Two cases can be distinguished regarding the computation of the Lagrange multipliers, depending on whether or not the right-hand sides in Eqs. (2.23b) and (2.29a)–(2.29b) are known. When the parameters ν and $\nu_1, \dots, \nu_{m+n}$ are unknown, the Lagrange multipliers can be identified by solving a statistical inverse problem in which the left-hand sides of the aforementioned equations are not estimated.

When the parameters $\nu_1, \dots, \nu_{m+n}$ are known, explicit expressions of the constraints can be derived as functions of the multipliers, owing to some properties exhibited by the probability laws under consideration. This enables the robust and efficient treatment of the left-hand sides in Eqs. (2.29a)–(2.29b) without resorting to Monte-Carlo simulations. More specifically, it can first be shown that the marginal probability density functions f_{U_k} and f_V of the random variables U_k, $1 \leqslant k \leqslant m+n$, and $V = 1 - \sum_{k=1}^{m+n-1} U_k$, correspond to beta distributions with parameters (λ_k, χ_k), where it is recalled that $\chi_k = (\sum_{\ell=1}^{m+n} \lambda_\ell) - \lambda_k$. These probability density functions thus read as

$$f_{U_k}(u) = \mathbb{1}_{(0,1)}(u) \frac{1}{\mathcal{B}(\lambda_k, \chi_k)} u^{\lambda_k - 1}(1-u)^{\chi_k - 1} \tag{2.47}$$

and

$$f_V(v) = \mathbb{1}_{(0,1)}(v) \frac{1}{\mathcal{B}(\lambda_{m+n}, \chi_{m+n})} v^{\lambda_{m+n} - 1}(1-v)^{\chi_{m+n} - 1} \, . \tag{2.48}$$

From the equality

$$\mathbb{E}\Big\{ \log\Big(1 - \sum_{k=1}^{m+n-1} U_k\Big)\Big\} = \{\mathcal{B}(\lambda_{m+n}, \chi_{m+n})\}^{-1} \int_0^1 \log(v) v^{\lambda_{m+n} - 1}(1-v)^{\chi_{m+n} - 1} \, dv \, , \tag{2.49}$$

it follows that

$$\begin{aligned} \mathbb{E}\Big\{ \log\Big(1 - \sum_{k=1}^{m+n-1} U_k\Big)\Big\} &= \{\mathcal{B}(\lambda_{m+n}, \chi_{m+n})\}^{-1} \frac{\partial}{\partial \lambda_{m+n}} \int_0^1 v^{\lambda_{m+n} - 1}(1-v)^{\chi_{m+n} - 1} \, dv \, , \\ &= \frac{\partial}{\partial \lambda_{m+n}} \log(\mathcal{B}(\lambda_{m+n}, \chi_{m+n})) \, . \end{aligned} \tag{2.50}$$

Since $\mathcal{B}(x,y) = \Gamma(x)\Gamma(y)/\Gamma(x+y)$ for all $(x,y) \in \mathbb{R}_*^+ \times \mathbb{R}_*^+$, it can be deduced that

$$\mathbb{E}\Big\{ \log\Big(1 - \sum_{k=1}^{m+n-1} U_k\Big)\Big\} = \frac{\Gamma'(\lambda_{m+n})}{\Gamma(\lambda_{m+n})} - \frac{\Gamma'(\sum_{k=1}^{m+n} \lambda_k)}{\Gamma(\sum_{k=1}^{m+n} \lambda_k)} \, . \tag{2.51}$$

Proceeding similarly for the random variables $U_1, \dots, U_{m+n-1}$, one has

$$\mathbb{E}\{\log(U_k)\} = \frac{\Gamma'(\lambda_k)}{\Gamma(\lambda_k)} - \frac{\Gamma'(\sum_{k=1}^{m+n} \lambda_k)}{\Gamma(\sum_{k=1}^{m+n} \lambda_k)} \, , \quad 1 \leqslant k \leqslant m+n-1 \, . \tag{2.52}$$

By letting ψ be the digamma function defined as $\psi(z) = \Gamma'(z)/\Gamma(z)$ for all $z > 0$ (see [87]), it follows that the constraints given by Eqs. (2.29a)-(2.29b) are finally given by (see [91] for similar results)

$$\psi(\lambda_k) - \psi\Big(\sum_{k=1}^{m+n} \lambda_k\Big) = \nu_k \, , \quad 1 \leqslant k \leqslant m+n \, . \tag{2.53}$$

In practice, the above system of $(m+n)$ nonlinear equations can be solved by using any suitable optimization algorithm, such as a nonlinear least-squares algorithm or a Newton-Rapshon algorithm. Given some initial guess $\boldsymbol{\lambda}^{(0)} \in \mathbb{D}_{\boldsymbol{\lambda}}$, the Newton-Raphson scheme is given by

$$\text{for} \quad \ell \geqslant 0 : \quad [K(\boldsymbol{\lambda}^{(\ell)})](\boldsymbol{\lambda}^{(\ell+1)} - \boldsymbol{\lambda}^{(\ell)}) = -\mathbf{r}(\boldsymbol{\lambda}^{(\ell)}) \,, \tag{2.54}$$

where the function $\mathbf{r}$ is defined as $r_k(\boldsymbol{\lambda}) = \nu_k - \Big(\psi(\lambda_k) - \psi\Big(\sum_{k=1}^{m+n} \lambda_k\Big)\Big)$ for $1 \leqslant k \leqslant m+n$, and the tangent matrix reads as

$$[K(\boldsymbol{\lambda})]_{jk} = \frac{\partial r_j(\boldsymbol{\lambda})}{\partial \lambda_k} = -\Big(\psi'(\lambda_j)\delta_{jk} - \psi'\Big(\sum_{i=1}^{m+n} \lambda_i\Big)\Big) \,, \quad 1 \leqslant j,k \leqslant m+n \,, \tag{2.55}$$

where ψ' is referred to as the trigamma function [87].

2.7 Stochastic modeling accounting for mean values, polyconvexity and small strain consistency

2.7.1 General derivations

Assume now that the repulsive constraints (2.29a)–(2.29b)) are supplemented with a constraint related to the mean value of $\mathbf{U}$, that is:

$$\mathbb{E}\{\mathbf{U}\} = \underline{\mathbf{u}} \,, \tag{2.56}$$

where $\underline{\mathbf{u}}$ is a given vector in $\mathcal{S}$. In this case, the probability density function $f_{\mathbf{U}}$ obtained through entropy maximization takes the form

$$f_{\mathbf{U}}(\mathbf{u}) = \mathbb{1}_{\mathcal{S}}(\mathbf{u})\, k_0 \left(\prod_{k=1}^{m+n-1} u_k^{\lambda_k - 1}\right)\left(1 - \sum_{k=1}^{m+n-1} u_k\right)^{\lambda_{m+n}-1} \exp\left(-\sum_{k=1}^{m+n-1} \xi_k u_k\right) , \tag{2.57}$$

where $\{\lambda_k\}_{k=1}^{m+n}$ and $\{\xi_k\}_{k=1}^{m+n-1}$ are the sets of Lagrange multipliers associated with the repulsive constraints (see Eqs. (2.29a–2.29b)) and Eq. (2.56). This probability density function corresponds to a multivariate Kummer-Beta distribution if $\xi_k = \xi$, $1 \leqslant k \leqslant m+n-1$, in which case an explicit algebraic expression for k_0 can be obtained in terms of confluent hypergeometric functions [92]. Furthermore, the proposition stated in Section 2.6 similarly holds when $\mathbf{U}$ follows the probability density function given by Eq. (2.57), hence ensuring the well-posedness of the stochastic boundary value problem.

The probability density function $f_{\mathbf{U}}$ is non-standard and can be sampled by using Markov Chain Monte Carlo approaches (see, *e.g.*, [93]). In the present study, sampling is achieved by solving a Langevin dynamics [94] with an adaptive stochastic time step [30].

2.7.2 Case of Mooney-Rivlin materials

For the incompressible Mooney-Rivlin model, the probability density function f_U corresponds to a Kummer-Beta distribution with parameters $(\lambda_1, \lambda_2, \xi_1)$, that is

$$f_U(u) = \mathbb{1}_{\mathcal{S}}(u)\, k_0\, u^{\lambda_1 - 1}(1-u)^{\lambda_2 - 1} \exp(-\xi_1 u) \,, \tag{2.58}$$

where $\lambda_1 \geqslant 1$, $\lambda_2 \geqslant 1$ and $\xi_1 \in \mathbb{R}$ [95, 96, 88]. It can be deduced that the normalization constant takes the form

$$k_0 = \frac{1}{\mathcal{B}(\lambda_1, \lambda_2)\mathcal{F}(\lambda_1, \lambda_1 + \lambda_2, -\xi_1)}\,, \tag{2.59}$$

in which $\mathcal{F}$ stands for the confluent hypergeometric function (see, *e.g.*, [87]), *i.e.*,

$$\mathcal{F}(x, y, z) = \frac{1}{\mathcal{B}(x, y-x)} \int_0^1 u^{x-1}(1-u)^{y-x-1} \exp(zu)\, du\,. \tag{2.60}$$

Upon evaluating the constraints given by Eqs. (2.29a)-(2.29b) and Eq. (2.56), it can be shown that the Lagrange multipliers satisfy the following set of nonlinear equations

$$\psi(\lambda_1) - \psi(\lambda_1 + \lambda_2) + \frac{\partial \log(\mathcal{F}(\lambda_1, \lambda_1 + \lambda_2, -\xi_1))}{\partial \lambda_1} = \nu_1\,, \tag{2.61a}$$

$$\psi(\lambda_2) - \psi(\lambda_1 + \lambda_2) + \frac{\partial \log(\mathcal{F}(\lambda_1, \lambda_1 + \lambda_2, -\xi_1))}{\partial \lambda_2} = \nu_2\,, \tag{2.61b}$$

$$\frac{\lambda_1}{\lambda_1 + \lambda_2} \frac{\mathcal{F}(\lambda_1 + 1, \lambda_1 + \lambda_2 + 1, -\xi_1)}{\mathcal{F}(\lambda_1, \lambda_1 + \lambda_2, -\xi_1)} = \mathbb{E}\{U\}\,. \tag{2.61c}$$

In practice, solving for ξ_1 in Eq. (2.61c) allows one to enforce the constraint on the mean value for given repulsive conditions at the boundaries of $\mathcal{S}$, controlled by the Lagrange multipliers λ_1 and λ_2.

2.8 Numerical illustrations

In the rest of this chapter, we consider a specimen of a hyperelastic material undergoing a homogeneous simple tension defined by a prescribed stretch υ along $\mathbf{e}_1$ (see, *e.g.*, [78, 79]) . In this case, the deformation gradient takes the form

$$[F] = \upsilon\, \mathbf{e}_1 \otimes \mathbf{e}_1 + \upsilon^{-1/2}(\mathbf{e}_2 \otimes \mathbf{e}_2 + \mathbf{e}_3 \otimes \mathbf{e}_3)\,. \tag{2.62}$$

The non-vanishing stochastic Cauchy stress (along $\mathbf{e}_1$) associated with the stochastic Ogden-type stored energy function is then given by

$$\Sigma(\upsilon) = \sum_{i=1}^{m} P_i \eta_i (\upsilon^{\eta_i} - \upsilon^{-\eta_i/2}) + \sum_{j=1}^{n} P_{j+m} \eta_{j+m} (\upsilon^{\eta_{j+m}/2} - \upsilon^{-\eta_{j+m}})\,, \quad \upsilon > 0\,. \tag{2.63}$$

Below, the computation of the Lagrange multipliers for given equality constraints is not addressed (see the discussion in Section 2.6.4). As an alternative, these multipliers are considered as free model parameters and parametric studies are performed in order to illustrate the modeling capabilities of the proposed stochastic models.

2.8.1 Monte Carlo simulations without mean constraints

2.8.1.1 Case of incompressible Neo-Hookean materials

For the incompressible Neo-Hookean model, the random Cauchy stress reduces to

$$\Sigma(\upsilon) = \mathbb{\mu}\Big(\upsilon^2 - \frac{1}{\upsilon}\Big)\,, \quad \forall\, \upsilon > 0\,. \tag{2.64}$$

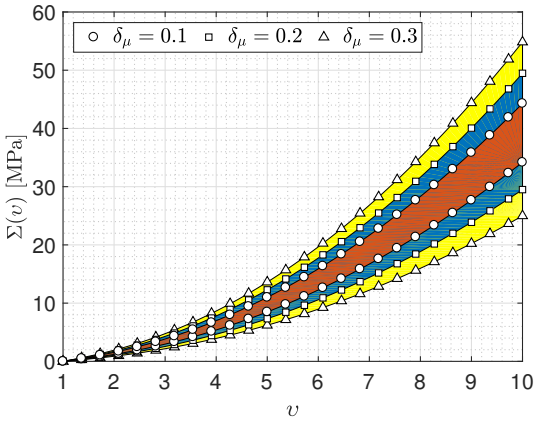

Figure 2.1 – Confidence regions with a probability level of 0.9 of the Cauchy stress for the incompressible Neo-Hookean model and coefficient of variations δ_{μ} ranging from 0.1 to 0.3.

The mean value $\underline{\mu}$ of the random shear modulus is chosen as $\underline{\mu} = 0.39$ MPa. Confidence regions at a 0.9 probability level for the random Cauchy stress are shown in Fig. 2.1 for different values of the coefficient of variation δ_{μ}. As expected, the probabilistic model allows one to generate different levels of statistical fluctuations around the given mean function $v \mapsto \underline{\mu}(v^2 - 1/v)$. For a given value of δ_{μ}, the variance thus exhibited turns out to increase along along with the stretch, which is in accordance with the experimental trends that can be found in the literature.

2.8.1.2 Case of incompressible Mooney-Rivlin materials

For incompressible Mooney-Rivlin materials, the stochastic Cauchy stress is given by

$$\Sigma(v) = \left(2P_1 + \frac{2P_2}{v}\right)\left(v^2 - \frac{1}{v}\right) , \tag{2.65}$$

where the random variables P_1 and P_2 are defined by Eqs. (2.42–2.43). Confidence regions for the random Cauchy stress are shown in Fig. 2.2 for $\lambda_1 = \lambda_2 = \lambda \in \{1, 5, 30\}$, $\delta_{\mu} = 0.1$ (left panel) and $\delta_{\mu} = 0.2$ (right panel). Similar results are displayed in Figs. 2.3 and 2.4, for various

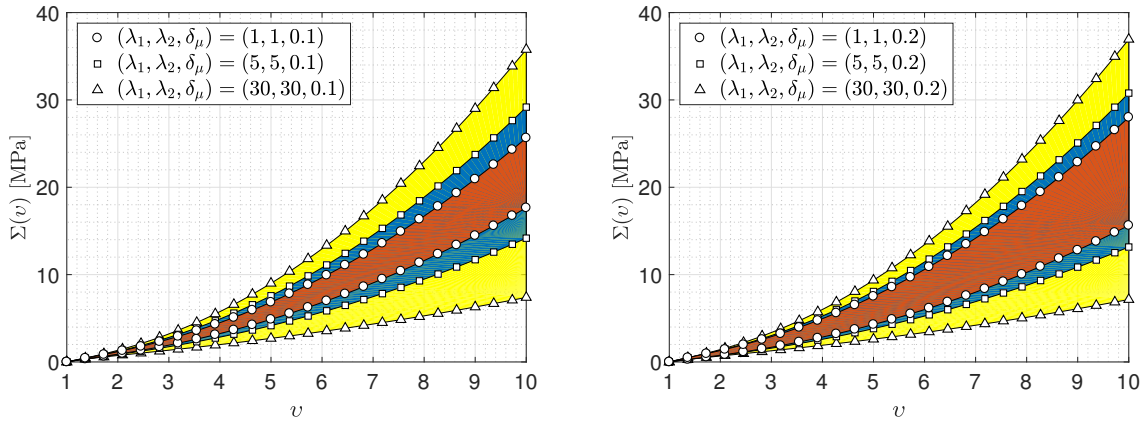

Figure 2.2 – Confidence regions at a 0.9 probability level of the Cauchy stress for $\lambda_1 = \lambda_2 = \lambda$, $\delta_{\mu} = 0.1$ (left panel) and $\delta_{\mu} = 0.2$ (right panel).

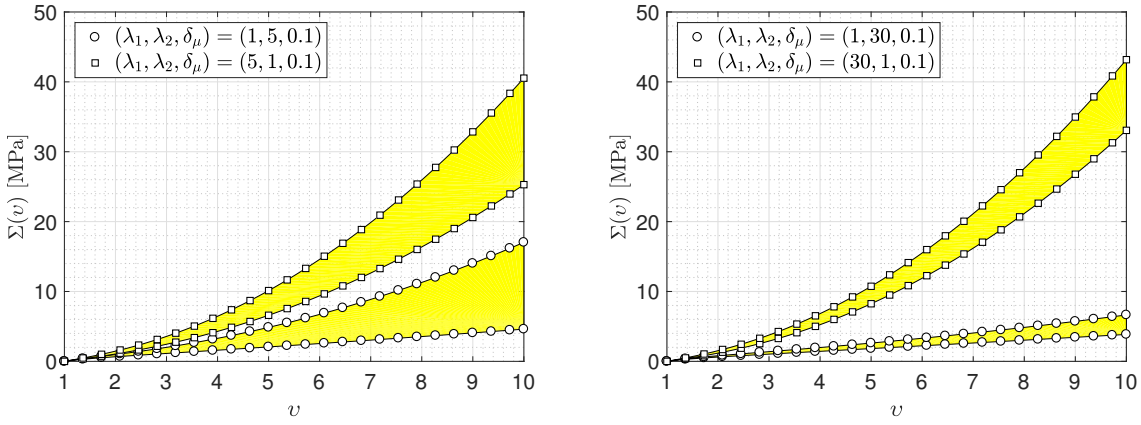

Figure 2.3 – Confidence regions at a 0.9 probability level of the Cauchy stress for different sets of Lagrange multipliers (λ_1, λ_2) and a fixed coefficient of variation $\delta_{\mathbb{U}} = 0.2$.

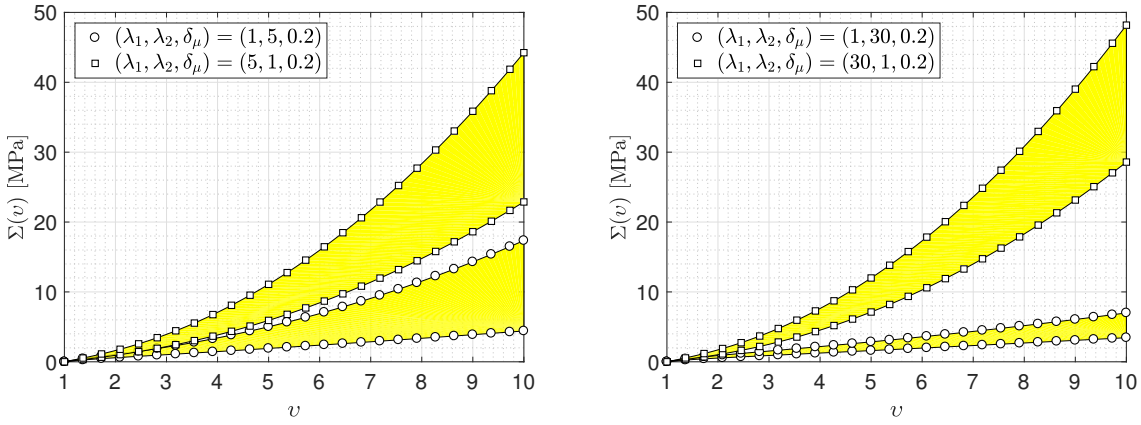

Figure 2.4 – Confidence regions at a 0.9 probability level of the Cauchy stress for different sets of Lagrange multipliers (λ_1, λ_2) and a fixed coefficient of variation $\delta_{\mathbb{U}} = 0.2$.

combinations of λ_1, λ_2 and $\delta_{\mathbb{U}}$. It is seen that different behaviors can be simulated by properly selecting the values of the Lagrange multipliers, hence illustrating the flexibility of the proposed stochastic model. More precisely, it is observed that increasing the value of λ_1 for fixed values of λ_2 and $\delta_{\mathbb{U}}$ pushes the lower bound of the confidence region upwards (meaning that the variability in the stress response is reduced). In a 'symmetric' way, increasing the value of λ_2 for fixed values of λ_1 and $\delta_{\mathbb{U}}$ pushes the upper bound of the confidence region downwards. As expected, the level of repulsion allowed is seen to depend on the selected value of $\delta_{\mathbb{U}}$.

2.8.2 Monte Carlo simulations with mean constraints

The stochastic model developed in Section 2.7 is now considered. In the case of a Mooney-Rivlin material, the random variable U follows a Kummer-Beta distribution defined by the probability density function given by Eq. (2.58) with parameters $\lambda_1 \geqslant 1$, $\lambda_2 \geqslant 1$ and $\xi_1 \in \mathbb{R}$. Confidence regions of the random Cauchy stress are displayed in Fig. 2.5 for $\lambda_1 = \lambda_2 = 15$ and several values of ξ_1 in $\mathbb{R}$. While the additional Lagrange multiplier ξ_1 allows for specifying the mean function for the Cauchy stress, it is seen that the value of this multiplier also slightly affects the level of fluctuations (for given repulsive conditions). In order to proceed with a target mean

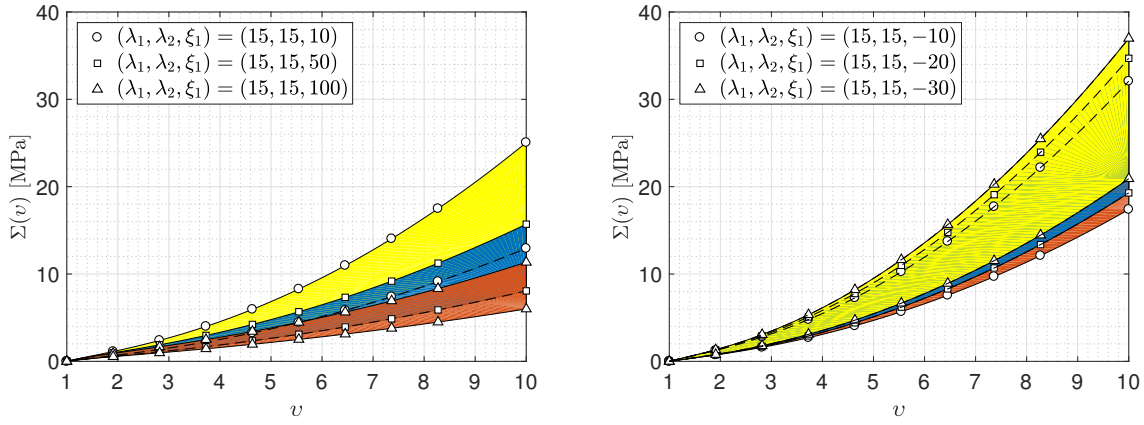

Figure 2.5 – Confidence regions with a 0.9 probability level of the Cauchy stress for $\lambda_1 = \lambda_2 = 15$, $\delta_{\mathbb{U}} = 0.2$ and various values for the remaining Lagrange multiplier $\xi_1 \in \mathbb{R}$.

function while being able to select a given level of statistical fluctuations, it is indeed necessary to enforce the mean constraint given by Eq. (2.61c) for arbitrary Lagrange multipliers (λ_1, λ_2). To illustrate this point, assume that the target mean value of the random variable U is given by $\mathbb{E}\{U\} = 0.4$. The Lagrange multiplier ξ_1 can hence be seen as a function of (λ_1, λ_2) and must satisfy the equation

$$\frac{\lambda_1}{\lambda_1 + \lambda_2} \frac{\mathcal{F}(\lambda_1 + 1, \lambda_1 + \lambda_2 + 1, -\xi_1)}{\mathcal{F}(\lambda_1, \lambda_1 + \lambda_2, -\xi_1)} = 0.4 \ . \tag{2.66}$$

The above equation can be solved by using, for instance, a nonlinear least-square algorithm, and the hypergeometric function can be computed following the algorithm proposed in [97]. The graph of $(\lambda_1, \lambda_2) \mapsto \xi_1(\lambda_1, \lambda_2)$ thus constructed is shown in Fig. 2.6.

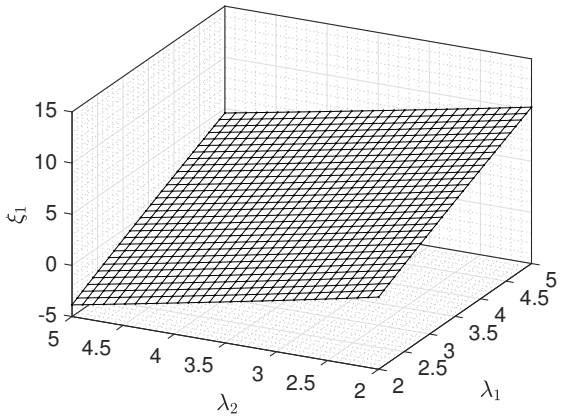

Figure 2.6 – Graph of $(\lambda_1, \lambda_1) \mapsto \xi_1(\lambda_1, \lambda_2)$ such that $\mathbb{E}\{U\} = 0.4$.

Confidence regions at 90% for the random Cauchy stress obtained for some values of $(\lambda_1, \lambda_2, \xi_1)$ such that $\mathbb{E}\{U\} = 0.4$ are shown in Fig. 2.7, and the probability density functions associated with the random variable U are further shown in Fig. 2.8.

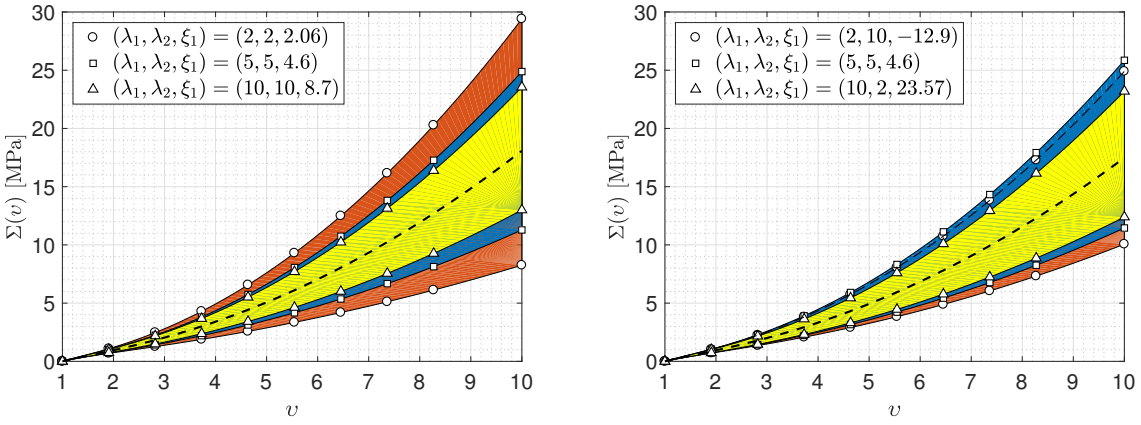

Figure 2.7 – Confidence regions with a 0.9 probability level of the Cauchy stress for selected values of (λ_1, λ_2) and ξ_1 such that $\mathbb{E}\{U\} = 0.4$.

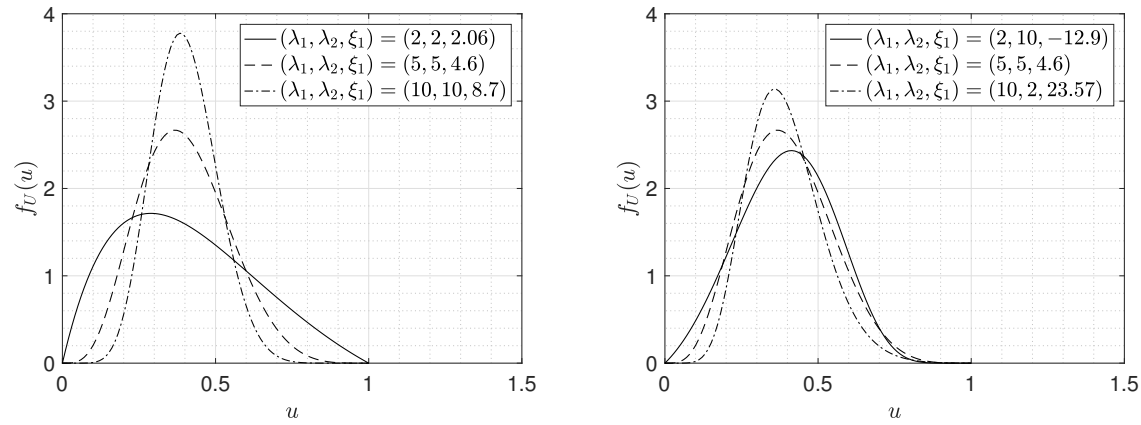

Figure 2.8 – Probability density function f_U of the Kummer-Beta random variable U for selected values of (λ_1, λ_2) and ξ_1 such that $\mathbb{E}\{U\} = 0.4$.

2.9 Identification of the stochastic models using experimental data

In this final section, a two-step methodology enabling the identification of model parameters is proposed and benchmarked on real data. More specifically, we consider the identification of stochastic hyperelastic models for soft biological tissues [46]. The experimental response of such materials typically exhibits a pronounced variability, as largely documented in the literature [6, 7, 8, 9, 10, 11, 12, 13, 14, 15, 16, 17]. While these uncertainties are routinely smoothed out through an averaging procedure along the loading path, they can critically impact simulation predictiveness or clinical diagnosis, for instance. A few attempts to model this variability using a Bayesian approach can be found in [98, 99, 100, 101]. It should be noticed that in contrast with the Bayesian approach where the posterior probability density function is generally unknown analytically, the proposed formulation allows existence results to be invoked and ensures the existence of solutions to the nonlinear boundary value problem almost surely. The developed models are therefore intended to constitute optimal choices for prior distributions.

2.9.1 Calibration of the mean model

Let $\boldsymbol{\lambda} = (\lambda_1, \dots, \lambda_{m+n})$ and $\boldsymbol{\rho} = (\rho_1, \rho_2)$ be the vectors of hyperparameters. In accordance with most available experimental setups, it is assumed that data are available in the form of mean values and standard deviations of the stress response along a given loading path. Homogeneous tensile tests are considered, and the associated non-zero first Piola-Kirchhoff stress is given by (see Eq. (2.63))

$$T(\upsilon) = \sum_{k=1}^{m+n} P_k f_k(\upsilon; \eta_k)\,, \quad \upsilon > 0\,, \tag{2.67}$$

where for notational convenience, the functions

$$f_k(\upsilon; \eta_k) = \begin{cases} \eta_k(\upsilon^{\eta_k - 1} - \upsilon^{-\eta_k/2-1})\,, & k = 1, \dots, m\,, \\ \eta_k(\upsilon^{\eta_k/2-1} - \upsilon^{-\eta_k-1})\,, & k = m+1, \dots, m+n\,, \end{cases} \tag{2.68}$$

were introduced. Below, $\{\underline{\xi}_k^{\exp}\}_{k=1}^N$ and $\{\varsigma_k^{\exp}\}_{k=1}^N$ denote the values of the mean and standard deviation of T at some prescribed stretches $\{\upsilon_k^{\exp}\}_{k=1}^N$: these values define the experimental information based on which the stochastic model has to be identified.

In the first step of the approach, the mean value

$$\underline{\mathbf{p}} = (\underline{p}_1, \dots, \underline{p}_{m+n}) = \mathbb{E}\{\mathbf{P}\}\,, \tag{2.69}$$

of the random variable $\mathbf{P}$ and the deterministic exponents $\boldsymbol{\eta} = (\eta_1, \dots, \eta_{m+n})$ are identified by fitting the mean experimental response with an Ogden-type constitutive model of order (m, n). This can be achieved by solving a least-square optimization problem [78, 79], *i.e.*,

$$(\underline{\mathbf{p}}, \boldsymbol{\eta}) = \underset{(\mathbf{a},\mathbf{b}) \in \mathbb{A}\times\mathbb{B}}{\operatorname{argmin}} \sum_{k=1}^{N} (\underline{t}(\upsilon_k^{\exp}; \mathbf{a}, \mathbf{b}) - \underline{\xi}_k^{\exp})^2\,, \tag{2.70}$$

where $\underline{t}(\upsilon_k^{\exp}; \mathbf{a}, \mathbf{b})$ is the predicted stress at stretch $\upsilon_k^{\exp}$:

$$\underline{t}(\upsilon_k^{\exp}; \mathbf{a}, \mathbf{b}) = \sum_{\ell=1}^{m+n} a_\ell f_\ell(\upsilon_k^{\exp}; b_\ell)\,. \tag{2.71}$$

The admissible sets are defined according to Section 2.2 and are given by

$$\mathbb{A} = (\mathbb{R}_*^+)^{m+n} \tag{2.72}$$

and

$$\mathbb{B} = \left\{ \boldsymbol{\eta} \in \mathbb{R}^{m+n} \,:\, \eta_1 \geqslant 2\,,\ \eta_{m+1} \geqslant 3/2\,,\ \eta_1 \geqslant \cdots \geqslant \eta_m \geqslant 1\,,\ \eta_{m+1} \geqslant \cdots \geqslant \eta_{m+n} \geqslant 1 \right\}. \tag{2.73}$$

The optimization problem defined by Eq. (2.70) can be solved by using standard algorithms for constrained nonlinear problems and may admit multiple solutions, given the nonlinearity of the function $\upsilon \mapsto \underline{t}(\upsilon; \mathbf{a}, \mathbf{b})$. Hereinafter, a randomization of the starting points will be considered in order to reduce the impact of the local optimizer.

2.9.2 Calibration of the Lagrange multipliers

Using Eq. (2.34) and the statistical independence of the random variables $\mathbb{\mu}$ and P_k, $1 \leqslant k \leqslant m+n$, it is first deduced that

$$\mathbb{E}\{P_k\} = \frac{2\mathbb{E}\{\mathbb{\mu}\}}{\eta_k^2}\mathbb{E}\{U_k\}\,, \quad 1 \leqslant k \leqslant m+n-1\,, \tag{2.74}$$

and

$$\mathbb{E}\{P_{m+n}\} = \frac{2\mathbb{E}\{\mathbb{\mu}\}}{\eta_{m+n}^2}\mathbb{E}\Big\{\Big(1 - \sum_{k=1}^{m+n-1} U_k\Big)\Big\}\,. \tag{2.75}$$

For notational convenience, let $\tau_1 = \rho_2$ and $\tau_2 = \rho_1^{-1}$, so that the random shear modulus follows a Gamma distribution with parameters (τ_1, τ_2) and

$$\underline{\mu} = \mathbb{E}\{\mathbb{\mu}\} = \tau_1\tau_2\ . \tag{2.76}$$

Since the random variable $\mathbf{U}$ follows a Dirichlet distribution with parameters $\lambda_1, \ldots, \lambda_{m+n}$, one has

$$\mathbb{E}\{P_k\} = \frac{2\tau_1\tau_2}{\eta_k^2}\frac{\lambda_k}{\|\boldsymbol{\lambda}\|_1}\,, \quad 1 \leqslant k \leqslant m+n-1\,, \tag{2.77}$$

with $\|\boldsymbol{\lambda}\|_1 = \sum_{i=1}^{m+n}|\lambda_i|$. Combining the results from Section 2.9.1 with Eqs. (2.76–2.77) then leads to a system of $m+n$ equations involving the sought-for Lagrange multipliers $\boldsymbol{\tau}$ and $\boldsymbol{\lambda}$. Solving for τ_2 and $\lambda_1, \ldots, \lambda_{m+n-1}$ yields

$$\tau_2 = \frac{\underline{\mu}}{\tau_1}\ , \qquad \lambda_k = \alpha_k\lambda_{m+n}\,, \quad \alpha_k = \frac{\eta_k^2\,\underline{p}_k}{2\underline{\mu} - \sum_{\ell=1}^{m+n-1}\eta_\ell^2\,\underline{p}_\ell}\,, \quad 1 \leqslant k \leqslant m+n-1\ . \tag{2.78}$$

Consequently, τ_1 and λ_{m+n} now appears as the only remaining hyperparameters to be calibrated. The identification can then be achieved by letting

$$(\tau_1, \lambda_{m+n}) = \underset{(x,y)\,\in\,\mathbb{R}_*^+\times[1,+\infty)}{\operatorname{argmin}} \sum_{k=1}^{N}\Big(\operatorname{Var}\{T(\upsilon_k^{\exp}; x, y)\}^{1/2} - \varsigma_k^{\exp}\Big)^2\,, \tag{2.79}$$

where $\operatorname{Var}\{T(\upsilon_k^{\exp}; x, y)\}$ denotes the variance of the random Piola-Kirchhoff stress $T(\upsilon_k^{\exp})$ at stretch $\upsilon_k^{\exp}$ obtained for

$$\mathbb{\mu} \sim \mathrm{G}\Big(x, \frac{\underline{\mu}}{x}\Big) \tag{2.80}$$

and

$$\mathbf{U} \sim \mathrm{Dir}(\alpha_1 y, \alpha_2 y, \ldots, \alpha_{m+n-1} y, y)\,. \tag{2.81}$$

In view of solving the optimization problem given by Eq. (2.79), an explicit expression of the variance of the random variable $T(\upsilon)$ in terms of the Lagrange multipliers is given in the next section, for any fixed $\upsilon > 0$.

2.9.2.1 Sampling-free resolution

In order to solve the optimization problem defined by Eq. (2.79), one has to compute the variance of the random variable $T(\upsilon)$ for any $\upsilon > 0$. An estimator for this variance can readily be computed by resorting to Monte Carlo simulations. However, given that the random variables

$\mathbb{\mu}$ and $\mathbf{U}$ are distributed according to labelled distributions, an explicit expression of the variance $\mathrm{Var}\{T(\upsilon)\}$ can be obtained to improve the robustness of the formulation and reduce the computational cost. From Eq. (2.67), it is seen that

$$\mathrm{Var}\{T(\upsilon)\} = \sum_{k=1}^{m+n}\sum_{\ell=1}^{m+n} \mathrm{Cov}\{P_k, P_\ell\} f_k(\upsilon;\eta_k) f_\ell(\upsilon;\eta_\ell)\,, \tag{2.82}$$

where $\mathrm{Cov}\{P_k, P_\ell\}$ denotes the covariance between the random variables P_k and P_ℓ for $1 \leqslant k, \ell \leqslant m+n$. Furthermore, the introduction of random variables $\mathbb{\mu}$ and $\mathbf{U}$ yields

$$\mathrm{Cov}\{P_k, P_\ell\} = \frac{4\mathbb{E}\{\mathbb{\mu}^2\}}{\eta_k^2\eta_\ell^2}\left(\mathbb{E}\{U_k U_\ell\} - \mathbb{E}\{U_k\}\mathbb{E}\{U_\ell\}\right)\,, \quad 1 \leqslant k, \ell \leqslant m+n-1\,, \tag{2.83}$$

$$\mathrm{Cov}\{P_k, P_{m+n}\} = \frac{4\mathbb{E}\{\mathbb{\mu}^2\}}{\eta_k^2\eta_{m+n}^2}\left(\mathbb{E}\Big\{U_k\Big(1-\sum_{\ell=1}^{m+n-1} U_\ell\Big)\Big\} - \mathbb{E}\{U_k\}\mathbb{E}\Big\{\Big(1-\sum_{\ell=1}^{m+n-1} U_\ell\Big)\Big\}\right)\,, \tag{2.84}$$

for $1 \leqslant k \leqslant m+n-1$, and

$$\mathrm{Cov}\{P_{m+n}, P_{m+n}\} = \frac{4\mathbb{E}\{\mathbb{\mu}^2\}}{\eta_{m+n}^4}\left(\mathbb{E}\Big\{\Big(1-\sum_{\ell=1}^{m+n-1} U_\ell\Big)^2\Big\} - \mathbb{E}\Big\{\Big(1-\sum_{\ell=1}^{m+n-1} U_\ell\Big)\Big\}^2\right)\,, \tag{2.85}$$

with

$$\mathbb{E}\{\mathbb{\mu}^2\} = \tau_1\tau_2^2(1+\tau_1)\,. \tag{2.86}$$

Since the marginal probability distributions of the random variables U_k and $1-\sum_{\ell=1}^{m+n-1} U_\ell$ coincide with beta laws with parameters (λ_k, χ_k) and $(\lambda_{m+n}, \chi_{m+n})$, it can then be deduced that

$$\mathbb{E}\{U_k\} = \frac{\lambda_k}{\|\boldsymbol{\lambda}\|_1}\,, \quad 1 \leqslant k \leqslant m+n-1\,, \quad \mathbb{E}\Big\{\Big(1-\sum_{\ell=1}^{m+n-1} U_\ell\Big)\Big\} = \frac{\lambda_{m+n}}{\|\boldsymbol{\lambda}\|_1}\,, \tag{2.87}$$

$$\mathbb{E}\{U_k^2\} = \frac{\lambda_k\chi_k + \lambda_k^2(\|\boldsymbol{\lambda}\|_1+1)}{\|\boldsymbol{\lambda}\|_1^2(\|\boldsymbol{\lambda}\|_1+1)}\,, \tag{2.88}$$

and

$$\mathbb{E}\Big\{\Big(1-\sum_{\ell=1}^{m+n-1} U_\ell\Big)^2\Big\} = \frac{\lambda_{m+n}\chi_{m+n} + \lambda_{m+n}^2(\|\boldsymbol{\lambda}\|_1+1)}{\|\boldsymbol{\lambda}\|_1^2(\|\boldsymbol{\lambda}\|_1+1)}\,. \tag{2.89}$$

Finally, for $1 \leqslant k, \ell \leqslant m+n-1$ with $k \neq \ell$, it can be shown that the marginal probability density function of the random variable (U_k, U_ℓ) is a Dirichlet distribution with parameters $(\lambda_k, \lambda_\ell, \|\boldsymbol{\lambda}\|_1 - \lambda_k - \lambda_\ell)$. Hence, it follows that

$$\mathbb{E}\{U_k U_\ell\} = \frac{\lambda_k\lambda_\ell}{\|\boldsymbol{\lambda}\|_1(1+\|\boldsymbol{\lambda}\|_1)}\,, \tag{2.90}$$

and similarly,

$$\mathbb{E}\Big\{U_k\Big(1-\sum_{\ell=1}^{m+n-1} U_\ell\Big)\Big\} = \frac{\lambda_k\lambda_{m+n}}{\|\boldsymbol{\lambda}\|_1(1+\|\boldsymbol{\lambda}\|_1)}\,. \tag{2.91}$$

Finally, the combination of Eqs. (2.83)–(2.91), allow us to compute the variance of the random stress $T(\upsilon)$ in Eqs. (2.79)–(2.82) for given values of the hyperparameters, without resorting to Monte Carlo simulations. In this work, the optimization problems are solved by using the Matlab function `fmincon` (with an `sqp` algorithm) for a set of 1000 initial guesses determined by Latin Hypercube sampling. Here, the randomization of the starting points aims at reducing (in part) the impact of the local optimizer.

2.9.2.2 Closed-form relations for first-order stochastic stored energy functions

For a first-order stochastic stored energy function, the Dirichlet distribution of the random variable U reduces to a beta distribution with parameters (λ_1, λ_2) and the random Piola-Kirchhoff stress simply writes

$$T(\upsilon) = P_1 f_1(\upsilon;\eta_1) + P_2 f_2(\upsilon;\eta_2)\,, \quad \forall \upsilon > 0\,. \tag{2.92}$$

From Eq. (2.82), it is deduced its variance reduces to

$$\mathrm{Var}\{T(\upsilon)\} = \mathrm{Var}\{P_1\} f_1^2(\upsilon;\eta_1) + \mathrm{Var}\{P_2\} f_2^2(\upsilon;\eta_2) + 2\mathrm{Cov}\{P_1,P_2\} f_1(\upsilon;\eta_1) f_2(\upsilon;\eta_2)\,, \tag{2.93}$$

where the variances $\mathrm{Var}\{P_j\}$ and covariance $\mathrm{Cov}\{P_1,P_2\}$ of the random variables P_1 and P_2 are given by

$$\mathrm{Var}\{P_1\} = \frac{4\tau_1\tau_2^2}{\eta_1^4}\frac{\lambda_1(\lambda_1+\lambda_2+\lambda_1\lambda_2+\lambda_1^2+\tau_1\lambda_2)}{(\lambda_1+\lambda_2)^2(1+\lambda_1+\lambda_2)}\,, \tag{2.94}$$

$$\mathrm{Var}\{P_2\} = \frac{4\tau_1\tau_2^2}{\eta_2^4}\frac{\lambda_2(\lambda_1+\lambda_2+\lambda_1\lambda_2+\lambda_2^2+\tau_1\lambda_1)}{(\lambda_1+\lambda_2)^2(1+\lambda_1+\lambda_2)}\,, \tag{2.95}$$

and

$$\mathrm{Cov}\{P_1,P_2\} = \frac{4\tau_1\tau_2^2}{\eta_1^2\eta_2^2}\frac{\lambda_1\lambda_2(\lambda_1+\lambda_2-\tau_1)}{(\lambda_1+\lambda_2)^2(1+\lambda_1+\lambda_2)}\,. \tag{2.96}$$

By substituting Eqs. (2.94–2.96) into Eq. (2.93), we obtain the variance of the random stress $T(\upsilon)$ for given values of the hyperparameters, which allows us to evaluate the variance of the random variable $T(\upsilon)$ in the optimization problem given by Eq. (2.79).

2.9.2.3 Discussion regarding the identification strategy

A number of remarks regarding the above calibration strategy are relevant at this point. First of all, it should be noticed that the dimension of the problem related to the calibration of τ_1 and λ_{m+n} is independent of the values of m and n. As a consequence, the methodology does not suffer from a curse of dimensionality and turns out to be very robust in that sense.

Secondly, and while the set of model parameters can be shown to be unique when the constraint equations can be estimated from experiments, considering the mean and variability of the stress response does not allow the hyperparameters to be uniquely defined (one may note that issues related to uniqueness are also encountered in a deterministic context. More specifically, it should be observed that the random stress involves nonlinear functions of $\mathbb{\mu}$ and $\mathbf{U}$. Therefore, a given variability in the random stress may equivalently be generated by different combinations of fluctuations in $\mathbb{\mu}$ and $\mathbf{U}$.

Additionally, the choice of the hyperparameters to be identified within the second step turns out to be arbitrary, so that the associated optimization problem may alternatively be formulated by selecting any couple (τ_k, λ_ℓ) for $1 \leqslant k \leqslant 2$ and $1 \leqslant \ell \leqslant m+n$. In accordance with the probabilistic modeling strategy, an approach to circumvent this limitation may consist in solving the set of $2(m+n)$ optimization problems thus defined, and in proceeding to model selection through the maximization of entropy.

Finally, it should be noted that Eq. (2.78) can be used in order to investigate the sensitivity of the cost function in the optimization problem given by Eq. (2.79) with respect to the second design variable λ_{m+n}. In particular, it may be useful in identifying the combination of parameters

that maximizes the gradient of the cost function over the search space. For instance, and focusing on the first-order model for illustration purposes, the coefficient of variation δ_U of U is given by

$$\delta_U = \sqrt{\frac{\lambda_2}{\lambda_1(\lambda_1+\lambda_2+1)}}\,, \tag{2.97}$$

with

$$\lambda_1 = \frac{\eta_1^2\,\underline{p}_1}{\eta_2^2\,\underline{p}_2}\lambda_2\ . \tag{2.98}$$

When the mean parameters and model exponents are such that $\lambda_1 \ll \lambda_2$, the random variable U takes small positive values and exhibits large statistical fluctuations. Similarly, when $\lambda_1 \gg \lambda_2$, the realizations of the random variable U are close to 1 and the statistical fluctuations are very small. In both cases, the coefficient of variation δ_U of the random variable U quickly reaches a plateau as λ_2 becomes larger, and this behavior may decrease the robustness of the optimization procedure.

2.9.3 Applications to soft biological tissues

In this section, the stochastic model and the identification methodology are applied to reproduce the experimental variability exhibited by various biological tissues, including brain tissues, liver tissues and spinal cord white matter [46].

2.9.3.1 Brain tissue

In this first application, the modeling of the variability exhibited by brain tissues is addressed by considering the experimental results provided in [12]. The database is composed of 72 samples of brain tissue tested for strains ranging up to 50% and for strain rates $\dot{\varepsilon} \in \{0.5, 5, 30\}$ s^{-1}. Below, we address the calibration task in unconfined compression for low and medium strain rates. Experimental data are given for white and gray matter, and final data are expressed in terms of mean and standard deviation plots at increasing stretches. The optimal mean parameters and exponents $(\underline{\mathbf{p}}, \boldsymbol{\eta})$ are reported in Tab. 2.1 for the compression tests at different strain rates (for $m = n = 1$). It should be noticed that the inequality constraints raised by the polyconvexity

$\dot{\varepsilon}$	$0.5\,\mathrm{s}^{-1}$	$5\,\mathrm{s}^{-1}$
$\underline{p}_1$ (kPa)	0.1467	0.1881
$\underline{p}_2$ (kPa)	0.0457	0.7823
η_1	5.5945	4.5907
η_2	1.991	1.5
$\underline{\mu}$ (kPa)	2.3863	2.3863
λ_1	253.5375	22.461
λ_2	9.9982	9.9732
τ_1	2.3679	6.6398
τ_2	1.0078	0.4311

$\dot{\varepsilon}$	$0.5\,\mathrm{s}^{-1}$	$5\,\mathrm{s}^{-1}$
$\underline{p}_1$ (kPa)	1.1131	1.4720
$\underline{p}_2$ (kPa)	1.1120	0.4897
η_1	2	2.6185
η_2	1.5	1.5
$\underline{\mu}$ (kPa)	3.4772	5.5973
λ_1	3.2290	91.5357
λ_2	1.8146	9.9919
τ_1	33.2721	6.6819
τ_2	0.1045	0.8377

Table 2.1 – calibrated parameters for $m = n = 1$ (left panel: gray matter in compression, right panel: white matter in compression).

and coerciveness properties are fulfilled, so that the mean model is admissible. Regarding the

computation of the Lagrange multipliers λ_{n_p} and τ_1, performed within the second step of the methodology, the algorithm is found to converge in a few iterations, regardless of the initial guess. It can be observed that the first-order stochastic stored energy function (that is, $m = n = 1$) can reproduce the experimental results very well. These data are quantitatively compared with the prediction of the calibrated stochastic model in Figs. 2.9 and 2.10, where the confidence interval at 95% is also reported. In accordance with the error values listed above, it is seen that the proposed probabilistic approach allows for properly reproducing the known features of the stress response.

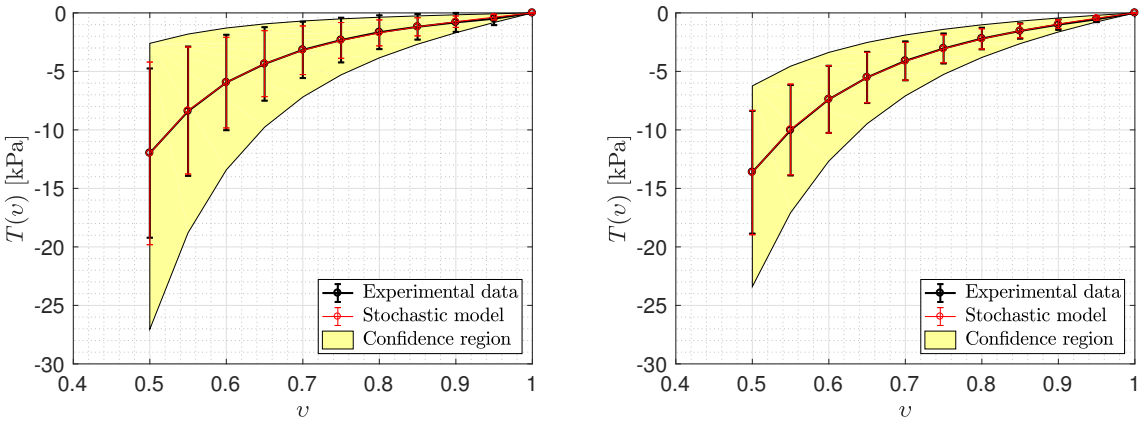

Figure 2.9 – Graph of $v \mapsto \underline{t}(v)$ (kPa) and $v \mapsto \mathrm{Var}\{T(v)\}$ for gray matter tissues in unconfined compression with $\dot{\varepsilon} = 0.5$ s^{-1} and $\dot{\varepsilon} = 5$ s^{-1}.

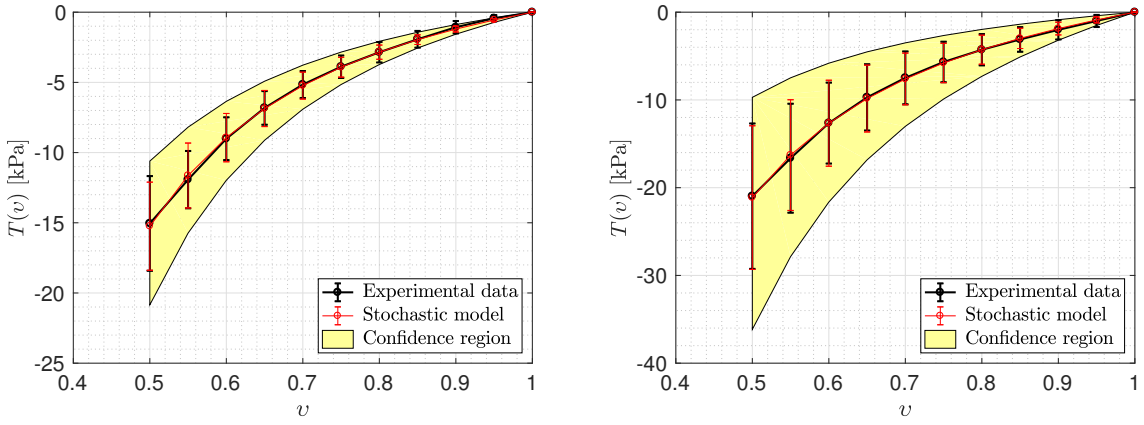

Figure 2.10 – Graph of $v \mapsto \underline{t}(v)$ (kPa) and $v \mapsto \mathrm{Var}\{T(v)\}$ for white matter tissues in unconfined compression with $\dot{\varepsilon} = 0.5$ s^{-1} and $\dot{\varepsilon} = 5$ s^{-1}.

2.9.3.2 Liver tissue

As a second example, we now turn to the modeling of bovine liver tissues. Specifically, the statistical results are extracted from [102], in which uniaxial compression tests were performed at a 0.01 s^{-1} strain rate. The orders of the stochastic stored energy function are chosen from a preliminary study as $m = 1$ and $n = 1$ – note that the deterministic fitting in the above reference

was obtained using an exponential-type stored energy function. The calibrated parameters are listed in Tab. 2.2. A qualitative comparison between the statistical properties estimated by means

$\dot{\varepsilon}$	$\underline{p}_1$	$\underline{p}_2$	η_1	η_2	$\underline{\mu}$	λ_1	λ_2	τ_1	τ_2
$0.01\,\mathrm{s}^{-1}$	0.1886	0.005	2.1783	12.0502	0.8088	314.6755	254.251	591.7831	0.0014

Table 2.2 – calibrated mean values and exponents for $m = n = 1$ (liver tissues in compression).

of Monte Carlo simulations with the calibrated stochastic model and those computed using the experimental data can be visualized in Fig. 2.11. Similarly to the case of brain tissues, it is seen

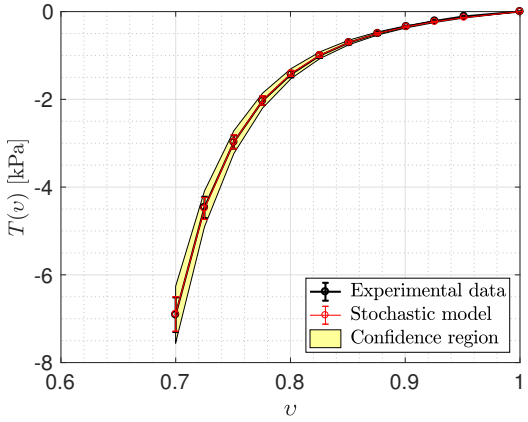

Figure 2.11 – Graph of $v \mapsto \underline{t}(v)$ (kPa) and $v \mapsto \mathrm{Var}\{T(v)\}$ (kPa) for liver tissues in uniaxial compression with $\dot{\varepsilon} = 0.01$ s^{-1}.

that the probabilistic model and the identification strategy allows the data to be reproduced with a reasonably high level of accuracy, hence showing the relevance of the overall methodology.

2.9.3.3 Spinal cord white matter

In this final application, we address the modeling of the variability exhibited by porcine spinal cord white matter under unconfined compression. Experimental data can be found in [103], where the mechanics of spinal cord injury and its finite element implementation are investigated. The database is composed of 104 independent samples extracted from Yorkshire pigs. Unconfined compression tests were performed for strains ranging up to 40% and for a strain rate $\dot{\varepsilon} \in \{0.005, 0.05, 0.5\}$ s^{-1}. The probabilistic potential defined with $m = n = 1$ is found to accurately reproduce the experimental descriptors, as shown in Fig. 2.12. The calibrated parameters are finally listed in Tab. 2.3.

2.10 Conclusion

In this chapter, we have addressed the construction, simulation and inverse identification of stochastic stored energy functions for homogeneous, isotropic and incompressible hyperelastic media [45, 46]. The approach relies on the maximum entropy principle, which is invoked to ensure the well-posedness of the stochastic nonlinear boundary value problem. Two probabilistic models were proposed and can be seen as stochastic extensions of Ogden-type stored energy

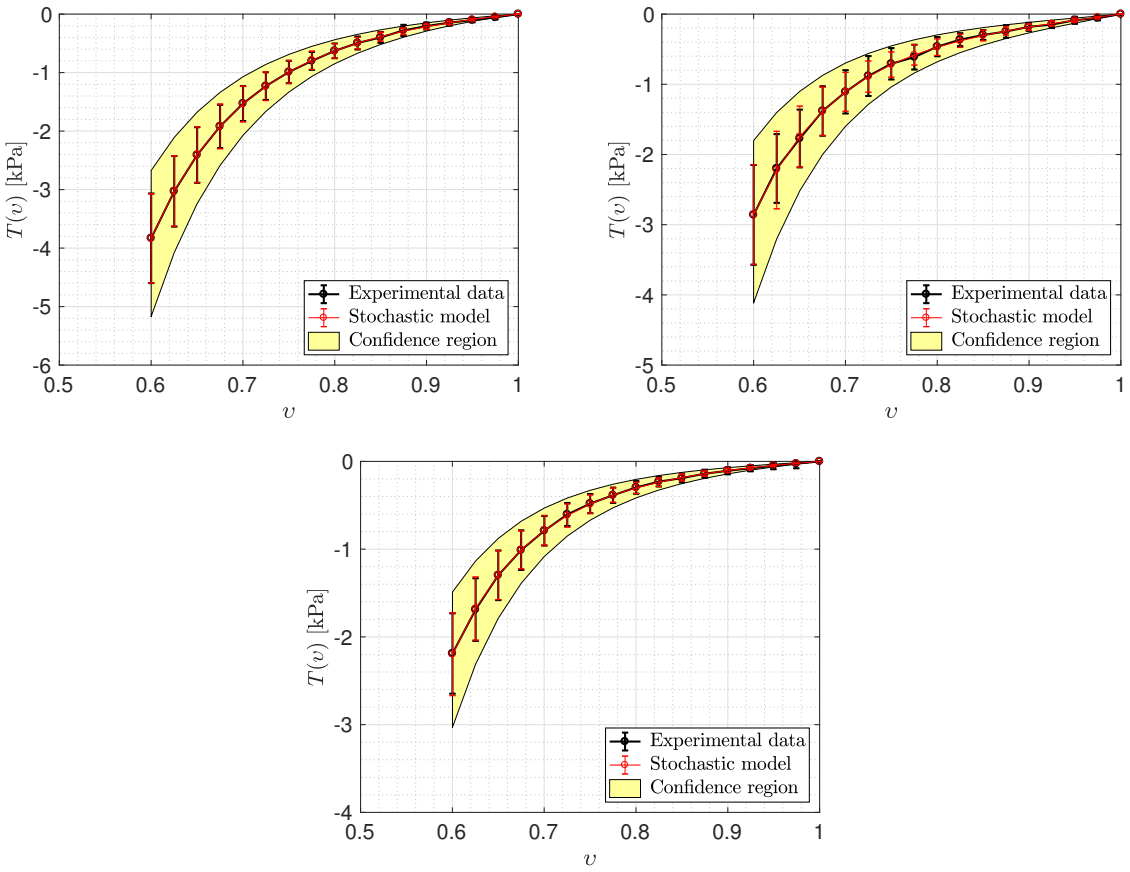

Figure 2.12 – Graph of $\upsilon \mapsto \underline{t}(\upsilon)$ (kPa) and $\upsilon \mapsto \mathrm{Var}\{T(\upsilon)\}$ for spinal cord white matter in unconfined compression with $\dot{\varepsilon} = 0.005\ \mathrm{s}^{-1}$, $\dot{\varepsilon} = 0.05\ \mathrm{s}^{-1}$ and $\dot{\varepsilon} = 0.5\ \mathrm{s}^{-1}$.

$\dot{\varepsilon}$	$0.005\,\mathrm{s}^{-1}$	$0.05\,\mathrm{s}^{-1}$	$0.5\,\mathrm{s}^{-1}$
$\underline{p}_1$ (kPa)	1.0003×10^{-10}	0.0103	0.0019
$\underline{p}_2$ (kPa)	0.0518	0.0060	0.0110
η_1	2	10.3688	11.4613
η_2	4.5327	4.2267	5.3704
$\underline{\mu}$ (kPa)	0.5317	0.6049	0.2864
λ_1	4.3716×10^{-9}	10.3103	3.7483×10^{4}
λ_2	11.6189	1.0021	4.6814×10^{4}
τ_1	25.3264	16.5984	21.7408
τ_2	0.0210	0.0364	0.0132

Table 2.3 – calibrated parameters for $m = n = 1$ (spinal white matter in compression).

functions. A simple identification procedure was further devised and applied on a variety of soft biological tissues. It was shown that the model allows the experimental mean behavior and variability to be accurately reproduced at various strain rates.

Chapter 3

Stochastic Modeling of Compressible Isotropic Hyperelastic Materials

Contents

3.1 Introduction

This chapter extends the framework presented in Chapter 2 to the case of homogeneous, isotropic and compressible hyperelastic materials [47]. This generalization raises two main difficulties. First, it requires the definition of the joint probability density function for the random bulk and shear moduli at small strains. In the present case, these elastic moduli satisfy an inequality constraint that will generate statistical dependencies. Second, the probabilistic model involves more complex algebraic constraints raised by consistency relations with linearized elasticity.

This chapter is organized as follows. The deterministic stored energy function for which a stochastic extension is sought is first presented in Section 3.2. Sections 3.3 and 3.4 are concerned with the construction of probabilistic models for Neo-Hookean and Ogden-type stored energy functions. Uncertainty propagation is finally performed in a nonlinear multiscale setting in Section 3.5.

3.2 Deterministic background

Let us consider a homogeneous, isotropic and compressible hyperelastic medium characterized by the Ogden-type stored energy function w [77, 76, 53, 51]:

$$w([F]) = \sum_{i=1}^{m} p_i(\mathrm{Tr}(([F]^T[F])^{\eta_i/2}) - 3) + \sum_{j=1}^{n} p_{j+m}(\mathrm{Tr}((\mathrm{Cof}([F]^T[F]))^{\eta_{j+m}/2}) - 3) + g(\det([F])) \,, \tag{3.1}$$

where $g : \mathbb{R}_*^+ \to \mathbb{R}$ is the convex function defined as

$$g(\delta) = \frac{p_{m+n+1}}{2}(\delta - 1)^2 - s\log(\delta)\,, \quad \forall \delta \in \mathbb{R}_*^+\,, \tag{3.2}$$

and such that $\lim_{\delta \downarrow 0} g(\delta) = +\infty$. When the model parameters satisfy (see [65, 53])

$$p_k > 0\,, \quad 1 \leqslant k \leqslant m+n+1\,, \quad s > 0\,, \tag{3.3}$$

and

$$\eta_1 \geqslant 2\,, \quad \eta_1 \geqslant \cdots \geqslant \eta_m \geqslant 1\,, \qquad \eta_{m+1} \geqslant \frac{3}{2}\,, \quad \eta_{m+1} \geqslant \cdots \geqslant \eta_{m+n} \geqslant 1\,, \tag{3.4}$$

then the stored energy function defined by Eq. (3.1) is polyconvex and satisfies

(i) the growth condition given by Eq. (1.30), that is, there exist $c_0 > 0$, $c_1 \in \mathbb{R}$, $p \geqslant 2$ and $q \geqslant 3/2$ such that

$$w([F]) \geqslant c_0(\|[F]\|_F^p + \|\mathrm{Cof}([F])\|_F^q) - c_1\,, \quad \forall [F] \in \mathbb{M}_+^3; \tag{3.5}$$

(ii) the physically-based condition $\lim_{\det([F]) \downarrow 0} w([F]) = +\infty$.

Under these assumptions, the existence of minimizers for the energy functional is ensured [65, 53, 66, 68].

The stored energy function can be expanded near the reference configuration as [53]

$$w([F]) = \frac{1}{2}[E] : [\![A]\!] : [E] + O(\|[E]\|_F^3)\,, \quad [E] = \frac{1}{2}\left([F]^{\mathrm{T}}[F] - [I_3]\right)\,, \tag{3.6}$$

where $[\![A]\!]$ denotes the fourth-order elasticity tensor of the form

$$[\![A]\!] = 3\kappa[\![E_1]\!] + 2\mu[\![E_2]\!]\,, \tag{3.7}$$

in which κ and μ correspond to the bulk and shear moduli of the isotropic material at small strains. In the present case, and following the methodology proposed in [54], Eq. (3.6) can equivalently be recast using the following conditions:

$$\widehat{w}(1,1,1) = 0\,, \quad \frac{\partial \widehat{w}}{\partial \upsilon_j}(1,1,1) = 0\,, \quad \frac{\partial^2 \widehat{w}}{\partial \upsilon_i \partial \upsilon_j}(1,1,1) = \lambda + 2\mu\delta_{ij}\,, \quad 1 \leqslant i,j \leqslant 3\,, \tag{3.8}$$

where $\widehat{w}$ corresponds to the stored energy function expressed in terms of the singular values $\{\upsilon_1([F])\}_{j=1}^3$ of $[F] \in \mathbb{M}_+^3$, that is

$$\begin{aligned}\widehat{w}(\upsilon_1,\upsilon_2,\upsilon_3) = &\sum_{i=1}^m p_i(\upsilon_1^{\eta_i} + \upsilon_2^{\eta_i} + \upsilon_3^{\eta_i} - 3)\\ &+ \sum_{j=1}^m p_{j+m}((\upsilon_1\upsilon_2)^{\eta_{j+m}} + (\upsilon_2\upsilon_3)^{\eta_{j+m}} + (\upsilon_1\upsilon_3)^{\eta_{j+m}} - 3)\\ &+ \frac{p_{m+n+1}}{2}(\upsilon_1\upsilon_2\upsilon_3 - 1)^2 - s\log(\upsilon_1\upsilon_2\upsilon_3)\,,\end{aligned} \tag{3.9}$$

and $\lambda = \kappa - 2\mu/3$ denotes the Lamé parameter. It can then be deduced that

$$\sum_{i=1}^m p_i\eta_i^2 - p_{m+n+1} = \frac{8}{3}\mu - \kappa\,, \tag{3.10a}$$

$$\sum_{j=1}^n p_{j+m}\eta_{j+m}^2 + p_{m+n+1} = \kappa - \frac{2}{3}\mu\,, \tag{3.10b}$$

and

$$s = \sum_{i=1}^{m} p_i \eta_i + 2 \sum_{j=1}^{n} p_{j+m} \eta_{j+m} \,. \tag{3.11}$$

The equality stated by Eq. (3.10b) shows that $\lambda > 0$, hence restricting the analysis to the class of (non-auxetic) materials with strictly positive Poisson ratio at small strains.

A compressible Mooney-Rivlin material is defined for $m = n = 1$ and $\eta_1 = \eta_2 = 2$ (see, *e.g.*, [104]):

$$w([F]) = p_1 \left(\|[F]\|_F^2 - 3 \right) + p_2 \left(\|\mathrm{Cof}([F])\|_F^2 - 3 \right) + \frac{p_3}{2} \left(\det([F]) - 1 \right)^2 - s \log(\det([F])) \,, \tag{3.12}$$

for all $[F]$ in $\mathbb{M}_+^3$, and the consistency relations then reduce to:

$$4p_1 - p_3 = \frac{8}{3}\mu - \kappa \,, \quad 4p_2 + p_3 = \kappa - \frac{2}{3}\mu \,, \quad s = 2p_1 + 4p_2 \,. \tag{3.13}$$

This stored energy function was proposed by Ciarlet and Geymonat in a slightly different form [69] (see also [53]).

A compressible Neo-Hookean material is defined by the stored energy function [54]:

$$w([F]) = \frac{\mu}{2} \left(\|[F]\|_F^2 - 3 \right) + \frac{\lambda}{2} \left(\det([F]) - 1 \right)^2 - \mu \log \left(\det \left([F] \right) \right) \,, \quad \forall [F] \in \mathbb{M}_+^3 \,. \tag{3.14}$$

The construction of a probabilistic model for the Neo-Hookean case is first addressed in Section 3.3. The general case of Ogden-type stored energy functions is subsequently tackled in Section 3.4.

3.3 Stochastic modeling of Neo-Hookean materials

Let $\mathbf{C} = (C_1, C_2)$ be the random variable corresponding to the stochastic modeling of the bulk and shear moduli, and let $[\![\mathbf{A}]\!]$ be the random elasticity tensor at small strains:

$$[\![\mathbf{A}]\!] = 3C_1 [\![E_1]\!] + 2C_2 [\![E_2]\!] \,. \tag{3.15}$$

The stochastic stored energy function associated with the compressible Neo-Hookean model defined by Eq. (3.14) is then written as

$$\mathcal{W}([F]) = \frac{C_2}{2} \left(\|[F]\|_F^2 - 3 \right) + \frac{\Lambda}{2} \left(\det([F]) - 1 \right)^2 - C_2 \log \left(\det \left([F] \right) \right) \,, \quad \forall [F] \in \mathbb{M}_+^3 \,, \tag{3.16}$$

with $\Lambda = C_1 - 2C_2/3$. By definition, the above stored energy function only depends on the random Lamé parameter Λ and the random shear modulus C_2 (or equivalently, on the random bulk modulus C_1 and the shear modulus C_2). In the present case, the polyconvexity property is only relevant to the two-dimensional case and implies that

$$\Lambda > 0 \,, \quad C_2 > 0 \,, \tag{3.17}$$

almost surely. The stochastic extension of the classical Neo-Hookean model is then completely defined by the probabilistic model of random variable $\mathbf{C}$. In order to proceed with the MaxEnt construction, assume that

$$\mathbb{E} \left\{ \mathbf{C} \right\} = \underline{\mathbf{c}} \tag{3.18}$$

and consider the repulsive constraints

$$\mathbb{E}\Big\{ \log\Big(C_1 - \frac{2}{3}C_2\Big)\Big\} = \nu_1\,, \quad |\nu_1| < +\infty \tag{3.19}$$

and

$$\mathbb{E}\{\log(C_2)\} = \nu_2\,, \quad |\nu_2| < +\infty\,, \tag{3.20}$$

associated with Eq. (3.17). Let $\mathscr{L}_1 \in \mathbb{R}$, $\mathscr{L}_2 \in \mathbb{R}$, $(1-\alpha) \in (-\infty, 1)$ and $(1-\beta) \in (-\infty, 1)$ be the Lagrange multipliers associated with Eqs. (3.18), (3.19) and (3.20), respectively. The probability density function induced by the MaxEnt principle is then given by

$$f_{\mathbf{C}}(\mathbf{c}) = \mathbb{1}_{\mathscr{S}_{\mathbf{C}}}(\mathbf{c})\, k_0 \Big(c_1 - \frac{2}{3}c_2\Big)^{\alpha-1} c_2^{\beta-1} \exp\left(-\mathscr{L}_1 c_1 - \mathscr{L}_2 c_2\right)\,. \tag{3.21}$$

where

$$\mathscr{S}_{\mathbf{C}} = \left\{ \mathbf{c} \in \mathbb{R}^2 \,:\, c_1 - \frac{2}{3}c_2 > 0\,, c_2 > 0 \right\}\,. \tag{3.22}$$

Furthermore, it can be deduced from Eq. (3.21) that Λ and C_2 are statistically independent random variables and are defined by the probability density functions

$$f_{\Lambda}(\lambda) = \mathbb{1}_{\mathbb{R}^+_*}(\lambda)\, \frac{1}{\Gamma(\alpha)\theta_1^{\alpha}}\, \lambda^{\alpha-1} \exp\left(-\frac{\lambda}{\theta_1}\right)\,, \tag{3.23}$$

and

$$f_{C_2}(c_2) = \mathbb{1}_{\mathbb{R}^+_*}(c_2)\, \frac{1}{\Gamma(\beta)\theta_2^{\beta}}\, c_2^{\beta-1} \exp\left(-\frac{c_2}{\theta_2}\right)\,, \tag{3.24}$$

with $\theta_1 = 1/\mathscr{L}_1$ and $\theta_2 = 3/(3\mathscr{L}_2 + 2\mathscr{L}_1)$. The equations (3.23) and (3.24) show that Λ and C_2 are, in the case of the Neo-Hookean materials, statistically independent Gamma-distributed random variables with parameters (α, θ_1) and (β, θ_2), respectively.

3.4 Stochastic modeling of Ogden-type stored energy functions

Let $\mathcal{W}$ be the stochastic stored energy function corresponding to the probabilistic modeling of an Ogden-type potential for isotropic compressible materials:

$$\begin{aligned}\mathcal{W}([F]) = &\sum_{i=1}^{m} P_i(\mathrm{Tr}(([F]^T[F])^{\eta_i/2}) - 3) + \sum_{j=1}^{n} P_{j+m}(\mathrm{Tr}((\mathrm{Cof}([F]^T[F]))^{\eta_{j+m}/2}) - 3)\\ &+ \frac{P_{m+n+1}}{2}(\det([F]) - 1)^2 - S\log(\det([F]))\,,\end{aligned} \tag{3.25}$$

where the random variables $P_1, \ldots, P_{m+n+1}$ correspond to the stochastic versions of model parameters $p_1, \ldots, p_{m+n+1}$ and the random variable S reads as (see Eq. (3.11))

$$S = \sum_{i=1}^{m} P_i\eta_i + 2\sum_{j=1}^{n} P_{j+m}\eta_{j+m}\,. \tag{3.26}$$

As for the incompressible case discussed in Section 2.3, it is assumed that the exponents $\{\eta_k\}_{k=1}^{m+n}$ are deterministic and satisfy the constraints given by Eq. (3.4). Let $\mathbf{P} = (P_1, \ldots, P_{m+n+1})$ and $\boldsymbol{\eta} = (\eta_1, \ldots, \eta_{m+n+1})$.

The constraints related to the existence theorems and consistency with linearized elasticity require that

(i) $P_k > 0$, $1 \leqslant k \leqslant m+n+1$, almost surely;

(ii) the random variables $\mathbf{C}$ and $\mathbf{P}$ satisfy

$$\sum_{i=1}^{m} P_i \eta_i^2 - P_{m+n+1} = \frac{8}{3} C_2 - C_1 \,, \tag{3.27a}$$

$$\sum_{j=1}^{n} P_{j+m} \eta_{j+m}^2 + P_{m+n+1} = C_1 - \frac{2}{3} C_2 \,. \tag{3.27b}$$

One way to ensure that Eqs. (3.10a)–(3.10b) hold without defining the probability measure on a manifold is to select two components of $\mathbf{P}$, say P_m and P_{m+n}, and to enforce the equalities afterwards, setting

$$P_m = \frac{1}{\eta_m^2} \Big(\frac{8}{3} C_2 - C_1 - \sum_{i=1}^{m-1} P_i \eta_i^2 + P_{m+n+1} \Big) \tag{3.28}$$

and

$$P_{m+n} = \frac{1}{\eta_{m+n}^2} \Big(C_1 - \frac{2}{3} C_2 - \sum_{j=m+1}^{m+n-1} P_j \eta_j^2 - P_{m+n+1} \Big) \,. \tag{3.29}$$

The above selection of P_m and P_{m+n} is arbitrary when $m > 1$ and $n > 1$. However, any other selection would yield similar algebraic forms for the constructed probability measures, given the symmetry of the constraint equations in terms of these variables. Imposing $P_m > 0$ and $P_{m+n} > 0$ then implies, in view of Eqs. (3.28) and (3.29), that

$$C_1 - \frac{8}{3} C_2 + \sum_{i=1}^{m-1} P_i \eta_i^2 < P_{m+n+1} < C_1 - \frac{2}{3} C_2 - \sum_{j=m+1}^{m+n-1} P_j \eta_j^2 \tag{3.30}$$

almost surely. In summary, the constraints to be accounted for in the MaxEnt formulation are given by

$$P_k > 0 \,, \quad 1 \leqslant k \leqslant m-1 \text{ and } m+1 \leqslant k \leqslant m+n-1 \tag{3.31}$$

and

$$C_1 - \frac{8}{3} C_2 + \sum_{i=1}^{m-1} P_i \eta_i^2 < P_{m+n+1} < C_1 - \frac{2}{3} C_2 - \sum_{j=m+1}^{m+n-1} P_j \eta_j^2 \tag{3.32}$$

almost surely. The constraint $P_{m+n+1} > 0$, combined with Eq. (3.32), then leads to the condition

$$P_{m+n+1} > \max \Big\{ 0, C_1 - \frac{8}{3} C_2 + \sum_{i=1}^{m-1} P_i \eta_i^2 \Big\} \,. \tag{3.33}$$

Assume next that

$$C_1 - \frac{8}{3} C_2 > 0 \tag{3.34}$$

almost surely. This inequality is stronger than the classical condition $C_1 - 2C_2/3 > 0$, but is satisfied by most materials in practice. Moreover, it allows for substantial simplifications in the algebraic results that will be presented below, and the inequality $P_{m+n+1} > 0$ then holds almost surely.

Let $\widetilde{\mathbf{P}}$ be the vector-valued random variable obtained by removing the entries P_m and P_{m+n} in the random vector $\mathbf{P}$, *i.e.*,

$$\widetilde{\mathbf{P}} = (P_1, \ldots, P_{m-1}, P_{m+1}, \ldots, P_{m+n-1}, P_{m+n+1}) \,. \tag{3.35}$$

Similarly, let $\widetilde{\boldsymbol{\eta}}$ be the vector given by

$$\widetilde{\boldsymbol{\eta}} = (\eta_1, \ldots, \eta_{m-1}, \eta_{m+1}, \ldots, \eta_{m+n-1}) \,. \tag{3.36}$$

The constraints given by Eqs. (3.31) and (3.30) then take the forms

$$\widetilde{P}_k > 0 \,, \quad 1 \leqslant k \leqslant m+n-1 \tag{3.37}$$

and

$$C_1 - \frac{8}{3} C_2 + \sum_{i=1}^{m-1} \widetilde{P}_i \widetilde{\eta}_i^2 < \widetilde{P}_{m+n-1} < C_1 - \frac{2}{3} C_2 - \sum_{j=m}^{m+n-2} \widetilde{P}_j \widetilde{\eta}_j^2 \,. \tag{3.38}$$

Let $f_{\mathbf{C},\widetilde{\mathbf{P}}}$ be the joint probability density function of random variables $\mathbf{C}$ and $\widetilde{\mathbf{P}}$. As for the incompressible case (see Section 2.3), the construction of the probabilistic model is achieved in a two-step strategy involving a conditioning on the elastic moduli:

$$f_{\mathbf{C},\widetilde{\mathbf{P}}}(\mathbf{c}, \mathbf{p}) = f_{\mathbf{C}}(\mathbf{c}) \times f_{\widetilde{\mathbf{P}}|\mathbf{C}=\mathbf{c}}(\mathbf{p}) \,, \tag{3.39}$$

where

- $f_{\mathbf{C}}$ is the marginal probability density function of random variable $\mathbf{C}$;
- $f_{\widetilde{\mathbf{P}}|\mathbf{C}=\mathbf{c}}$ is the conditional probability density function of random variable $\widetilde{\mathbf{P}}$ given $\mathbf{C}$.

In this approach, the MaxEnt principle is applied sequentially (as opposed as the strategy that would involve a conditional entropy), first to construct the probability law for the elastic moduli at small strains, and then to derive the expression of the conditional probability measures. These points are addressed in order in Sections 3.4.1, 3.4.2 and 3.4.3.

3.4.1 Stochastic modeling of C

Assume that the available information on the random variable $\mathbf{C}$ is given by

$$\mathbb{E}\{C_1\} = \underline{c}_1 \,, \quad \mathbb{E}\{C_2\} = \underline{c}_2 \,, \tag{3.40}$$

where $(\underline{c}_1, \underline{c}_2) \in \mathscr{S}_{\mathbf{C}}$, and by constraints related to the inequality given by Eq. (3.34) and the condition $C_2 > 0$:

$$\mathbb{E}\left\{\log\left(C_1 - \frac{8}{3} C_2\right)\right\} = \nu_1 \,, \quad |\nu_1| < +\infty \,, \tag{3.41}$$

$$\mathbb{E}\{\log(C_2)\} = \nu_2 \,, \quad |\nu_2| < +\infty \,. \tag{3.42}$$

Let $\mathscr{L}_1 \in \mathbb{R}$, $\mathscr{L}_2 \in \mathbb{R}$, $(1-\alpha) \in (-\infty, 1)$ and $(1-\beta) \in (-\infty, 1)$ be the Lagrange multipliers associated with the above constraints. It follows that the probability density function $f_{\mathbf{C}}$, induced by the MaxEnt principle, writes:

$$f_{\mathbf{C}}(\mathbf{c}) = \mathbb{1}_{\mathscr{S}_{\mathbf{C}}}(\mathbf{c})\, k_0 \left(c_1 - \frac{8}{3} c_3\right)^{\alpha-1} c_2^{\beta-1} \exp\left(-\mathscr{L}_1 c_1 - \mathscr{L}_2 c_2\right) \,, \tag{3.43}$$

in which the support $\mathscr{S}_{\mathbf{C}}$ is defined as:

$$\mathscr{S}_{\mathbf{C}} = \left\{ \mathbf{c} \in \mathbb{R}^2 \, : \, c_1 - \frac{8}{3} c_2 > 0 \, , c_2 > 0 \right\} . \tag{3.44}$$

Note that by construction, this support is different from the one introduced in Section 3.3. Let $\widetilde{\Lambda}$ be the random variable defined as:

$$\widetilde{\Lambda} = C_1 - \frac{8}{3} C_2 \, . \tag{3.45}$$

Performing the measure transformation then yields

$$f_{\widetilde{\Lambda},C_2}(\lambda, c_2) = k_0 \, \mathbb{1}_{\mathbb{R}_*^+}(\lambda) \lambda^{\alpha-1} \exp\left(-\frac{\lambda}{\theta_1} \right) \times \mathbb{1}_{\mathbb{R}_*^+}(c_2) c_2^{\beta-1} \exp\left(-\frac{c_2}{\theta_2} \right) , \tag{3.46}$$

which shows that $\widetilde{\Lambda}$ and C_2 turn out to be statistically independent Gamma-distributed random variables defined by the parameters (α, θ_1) and (β, θ_2), respectively. Note that similar results were obtained in [28, 29] where it was found, under less restrictive constraints, that C_1 and C_2 are statistically independent Gamma-distributed random variables in the context of linearized elasticity.

3.4.2 Stochastic modeling under inequality constraints

We now proceed with the second step of the modeling strategy, and address the construction of a probabilistic model for $\widetilde{\mathbf{P}}|\mathbf{C}$. Here, the constraints are given by (see Eqs. (3.37) and (3.38))

$$\widetilde{P}_k > 0 \, , \quad k = 1, \ldots, m+n-1 \, , \tag{3.47}$$

and

$$C_1 - \frac{8}{3} C_2 + \sum_{i=1}^{m-1} \widetilde{P}_i \widetilde{\eta}_i^2 < \widetilde{P}_{m+n-2} < C_1 - \frac{2}{3} C_2 - \sum_{j=m}^{m+n-1} \widetilde{P}_j \widetilde{\eta}_j^2 \, . \tag{3.48}$$

In order to simplify the algebraic expressions in the above inequality constraints, consider an auxiliary random variable $\mathbf{U}$ with values in a subset of $\mathbb{R}^{m+n+1}$ and let $\widetilde{\mathbf{U}}$ be the random vector obtained by removing the entries U_m and U_{m+n} from $\mathbf{U}$. Let $\widetilde{\mathbf{P}}$ be subsequently defined as

$$\widetilde{\mathbf{P}} = \mathbf{h}(\widetilde{\mathbf{U}}, \mathbf{C}) \, , \tag{3.49}$$

where $\mathbf{h}$ is the mapping given by

$$h_j(\mathbf{u}, \mathbf{c}) = \frac{2 c_2 u_j}{\widetilde{\eta}_j^2} \, , \quad j = 1, \ldots, m+n-2 \, , \tag{3.50}$$

and

$$h_{m+n-1}(\mathbf{u}, \mathbf{c}) = 2 c_2 \left(1 - \sum_{i=1}^{m+n-2} u_i \right) u_{m+n-1} + c_1 - \frac{8}{3} c_2 + 2 c_2 \sum_{j=1}^{m-1} u_j \, . \tag{3.51}$$

By substituting these relations into Eq. (3.48), it can be deduced that

$$\left(1 - \sum_{j=1}^{m+n-2} \widetilde{U}_j \right) \widetilde{U}_{m+n-1} > 0 \tag{3.52}$$

and

$$\left(1 - \sum_{j=1}^{m+n-2} \widetilde{U}_j\right)\left(1 - \widetilde{U}_{m+n-1}\right) > 0\,, \tag{3.53}$$

with

$$\widetilde{U}_j > 0\,, \quad j = 1, \ldots, m+n-2\,, \tag{3.54}$$

in view of Eqs. (3.47) and (3.50). It follows that the random variable $\widetilde{\mathbf{U}}$ takes its values in the set $\mathscr{U}$ defined as

$$\mathscr{U} = \left\{\mathbf{u} \in (0,1)^{m+n-1} \;:\; 1 - \sum_{k=1}^{m+n-2} u_k > 0\right\}. \tag{3.55}$$

The conditional probability density function $f_{\widetilde{\mathbf{P}}|\mathbf{C}}$ is then given by

$$f_{\widetilde{\mathbf{P}}|\mathbf{C}=\mathbf{c}}(\mathbf{p}) = f_{\widetilde{\mathbf{U}}}(\mathbf{h}^{-1}(\mathbf{p},\mathbf{c})) \times |\det([J(\mathbf{p},\mathbf{c})])|\,, \tag{3.56}$$

where $[J(\mathbf{p},\mathbf{c})]$ denotes the jacobian matrix defined component-wise as

$$[J(\mathbf{q},\mathbf{c})]_{jk} = \frac{\partial h_j^{-1}(\mathbf{q},\mathbf{c})}{\partial q_k}\,, \quad 1 \leqslant j,k \leqslant m+n-1\,. \tag{3.57}$$

As a consequence, the conditional probability density function $f_{\widetilde{\mathbf{P}}|\mathbf{C}=\mathbf{c}}$ writes

$$f_{\widetilde{\mathbf{P}}|\mathbf{C}=\mathbf{c}}(\mathbf{p}|\mathbf{c}) = f_{\widetilde{\mathbf{U}}}(\mathbf{h}^{-1}(\mathbf{p},\mathbf{c})) \times \left(\prod_{k=1}^{m+n-2} \frac{\widetilde{\eta}_k^2}{2c_2}\right) \frac{1}{2c_2 - \sum_{i=1}^{m+n-2} p_i \widetilde{\eta}_i^2}\,. \tag{3.58}$$

Let us now construct the probability density function $f_{\widetilde{\mathbf{U}}}$. The constraints induced by Eq. (3.52) are defined as

$$\mathbb{E}\left\{\log\left(1 - \sum_{i=1}^{m+n-2} \widetilde{U}_i\right)\right\} = \chi_1\,, \quad |\chi_1| < +\infty\,, \tag{3.59}$$

and

$$\mathbb{E}\{\log(\widetilde{U}_{m+n-1})\} = \nu_{m+n-1}\,, \quad |\nu_{m+n-1}| < +\infty\,, \tag{3.60}$$

and are supplemented with (see Eq. (3.53))

$$\mathbb{E}\{\log(1 - \widetilde{U}_{m+n-1})\} = \chi_2\,, \quad |\chi_2| < +\infty\,. \tag{3.61}$$

Furthermore, Eq. (3.54) is taken into account by imposing that

$$\mathbb{E}\{\log(\widetilde{U}_j)\} = \nu_j\,, \quad |\nu_j| < +\infty\,, \quad j = 1, \ldots, m+n-2\,. \tag{3.62}$$

Let $(1-\tau_{m+n-1}) \in (-\infty, 1)$, $(1-\rho_1) \in (-\infty, 1)$, $(1-\rho_2) \in (-\infty, 1)$ and $(1-\tau_k) \in (-\infty, 1)$, $1 \leqslant k \leqslant m+n-2$, be the Lagrange multipliers associated with Eqs. (3.59), (3.60), (3.61) and (3.62), respectively. The probability density function $f_{\widetilde{\mathbf{U}}}$ then takes the form

$$f_{\widetilde{\mathbf{U}}}(\mathbf{u}) = \mathbb{1}_{\mathscr{U}}(\mathbf{u})\, k_0 \left(\prod_{k=1}^{m+n-2} u_k^{\tau_k - 1}\right)\left(1 - \sum_{i=1}^{m+n-2} u_i\right)^{\tau_{m+n-1}-1} u_{m+n-1}^{\rho_1 - 1}(1 - u_{m+n-1})^{\rho_2 - 1} \tag{3.63}$$

and can be written as

$$f_{\widetilde{\mathbf{U}}}(\mathbf{u}) = f_{\widetilde{U}_1\ldots\widetilde{U}_{m+n-2}}(u_1,\ldots,u_{m+n-2}) \times f_{\widetilde{U}_{m+n-1}}(u_{m+n-1})\,, \tag{3.64}$$

in which

$$\begin{aligned} f_{\widetilde{U}_1\ldots\widetilde{U}_{m+n-2}}(u_1,\ldots,u_{m+n-2}) &= \mathbb{1}_{\mathcal{S}}(u_1,\ldots,u_{m+n-2}) \\ &\times \left\{\frac{\Gamma\left(\sum_{k=1}^{m+n-1}\tau_k\right)}{\prod_{k=1}^{m+n-1}\Gamma(\tau_k)}\right\}\left(\prod_{k=1}^{m+n-2}u_k^{\tau_k-1}\right)\left(1-\sum_{k=1}^{m+n-2}u_k\right)^{\tau_{m+n-1}-1} \end{aligned} \tag{3.65}$$

and

$$f_{\widetilde{U}_{m+n-1}}(v) = \mathbb{1}_{(0,1)}(v)\frac{1}{\mathcal{B}(\rho_1,\rho_2)}v^{\rho_1-1}(1-v)^{\rho_2-1}\,. \tag{3.66}$$

Here, the support $\mathcal{S}$ is given by

$$\mathcal{S} = \left\{\mathbf{u}\in(0,1)^{m+n-2} \,:\, 1-\sum_{k=1}^{m+n-2}u_k > 0\right\}\,. \tag{3.67}$$

As a consequence, it is seen that

- the random variables $(\widetilde{U}_1,\ldots,\widetilde{U}_{m+n-2})$ and $\widetilde{U}_{m+n-1}$ are statistically independent;
- $(\widetilde{U}_1,\ldots,\widetilde{U}_{m+n-2})$ follows a Dirichlet distribution with parameters $(\tau_1,\ldots,\tau_{m+n-1})$;
- $\widetilde{U}_{m+n-1}$ follows a Beta distribution with parameters (ρ_1,ρ_2).

Note that the integration constants in Eqs. (3.65) and (3.66) were readily inferred from the analytical expressions of the labeled statistical distributions under consideration.

The main result can be summarized in the following proposition.

Proposition 3.1. *For $m \geqslant 1$ and $n \geqslant 1$, let $\mathcal{W}$ be the stochastic Ogden-type stored energy function defined as*

$$\begin{aligned} \mathcal{W}([F]) = &\sum_{i=1}^{m} P_i(\mathrm{Tr}(([F]^T[F])^{\eta_i/2})-3) + \sum_{j=1}^{n} P_{j+m}(\mathrm{Tr}((\mathrm{Cof}([F]^T[F]))^{\eta_{j+m}/2})-3) \\ &+ \frac{P_{m+n+1}}{2}(\det([F])-1)^2 - S\log(\det([F]))\,, \end{aligned} \tag{3.68}$$

for all $[F]\in\mathbb{M}^3_+$, where

$$P_k = \frac{2C_2}{\eta_k^2}U_k\,,\quad 1\leqslant k\leqslant m-1\,,\quad m+1\leqslant k\leqslant m+n-1\,, \tag{3.69}$$

$$P_m = \frac{2C_2}{\eta_m^2}\Big(1-\sum_{i=1}^{m-1}U_i-\sum_{j=m+1}^{m+n-1}U_j\Big)U_{m+n+1}\,, \tag{3.70}$$

$$P_{m+n} = \frac{2C_2}{\eta_{m+n}^2}\Big(1-\sum_{i=1}^{m-1}U_i-\sum_{j=m+1}^{m+n-1}U_j\Big)(1-U_{m+n+1})\,, \tag{3.71}$$

$$P_{m+n+1} = 2C_2\Big(1-\sum_{i=1}^{m-1}U_i-\sum_{j=m+1}^{m+n-1}U_j\Big)U_{m+n+1} + C_1 - \frac{8}{3}C_2 + 2C_2\sum_{i=1}^{m-1}U_i\,. \tag{3.72}$$

and

- $\boldsymbol{\eta}$ *is such that* $\eta_1 \geqslant 2$, $\eta_1 \geqslant \ldots \eta_m \geqslant 1$, $\eta_{m+1} \geqslant 3/2$ *and* $\eta_{m+1} \geqslant \cdots \geqslant \eta_{m+n} \geqslant 1$;
- $\widetilde{\Lambda} = C_1 - 8C_2/3$ *follows a Gamma distribution with parameters* (α, θ_1);
- C_2 *follows a Gamma distribution with parameters* (β, θ_2);
- $(U_1, \ldots, U_{m-1}, U_{m+1}, \ldots, U_{m+n-1})$ *and* U_{m+n+1} *are statistically independent;*
- $(U_1, \ldots, U_{m-1}, U_{m+1}, \ldots, U_{m+n-1})$ *follows a Dirichlet distribution with the vector-valued parameter* $\boldsymbol{\tau} = (\tau_1, \ldots, \tau_{m+n-1})$;
- U_{m+n+1} *follows a Beta distribution with parameter* $\boldsymbol{\rho} = (\rho_1, \rho_2)$;
- S *is the* $\mathbb{R}_*^+$*-valued random variable defined by Eq.* (3.11).

Then the stored energy function $\mathcal{W}$ *is polyconvex, coherent at small strains, and coercive almost surely.*

As with the case of incompressible materials, this proposition underlines the key role played by the stochastic model to ensure that the stochastic nonlinear boundary value problem is well posed. In addition, it should be noticed that robust generators are available for sampling the involved probability density functions.

Example. *The case of Mooney-Rivlin materials corresponds to* $m = n = 1$ *and* $\eta_1 = \eta_2 = 2$, *so that* $m + n + 1 = 3$, $\mathbf{P} = (P_1, P_2, P_3)$ *and* $\widetilde{P} = P_3$. *The stochastic stored energy function then writes*

$$\begin{aligned}\mathcal{W}([F]) =& P_1 \left(\|[F]\|_F^2 - 3 \right) + P_2 \left(\|\mathrm{Cof}([F])\|_F^2 - 3 \right) \\ &+ \frac{P_3}{2} \left(\det([F]) - 1 \right)^2 - (2P_1 + 4P_2) \log \left(\det([F]) \right) ,\end{aligned} \tag{3.73}$$

for all $[F] \in \mathbb{M}_+^3$. *The random variables* P_1 *and* P_2 *are given by*

$$P_1 = \frac{2C_2}{4} U \,, \quad P_2 = \frac{2C_2}{4} (1 - U) \,. \tag{3.74}$$

The probability density function of the random variable $\mathbf{C}$ *is given by Eq.* (3.43), *and the random variable* P_3 *is given by*

$$P_3 = 2C_2 U + C_1 - \frac{8}{3} C_2 \,, \tag{3.75}$$

where U *is a Beta distributed random variable with parameters* (ρ_1, ρ_2).

Remark 3.4.1. *Proceeding similarly as in the incompressible case (see Eq.* (2.53) *in Section 2.6.1), the set of nonlinear equations to be solved, induced by Eqs.* (3.59)-(3.62), *reads as:*

$$\begin{aligned}&\psi(\tau_{m+n-1}) - \psi\Big(\sum_{k=1}^{m+n-1} \tau_k \Big) = \chi_1 \,, \\ &\psi(\tau_j) - \psi\Big(\sum_{k=1}^{m+n-1} \tau_k \Big) = \nu_j \,, \quad j = 1, \ldots, m+n-2 \,,\end{aligned} \tag{3.76}$$

and

$$\begin{aligned}&\psi(\rho_1) - \psi(\rho_1 + \rho_2) = \nu_{m+n-1} \,, \\ &\psi(\rho_2) - \psi(\rho_1 + \rho_2) = \chi_2 \,,\end{aligned} \tag{3.77}$$

where it is recalled that ψ *is the digamma function [87]. In practice, this system of* $m + n + 1$ *equations can be solved by using a nonlinear least-square algorithm for instance.*

3.4.3 Stochastic modeling under inequality and mean constraints

In this section, additional constraints related to the mean values of random variables $\widetilde{P}_j$, $j = 1, \ldots, m+n-1$ are considered. The probabilistic model is therefore constructed under the constraints given by Eqs. (3.59)-(3.62), which are complemented with

$$\mathbb{E}\{\widetilde{\mathbf{U}}\} = \underline{\widetilde{\mathbf{u}}}\,, \tag{3.78}$$

where $\underline{\widetilde{\mathbf{u}}} \in \mathscr{U}$. The probability density function of random variable $\widetilde{\mathbf{U}}$ then takes the form:

$$\begin{aligned} f_{\widetilde{\mathbf{U}}}(\mathbf{u}) =& \mathbb{1}_{\mathscr{U}}(\mathbf{u})\, k_0 \left(\prod_{k=1}^{m+n-2} u_k^{\tau_k - 1}\right)\left(1 - \sum_{i=1}^{m+n-2} u_i\right)^{\tau_{m+n-1}-1} u_{m+n-1}^{\rho_1-1}(1-u_{m+n-1})^{\rho_2-1} \\ & \times \exp\left(-\sum_{k=1}^{m+n-2} \xi_k u_k - \varpi u_{m+n-1}\right), \end{aligned} \tag{3.79}$$

where $\xi_k \in \mathbb{R}$, $1 \leqslant k \leqslant m+n-2$ and $\varpi \in \mathbb{R}$ are additional Lagrange multipliers associated with the mean constraint. It is observed that

$$f_{\widetilde{\mathbf{U}}}(u_1, \ldots, u_{m+n-2}, u_{m+n-1}) = f_{\widetilde{U}_1 \ldots \widetilde{U}_{m+n-2}}(u_1, \ldots, u_{m+n-2}) \times f_{\widetilde{U}_{m+n-1}}(u_{m+n-1})\,, \tag{3.80}$$

hence showing that $(\widetilde{U}_1, \ldots, \widetilde{U}_{m+n-2})$ and $\widetilde{U}_{m+n-1}$ are statistically independent. The associated probability density functions write

$$\begin{aligned} f_{\widetilde{U}_1 \ldots \widetilde{U}_{m+n-2}}(u_1, \ldots, u_{m+n-2}) =& \mathbb{1}_{\mathcal{S}}(u_1, \ldots, u_{m+n-2})\, k_0 \left(\prod_{k=1}^{m+n-2} u_k^{\tau_k - 1}\right) \\ & \times \left(1 - \sum_{k=1}^{m+n-2} u_k\right)^{\tau_{m+n-1}-1} \times \exp\left(-\sum_{k=1}^{m+n-2} \xi_k u_k\right), \end{aligned} \tag{3.81}$$

and

$$f_{\widetilde{U}_{m+n-1}}(v) = \mathbb{1}_{(0,1)}(v) \frac{v^{\rho_1-1}(1-v)^{\rho_2-1}\exp(-\varpi v)}{\mathcal{B}(\rho_1,\rho_2)\mathcal{F}(\rho_1, \rho_1+\rho_2, -\varpi)}\,. \tag{3.82}$$

The main result stated in Proposition 3.1 still holds with the probability density functions $f_{\widetilde{U}_1 \ldots \widetilde{U}_{m+n-2}}$ and $f_{\widetilde{U}_{m+n-1}}$ defined by Eqs. (3.81) and (3.82), respectively. In the particular case where $\xi_k = \xi$, $1 \leqslant k \leqslant m+n-2$, an explicit expression for the normalization constant k_0 in Eq. (3.81) can be obtained in terms of confluent hypergeometric functions [92].

Example. *In the particular case of a Mooney-Rivlin material, the stochastic stored energy function is defined by Eqs. (3.73) and (3.74), where P_3 takes the form*

$$P_3 = 2C_2\widetilde{U} + C_1 - \frac{8}{3}C_2\,, \tag{3.83}$$

and $\widetilde{U}$ follows a Kummer-Beta distribution with parameters ρ_1, ρ_2 and ϖ (see Eq. (3.82)). In this case and following previous developments, it can be shown that these parameters satisfy the following system of equations:

$$\chi_1 = \psi(\rho_1) - \psi(\rho_1+\rho_2) + \frac{\partial}{\partial\rho_1}\log\left(\mathcal{F}(\rho_1, \rho_1+\rho_2, -\varpi)\right), \tag{3.84a}$$

$$\chi_2 = \psi(\rho_2) - \psi(\rho_1+\rho_2) + \frac{\partial}{\partial\rho_2}\log\left(\mathcal{F}(\rho_1, \rho_1+\rho_2, -\varpi)\right),, \tag{3.84b}$$

$$\underline{\widetilde{u}} = \frac{\rho_1}{\rho_1+\rho_2}\frac{\mathcal{F}(\rho_1+1, \rho_1+\rho_2+1, -\varpi)}{\mathcal{F}(\rho_1, \rho_1+\rho_2, -\varpi)}\,. \tag{3.84c}$$

3.5 Uncertainty propagation in computational homogenization

As a numerical illustration, the proposed probabilistic formulation is used in this section to model uncertainties in the nonlinear properties of constitutive phases within a multiscale setup (see, *e.g.*, [38] for the propagation of microstructural randomness). A two-dimensional microstructure composed of a Neo-Hookean matrix reinforced by stiffer Neo-Hookean circular inclusions is considered. The volume fraction is fixed to 0.4, and forty inclusions (with equal diameters) are randomly placed by using the packing generation algorithm detailed in [105]. The considered representative volume element $\mathscr{B} \subset \mathbb{R}^2$ is shown in Fig. 3.1.

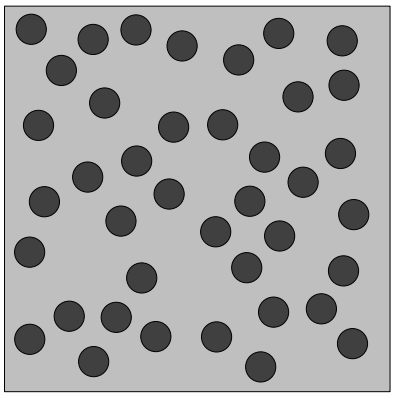

Figure 3.1 – Realization of the random microstructure under consideration.

3.5.1 Homogenization framework for hyperelastic composites

Since the properties of the inclusion phase are assumed deterministic and defined by an isotropic Neo-Hookean model, it follows that

$$w^{(f)}([F]) = \frac{\mu^{(f)}}{2}\left(\|[F]\|_F^2 - 3\right) + \frac{\lambda^{(f)}}{2}\left(\det([F]) - 1\right)^2 - \mu^{(f)}\log\left(\det([F])\right) , \tag{3.85}$$

with $\lambda^{(f)} > 0$ and $\mu^{(f)} > 0$. Here, uncertainties on the constitutive behavior of the matrix phase are taken into account through the stochastic Neo-Hookean stored energy function (see Section 3.3)

$$\mathcal{W}^{(m)}([F]) = \frac{C_2}{2}(\|[F]\|_F^2 - 3) + \frac{\Lambda}{2}(\det([F]) - 1)^2 - C_2\log(\det([F]))\,, \tag{3.86}$$

where the random variables Λ and C_2 follow Gamma distributions with parameters (α, θ_1) and (β, θ_2), respectively. The local stochastic stored energy function is then defined as

$$\mathcal{W}(\mathbf{x}, [F]) = \chi^{(m)}(\mathbf{x})\mathcal{W}^{(m)}([F]) + \chi^{(f)}(\mathbf{x})w^{(f)}([F])\,, \quad \forall \mathbf{x} \in \mathscr{B}\,, \quad \forall [F] \in \mathbb{M}_+^3\,, \tag{3.87}$$

where $\chi^{(r)}$, $r \in \{f, m\}$, is the characteristic function of phase r. When $\mathscr{B}$ undergoes linear deformations on its boundaries, and assuming the separation of scales (in practice, this key assumption is checked through a convergence analysis with respect to the measure of $\mathscr{B}$), the stochastic effective stored energy function is then defined as (see [106, 107, 108] for reviews in a deterministic context)

$$\overline{\mathcal{W}}_{\text{eff}}([\overline{F}]) = \min_{\mathbf{z} \in \mathcal{K}([\overline{F}])} \frac{1}{|\mathscr{B}|}\int_{\mathscr{B}} \mathcal{W}(\mathbf{x}, [\overline{F}] + [\nabla \mathbf{z}(\mathbf{x})])\, d\mathbf{x}\,, \tag{3.88}$$

where $\mathcal{K}([\overline{F}])$ is the set of admissible fluctuations fields:

$$\mathcal{K}([\overline{F}]) = \{\mathbf{z} \in W^{1,p}(\mathscr{B}, \mathbb{R}^3) \,:\, \mathbf{z}(\mathbf{x}) = \mathbf{0} \text{ on } \partial\mathscr{B}\} \,. \tag{3.89}$$

Since the microscopic stored energy functions $w^{(f)}$ and $\mathcal{W}^{(m)}$ are almost surely frame-invariant, it follows that there exists an effective potential $\overline{\mathcal{W}}$ such that

$$\overline{\mathcal{W}}([\overline{C}]) = \overline{\mathcal{W}}_{\text{eff}}([\overline{F}]) \,, \quad [\overline{C}] = [\overline{F}]^{\mathrm{T}}[\overline{F}] \,, \tag{3.90}$$

for all $[\overline{F}] \in \mathbb{M}^3_+$. From a numerical standpoint, the finite element mesh for the microstructure shown in Fig. 3.1 is composed of 5 431 nodes and 10 660 linear triangular elements. The nonlinear boundary value problems are solved with a standard nonlinear finite element method [109] implemented with the C++ library Eigen3 [110].

Below, the propagation of the uncertainties from the microscale to the macroscale is addressed. The framework is first presented in Section 3.5.2. The numerical results are then discussed in Section 3.5.3.

3.5.2 Polynomial chaos expansion of the stochastic effective potential

In this section, the stochastic effective stored energy function is modeled using a polynomial chaos expansion (PCE) [111, 112, 1]. Let $\mathbf{Y}$ be the random variable such that

$$Y_1 = \frac{\Lambda}{\theta_1} \,, \quad Y_2 = \frac{C_2}{\theta_2} \,. \tag{3.91}$$

By construction, the random variables Y_1 and Y_2 are statistically independent and follow Gamma distributions with parameters $(\alpha, 1)$ and $(\beta, 1)$. It is assumed below that the stochastic effective stored energy function is a second-order random variable, regardless of the macroscopic right Cauchy-Green tensor $[\overline{C}]$ under consideration, *i.e.*,

$$\mathbb{E}\{\overline{\mathcal{W}}^2([\overline{C}])\} < +\infty \,, \quad \forall [\overline{C}] \in \mathbb{K} \,, \tag{3.92}$$

where $\mathbb{K}$ is a given subset of $\mathbb{S}^3_+$. Note here that the homogenization is performed at small strains, and that no local instability can occur. Therefore, and for all $[\overline{C}]$ fixed in $\mathbb{K}$, the random variable $\overline{\mathcal{W}}([\overline{C}])$ admits the following decomposition:

$$\overline{\mathcal{W}}([\overline{C}]) = \sum_{|\boldsymbol{\zeta}|=0}^{+\infty} z_{\boldsymbol{\zeta}}([\overline{C}])\, \Psi_{\boldsymbol{\zeta}}(\mathbf{Y}) \,, \tag{3.93}$$

where $\boldsymbol{\zeta} \in \mathbb{N}^2$ is a multi-index, $|\boldsymbol{\zeta}| = \zeta_1 + \zeta_2$, and $\{\Psi_{\boldsymbol{\zeta}}\}_{\boldsymbol{\zeta}}$ is a set of multivariate polynomials that are orthonormal with respect to the probability measure $P_{\mathbf{Y}}(\mathrm{d}\mathbf{y})$ of $\mathbf{Y}$:

$$\mathbb{E}\left\{\Psi_{\boldsymbol{\zeta}}(\mathbf{Y})\, \Psi_{\boldsymbol{\varsigma}}(\mathbf{Y})\right\} = \delta_{\boldsymbol{\zeta}\boldsymbol{\varsigma}} \,, \tag{3.94}$$

where $\delta_{\boldsymbol{\zeta}\boldsymbol{\varsigma}} = \delta_{\zeta_1\varsigma_1} \times \delta_{\zeta_2\varsigma_2}$ and δ_{ij} denotes the Kronecker symbol. Note that the above polynomials implicitly depend on the parameters α and β defining the probability distribution of $\mathbf{Y}$. The coefficients $\{z_{\boldsymbol{\zeta}}([\overline{C}])\}_{\boldsymbol{\zeta}}$ are then given by

$$z_{\boldsymbol{\zeta}}([\overline{C}]) = \mathbb{E}\left\{\overline{\mathcal{W}}([\overline{C}])\Psi_{\boldsymbol{\zeta}}(\mathbf{Y})\right\} \,, \tag{3.95}$$

for all $\boldsymbol{\zeta} \in \mathbb{N}^2$. The orthonormal polynomials $\{\Psi_{\boldsymbol{\zeta}}\}_{\boldsymbol{\zeta}}$ correspond to the bivariate normalized and generalized Laguerre polynomials [113] defined as [87]

$$\Psi_{\boldsymbol{\zeta}}(\mathbf{Y}) = \varphi_{\zeta_1}(Y_1) \times \varphi_{\zeta_2}(Y_2)\,, \tag{3.96}$$

where φ_{ζ_1} and φ_{ζ_2} are given by

$$\varphi_{\zeta_1}(Y_1) = \sqrt{\frac{\zeta_1!\Gamma(\alpha)}{\Gamma(\zeta_1+\alpha)}} L_{\zeta_1}^{(\alpha-1)}(Y_1)\,, \quad \varphi_{\zeta_2}(Y_2) = \sqrt{\frac{\zeta_2!\Gamma(\beta)}{\Gamma(\zeta_2+\beta)}} L_{\zeta_2}^{(\beta-1)}(Y_2)\,. \tag{3.97}$$

In Eq. (3.97), the polynomial $L_n^{(\xi-1)}$ stands for the classical generalized Laguerre polynomial of order $n \in \mathbb{N}$ with parameter $\xi > 0$. In practice, the polynomial chaos expansion given by Eq. (3.93) is truncated at an order p, yielding the mean-square convergent approximation

$$\overline{\mathcal{W}}_p([\overline{C}]) = \sum_{|\boldsymbol{\zeta}| \in \mathscr{A}_p}^{p} z_{\boldsymbol{\zeta}}([\overline{C}]) \Psi_{\boldsymbol{\zeta}}(\mathbf{Y})\,, \tag{3.98}$$

where $\mathscr{A}_p = \{\boldsymbol{\zeta} \in \mathbb{N}^2 \,:\, |\boldsymbol{\zeta}| \leqslant p\}$ and $\mathrm{card}(\mathscr{A}_p) = (2+p)!/(2p!)$. In practice, the polynomial coefficients can be computed by using the Monte Carlo method, quadrature rules or stochastic collocation methods (see [2] for extensive surveys in both low and high dimensions). Given the low stochastic dimension of the problem, the polynomial coefficients given by Eq. (3.95) are computed thanks to a generalized Gauss-Laguerre quadrature rule [87, 114]:

$$z_{\boldsymbol{\zeta}}([\overline{C}]) \simeq z_{\boldsymbol{\zeta}}^{\star}([\overline{C}]) = \frac{1}{\Gamma(\alpha)\Gamma(\beta)} \sum_{i=1}^{n_{\mathcal{Q}}} \sum_{j=1}^{n_{\mathcal{Q}}} \omega_{ij}^{(n_{\mathcal{Q}})} \overline{w}([\overline{C}]; \mathbf{y}^{(i,j)}) \Psi_{\boldsymbol{\zeta}}(\mathbf{y}^{(i,j)})\,, \tag{3.99}$$

where $\{\omega_{ij}^{(n_{\mathcal{Q}})}, \mathbf{y}^{(i,j)}\}_{i,j=1}^{n_{\mathcal{Q}}}$ is the set of weights and nodes for the two-dimensional generalized Gauss-Laguerre quadrature rule, and $\overline{w}([\overline{C}]; \mathbf{y}^{(i,j)})$ denotes the value of the stochastic stored energy function $\overline{W}([\overline{C}])$ for $Y_1 = y_1^{(i,j)}$ and $Y_2 = y_2^{(i,j)}$.

The optimal order p and number of quadrature points $n_{\mathcal{Q}}$ must be determined through convergence studies. For a given order of expansion, the number of integration points $n_{\mathcal{Q}}^{\mathrm{opt}}$ is determined by studying the error function $\varepsilon_{\mathcal{Q}}$ defined as

$$\varepsilon_{\mathcal{Q}}(n_{\mathcal{Q}}) = \frac{\|\mathbf{z}^{\star}(n_{\mathcal{Q}}+1) - \mathbf{z}^{\star}(n_{\mathcal{Q}})\|}{\|\mathbf{z}^{\star}(n_{\mathcal{Q}})\|}\,, \quad n_{\mathcal{Q}} \geqslant 1\,, \tag{3.100}$$

where $\mathbf{z}^{\star}(n_{\mathcal{Q}})$ gathers the polynomial coefficients $\{z_{\boldsymbol{\zeta}}^{\star}\}_{\boldsymbol{\zeta}}$ computed with $n_{\mathcal{Q}}$ quadrature points along each direction. The optimal number $n_{\mathcal{Q}}^{\mathrm{opt}}$ is then chosen such that $\varepsilon_{\mathcal{Q}}(n_{\mathcal{Q}}^{\mathrm{opt}}) < \varepsilon_{\mathcal{Q}}^{\mathrm{tol}}$, where $\varepsilon_{\mathcal{Q}}^{\mathrm{tol}}$ is some user-specified tolerance parameter. The optimal order p^{opt} is determined such that $\varepsilon(p^{\mathrm{opt}}) < \varepsilon^{\mathrm{tol}}$, where $\varepsilon(p)$ is the following L^2 error measure:

$$\varepsilon(p) = \frac{\mathbb{E}\{(\overline{\mathcal{W}}([\overline{C}]) - \overline{\mathcal{W}}_p([\overline{C}]))^2\}}{\mathbb{E}\{\overline{\mathcal{W}}([\overline{C}])^2\}}\,, \tag{3.101}$$

and $\varepsilon^{\mathrm{tol}}$ denotes a tolerance parameter. The above error measure is computed with the generalized Gauss-Laguerre quadrature rule (note that the number of integration points that is necessary to reach convergence may be higher than $n_{\mathcal{Q}}^{\mathrm{opt}}$).

3.5.3 Results for a two-dimensional loading

For numerical purposes, we consider the macroscopic loading path defined by the following set $\mathscr{M} \subset \mathbb{S}^3_+$ of macroscopic Cauchy-Green tensors:

$$\mathscr{M} = \left\{ [\overline{C}] \in \mathbb{S}^3_+ \mid (\overline{C}_{11}, \overline{C}_{22}) \in ([0.8, 1.5])^2,\ \overline{C}_{33} = 1,\ \overline{C}_{ij} = 0 \text{ for } i \neq j \right\} . \tag{3.102}$$

For the stochastic matrix phase, the mean values of the material parameters are chosen as $\underline{c}_1^{(1)} = 1750$ MPa and $\underline{c}_2^{(1)} = 358.125$ MPa. The associated shape parameters (α, θ_1) and (β, θ_2) are such that $\theta_1 = \underline{\lambda}^{(1)}/\alpha$ and $\theta_2 = \underline{c}_2^{(1)}/\beta$, where $\underline{\lambda}^{(1)} = \underline{c}_1^{(1)} - 2\underline{c}_2^{(1)}/3$. The parameters α and β are further chosen as $\alpha = \beta = 25$, hence inducing a coefficient of variation for random variables $\Lambda^{(1)}$ and $C_2^{(1)}$ equal to 20%. The deterministic material parameters characterizing the inclusions are chosen as $c_1^{(2)} = 100\underline{c}_1^{(1)}$ and $c_2^{(2)} = 100c_2^{(1)}$, so that the elastic contrast between the matrix (in mean) and the fillers is equal to 100. The mean computation time associated with each call to the nonlinear finite element solver is 0.8664 second on a 2,9 GHz core. The convergence analysis of the polynomial chaos expansion with respect to p and $n_{\mathcal{Q}}$ is performed for a given macroscopic loading defined by

$$[\overline{C}_0] = 1.5(\mathbf{e}_1 \otimes \mathbf{e}_1 + \mathbf{e}_2 \otimes \mathbf{e}_2) + 0.3(\mathbf{e}_1 \otimes \mathbf{e}_2 + \mathbf{e}_2 \otimes \mathbf{e}_1) . \tag{3.103}$$

The tolerance parameter $\varepsilon_{\mathcal{Q}}^{\text{tol}}$ associated with the convergence of numerical integration is chosen as 10^{-10}. The graphs of the error functions $n_{\mathcal{Q}} \mapsto \varepsilon_{\mathcal{Q}}(n_{\mathcal{Q}})$ and $p \mapsto \varepsilon(p)$ are shown in Fig. (3.2) for $1 \leqslant n_{\mathcal{Q}} \leqslant 20$ and $p = 2k+1$, $k \in \{0, 1, 2, 3\}$. The associated results are summarized in Tab. 3.1.

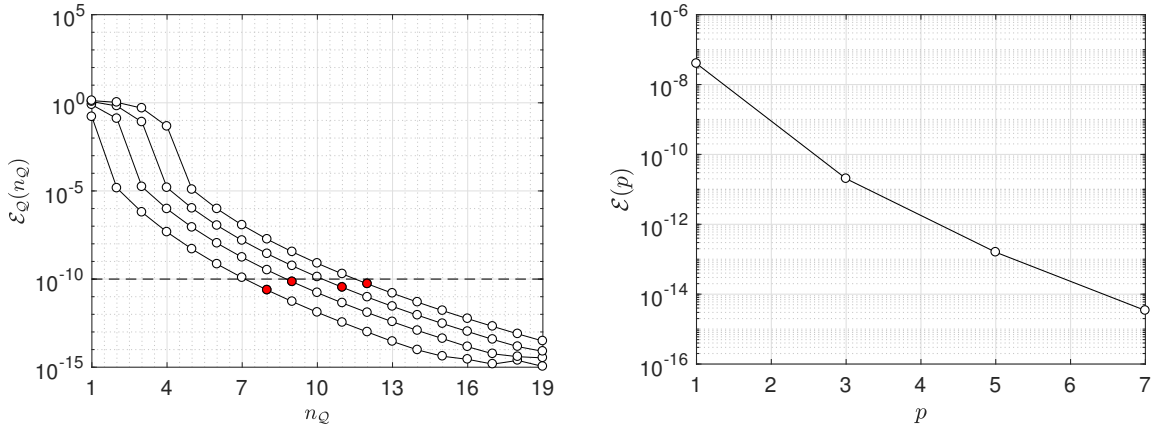

Figure 3.2 – Graphs of the error functions $n_{\mathcal{Q}} \mapsto \varepsilon_{\mathcal{Q}}(n_{\mathcal{Q}})$ (left panel) and $p \mapsto \varepsilon(p)$ (right panel), for $1 \leqslant n_{\mathcal{Q}} \leqslant 20$ and $p = 2k+1$, $k \in \{0, 1, 2, 3\}$.

Based on the convergence study, the optimal order p^{opt} is chosen as $p^{\text{opt}} = 7$ with $n_{\mathcal{Q}}^{\text{opt}} = 12$. In order to illustrate the accuracy of the polynomial chaos expansion, some probability density functions estimated by sampling the PCE are compared with reference solutions obtained by direct Monte Carlo simulations (20 000 samples are used). The probability density function of the stochastic effective potential for the macroscopic Cauchy-Green tensor $[\overline{C}_0]$ is shown in Fig. (3.3) (left panel). In addition, a comparison for the joint probability density function of the stochastic effective potential at points $[\overline{C}_0]$ and $[\overline{C}_1]$, with

$$[\overline{C}_1] = 1.6(\mathbf{e}_1 \otimes \mathbf{e}_1 + \mathbf{e}_2 \otimes \mathbf{e}_2) + 0.2(\mathbf{e}_1 \otimes \mathbf{e}_2 + \mathbf{e}_2 \otimes \mathbf{e}_1) , \tag{3.104}$$

p	1	3	5	7
$n_{\mathcal{Q}}^{\text{opt}}$	8	9	11	12
$\varepsilon_{\mathcal{Q}}(n_{\mathcal{Q}}^{\text{opt}})$	0.2370×10^{-11}	0.6976×10^{-11}	0.3377×10^{-11}	0.5318×10^{-11}
$\varepsilon(p)$	3.98×10^{-8}	2.02×10^{-11}	1.59×10^{-13}	3.47×10^{-15}

Table 3.1 – Optimal numbers of integration points $n_{\mathcal{Q}}^{\text{tol}}$ for odd orders $p = 1, 3, 5, 7$ and associated errors and for $[\overline{C}] = [\overline{C}_0]$.

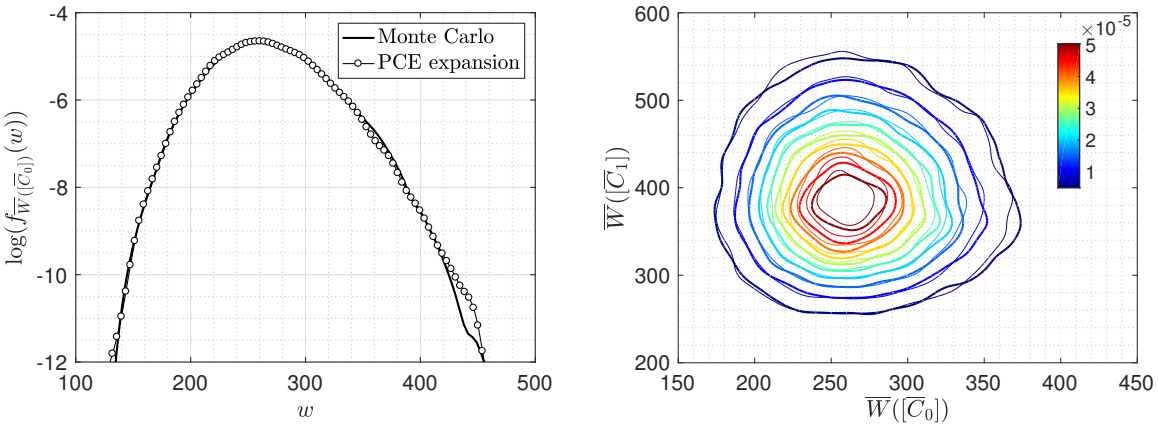

Figure 3.3 – Left: Probability density function of the stochastic effective potential for $[\overline{C}] = [\overline{C}_0]$. Thick black line: according to 20000 Monte Carlo simulations. Red dots: According to the PC expansion truncated at order $p = 7$. Right: Graph of the joint probability density function $f_{\overline{W}([\overline{C}_0])\overline{W}([\overline{C}_1])}$. Thick line: Monte Carlo simulations. Thin line: PCE.

is also provided in the same figure (right panel) In both cases, a very good match is observed. Finally, we characterize below the mean and variance fields of the stochastic effective stored energy function on a regular grid composed of 100 points belonging to $\mathscr{M}$. The grid is specifically constructed with 10 equally-spaced points along each direction in the plane $(\overline{C}_{11}, \overline{C}_{22})$. For each macroscopic point, the polynomial chaos is constructed with $p = 7$ and $n_{\mathcal{Q}} = 12$, resulting in 144×100 nonlinear simulations. According to Eq. (3.98), the mean value $\mathbb{E}\{\overline{W}_p([\overline{C}])\}$ and variance $\mathbb{E}\{\overline{W}_p^2([\overline{C}])\}$ can be estimated as

$$\mathbb{E}\{\overline{W}_p([\overline{C}])\} = z_{\boldsymbol{\zeta}^{(1)}}([\overline{C}])\,, \quad \mathbb{E}\{\overline{W}_p^2([\overline{C}])\} = \sum_{|\boldsymbol{\zeta}|=0}^{p} z_{\boldsymbol{\zeta}}^2([\overline{C}])\,. \tag{3.105}$$

The mean and variance fields are shown in Fig. (3.4).

3.6 Conclusion

This chapter was dedicated to the construction of Ogden-type stochastic stored energy functions for homogeneous, isotropic and compressible materials [47]. As with the incompressible case, the methodology consists in ensuring the well-posedness of the stochastic nonlinear boundary value problem through an entropy maximization. Explicit forms were derived for Neo-Hookean and Mooney-Rivlin models, as well as for general-order Ogden potentials. The use of the proposed models was finally illustrated by propagating constitutive-model uncertainties through a

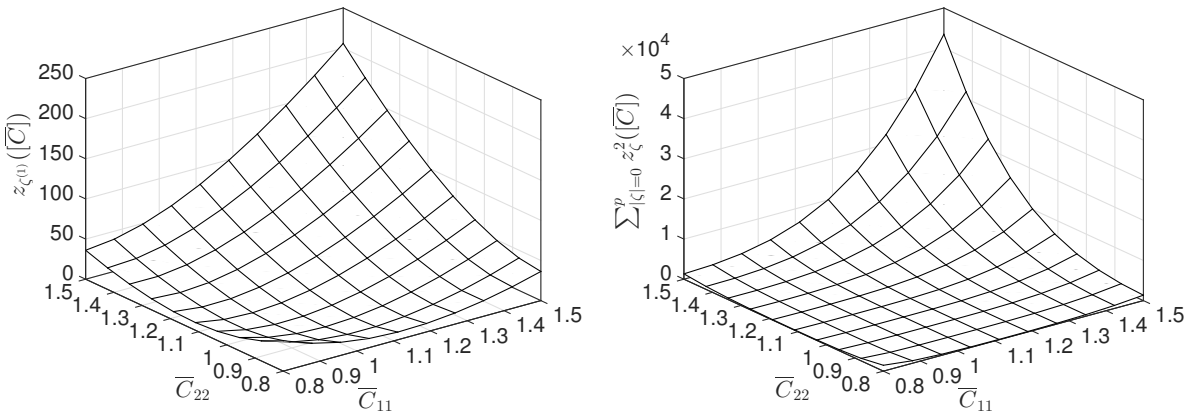

Figure 3.4 – (Left panel) Graph of the mean effective stored energy function $[\overline{C}] \mapsto z_{\boldsymbol{\zeta}^{(1)}}([\overline{C}])$. (Right panel) Graph of the variance of the effective stored energy function $[\overline{C}] \mapsto \sum_{|\boldsymbol{\zeta}|=0}^{p} z_{\boldsymbol{\zeta}}^2([\overline{C}])$.

multiscale operator.

Chapter 4

Projection of Effective Strain Energy Functions

Contents

4.1 Introduction

The growing use of composite materials for structural applications and the continuous increase of the computational capacities have motivated the development of coupling strategies where information is exchanged back-and-forth between the microscopic and macroscopic scales (see Fig. 4.1). This class of methods includes the multilevel FE^2 method [115, 116], which offers a

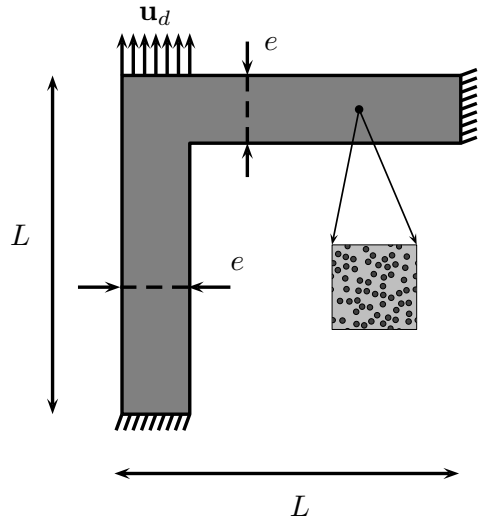

Figure 4.1 – Schematic representation of the FE^2 method: here, information is sent back-and-forth between the microscopic and macroscopic scales, at every Gauss point of the coarse mesh.

great versatility in terms of handled constitutive equations. Although the associated algorithms can easily be made parallel (see, *e.g.*, [117] for a large-scale simulation), such approaches still suffer from their computational cost. Many alternative approaches were then proposed to address general situations, such as the Multiscale Finite Element Methods (MsFEMs) [118, 119], where multiscale basis functions are constructed in finite element spaces as the simulation goes on, and the Finite Element Heterogeneous Multiscale Methods (FE-HMMs) [120, 121, 122, 123].

Alternatively, various methodologies aiming at the definition of surrogate models were also proposed in the last few years. Here, the basic idea is to construct a response surface mapping the relevant macroscopic variables onto the nonlinear effective behavior; thanks to a post-processing procedure defined on a set of offline microscale computations. Such a strategy has been followed in [124, 125, 126] by means of proper orthogonal decomposition, low-rank approximations and spline interpolations, in [127] by resorting on Neural Networks or in [128, 129, 130, 131] to list a few. A overview of the predictive models in nonlinear computational homogenization can be found in, *e.g.*, [132, 133]. In particular, the contribution in [134] is concerned with an expansion in orthogonal polynomials, and proposes the use of compressive sampling [135] in order to compute the coefficients involved in the polynomial series.

In this chapter, the construction of surrogate models for the homogenized stored energy functions is constructed using polynomial series in terms of the macroscopic deformations and projections onto given classes of potentials. This chapter is organized as follows. Section 4.2 is devoted to a brief review of homogenization theory for nonlinear hyperelastic materials. The construction of surrogate model using a polynomial series is then investigates, in Section 4.3. The accuracy of the approximation is then extensively assessed on various deterministic and disordered microstructures. Finally, in Section 4.4, the definition of projections onto classical sets of stored energy functions is explored. The relevance of this approach is illustrated on several examples, including a two-scale structural problem.

4.2 Background on concurrent multiscale coupling

4.2.1 Definition of the macroscopic boundary value problem

Let $\mathscr{B}_{\text{macro}}$ be the reference configuration occupied by the structure of interest. The latter undergoes a deformation map $\boldsymbol{\psi} : \mathscr{B}_{\text{macro}} \to \mathbb{R}^3$, and the associated deformation gradient is denoted by

$$[\overline{F}(\mathbf{y})] = [\nabla \boldsymbol{\psi}(\mathbf{y})] \,, \quad \forall \mathbf{y} \in \mathscr{B}_{\text{macro}} \,. \tag{4.1}$$

The potential defining the hyperelastic medium at the macroscale is denoted by $\overline{w}_{\text{macro}} : \mathbb{M}^3_+ \to \mathbb{R}$ and such that the effective first Piola-Kirchhoff stress tensor writes

$$[\overline{P}([\overline{F}])] = \sum_{k=1}^{3} \sum_{\ell=1}^{3} \frac{\partial \overline{w}_{\text{macro}}([\overline{F}])}{\partial \overline{F}_{k\ell}} \, \mathbf{e}_k \otimes \mathbf{e}_\ell \,, \quad \forall [\overline{F}] \in \mathbb{M}^3_+ \,. \tag{4.2}$$

By letting $\mathbf{h}^{(\text{macro})} : \Gamma_N^{\text{macro}} \to \mathbb{R}^3$ be the vector corresponding to the natural boundary conditions applied on the portion Γ_N^{macro} of $\partial \mathscr{B}_{\text{macro}}$, the energy functional $\mathcal{I}^{(\text{macro})} : \mathcal{X}^{\text{macro}} \to \mathbb{R}$ writes

$$\mathcal{I}^{(\text{macro})}(\boldsymbol{\psi}) = \int_{\mathscr{B}_{\text{macro}}} \overline{w}_{\text{macro}}([\nabla \boldsymbol{\psi}(\mathbf{y})]) \, d\mathbf{y} - \int_{\overline{\Gamma}_N} \langle \mathbf{h}^{(\text{macro})}(\mathbf{y}), \boldsymbol{\psi}(\mathbf{y}) \rangle \, d\mathbf{y} \,, \tag{4.3}$$

with $\mathcal{X}^{\text{macro}} = \{\boldsymbol{\psi} \in W^{1,p}(\mathscr{B}_{\text{macro}}, \mathbb{R}^3) \, : \, \mathcal{I}^{(\text{macro})}(\boldsymbol{\psi}) < +\infty \,, \, \boldsymbol{\psi} = \boldsymbol{\psi}_d|_{\overline{\Gamma}_D}\}$, in which $\boldsymbol{\psi}_d : \overline{\Gamma}_D \to \mathbb{R}^3$ some essential boundary conditions.

4.2.2 Definition of the homogenization problem

Let us consider the representative volume element $\mathscr{B}_{\text{micro}}$ located at point $\mathbf{y}$ in the structure, and denote its boundary by $\partial\mathscr{B}_{\text{micro}}$. Let $L_{\mathscr{B}_{\text{micro}}}$ be the characteristic length of $\mathscr{B}_{\text{micro}}$. This volume element is constituted of n_r homogeneous phases, with each phase r occupying a domain $\mathscr{B}^{(r)}_{\text{micro}}$ such that $\mathscr{B}_{\text{micro}} = \bigcup_{r=1}^{n_r} \mathscr{B}^{(r)}_{\text{micro}}$ and $\bigcap_{r=1}^{n_r} \mathscr{B}^{(r)}_{\text{micro}} = \varnothing$. The local stored energy function $w : \mathscr{B}_{\text{micro}} \times \mathbb{M}^3_+ \to \mathbb{R}$ then takes the form

$$w(\mathbf{x}, [F]) = \sum_{r=1}^{n_r} \chi^{(r)}(\mathbf{x}) w^{(r)}([F]) \,, \quad \forall \mathbf{x} \in \mathscr{B}_{\text{micro}} \,, \quad \forall [F] \in \mathbb{M}^3_+ \,, \tag{4.4}$$

where $\chi^{(r)}$ and $w^{(r)}$ are the characteristic function and stored energy function associated with phase r, respectively. Assume that the stored energy functions of the n_r homogeneous phases are objective, so that they can be expressed in terms of the right Cauchy-Green tensor. Hence, there exist $\widetilde{w}$ and $\widetilde{w}^{(r)}$, $1 \leqslant r \leqslant n_r$, such that for an associated pair $([F], [C])$, $w^{(r)}([F]) = \widetilde{w}^{(r)}([C])$ and $w(\mathbf{x}, [F]) = \widetilde{w}(\mathbf{x}, [C])$ for all $\mathbf{x}$ in $\mathscr{B}_{\text{micro}}$. In addition, it is assumed that the stored energy functions $\{w^{(r)}\}_{r=1}^{n_r}$ are admissible in the sense considered in the previous chapters (that is, they are polyconvex and coercive, and satisfy the consistency condition for vanishing deformation gradients).

Following [106], and upon neglecting body forces, the macroscopic deformation gradient $[\overline{F}(\mathbf{y})]$ and effective first Piola-Kirchhoff stress $[\overline{P}(\mathbf{y})]$ are defined as

$$[\overline{F}(\mathbf{y})] = \frac{1}{|\mathscr{B}_{\text{micro}}|} \int_{\partial\mathscr{B}_{\text{micro}}} \boldsymbol{\varphi}(\mathbf{x}; \mathbf{y}) \otimes \mathbf{n}(\mathbf{x}) \, ds = \frac{1}{|\mathscr{B}_{\text{micro}}|} \int_{\mathscr{B}_{\text{micro}}} [\nabla \boldsymbol{\varphi}(\mathbf{x}; \mathbf{y})] \, d\mathbf{x} \tag{4.5}$$

and

$$[\overline{P}(\mathbf{y})] = \frac{1}{|\mathscr{B}_{\text{micro}}|} \int_{\partial\mathscr{B}_{\text{micro}}} [P(\mathbf{x}; [\nabla \boldsymbol{\varphi}(\mathbf{x}; \mathbf{y})])] \mathbf{n}(\mathbf{x}) \otimes \mathbf{x} \, ds = \frac{1}{|\mathscr{B}_{\text{micro}}|} \int_{\mathscr{B}_{\text{micro}}} [P(\mathbf{x}; [\nabla \boldsymbol{\varphi}(\mathbf{x}; \mathbf{y})])] \, d\mathbf{x} \,, \tag{4.6}$$

where $\mathbf{n}(\mathbf{x})$ is the unit outer normal vector at $\mathbf{x} \in \partial\mathscr{B}_{\text{micro}}$ and $[P]$ is the first Piola-Kirchhoff stress at the microscale. The microscopic deformation map $\boldsymbol{\varphi}(\cdot; \mathbf{y}) : \mathscr{B}_{\text{micro}} \to \mathbb{R}^3$ is assumed to take the form of a linear contribution $\mathbf{x} \mapsto [\overline{F}(\mathbf{y})]\mathbf{x}$ superimposed with a fluctuation field $\mathbf{z} : \mathscr{B}_{\text{micro}} \to \mathbb{R}^3$, that is [136, 108, 137, 133]

$$\boldsymbol{\varphi}(\mathbf{x}; \mathbf{y}) = [\overline{F}(\mathbf{y})]\mathbf{x} + \mathbf{z}(\mathbf{x}) \,, \quad \mathbf{x} \in \mathscr{B}_{\text{micro}} \,, \tag{4.7}$$

By substituting the above equation into Eq. (4.5), it is deduced that the fluctuation field must satisfy the condition

$$\frac{1}{|\mathscr{B}_{\text{micro}}|} \int_{\partial\mathscr{B}_{\text{micro}}} \mathbf{z}(\mathbf{x}) \otimes \mathbf{n}(\mathbf{x}) \, ds = [0] \,. \tag{4.8}$$

In what follows, a fluctuation field vanishing on $\partial\mathscr{B}_{\text{micro}}$ (that is, $\mathbf{z}(\mathbf{x}) = \mathbf{0}$ for all $\mathbf{x} \in \partial\mathscr{B}_{\text{micro}}$) is considered, so that $\boldsymbol{\varphi}(\mathbf{x}; \mathbf{y}) = [\overline{F}(\mathbf{y})]\mathbf{x}$ for all $\mathbf{x} \in \partial\mathscr{B}_{\text{micro}}$ and Hill's lemma is satisfied [106]. The effective stored energy function $\overline{w}_{\text{macro}}$ is then defined by the following variational formulation [106, 107, 108]:

$$\overline{w}_{\text{macro}}([\overline{F}]) = \min_{\mathbf{z} \in \mathcal{K}([\overline{F}])} \frac{1}{|\mathscr{B}_{\text{micro}}|} \int_{\mathscr{B}_{\text{micro}}} w(\mathbf{x}, [\overline{F}] + [\nabla \mathbf{z}(\mathbf{x})]) \, d\mathbf{x} \,, \tag{4.9}$$

where $\mathcal{K}([\overline{F}])$ is the set of admissible fluctuations fields

$$\mathcal{K}([\overline{F}]) = \{\mathbf{z} \in W^{1,p}(\mathscr{B}_{\text{micro}}, \mathbb{R}^3) \, : \, \mathbf{z}(\mathbf{x}) = \mathbf{0} \text{ on } \partial\mathscr{B}_{\text{micro}}\} \,. \tag{4.10}$$

Note that the use of non-convex stored energy functions rises additional difficulties in the case of finite deformations, such that the non-uniqueness of the solution and the development of microscopic and macroscopic instabilities (which require an adaptation of the mathematical definition of the effective stored energy function, see, *e.g.*, [138, 139, 140]).

4.2.3 FE^2 method

In the FE^2 method [115, 116], information is exchanged back-and-forth between the microscopic and macroscopic scales. Consider first the weak formulation [141, 109] associated with the macroscopic problem: find $\boldsymbol{\psi} \in \mathbf{H}^1_0(\mathscr{B}_{\text{macro}}, \mathbb{R}^3)$ such that

$$\overline{a}(\boldsymbol{\psi}, \mathbf{v}) = \overline{\ell}(\mathbf{v}) - \overline{a}(\boldsymbol{\psi}_d, \mathbf{v}) \,, \quad \forall \mathbf{v} \in \mathbf{H}^1_0(\mathscr{B}_{\text{macro}}, \mathbb{R}^3) \,, \tag{4.11}$$

where

$$\overline{a}(\boldsymbol{\psi}, \mathbf{v}) = \int_{\mathscr{B}_{\text{macro}}} [\overline{P}(\mathbf{y})] : [\nabla \mathbf{v}(\mathbf{y})] \, d\mathbf{y} \,, \quad \overline{\ell}(\mathbf{v}) = \int_{\overline{\Gamma}_N} \langle \mathbf{h}^{(\text{macro})}(\mathbf{y}), \mathbf{v}(\mathbf{y}) \rangle \, d\mathbf{y} \,. \tag{4.12}$$

Using successive linearizations, the above weak formulation is solved with a Newton-Raphson algorithm (see, *e.g.*, [109, 142]), *i.e.*,

$$\text{for } k \geqslant 0 : \quad \overline{a}'(\boldsymbol{\psi}^{(k)}, \mathbf{v}) \cdot (\Delta \boldsymbol{\psi}^{(k+1)}) = \overline{\ell}(\mathbf{v}) - \overline{a}(\boldsymbol{\psi}_d, \mathbf{v}) - \overline{a}(\boldsymbol{\psi}^{(k)}, \mathbf{v}) \,, \tag{4.13}$$

where $\overline{a}'(\boldsymbol{\varphi}^{(k)}, \cdot) \cdot (\Delta \boldsymbol{\psi}^{(k+1)})$ denotes the Gateaux derivative of $\overline{a}(\boldsymbol{\psi}, \cdot)$ at $\boldsymbol{\psi}^{(k)}$ with the increment $\Delta \boldsymbol{\psi}^{(k+1)} = \boldsymbol{\psi}^{(k+1)} - \boldsymbol{\psi}^{(k)}$. Given the deformation map $\mathbf{y} \mapsto \boldsymbol{\psi}^{(k)}(\mathbf{y})$ at the k-th iteration, one has to determine the effective stored energy function (in order to compute the associated first or second Piola-Kirchhoff stress tensor) by solving the microscopic boundary value problems at every location $\mathbf{y}$ in $\mathscr{B}_{\text{macro}}$. The weak formulation of the microscopic problem at $\mathbf{y} \in \mathscr{B}_{\text{micro}}$ is given by: find $\boldsymbol{\varphi}(\cdot; \mathbf{y}) \in \mathbf{H}^1_0(\mathscr{B}_{\text{macro}}, \mathbb{R}^3)$ such that

$$a(\boldsymbol{\varphi}(\cdot; \mathbf{y}), \mathbf{v}) = \ell(\mathbf{v}) - a(\boldsymbol{\varphi}_d(\cdot; \mathbf{y}), \mathbf{v}) \,, \quad \forall \, \mathbf{v} \in \mathbf{H}^1_0(\mathscr{B}_{\text{micro}}, \mathbb{R}^3) \,, \tag{4.14}$$

with $\boldsymbol{\varphi}_d(\mathbf{x}; \mathbf{y}) = ([\overline{F}(\mathbf{y})] - [I_3])\mathbf{x}$ for $\mathbf{x} \in \Gamma_D$ and

$$a(\boldsymbol{\varphi}(\cdot; \mathbf{y}), \mathbf{v}) = \int_{\mathscr{B}_{\text{micro}}} [P(\mathbf{x}, [\nabla \boldsymbol{\varphi}(\mathbf{x}; \mathbf{y})])] : [\nabla \mathbf{v}(\mathbf{x})] \, d\mathbf{x} \,, \quad \ell(\mathbf{v}) = \int_{\Gamma_N} \langle \mathbf{h}(\mathbf{x}), \mathbf{v}(\mathbf{x}) \rangle \, d\mathbf{x} \,. \tag{4.15}$$

For each iteration $k \geqslant 0$, the above weak formulation must be solved at every location $\mathbf{y}$ in the structure (in order to determine the effective stored energy function defined by Eq. (4.9)). While such an approach enables the treatment of any nonlinear constitutive behavior, it remains computationally expensive. In order to avoid these issues, the construction of a polynomial approximation for the effective stored energy function is investigated in Section 4.3.

4.3 Polynomial approximation of stored energy functions

4.3.1 Vector representation of the macroscopic right Cauchy-Green tensor

Let $\{[b^{(ij)}], \; 1 \leqslant i \leqslant j \leqslant 3\}$ be the orthogonal basis of $\mathbb{S}^3$ defined as [73]:

$$[b^{(ii)}] = \mathbf{e}_i \otimes \mathbf{e}_i \,, \quad 1 \leqslant i \leqslant 3 \,, \quad [b^{(ij)}] = \frac{1}{\sqrt{2}} \left(\mathbf{e}_i \otimes \mathbf{e}_j + \mathbf{e}_j \otimes \mathbf{e}_i \right) \,, \quad 1 \leqslant i < j \leqslant 3 \,. \tag{4.16}$$

For three-dimensional applications, $[\overline{C}]$ admits the decomposition

$$[\overline{C}] = \sum_{1 \leqslant i \leqslant 3} \overline{C}_{ii} [b^{(ii)}] + \sqrt{2} \sum_{1 \leqslant i < j \leqslant 3} \overline{C}_{ij} [b^{(ij)}] \,, \tag{4.17}$$

where the coefficients $\{\overline{C}_{ij}\}_{1 \leqslant i \leqslant j \leqslant 3}$ belong to a given 6-dimensional set such that $[\overline{C}]$ is positive-definite. Let $\overline{\mathbf{c}} = (\overline{c}_1, \ldots, \overline{c}_6)$ be the vector representation of $[\overline{C}]$ defined component-wise as

$$\overline{c}_i = \overline{C}_{ii} \,, \quad 1 \leqslant i \leqslant 3 \,, \quad \overline{c}_{9-(i+j)} = \overline{C}_{ij} \,, \quad 1 \leqslant i < j \leqslant 3 \,. \tag{4.18}$$

We finally denote by $\overline{w}$ the effective stored energy function expressed in terms of $\overline{\mathbf{c}}$:

$$\overline{w}(\overline{\mathbf{c}}) = \overline{w}_{\text{macro}}([\overline{F}]) \,, \tag{4.19}$$

with $\overline{\mathbf{c}}$ the vector representation of $[\overline{C}] = [\overline{F}]^T [\overline{F}]$ defined by Eqs. (4.17)-(4.18).

Remark 4.3.1. *The above convention can be readily adapted for plane-strain deformations. In particular, and when non-vanishing strain deformations are contained in the plane spanned by* $\mathbf{e}_1$ *and* $\mathbf{e}_2$*, the above vector representation reads as* $\overline{\mathbf{c}} = (\overline{c}_1, \overline{c}_2, \overline{c}_3)$*, with* $\overline{c}_1 = \overline{C}_{11}$*,* $\overline{c}_2 = \overline{C}_{22}$ *and* $\overline{c}_3 = \overline{C}_{12}$*.*

4.3.2 Polynomial approximation of the effective stored energy function

Below, an approximation of the effective stored energy function $\overline{w}$ that is uniformly accurate over a given set $\mathbb{K} \subset \mathbb{R}^d$ is sought, with $d = 3$ and $d = 6$ for two- and three-dimensional applications respectively. It is assumed that $\mathbb{K}$ is located sufficiently far away from the boundary of the cone of positive semidefinite matrices, expressed in vector form. This situation is frequently met in practice, at least for small perturbations around the configuration at equilibrium. In the sequel, $\mathbb{K}$ is taken as

$$\mathbb{K} = \bigtimes_{i=1}^{d} [a_i, b_i] \,. \tag{4.20}$$

Let $L^2_\rho(\mathbb{K}, \mathbb{R})$ be the space of functions that are square integrable with respect to the uniform measure $\rho(\mathbf{c}) d\mathbf{c}$, with

$$\rho(\mathbf{c}) = \frac{1}{|\mathbb{K}|} \mathbb{1}_{\mathbb{K}}(\mathbf{c}) \,. \tag{4.21}$$

This space is endowed with the inner product

$$\langle f, g \rangle_{L^2_\rho(\mathbb{K},\mathbb{R})} = \int_{\mathbb{K}} f(\mathbf{c}) g(\mathbf{c}) \, \rho(\mathbf{c}) d\mathbf{c} \,, \tag{4.22}$$

and the associated norm $\|f\|_{L^2_\rho(\mathbb{K},\mathbb{R})} = \langle f, f \rangle^{1/2}_{L^2_\rho(\mathbb{K},\mathbb{R})}$. Let $\mathbb{P}_{\mathscr{A}_p} \subset L^2_\rho(\mathbb{K}, \mathbb{R})$ be the polynomial space spanned by the multivariate polynomials $\Psi_{\boldsymbol{\alpha}}$ that are orthonormal with respect to $\rho(\mathbf{c}) d\mathbf{c}$:

$$\int_{\mathbb{K}} \Psi_{\boldsymbol{\alpha}}(\mathbf{c}) \Psi_{\boldsymbol{\beta}}(\mathbf{c}) \, \rho(\mathbf{c}) \, d\mathbf{c} = \delta_{\boldsymbol{\alpha}\boldsymbol{\beta}} \,, \quad \forall \boldsymbol{\alpha}, \boldsymbol{\beta} \in \mathscr{A}_p \,, \tag{4.23}$$

where $\delta_{\boldsymbol{\alpha}\boldsymbol{\beta}}$ is a generalized Kronecker symbol defined as $\delta_{\boldsymbol{\alpha}\boldsymbol{\beta}} = \delta_{\alpha_1\beta_1} \times \cdots \times \delta_{\alpha_d\beta_d}$ and $\mathscr{A}_p$ is a set of multi-indexes given by $\mathscr{A}_p = \{\boldsymbol{\alpha} \in \mathbb{N}^d : |\boldsymbol{\alpha}| \leqslant p\}$, with $|\boldsymbol{\alpha}| = \alpha_1 + \cdots + \alpha_d$. Assume that the effective stored energy function $\overline{w}$ belongs to $L^2_\rho(\mathbb{K}, \mathbb{R})$, that is

$$\|\overline{w}\|_{L^2_\rho(\mathbb{K},\mathbb{R})} < +\infty \,. \tag{4.24}$$

In this context, the projection $\overline{w}_p$ of the effective stored energy function $\overline{w}$ is defined as

$$\|\overline{w}_p - \overline{w}\|_{L^2_\rho(\mathbb{K},\mathbb{R})} = \inf_{v \in \mathbb{P}_{\mathscr{A}_p}} \|\overline{w} - v\|_{L^2_\rho(\mathbb{K},\mathbb{R})} \,. \tag{4.25}$$

Using the orthonormal property of the polynomial basis in $\mathbb{P}_{\mathscr{A}_p}$, the polynomial coefficients of the projection

$$\overline{w}_p(\overline{\mathbf{c}}) = \sum_{|\boldsymbol{\alpha}|=0}^{p} z_{\boldsymbol{\alpha}} \Psi_{\boldsymbol{\alpha}}(\overline{\mathbf{c}}) \tag{4.26}$$

are given by

$$z_{\boldsymbol{\alpha}} = \langle \overline{w}, \Psi_{\boldsymbol{\alpha}} \rangle_{L^2_\rho(\mathbb{K},\mathbb{R})} \,, \tag{4.27}$$

Upon introducing the linear mapping $\mathbf{u} \mapsto \overline{\mathbf{c}} = \mathbf{q}(\mathbf{u}) = [D]\mathbf{u} + \mathbf{m}$, with $[D]$ a $(d \times d)$ diagonal matrix and $\mathbf{m}$ in $\mathbb{R}^d$ such that:

$$D_{ii} = \frac{1}{2}(b_i - a_i) \,, \quad m_i = \frac{1}{2}(a_i + b_i) \,, \quad 1 \leqslant i \leqslant d \,, \tag{4.28}$$

the orthogonality property can be rewritten as

$$\frac{1}{2^d} \int_{[-1,1]^d} \Psi_{\boldsymbol{\alpha}}(\mathbf{q}(\mathbf{u})) \Psi_{\boldsymbol{\beta}}(\mathbf{q}(\mathbf{u})) \, d\mathbf{u} = \delta_{\boldsymbol{\alpha}\boldsymbol{\beta}} \,, \tag{4.29}$$

and shows that the polynomials $\ell_{\boldsymbol{\alpha}}(\mathbf{u}) = \Psi_{\boldsymbol{\alpha}}(\mathbf{q}(\mathbf{u}))$ correspond to the multivariate normalized Legendre polynomials. More specifically, the polynomials $\ell_{\boldsymbol{\alpha}} : [-1,1]^d \to \mathbb{R}$ are given by

$$\ell_{\boldsymbol{\alpha}}(\mathbf{u}) = \ell_{\alpha_1}(u_1) \times \cdots \times \ell_{\alpha_d}(u_d) \,, \tag{4.30}$$

with $\ell_{\alpha_i} : [-1,1] \to \mathbb{R}$ the normalized one-dimensional Legendre polynomials on $[-1,1]$ such that

$$\ell_n(u) = \sqrt{2n+1}\, P_n(u) \,. \tag{4.31}$$

In the above equation, the Legendre polynomials $P_n : [-1,1] \to \mathbb{R}$ are given by

$$P_{n+1}(u) = \frac{1}{2^k} \sum_{l=0}^{[n/2]} (-1)^l \mathcal{C}_n^l \mathcal{C}_{2n-2l}^n x^{n-2l} \,, \quad n \geqslant 0 \,, \tag{4.32}$$

where $\mathcal{C}_n^k$ the binomial coefficient, and they satisfy the recurrence relation [87]:

$$\begin{aligned} &P_{n+1}(u) = \frac{2n+1}{n+1}\, u\, P_n(u) - \frac{n}{n+1}\, P_{n-1}(u) \,, \quad n \geqslant 1 \,, \\ &P_0(u) = 1 \,, \quad P_1(u) = u \,. \end{aligned} \tag{4.33}$$

The orthonormal multivariate Legendre polynomials are then obtained by using Eqs. (4.30)-(4.31). Equivalently, the polynomials $\Psi_{\boldsymbol{\alpha}}$ can be defined as $\Psi_{\boldsymbol{\alpha}}(\mathbf{c}) = \ell_{\boldsymbol{\alpha}}(\mathbf{q}^{-1}(\mathbf{c}))$ and seen as shifted Legendre polynomials, where $\mathbf{q}^{-1}(\overline{\mathbf{c}}) = [D]^{-1}(\overline{\mathbf{c}} - \mathbf{m})$. The coefficients $z_{\boldsymbol{\alpha}}$ of the polynomial expansion can then be rewritten as

$$z_{\boldsymbol{\alpha}} = \langle \overline{w}, \ell_{\boldsymbol{\alpha}} \rangle_{L^2_\varpi([-1,1]^d,\mathbb{R})} = \frac{1}{2^d} \int_{[-1,1]^d} \overline{w}(\mathbf{q}(\mathbf{u})) \ell_{\boldsymbol{\alpha}}(\mathbf{u}) \, d\mathbf{u} \,, \quad \forall\, \boldsymbol{\alpha} \in \mathscr{A}_p \,, \tag{4.34}$$

where $\varpi : [-1,1]^d \to \mathbb{R}$ denotes the uniform density on $[-1,1]^d$. In practice, the above integral can be evaluated by using either a quadrature rule or numerical Monte Carlo simulations (see

[143] for a recent survey). In this work, given the low stochastic dimension which is considered for numerical purposes (where $\dim(\mathbb{K}) = 3$) and the choice of the uniform measures on $\mathbb{K}$, we will resort on a Gauss-Legendre quadrature rule. In order to derive closed-form expressions for the second Piola-Kirchhoff stress tensor and tangent elastic moduli matrix, the approximated effective stored energy function can then be rewritten as a generalized Fourier-Legendre series at order p:

$$\overline{w}_p(\overline{\mathbf{c}}) = \sum_{|\boldsymbol{\alpha}|=0}^{p} z_{\boldsymbol{\alpha}} \prod_{k=1}^{d} \sqrt{2\alpha_k + 1}\, P_{\alpha_k}(q_k^{-1}(\overline{c}_k))\,. \tag{4.35}$$

In the three dimensional case, the vector form of the second effective Piola-Kirchhoff stress tensor reads as

$$\overline{\mathbf{s}} = (\overline{S}_{11}, \overline{S}_{22}, \overline{S}_{33}, \overline{S}_{23}, \overline{S}_{13}, \overline{S}_{12})\,, \tag{4.36}$$

with $\overline{S}_{ij}$ the entries of the second Piola-Kirchhoff stress tensor for the *projected* stored energy function. It can be deduced that

$$\overline{s}_j(\overline{\mathbf{c}}) = \eta_j \sum_{|\boldsymbol{\alpha}|=0}^{p} z_{\boldsymbol{\alpha}} \sqrt{2\alpha_j + 1}\, \frac{dP_{\alpha_j}(q_j^{-1}(\overline{c}_j))}{d\overline{c}_j} \prod_{\ell=1,\,\ell\neq j}^{3} \sqrt{2\alpha_\ell + 1}\, P_{\alpha_\ell}(q_\ell^{-1}(\overline{c}_\ell))\,, \tag{4.37}$$

for $1 \leqslant j \leqslant 6$, with $\eta_1 = \eta_2 = \eta_3 = 2$ and $\eta_4 = \eta_5 = \eta_6 = 1$. Let $[\overline{L}]$ be the tangent elastic moduli matrix defined as

$$[\overline{L}] = \begin{bmatrix} \overline{L}_{1111} & \overline{L}_{1122} & \overline{L}_{1133} & \overline{L}_{1123} & \overline{L}_{1123} & \overline{L}_{1112} \\ \overline{L}_{2211} & \overline{L}_{2222} & \overline{L}_{2233} & \overline{L}_{2223} & \overline{L}_{2223} & \overline{L}_{2212} \\ \overline{L}_{3311} & \overline{L}_{3322} & \overline{L}_{3333} & \overline{L}_{3323} & \overline{L}_{3323} & \overline{L}_{3312} \\ \overline{L}_{2311} & \overline{L}_{2322} & \overline{L}_{2333} & \overline{L}_{2323} & \overline{L}_{2323} & \overline{L}_{2312} \\ \overline{L}_{1311} & \overline{L}_{1322} & \overline{L}_{1333} & \overline{L}_{1323} & \overline{L}_{1323} & \overline{L}_{1312} \\ \overline{L}_{1211} & \overline{L}_{1222} & \overline{L}_{1233} & \overline{L}_{1223} & \overline{L}_{1223} & \overline{L}_{1212} \end{bmatrix}\,. \tag{4.38}$$

One has

$$\overline{L}_{ij}(\overline{\mathbf{c}}) = \varsigma_{ij} \sum_{|\boldsymbol{\alpha}|=0}^{p} z_{\boldsymbol{\alpha}} \left(\prod_{k=1}^{3} \sqrt{2\alpha_k + 1} \right) \frac{dP_{\alpha_i}(q_i^{-1}(\overline{c}_i))}{d\overline{c}_i} \frac{dP_{\alpha_j}(q_j^{-1}(\overline{c}_j))}{d\overline{c}_j} P_{\alpha_\ell}(q_\ell^{-1}(\overline{c}_\ell))\,, \tag{4.39}$$

for $1 \leqslant i < j \leqslant 6$ and $\ell = 9 - i - j$, and

$$\overline{L}_{jj}(\overline{\mathbf{c}}) = \varsigma_{jj} \sum_{|\boldsymbol{\alpha}|=0}^{p} z_{\boldsymbol{\alpha}} \left(\prod_{k=1}^{3} \sqrt{2\alpha_k + 1} \right) \frac{d^2 P_{\alpha_j}(q_j^{-1}(\overline{c}_j))}{d\overline{c}_j^2} \prod_{\ell=1,\,\ell\neq j}^{3} P_{\alpha_\ell}(q_\ell^{-1}(\overline{c}_\ell)) \tag{4.40}$$

for $1 \leqslant j \leqslant 6$. In the above equations, $[\varsigma]$ is a (6×6) matrix given by

$$[\varsigma] = \begin{bmatrix} 4 & 4 & 4 & 2 & 2 & 2 \\ 4 & 4 & 4 & 2 & 2 & 2 \\ 4 & 4 & 4 & 2 & 2 & 2 \\ 2 & 2 & 2 & 1 & 1 & 1 \\ 2 & 2 & 2 & 1 & 1 & 1 \\ 2 & 2 & 2 & 1 & 1 & 1 \end{bmatrix}\,, \tag{4.41}$$

and the derivatives of the Legendre polynomials are given by

$$\frac{dP_{\alpha_j}(q_j^{-1}(\overline{c}_j))}{d\overline{c}_j} = \frac{2(1+\alpha_j)}{(b_j - a_j)(1 - q_j^{-2}(\overline{c}_j))} \left(q_j^{-1}(\overline{c}_j) P_{\alpha_j}(q_j^{-1}(\overline{c}_j)) - P_{\alpha_j+1}(q_j^{-1}(\overline{c}_j)) \right) \tag{4.42}$$

for $1 \leqslant j \leqslant 6$ and $\bar{c}_j \neq a_j, b_j$. The above relations can easily be adapted to the two-dimensional case ($d = 3$).

4.3.3 Computation of the coefficients and orthonormal polynomials

Let $\{\gamma_i, \hat{\mathbf{u}}^{(i)}\}_{i=1}^{N_\mathcal{Q}}$ be the $N_\mathcal{Q}$ weights and integration nodes determined according to the Gauss-Legendre quadrature rule (recall here that the integration is performed with respect to univariate uniform measures). The polynomial coefficients are thus approximated as follows:

$$z_{\boldsymbol{\alpha}} \approx z^*_{\boldsymbol{\alpha}}(N_\mathcal{Q}) = \frac{1}{2^d} \sum_{i=1}^{N_\mathcal{Q}} \gamma_i \, \overline{w}(\mathbf{q}(\hat{\mathbf{u}}^{(i)})) \ell_{\boldsymbol{\alpha}}(\hat{\mathbf{u}}^{(i)}) \,, \quad \forall \, \boldsymbol{\alpha} \in \mathscr{A}_p \,. \tag{4.43}$$

When resorting on quadrature rules, the orthogonal polynomials can be constructed using, *e.g.*, analytical expressions or recurrence relations. In practice, and following [144, 145], the numerical orthogonality of this basis must be controlled. To this aim, let $[M]$ be the $(N \times N)$ matrix defined as

$$M_{ij} = \langle \ell_{\boldsymbol{\alpha}^{(i)}}, \ell_{\boldsymbol{\alpha}^{(j)}} \rangle_{L^2_{\overline{w}}([-1,1]^d, \mathbb{R})} \,, \quad 1 \leqslant i, j \leqslant N \,, \tag{4.44}$$

where $N = \mathrm{card}(\mathscr{A}_p) = (d+p)!/(d!p!)$ and the inner product is computed through the Gauss-Legendre quadrature rule. Since the relation $[M] = [I_N]$ holds theoretically, the orthogonality of the polynomials can be evaluated by considering the normalized error ε_M given by

$$\varepsilon_M = \frac{\|[M] - [I_N]\|_F}{\sqrt{N}} \,. \tag{4.45}$$

For $d = 3$, $p = 10$ (hence, $N = 286$) and using 20 quadrature points along each direction (so that $N_\mathcal{Q} = 8\,000$), the numerical construction of the polynomials based on the above recurrence relation yields $\varepsilon_M = 8.5 \times 10^{-15}$, whereas the computational algorithm proposed in [145] induces an error $\varepsilon_M = 5.7 \times 10^{-12}$. Denoting by $\{\rho_k\}_{k=1}^N$ the set of ordered eigenvalues of $[M]$, the numerical degree of orthogonality can be further confirmed and illustrated by the graph of mapping $k \mapsto |\rho_k - 1|$, which is shown in Fig. (4.2) for both the analytical and computational generation techniques.

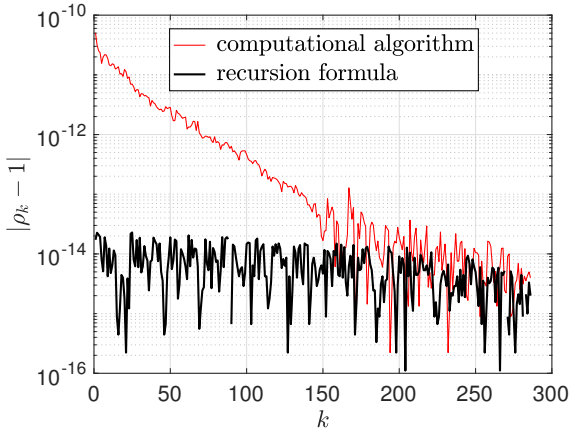

Figure 4.2 – Graph of $k \mapsto |\rho_k - 1|$, $1 \leqslant k \leqslant N$.

The convergence analysis with respect to the parameters of the formulation, namely the order p of the polynomial approximation and the total number $N_\mathcal{Q}$ of quadrature points, is completed

as follows. Without loss of generality, we first set $N_{\mathcal{Q}} = n_{\mathcal{Q}}^d$, with $n_{\mathcal{Q}}$ the number of points along a given direction in the quadrature grid. For a given order p, the optimal number of points $N_{\mathcal{Q}}^{\text{opt}} = (n_{\mathcal{Q}}^{\text{opt}})^d$ is selected such that $\varepsilon_{\mathcal{Q}}(n_{\mathcal{Q}}^{\text{opt}}) \leqslant \varepsilon_{\mathcal{Q}}^{\text{tol}}$ for some tolerance parameter $\varepsilon_{\mathcal{Q}}^{\text{tol}} > 0$, with $n_{\mathcal{Q}} \mapsto \varepsilon_{\mathcal{Q}}(n_{\mathcal{Q}})$ the error function

$$\varepsilon_{\mathcal{Q}}(n_{\mathcal{Q}}) = \frac{\|\mathbf{z}^*((n_{\mathcal{Q}}+1)^d) - \mathbf{z}^*(n_{\mathcal{Q}}^d)\|}{\|\mathbf{z}^*(n_{\mathcal{Q}}^d)\|}\,, \quad n_{\mathcal{Q}} \geqslant 1\,, \tag{4.46}$$

and $\mathbf{z}^* = (z^*_{\boldsymbol{\alpha}^{(1)}}, \ldots, z^*_{\boldsymbol{\alpha}^{(N)}})$ (see Eq. (4.43)). In order to perform the convergence analysis with respect to the order p of the polynomial expansion, we further introduce the L^2 error measure $p \mapsto \varepsilon(p)$ such that

$$\varepsilon(p) = \frac{\|\overline{w}_p - \overline{w}\|_{L^2_\rho(\mathbb{K},\mathbb{R})}}{\|\overline{w}\|_{L^2_\rho(\mathbb{K},\mathbb{R})}}\,, \tag{4.47}$$

where $\overline{w}$ is the reference value for the effective stored energy function (as obtained by the nonlinear finite element analysis). The above L^2 error is again computed through the Gauss-Legendre quadrature rule. Note that this estimation may require a number of quadrature points that is slightly larger than $n_{\mathcal{Q}}^{\text{opt}}$, so that the associated convergence must be characterized as well. The optimal order p^{opt} is then chosen such that $\varepsilon(p^{\text{opt}}) \leqslant \varepsilon^{\text{tol}}$, with $\varepsilon^{\text{tol}} > 0$ an error parameter.

4.3.4 Numerical applications

The aim of this section is to assess the capability of the polynomial approximation to model the effective nonlinear response of selected microstructures. At this point, it should be noted that:

- alternative approaches, such as mean-field (*i.g* Hashin-Shtrikman) bounds and estimates [146, 147, 148], provide accurate estimates of the effective nonlinear behavior for fiber-reinforced composites. Benchmark studies on these approaches can be found elsewhere [149, 150];
- whenever required, the characterization of the scale transition from the apparent behavior to the effective one can be performed by following, for instance, the methodology proposed in [151].

For the sake of simplicity, plane-strain deformations are considered in the sequel ($d = 3$). The polynomial basis $\{\Psi_{\boldsymbol{\alpha}}, \boldsymbol{\alpha} \in \mathscr{A}_p\}$ is then orthonormal with respect to the uniform measure $\rho(\mathbf{c})d\mathbf{c}$ such that

$$\rho(\mathbf{c})d\mathbf{c} = \prod_{i=1}^{3} \rho(c_i)(dc_i)\,, \tag{4.48}$$

with

$$\rho(c_i)(dc_i) = \frac{1}{|b_i - a_i|}\mathbb{1}_{[a_i,b_i]}(c_i)dc_i\,, \quad 1 \leqslant i \leqslant 3\,. \tag{4.49}$$

Random and deterministic microstructures are considered in Sections 4.3.4.1-§4.3.4.2, and the accuracy of the polynomial approximation is illustrated for different macroscopic loadings and contrasts. The nonlinear boundary value problems are solved by using the finite element method with a Galerkin approximation [152, 153] (with either 3-node or 6-node triangular elements, depending on the application under consideration) combined to a classical Newton-Raphson scheme [109], using the library Eigen3 [110].

4.3.4.1 Case of a quasi-isotropic random microstructure.

In this first application, we consider a composite made up of a Neo-Hookean matrix reinforced by stiff Neo-Hookean inclusions of diameter D. In practice, and following the methodology detailed in [151], the value of D must be chosen such that the ratio $L_{\mathscr{B}_{\text{micro}}}/D$ is large enough; here, $L_{\mathscr{B}_{\text{micro}}}/D \approx 15$. In this case, the homogenized stored energy function exhibits small statistical fluctuations (the coefficient of variation of the homogenized potential, estimated by means of Monte Carlo simulations, is estimated at 1.45%) and the scale of separation can reasonably be assumed (in which case the effective behavior is independent of the prescribed conditions). The microstructure contains 59 inclusions and is sampled by using the packing generation algorithm (with periodic boundary conditions) detailed in [105]. The Neo-Hookean model for the matrix phase is characterized by the parameters $\kappa^{(m)} = 1750$ and $\mu^{(m)} = 328.125$ (both in [MPa]), whereas the parameters for the inclusions are such that the elastic constraint ϱ is equal to 100, *i.e.*,

$$\varrho = \frac{\kappa^{(f)}}{\kappa^{(m)}} = \frac{\mu^{(f)}}{\mu^{(m)}} = 100\,. \tag{4.50}$$

The support $\mathbb{K}$ is chosen as

$$\mathbb{K} = [0.9, 1.5] \times [0.9, 1.5] \times (1/\sqrt{2})[-0.1, 0.5]\,. \tag{4.51}$$

The considered microstructure is shown in Fig. 4.3 and the associated finite element mesh contains 17486 elements, The graphs of the error functions $n_{\mathcal{Q}} \mapsto \varepsilon_{\mathcal{Q}}(n_{\mathcal{Q}})$ and $p \mapsto \varepsilon(p)$ are shown in

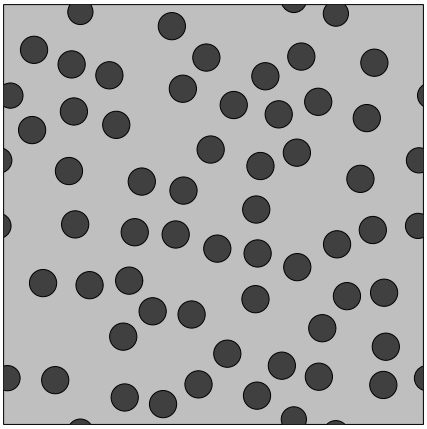

Figure 4.3 – Representative volume element with volume fraction $\phi = 0.2$.

Fig. (4.4) for $p = 2k + 1$, $2 \leqslant k \leqslant 8$. The optimal number of quadrature points and associated errors are summarized in Tab. 4.1 for $p \geqslant 9$. In order to further investigate the relevance of the

p	9	11	13	15	17
$n_{\mathcal{Q}}^{\text{opt}}$	11	12	13	14	15
$\varepsilon_{\mathcal{Q}}(n_{\mathcal{Q}}^{\text{opt}})$	3.4847×10^{-12}	3.832×10^{-12}	3.826×10^{-12}	3.824×10^{-12}	3.823×10^{-12}
$\varepsilon(p)$	3.17×10^{-7}	2.06×10^{-8}	1.45×10^{-9}	1.05×10^{-10}	7.43×10^{-12}

Table 4.1 – Optimal number of quadrature points and associated errors for $p = 2k+1$, $4 \leqslant k \leqslant 8$.

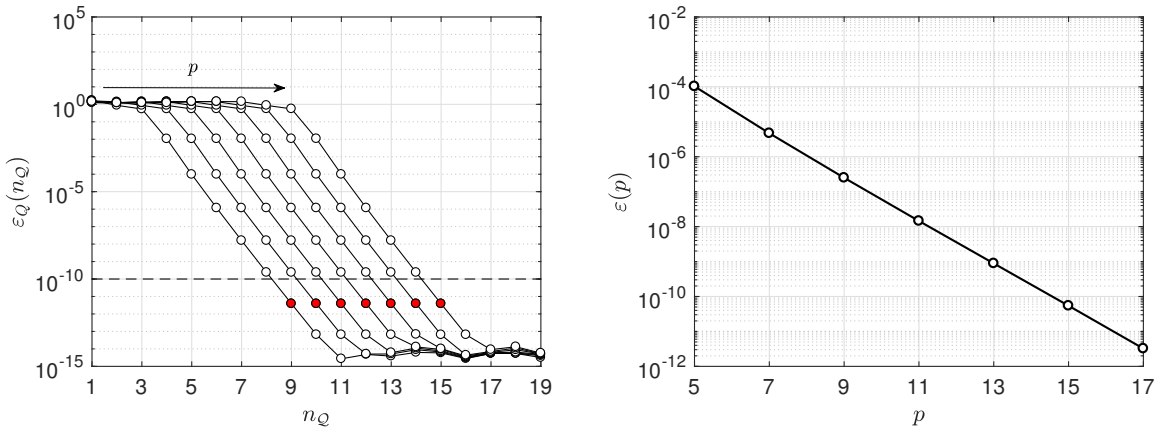

Figure 4.4 – Left: graph of $n_{\mathcal{Q}} \mapsto \varepsilon_{\mathcal{Q}}(n_{\mathcal{Q}})$ for $p = 2k+1$, $2 \leqslant k \leqslant 8$. The red dots denote the optimal numbers of integration points for each case, for $\varepsilon_{\mathcal{Q}}^{\text{tol}} = 10^{-10}$. Right: graph of $p \mapsto \varepsilon(p)$ for $p = 2k+1$, $2 \leqslant k \leqslant 8$.

proposed approach, the latter is now compared with the N.E.X.P. method proposed in [126]. This method essentially relies on the combination of parallel factor decomposition and cubic spline interpolation over a regular grid. For comparison purposes, the reference values for the effective stored energy function are computed for particular plane-strain states of deformation. These states are chosen different from those used to construct the projection (for the proposed approach) and the interpolation (for the N.E.X.P. scheme), and define a much finer grid (denoted by $\mathscr{G}$) as compared to the aforementioned ones. The following pointwise distance function is next introduced:

$$\mathcal{E}(\overline{\mathbf{c}}) = |\mathcal{P}\{\overline{w}\}(\overline{\mathbf{c}}) - \overline{w}(\overline{\mathbf{c}})|\,, \quad \forall\, \overline{\mathbf{c}} \in \mathscr{G}\,, \tag{4.52}$$

where $\mathcal{P}\{\overline{w}\}$ is the surrogate model for the effective stored energy function defined either through the proposed approach or by the spline interpolation (corresponding to the N.E.X.P. method) constructed with 17 equally-spaced points along each direction (hence requiring 4 913 nonlinear computations). The graphs of $\overline{\mathbf{c}} \mapsto \mathcal{E}(\overline{\mathbf{c}})$ computed for particular tensile and shear tests are displayed in Fig. 4.5 – in both cases, the loading interval is discretized with 100 equally-spaced points.

The case of a biaxial stretching is further addressed in Fig. 4.7, with the grid $\mathscr{G}$ shown in Fig. 4.6. In order the presented spline-based response to be consistently compared with the proposed approach, the associated results are reconstructed based on the full three-dimensional interpolation. – see Fig. 4.6. For the cases under consideration, it is seen that the polynomial expansion and the spline interpolation both yield accurate approximations of the effective stored energy function, and that the error induced by the proposed approach is much smaller than the one obtained with the interpolation scheme, with a decrease of almost four orders of magnitude on average for $p = 15$ and 2 744 nonlinear computations. Finally, the stability of the surrogate model with respect to the elastic contrast is depicted in Fig. 4.8, where the graph of $\overline{c}_1 \mapsto \mathcal{E}(\overline{c}_1, 0, 0)$ is shown for $\varrho \in \{100, 1000, 10000\}$ (note that large contrasts require a finer finite mesh; here , the finest mesh contains 63 708 elements). Based on the convergence criterion detailed in Section 4.3.3, the optimal order of expansion is found to be equal to 17 in all cases. It is seen that the surrogate model remains very accurate regardless of the elastic contrast. Additionally, the error profile is found to exhibit a similar structure for all values of ϱ. This result can be explained by noticing that

- in all cases, the homogenized potential is expanded by using the same polynomial basis

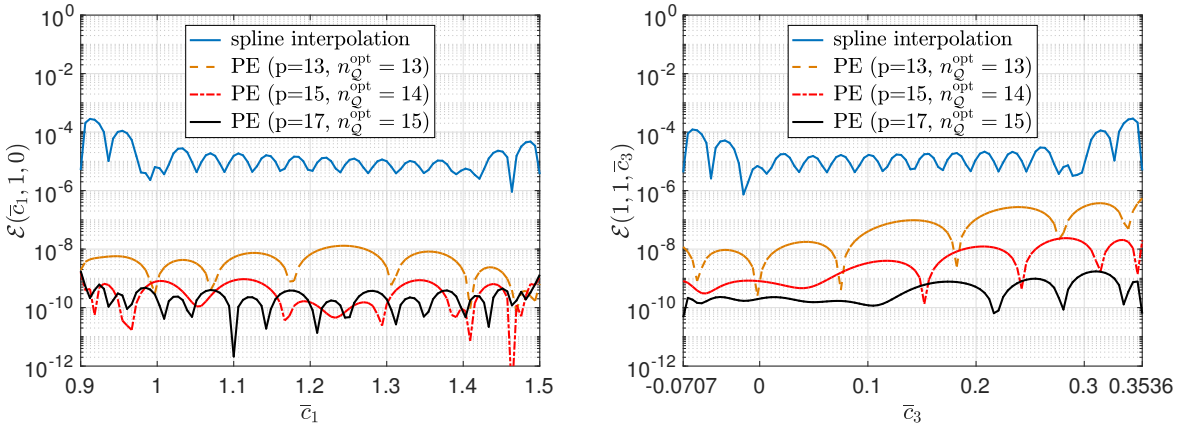

Figure 4.5 – Left panel: graph of mapping $\bar{c}_1 \mapsto \mathcal{E}(\bar{c}_1, 1, 0)$ for $\bar{c}_1 \in [0.9, 1.5]$. Right panel: graph of mapping $\bar{c}_3 \mapsto \mathcal{E}(1, 1, \bar{c}_3)$ for $\bar{c}_3 \in (1/\sqrt{2})[-0.1, 0.5]$. The polynomial expansions and spline interpolations appear in thick black lines and thin blue lines, respectively.

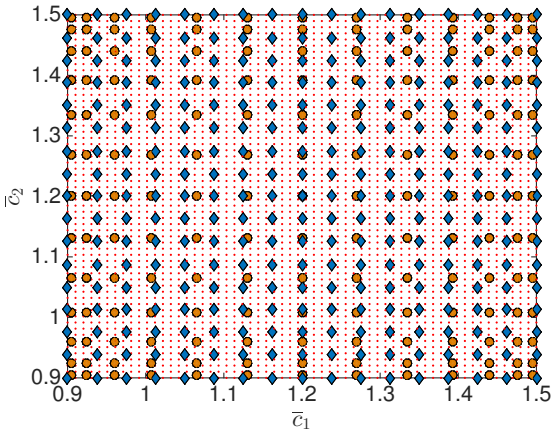

Figure 4.6 – Discretization of the macroscopic states of deformation (partial view). Red dots: comparison points. Blue squares: interpolation points (N.E.X.P. method). Orange disks: quadrature points (proposed approach).

(since the optimal orders of expansion are the same);

- the homogenized potential involved in the computation of the coefficients does not change significantly for $\varrho \geqslant 100$ in this particular application.

4.3.4.2 Case of an anisotropic deterministic microstructure

We now turn to the anisotropic case and Mooney-Rivlin matrix reinforced by a rectangular Mooney-Rivlin inclusion. The model parameters (in [MPa]) are chosen as $\alpha^{(m)} = 164.0625$, $s_1^{(m)} = 1.6953 \times 10^3$ and $\beta^{(m)} = 10$ for the matrix phase, and as $\alpha^{(f)} = 100\alpha^{(m)}$, $\beta^{(f)} = 10\beta^{(m)}$ and $\kappa^{(f)} = 100\kappa^{(m)}$ for the inclusions. The microstructure is shown in Fig. 4.9. The support of the density function ρ is chosen as $\mathbb{K} = [0.9, 1.5] \times [0.9, 1.5] \times [0, 0.3]$. The values of parameters p and $n_{\mathcal{Q}}$ are deduced from a convergence analysis and set to 15 and 14 respectively. For the particular plane-strain condition defined by $\bar{c}_1 \in [0.9, 1.5]$, $\bar{c}_2 = \bar{c}_1$ and $\bar{c}_3 \in [0, 0.3]$, the approximate effective shear stress $\overline{S}_{12}$ and tangent elastic modulus $\overline{L}_{1122}$ are compared with their reference

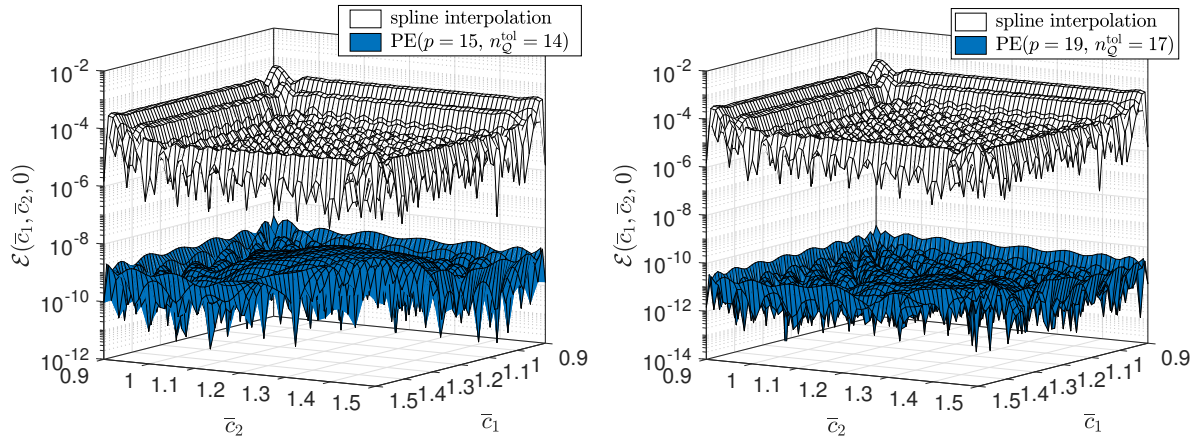

Figure 4.7 – Graph of mapping $(\overline{c}_1, \overline{c}_2) \mapsto \mathcal{E}(\overline{c}_1, \overline{c}_2, 0)$ estimated with the polynomial expansion at different orders (blue surface) and the spline interpolation (white surface), for $(\overline{c}_1, \overline{c}_2) \in [0.9, 1.5] \times [0.9, 1.5]$.

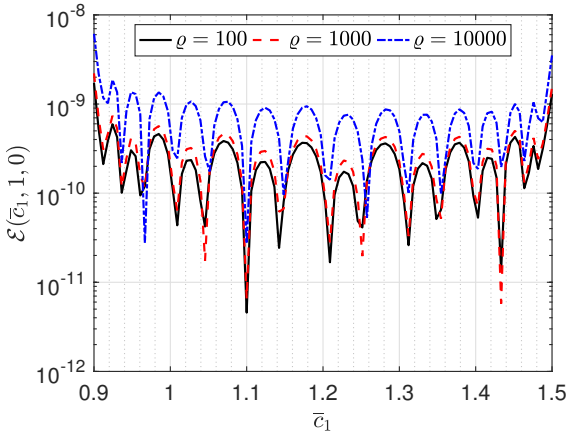

Figure 4.8 – Graph of the mapping $\overline{c}_1 \mapsto \mathcal{E}(\overline{c}_1, 1, 0)$ [MPa] for $\overline{c}_1 \in [0.9, 1.5]$ and several values of the elastic contrast ϱ.

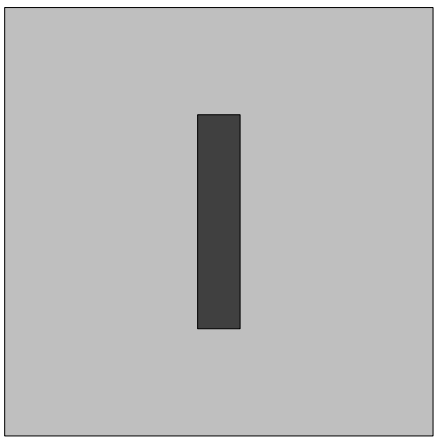

Figure 4.9 – View of the deterministic microstructure containing the rectangular inclusion.

values in Figs. 4.10 and 4.11 respectively. In both cases, and despite the anisotropic nature of

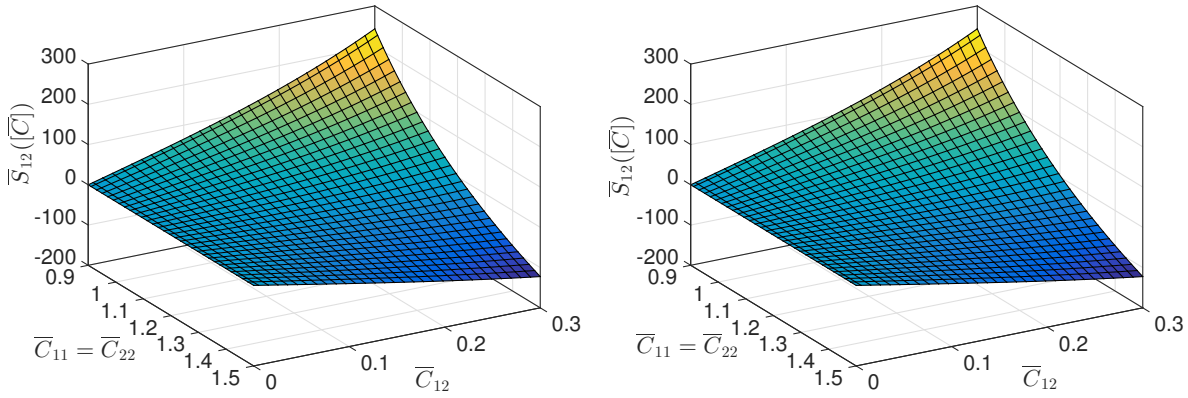

Figure 4.10 – Effective shear stress $[\overline{S}]_{12}$: reference solution (left panel) and polynomial expansion (right panel).

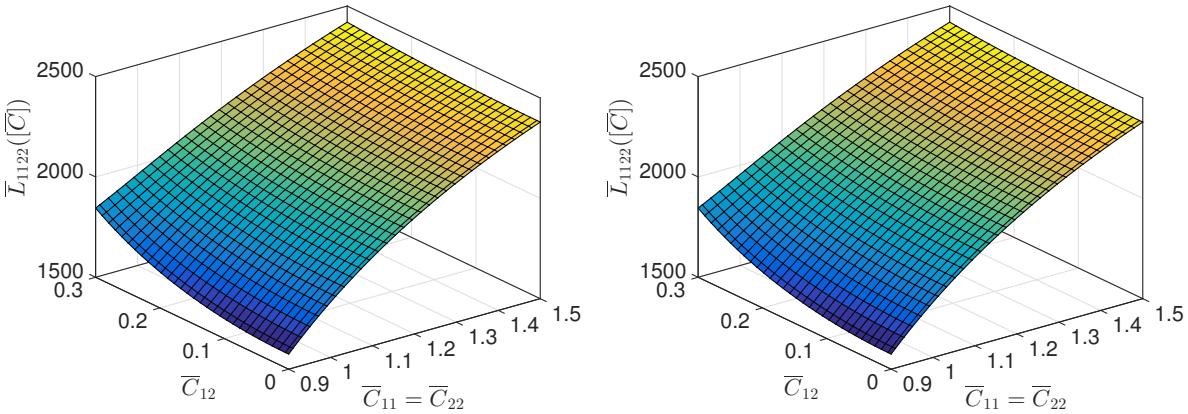

Figure 4.11 – Effective tangent elastic modulus $\overline{L}_{1122}$: reference solution (left panel) and polynomial expansion (right panel).

the mechanical response, it is seen that the polynomial expansion still provides a very accurate representation for the effective nonlinear behavior. Finally, we now consider the projection of the potential associated with the matrix phase onto the same Hilbert basis (that is, using the same order of expansion) as the effective potential, namely $\overline{w}_p^{(m)}(\overline{\mathbf{c}}) = \sum_{\boldsymbol{\alpha} \in \mathscr{A}_p} z_{\boldsymbol{\alpha}}^{(m)} \Psi_{\boldsymbol{\alpha}}(\overline{\mathbf{c}})$ with $n_{\mathcal{Q}} = 14$. The graphs of mappings $k \mapsto z_{\boldsymbol{\alpha}^{(k)}}$ and $k \mapsto z_{\boldsymbol{\alpha}^{(k)}}^{(m)}$ are shown in Fig. 4.12, for $1 \leqslant k \leqslant 30$. It is observed that the two series exhibit a very similar signature, hence suggesting that the effective behavior may accurately be *approximated* by a Neo-Hookean model. A natural question here is then to determine how to define such a projection in a more general setting, and to determine whether this approximation is satisfactory or not. These points are specifically addressed in the next section.

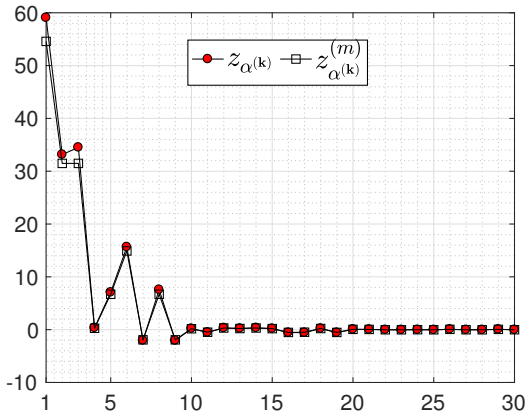

Figure 4.12 – Graphs of mappings $k \mapsto z_{\boldsymbol{\alpha}^{(k)}}$ (red-filled circles) and $k \mapsto z^{(m)}_{\boldsymbol{\alpha}^{(k)}}$ (squares) for $1 \leqslant k \leqslant 30$.

4.4 Defining projections onto sets of stored energy functions

In the previous sections, the effective stored energy function was approximated by a polynomial series in terms of orthonormal Legendre polynomials. The surrogate model has been found to provide an accurate approximation for various microstructures, contrasts and loading paths. However, this polynomial approximation is valid for macroscopic loadings $\overline{\mathbf{c}}$ with values in the set $\mathbb{K}$ chosen beforehand. In this section, we propose to project the effective potential on sets of stored energy functions, such that the resulting surrogate model can be used for any macroscopic loading conditions and can easily be used in any commercial finite element software.

4.4.1 Mathematical formulation

Let $\mathscr{C} \subset L^2_\rho(\mathbb{K},\mathbb{R})$ denote a given set of stored energy functions defined from $\mathbb{K}$ into $\mathbb{R}$ (we recall here that a vector representation of the right Cauchy-Green tensor is used). Accordingly, the notations $\mathscr{C}^{\mathrm{NH}}$ and $\mathscr{C}^{\mathrm{MR}}$ denote the sets of stored energy functions corresponding to Neo-Hookean and Mooney-Rivlin materials, respectively. Each element $\overline{w}_{\mathscr{C}}(\cdot;\boldsymbol{\pi}) : \mathbb{K} \to \mathbb{R}$ of $\mathscr{C}$ is therefore seen as a mapping indexed by a vector-valued parameter $\boldsymbol{\pi}$ (of length $n_{\boldsymbol{\pi}}$) belonging to an admissible set $\mathbb{A} \subset (\mathbb{R}^*_+)^{n_{\boldsymbol{\pi}}}$ such that

$$\mathbb{A} = \bigtimes_{i=1}^{n_{\boldsymbol{\pi}}} [\pi_i^{\min}, \pi_i^{\max}]\,, \tag{4.53}$$

with $\pi_i^{\min} > 0$, $1 \leqslant i \leqslant n_{\boldsymbol{\pi}}$. In practice, and when the stored energy functions of all constitutive phases belong to the same class of potentials, the sets of bounds $\{\pi_i^{\min}\}_{i=1}^{n_{\boldsymbol{\pi}}}$ and $\{\pi_i^{\max}\}_{i=1}^{n_{\boldsymbol{\pi}}}$ may be inferred by taking the minimum and maximum over the parameters defining the constitutive phases, for instance. It should be pointed out that for a given $\overline{\mathbf{c}} \in \mathbb{K}$, the mapping $\mathbb{A} \to \overline{w}_{\mathscr{C}}(\cdot;\boldsymbol{\pi})$ may be nonlinear in general.

We propose to define the closest approximation of $\overline{w}$ in the set $\mathscr{C}$ by minimizing the distance $\|\overline{w}_{\mathscr{C}}(\cdot;\boldsymbol{\pi}) - \overline{w}\|^2_{L^2_\rho(\mathbb{K},\mathbb{R})}$ with respect to the vector-valued parameter $\boldsymbol{\pi} \in \mathbb{A}$. While this can be achieved by resorting on Monte Carlo simulations or a Gauss-Legendre rule as in the previous sections, we will rely on the polynomial approximations of the effective stored energy functions $\overline{w} \in L^2_\rho(\mathbb{K},\mathbb{R})$ and $\overline{w}_{\mathscr{C}}(\cdot;\boldsymbol{\pi}) \in \mathscr{C}$. More precisely, let $\overline{w}_{p,\mathscr{C}}(\cdot;\boldsymbol{\pi})$ be the polynomial approximation

of $\overline{w}_{\mathscr{C}}(\cdot;\boldsymbol{\pi})$, *i.e.*,

$$\overline{w}_{p,\mathscr{C}}(\overline{\mathbf{c}};\boldsymbol{\pi}) = \sum_{|\boldsymbol{\alpha}|=0}^{p} y_{\boldsymbol{\alpha}}(\boldsymbol{\pi})\Psi_{\boldsymbol{\alpha}}(\overline{\mathbf{c}})\,, \tag{4.54}$$

in which the polynomial coefficients are given by $y_{\boldsymbol{\alpha}}(\boldsymbol{\pi}) = \langle \overline{w}_{\mathscr{C}}(\cdot;\boldsymbol{\pi}), \Psi_{\boldsymbol{\alpha}}\rangle$. We then define the closest approximation $\overline{w}^{\star}_{\mathscr{C}}$ of the stored energy function $\overline{w}_p$ as

$$\overline{w}^{\star}_{\mathscr{C}}(\overline{\mathbf{c}}) = \sum_{|\boldsymbol{\alpha}|=0}^{p} y_{\boldsymbol{\alpha}}(\boldsymbol{\pi}^{\star})\Psi_{\boldsymbol{\alpha}}(\overline{\mathbf{c}})\,, \quad \boldsymbol{\pi}^{\star} = \underset{\boldsymbol{\pi}\,\in\,\mathbb{A}}{\operatorname{argmin}} \, \|\overline{w}_{p,\mathscr{C}}(\cdot;\boldsymbol{\pi}) - \overline{w}_p\|^2_{L^2_\rho(\mathbb{K},\mathbb{R})}\,, \tag{4.55}$$

where

$$\|\overline{w}_{p,\mathscr{C}}(\cdot;\boldsymbol{\pi}) - \overline{w}_p\|^2_{L^2_\rho(\mathbb{K},\mathbb{R})} = \sum_{|\boldsymbol{\alpha}|=0}^{p} (y_{\boldsymbol{\alpha}}(\boldsymbol{\pi}) - z_{\boldsymbol{\alpha}})^2 = \|\mathbf{y}(\boldsymbol{\pi}) - \mathbf{z}\|^2\,, \tag{4.56}$$

where the vectors $\mathbf{y}(\boldsymbol{\pi}) = (y_{\boldsymbol{\alpha}^{(1)}}(\boldsymbol{\pi}), \ldots, y_{\boldsymbol{\alpha}^{(N)}}(\boldsymbol{\pi}))$ and $\mathbf{z} = (z_{\boldsymbol{\alpha}^{(1)}}, \ldots, z_{\boldsymbol{\alpha}^{(N)}})$ gathering the polynomial coefficients of the expansions $\overline{w}_{p,\mathscr{C}}$ and $\overline{w}_p$ have been introduced. In the next section, we considere the particular case of Ogden's class of stored energy functions.

4.4.2 Case of Ogden-type stored energy functions

In the sequel of this chapter, we restrict ourselves to a class $\mathscr{C}$ of stored energy functions which depend linearly on the model parameters $\boldsymbol{\pi} \in \mathbb{A}$. In this case, each element $\overline{w}_{\mathscr{C}} \in \mathscr{C}$ can be written as

$$\overline{w}_{\mathscr{C}}(\overline{\mathbf{c}};\boldsymbol{\pi}) = \sum_{j=1}^{n_{\boldsymbol{\pi}}} \pi_j g_j(\overline{\mathbf{c}})\,, \tag{4.57}$$

where $\overline{\mathbf{c}} \mapsto g_j(\overline{\mathbf{c}})$ are given real-valued mappings for $1 \leqslant j \leqslant n_{\boldsymbol{\pi}}$. The set of stored energy functions $\mathscr{C}$ is then defined as

$$\mathscr{C} = \left\{ \overline{w}_{\mathscr{C}}(\cdot;\boldsymbol{\pi}) \in L^2_\rho(\mathbb{K},\mathbb{R}) \,:\, \overline{w}_{\mathscr{C}}(\overline{\mathbf{c}};\boldsymbol{\pi}) = \sum_{j=1}^{n_{\boldsymbol{\pi}}} \pi_j g_j(\overline{\mathbf{c}})\,, \boldsymbol{\pi} \in \mathbb{A} \right\}, \tag{4.58}$$

The projection $\overline{w}_{p,\mathscr{C}}$ of $\overline{w}_{\mathscr{C}} \in \mathscr{C}$ onto $\mathbb{P}_{\mathscr{A}_p}$ reduces to

$$\overline{w}_{p,\mathscr{C}}(\overline{\mathbf{c}};\boldsymbol{\pi}) = \sum_{|\boldsymbol{\alpha}|=0}^{p} \sum_{j=1}^{n_{\boldsymbol{\pi}}} \pi_j v^{(j)}_{\boldsymbol{\alpha}} \Psi_{\boldsymbol{\alpha}}(\overline{\mathbf{c}})\,, \tag{4.59}$$

where the polynomial coefficients $v^{(j)}_{\boldsymbol{\alpha}}$ are given by $v^{(j)}_{\boldsymbol{\alpha}} = \langle \Psi_{\boldsymbol{\alpha}}, g_j\rangle_{L^2_\rho(\mathbb{K},\mathbb{R})}$ for all $\boldsymbol{\alpha} \in \mathscr{A}_p$ and $1 \leqslant j \leqslant n_{\boldsymbol{\pi}}$. The optimization problem given by Eq. (4.60) can then be rewritten as follows

$$\overline{w}_{p,\mathscr{C}_p}(\overline{\mathbf{c}}) = \sum_{|\boldsymbol{\alpha}|=0}^{p} \sum_{j=1}^{n_{\boldsymbol{\pi}}} \pi^{\star}_j v^{(j)}_{\boldsymbol{\alpha}} \Psi_{\boldsymbol{\alpha}}(\overline{\mathbf{c}})\,, \quad \boldsymbol{\pi}^{\star} = \underset{\boldsymbol{\pi}\,\in\,\mathbb{A}}{\operatorname{argmin}} \, \|[V]\boldsymbol{\pi} - \mathbf{z}\|^2\,, \tag{4.60}$$

where the additional matrix $[V]$ is defined as $V_{ki} = \langle \Psi_{\boldsymbol{\alpha}^{(k)}}, g_i\rangle_{L^2_\rho(\mathbb{K},\mathbb{R})}$ for $1 \leqslant i \leqslant n_{\boldsymbol{\pi}}$ and $1 \leqslant j \leqslant N$, with $N \gg n_{\boldsymbol{\pi}}$ in practice. Hence, the above optimization problem corresponds to a constrained least-squares problem (recall that the solution is sought over the admissible set $\mathbb{A}$):

$$\boldsymbol{\pi}^{\star} = \underset{\boldsymbol{\pi}\,\in\,\mathbb{A}}{\operatorname{argmin}} \, \mathcal{J}(\boldsymbol{\pi})\,, \tag{4.61}$$

where the quadratic cost function $\mathcal{J}$ is defined as

$$\mathcal{J}(\boldsymbol{\pi}) = \frac{1}{2}\langle \boldsymbol{\pi}, [D]\boldsymbol{\pi}\rangle + \langle \mathbf{f}, \boldsymbol{\pi}\rangle\,, \quad \forall \boldsymbol{\pi} \in \mathbb{A}\,, \tag{4.62}$$

and

$$[D] = [V]^T[V]\,, \quad \mathbf{f} = -[V]^T\mathbf{z}\,. \tag{4.63}$$

By construction, the matrix $[D]$ is symmetric and at least positive semidefinite, hence implying the convexity of the cost function $\mathcal{J}$. In some cases of practical interest, such as the case of Neo-Hookean materials, $[D]$ can be shown to be positive definite, thus ensuring the strict convexity of the cost function. Note finally that the case of microstructures involving hyperelastic phases defined by different classes of stored energy functions can be handled by searching for the minimum of the residual distance over the classes onto which the effective stored energy function may be projected.

Example. *In the case of Neo-Hookean materials, any stored energy function in the class* $\mathscr{C}^{\mathrm{NH}}$ *can be written as*

$$\overline{w}_{\mathrm{NH}}(\overline{\mathbf{c}}; \boldsymbol{\pi}) = \pi_1 g_1(\overline{\mathbf{c}}) + \pi_2 g_2(\overline{\mathbf{c}})\,, \tag{4.64}$$

where the functions g_1 *and* g_2 *are given by*

$$g_1(\overline{\mathbf{c}}) = \frac{1}{2}(\overline{c}_1 + \overline{c}_2 - 2) - \log(\overline{c}_1\overline{c}_2 - \overline{c}_3^2)\,, \tag{4.65a}$$

$$g_2(\overline{\mathbf{c}}) = \frac{1}{2}\left(\sqrt{\overline{c}_1\overline{c}_2 - \overline{c}_3^2} - 1\right)^2, \tag{4.65b}$$

in the two-dimensional case ($d = 3$)*. The matrix* $[V]$ *involved in the convex cost function* $\mathcal{J}$ *given by Eq.* (4.62) *writes*

$$[V] = \begin{bmatrix} \langle g_1, \Psi_{\boldsymbol{\alpha}^{(1)}}\rangle_{L^2_\rho(\mathbb{K},\mathbb{R})} & \langle g_2, \Psi_{\boldsymbol{\alpha}^{(1)}}\rangle_{L^2_\rho(\mathbb{K},\mathbb{R})} \\ \vdots & \vdots \\ \langle g_1, \Psi_{\boldsymbol{\alpha}^{(N)}}\rangle_{L^2_\rho(\mathbb{K},\mathbb{R})} & \langle g_2, \Psi_{\boldsymbol{\alpha}^{(N)}}\rangle_{L^2_\rho(\mathbb{K},\mathbb{R})} \end{bmatrix}. \tag{4.66}$$

For Mooney-Rivlin materials, any $\overline{w}_{\mathrm{MR}} \in \mathscr{C}^{\mathrm{MR}}$ *can be written as*

$$\overline{w}_{\mathrm{MR}}(\overline{\mathbf{c}}; \boldsymbol{\pi}) = \sum_{j=1}^{3} \pi_j g_j(\overline{\mathbf{c}})\,, \quad \forall \overline{\mathbf{c}} \in \mathbb{K}\,, \tag{4.67}$$

where

$$g_1(\overline{\mathbf{c}}) = \overline{c}_1 + \overline{c}_2 - 2 - \log(\overline{c}_1\overline{c}_2 - \overline{c}_3^2)\,, \tag{4.68a}$$

$$g_2(\overline{\mathbf{c}}) = \overline{c}_1 + \overline{c}_2 + \overline{c}_1\overline{c}_2 - 3 - \overline{c}_3^2 - 2\log(\overline{c}_1\overline{c}_2 - \overline{c}_3^2)\,, \tag{4.68b}$$

$$g_3(\overline{\mathbf{c}}) = \frac{1}{2}\left(\sqrt{\overline{c}_1\overline{c}_2 - \overline{c}_3^2} - 1\right)^2, \tag{4.68c}$$

in the two-dimensional case. The expression of the matrix $[V]$ *can easily be deduced as well.*

In order to investigate the existence and uniqueness of a solution to the optimization problem defined by Eqs. (4.53) and (4.60), we consider the definition of a closest approximation $\overline{w}^\star_{\mathscr{C}}$ in

the subset $\mathscr{C}$ defined by Eq. (4.58). Given the definition of the admissible set $\mathbb{A}$, the set $\mathscr{C}$ is a non-empty closed subset of $L^2_\rho(\mathbb{K},\mathbb{R})$. In addition, for all $\boldsymbol{\pi}$, $\boldsymbol{\pi}'$ in $\mathbb{A}$ and $t \in [0,1]$, one has

$$t\overline{w}_{\mathscr{C}}(\overline{\mathbf{c}};\boldsymbol{\pi}) + (1-t)\overline{w}_{\mathscr{C}}(\overline{\mathbf{c}};\boldsymbol{\pi}') = \sum_{i=1}^{n_{\boldsymbol{\pi}}} (t\pi_i + (1-t)\pi'_i) g_i(\overline{\mathbf{c}})\,. \tag{4.69}$$

The admissible set $\mathbb{A}$ being convex, it is deduced $t\boldsymbol{\pi} + (1-t)\boldsymbol{\pi}' \in \mathbb{A}$ for every $t \in [0,1]$. Hence, it follows that

$$t\overline{w}_{\mathscr{C}}(\overline{\mathbf{c}};\boldsymbol{\pi}) + (1-t)\overline{w}_{\mathscr{C}}(\overline{\mathbf{c}};\boldsymbol{\pi}') \in \mathscr{C}_p\,, \quad \forall t \in [0,1]\,, \tag{4.70}$$

which shows the strict convexity of $\mathscr{C}_p$. By virtue of the projection theorem in a Hilbert space [72], it can be deduced that there exists a unique solution to the approximation problem defined by Eq. (4.60).

4.4.3 Numerical applications

4.4.3.1 Case of a random microstructure

As a first application, we consider the random microstructure described in Section 4.3.4.1. The optimization problem defined by Eqs. (4.61)-(4.62) is solved using an interior-point algorithm with the initial guess defined by the material parameters $(\mu^{(m)}, \lambda^{(m)})$ associated with the matrix phase. The support of the density function ρ is chosen as $\mathbb{K} = [0.9, 1.5] \times [0.9, 1.5] \times (1/\sqrt{2})[-0.1, 0.5]$. The closest Neo-Hookean model is found to be characterized by the material parameters $\mu^\star = \pi_1^\star$ and $\lambda^\star = \pi_2^\star$ given by

$$\mu^\star = 1.7529\,\mu^{(m)} = 575.2783 \text{ MPa} \tag{4.71}$$

and

$$\lambda^\star = 1.3170\,\lambda^{(m)} = 2.0167 \text{ GPa}\,. \tag{4.72}$$

The associated residual distance is given by

$$\|\overline{w}^\star_{p,\mathscr{C}} - \overline{w}_p\|_{L^2_\rho(\mathbb{K},\mathbb{R})} \approx 1.56\,. \tag{4.73}$$

In order to investigate the influence of the support $\mathbb{K}$ (which defines the measure of $\overline{\mathbf{c}}$ and may therefore impact the approximation in a given class of stored energy function) on the Neo-Hookean parameters $\mu^\star$ and $\kappa^\star$, we consider a sequence $\{\mathbb{K}^{(i)}\}_{i=1}^{10}$ of imbricated supports such that

$$\mathbb{K}^{(\ell)} = \bigtimes_{i=1}^{3} [a_i^{(\ell)}, b_i^{(\ell)}]\,, \quad 1 \leqslant \ell \leqslant 10\,. \tag{4.74}$$

For each support, the optimal order of expansion and number of quadrature points are obtained from a convergence analysis on the error functions $n_{\mathcal{Q}} \mapsto \varepsilon_{\mathcal{Q}}(n_{\mathcal{Q}})$ and $p \mapsto \varepsilon(p)$ defined in Section 4.3.3 (see Eqs. (4.46) and (4.47)). Below, the error parameters $\varepsilon^{\text{tol}}_{\mathcal{Q}}$ and ε^{tol} are respectively set to 5×10^{-12} and 5×10^{-10}. The definition of these supports and the associated parameters are listed in Tab. 4.2, and the sequence of imbricated supports can be visualized in Fig. 4.13.

For a given support $\mathbb{K}^{(\ell)}$, we introduce the following relative error $\varepsilon^\star(\ell)$ characterizing the accuracy of the approximation in the class under consideration:

$$\varepsilon^\star(\ell) = \frac{\|[V(\ell)]\boldsymbol{\pi}^\star(\ell) - \mathbf{z}(\ell)\|}{\|\mathbf{z}(\ell)\|}\,. \tag{4.75}$$

	$\ell = 1$	$\ell = 2$	$\ell = 3$	$\ell = 4$	$\ell = 5$	$\ell = 6$	$\ell = 7$	$\ell = 8$	$\ell = 9$	$\ell = 10$
$a_1^{(\ell)} = a_2^{(\ell)}$	0.95	0.93	0.91	0.88	0.86	0.84	0.82	0.79	0.77	0.75
$b_1^{(\ell)} = b_2^{(\ell)}$	1.10	1.14	1.19	1.23	1.28	1.32	1.37	1.41	1.46	1.50
$a_3^{(\ell)}$	-0.05	-0.07	-0.09	-0.12	-0.14	-0.16	-0.18	-0.21	-0.23	-0.25
$b_3^{(\ell)}$	0.05	0.07	0.09	0.12	0.14	0.16	0.18	0.21	0.23	0.25
$\lvert\mathbb{K}^{(\ell)}\rvert$	0.002	0.007	0.015	0.029	0.048	0.075	0.111	0.156	0.213	0.281
p^{opt}	9	9	11	11	13	13	13	15	17	17
$n_{\mathcal{Q}}^{\mathrm{opt}}$	10	10	12	12	13	14	14	15	17	17

Table 4.2 – Definition of the supports $\mathbb{K}^{(\ell)}$, $1 \leqslant \ell \leqslant 10$, under consideration.

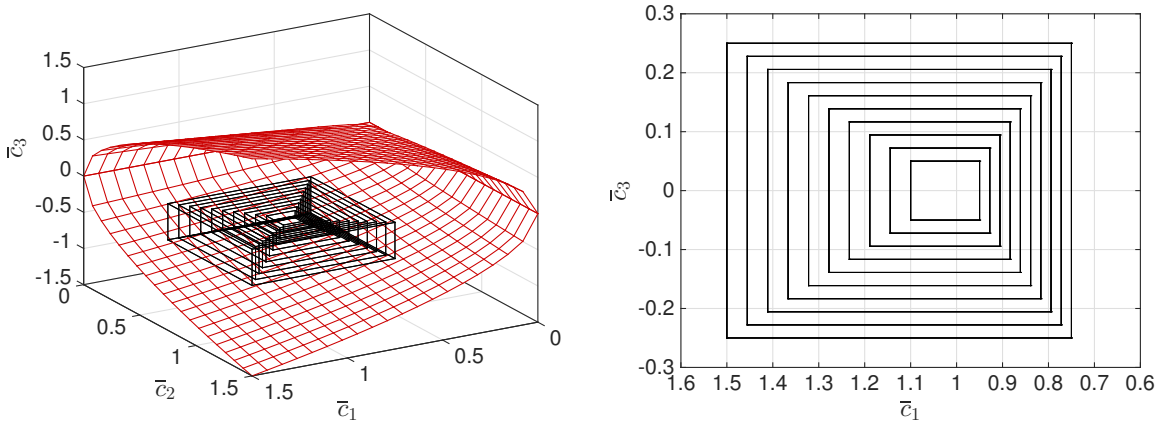

Figure 4.13 – Left panel: graphs of the supports $\mathbb{K}^{(\ell)}$, $1 \leqslant \ell \leqslant 10$ (black lines), and graph of the boundary for the admissible set (red lines). Right panel: graphs of the supports in the plane $(\overline{c}_1, \overline{c}_3)$.

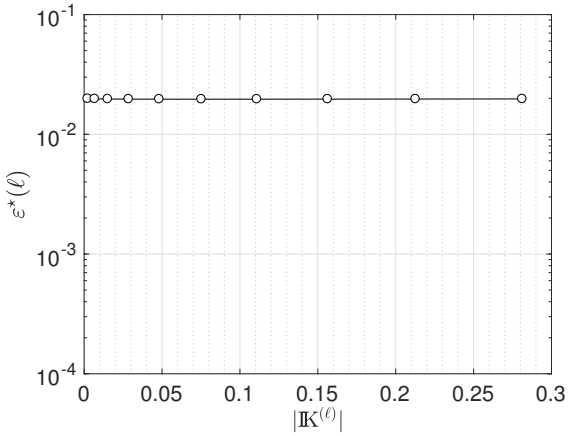

Figure 4.14 – Graph of mapping $|\mathbb{K}^{(\ell)}| \mapsto \varepsilon^\star(\ell)$, $1 \leqslant \ell \leqslant 10$.

Above, the use of variable ℓ on the right-hand side underlines the fact that all quantities are computed considering $\mathbb{K}^{(\ell)}$ as the support for the measure of $\overline{\mathbf{c}}$. The graph of $|\mathbb{K}^{(\ell)}| \mapsto \varepsilon^\star(\ell)$,

$1 \leqslant \ell \leqslant 10$, is shown in Fig. 4.14. On the one hand, it is seen that the relative error between the surrogate representation of the effective stored energy function and its approximation in the class of Neo-Hookean materials is less than two percent, regardless of the support under consideration. On the other hand, it is further observed that the error is almost independent of the measure of the support, hence suggesting the use of smaller supports (which require smaller numbers of quadrature points) in order to estimate the sought closest approximation. Recalling that $\boldsymbol{\pi}^\star = (\mu^\star, \lambda^\star)$, the previous result can also be illustrated by considering the Lamé constants, as shown in Fig. 4.15.

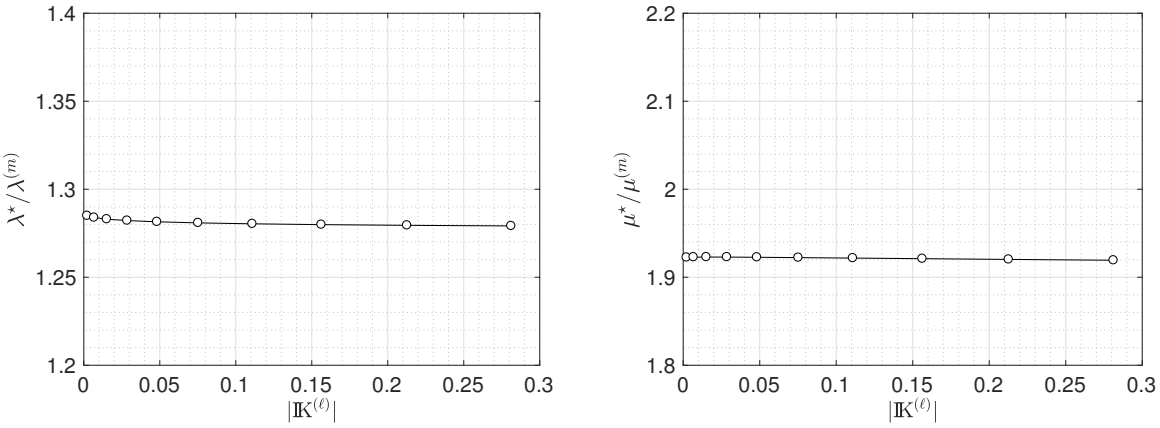

Figure 4.15 – Graph of mappings $|\mathbb{K}^{(\ell)}| \mapsto \lambda^\star(\ell)/\lambda^{(m)}$ and $|\mathbb{K}^{(\ell)}| \mapsto \mu^\star(\ell)/\mu^{(m)}$, $1 \leqslant \ell \leqslant 10$.

4.4.3.2 Case of a deterministic microstructure: sensitivity with respect to the elastic contrast and volume fraction

In this second application, we consider a deterministic representative volume element made of a Neo-Hookean matrix reinforced by a single circular inclusion (see below), with the aim to investigate the impact of both the measure of the domain occupied by the inclusion and the elastic contrast on the definition of the closest approximation. Let ϕ denote the above measure, and ϱ denote the contrast between the elastic properties of the constitutive phases (see Eq. (4.50). The microstructure with the case $\phi = 0.1$ is shown in Fig. 4.16.

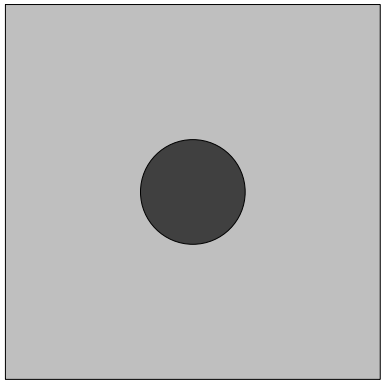

Figure 4.16 – View of the deterministic microstructure with the circular inclusion ($\phi = 0.1$).

The support of the density function ρ is chosen as $\mathbb{K} = [0.9, 1.5] \times [0.9, 1.5] \times (1/\sqrt{2})[-0.1, 0.5]$. The evolution of the relative error $\varepsilon^\star$ (see Eq. (4.75)) with respect to parameters ϕ and ϱ is shown in Fig. 4.17 (note here that the measure of the support is now constant).

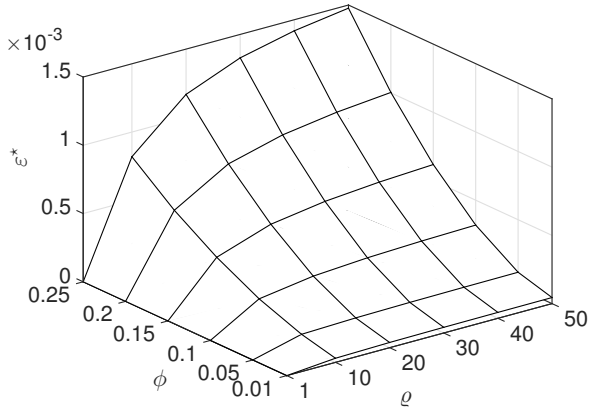

Figure 4.17 – Graph of the distance $\varepsilon^\star$ as a function of the contrast ϱ and the initial volume fraction ϕ.

As expected, it is found that the error increases with ϕ, regardless of the elastic contrast. In addition, the impact of the elastic contrast turns out to be negligible for $\phi \leqslant 0.1$, but tends to become more pronounced for larger values of ϕ. It is however worth noticing that the relative error is smaller than one percent for all the configurations under consideration. The evolution of the Neo-Hookean parameters $\lambda^\star$ and $\mu^\star$ with respect to ϕ and ϱ is finally shown in Fig. 4.18, and confirms the trends observed on the relative error measure.

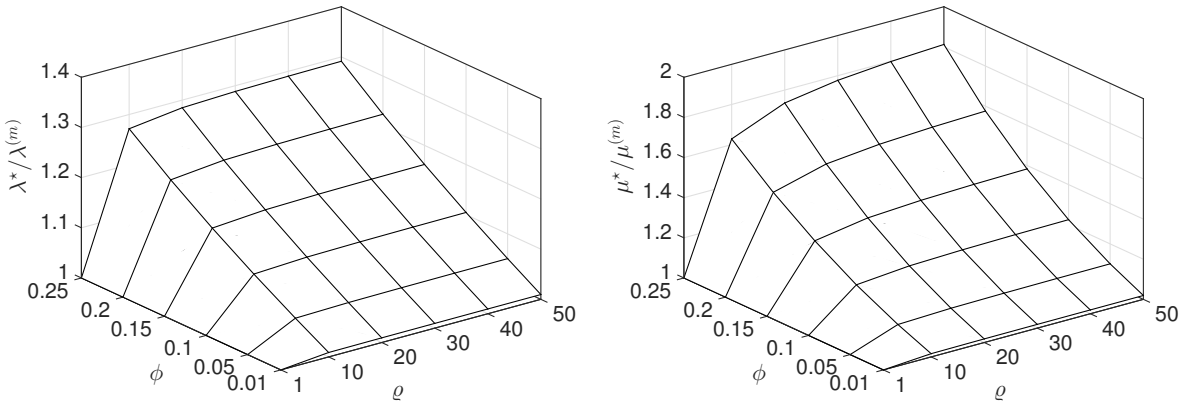

Figure 4.18 – Graph of $\lambda^\star/\lambda^{(m)}$ and $\mu^\star/\mu^{(m)}$ as a function of the contrast ϱ and the initial volume fraction ϕ.

4.4.3.3 Case of a deterministic microstructure: sensitivity with respect to the anisotropy

As a complementary numerical illustration, we address the case of a deterministic microstructure made of a Neo-Hookean matrix reinforced by a Neo-Hookean ellipsoidal inclusion. Denoting by a

and b the minor and major axis of the ellipse respectively (the minor axis being aligned with the horizontal direction), we consider four microstructures, each of which being defined by a specific value of the anisotropy ratio b/a (see Fig. 4.19). The values of a and b are specifically chosen such that the volume fraction remains constant over the different configurations.

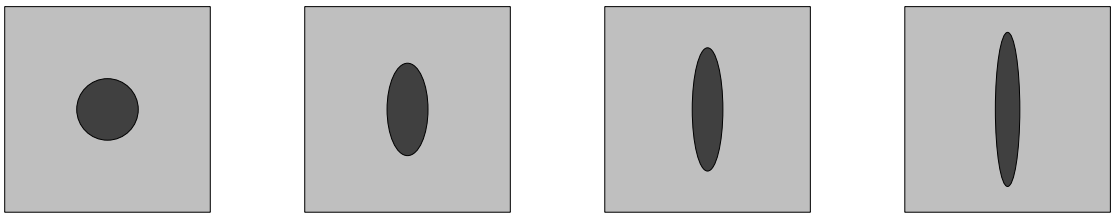

Figure 4.19 – Meshed views of the microstructures under consideration, with $b/a \in \{1, 2.25, 4, 6.25\}$ from left to right.

In order to ensure the numerical stability in the case of slender inclusions, the approximation is sought over $\mathbb{K} = [0.9, 1.5] \times [0.9, 1.5] \times [0, 0.3]$. For $\varepsilon^{\text{tol}} = 10^{-10}$, the optimal order of expansion is found to be $p^{\text{opt}} = 15$, regardless of the microstructure under consideration. This result shows the capability of the retained polynomial basis to accurately represent anisotropic potentials, even with reduced expansion orders. The signature of the anisotropy can be further visualized by considering the ordered sequence $z_{\alpha_s^{(1)}} \geqslant \ldots \geqslant z_{\alpha_s^{(N)}}$ of polynomial coefficients and by characterizing the evolution of this signature as the ratio b/a increases. The graph of the mapping $k \mapsto z_{\alpha_s^{(k)}}$ is shown in Fig. 4.20 for the ten larger coefficients.

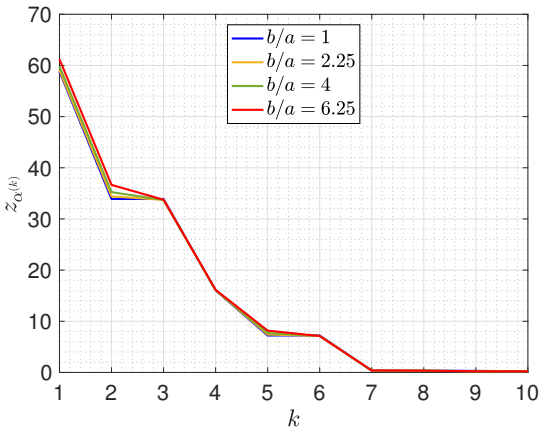

Figure 4.20 – Graph of $k \mapsto z_{\alpha_s^{(k)}}$ for $1 \leqslant k \leqslant 10$.

While some coefficients remain almost constant whatever the ratio b/a, some coefficients (namely, the first, second and fifth ones in the ordered sequence) are impacted by the anisotropy level, hence allowing the associated polynomials, which actually enrich the isotropic response, to be identified. Finally, the evolution of the residual with respect to the projection onto the set of isotropic Neo-Hookean potentials (see Eq. (4.75)) is depicted in Fig. 4.21.

As expected, it is seen that the residual increases as the underlying microstructure becomes more anisotropic.

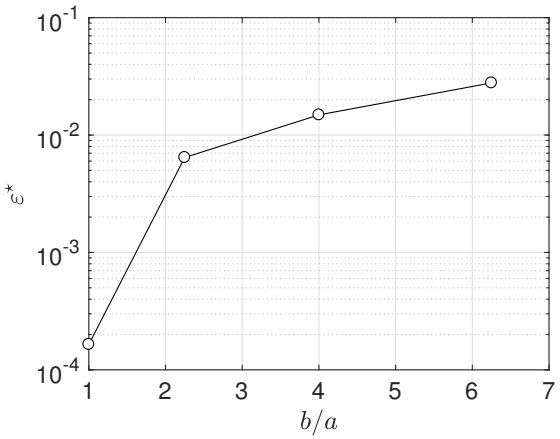

Figure 4.21 – Evolution of the distance $\varepsilon^\star$ as a function of the ratio b/a.

4.4.3.4 Two-scale structural application

In this last section, we investigate the accuracy of the polynomial expansion and that of the closest isotropic stored energy function for a two-scale structural problem. In particular, these surrogate solutions are compared with a reference solution obtained by the FE^2 multiscale approach [115, 116]. The structure under consideration is depicted in Fig. 4.22, where $L = 1\text{m}$, $e = 0.15\text{m}$ and $\mathbf{u}_d = 0.1x_2\mathbf{e}_2$. In this application, the domain is discretized using 6-node triangular elements [109], and the convergence in the L^2 sense of the displacement field is reached with 15288 elements (note that local mesh refinement is performed wherever necessary). The

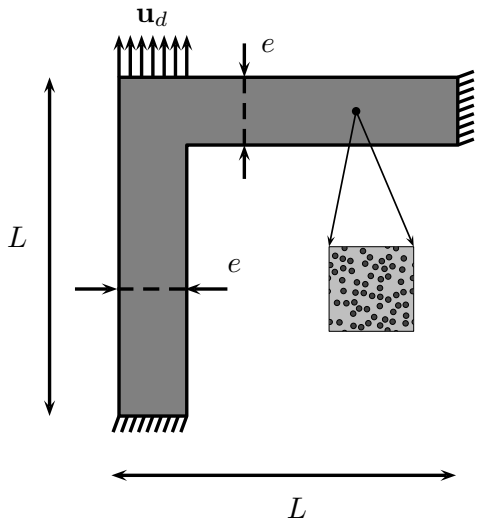

Figure 4.22 – Geometry of the structure and definition of boundary conditions.

associated microstructure is the same as the one described in Section 4.3.4.1 (consisting of a Neo-Hookean matrix reinforced by randomly distributed circular inclusions), and is replicated at each macroscopic point. The support $\mathbb{K}$ is set to $\mathbb{K} = [0.75, 1.5] \times [0.75, 1.5] \times [-0.25, 0.15]$, and the polynomial expansion is constructed with $\varepsilon_{\mathcal{Q}}^{\text{tol}} = 5 \times 10^{-12}$ and $\varepsilon^{\text{tol}} = 5 \times 10^{-11}$. Based on the preliminary study, it is deduced that $p^{\text{opt}} = 17$ and $n_{\mathcal{Q}}^{\text{opt}} = 16$. The distance between the effective stored energy function and its closest Neo-Hookean approximation is given by 0.2142.

The associated parameters $\lambda^\star$ and $\mu^\star$ are given by $\lambda^\star = 1.9504 \times 10^3$ MPa and $\mu^\star = 640.8884$ MPa, or equivalently by $\mu^\star = 1.9532\,\mu$ and $\lambda^\star = 1.2737\,\lambda$. Note that these results are coherent with the ones obtained in Section 4.4.3.1 (see Figs. 4.14 and 4.15). The plots of the Von Mises stress computed by using the FE^2 method, the PCE-based surrogate model and the closest Neo-Hookean approximation are shown in Figs. 4.23 and 4.24.

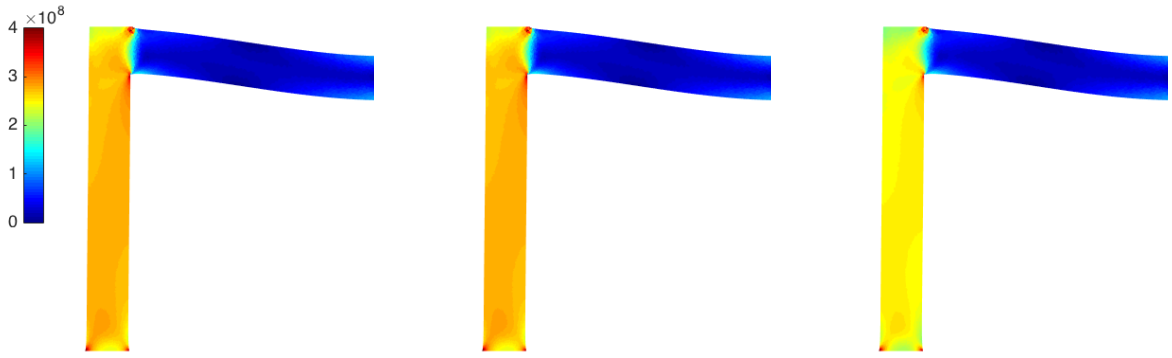

FE^2 solution | Polynomial approximation | Closest Neo-Hookean approximation

Figure 4.23 – Plot of the Von Mises stress [Pa]: reference solution (left panel), solution based on the $\mathbb{P}_{\mathscr{A}_p}$ projection (middle panel) and solution based on the $\mathscr{C}^{\mathrm{NH}}$ projection (right panel).

In accordance with the previous numerical results, it is seen that the closest approximation in the class of Neo-Hookean models provides a good approximation, especially for the peak values of the Von Mises stress. Whereas the construction of the surrogate model requires some preprocessing steps, including the call to nonlinear finite element computations, it is important to note that the estimation of the closest Neo-Hookean parameters allows one to consider values of the Cauchy-Green tensor that fall outside the support $\mathbb{K}$. Hence, the proposed approach does not suffer from boundary effects, such as those typically encountered in interpolation-based schemes, and allows for a direct coupling with commercial codes for nonlinear finite element analysis.

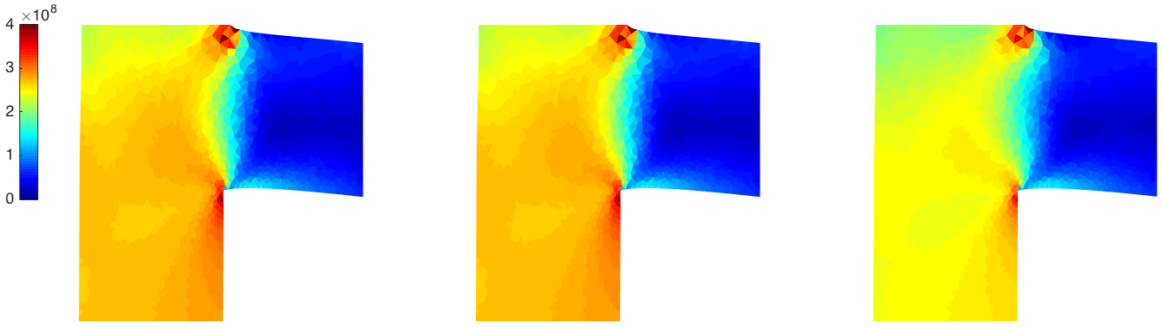

FE^2 solution | Polynomial approximation | Closest Neo-Hookean approximation

Figure 4.24 – Zoom-in plots of the Von Mises stress [Pa]: reference solution (left), solution based on the $\mathbb{P}_{\mathscr{A}_p}$ projection (middle) and solution based on the $\mathscr{C}^{\mathrm{NH}}$ projection (right).

4.5 Conclusion

In this chapter, the approximation of homogenized stored energy functions has been addressed by resorting to projections onto polynomial spaces and relevant sets of stored energy functions [154]. A surrogate model for the homogenized stored energy function was first constructed using Legendre polynomials. The efficiency of the approach was assessed on two problems and compared with another interpolation scheme proposed elsewhere. While the polynomial surrogate approximates the solution map with a very good accuracy, the approach suffers from a curse of dimensionality in three-dimensional applications. Other strategies could be pursued to circumvent this issue; see, *e.g.*, [155, 156, 157, 158, 159] and the references therein. The functional framework further allowed for the precise definition of closest approximations of arbitrary stored energy functions in well-defined classes, such as Ogden-type potentials. The relevance of the methodology and its sensitivity with respect to some parameters related to the microstructure were also investigated by considering two microstructures a structural problem relying on a non-concurrent coupling. The definition of such closest approximations is particularly appealing from an engineering point of view, since it allows information to be readily transferred into commercial finite elements softwares.

Chapter 5

Random Field Models for Anisotropic Stored Energy Functions

Contents

5.1 Introduction

This chapter is concerned with the modeling and simulation of spatially varying anisotropic stored energy functions for nearly incompressible materials, defined on complex geometries. This chapter is organized as follows. The definition of a prototypical anisotropic stored energy function is first presented in Section 5.2. The probabilistic model is then constructed in Section 5.3. A sampling strategy based on the resolution of a stochastic partial differential equation is proposed in Section 5.4. Uncertainty propagation is finally addressed in Section 5.5, where the modeling of an arterial wall is investigated in detail.

5.2 Background on anisotropic stored energy functions

The construction of anisotropic stored energy functions has been extensively addressed in the past few years, especially for the modeling of soft biological tissues (see, *e.g.*, [80]). In the case of arterial walls, the anisotropy is associated with the presence of families of fibers with non-orthogonal preferred directions. For instance, in [104] the arterial wall is modeled as a nearly incompressible hyperelastic materials with two non-orthogonal preferred directions. Anisotropy is taken into account by relying on the structural approach which consists in introducing structural tensors [59, 60] that reflect the symmetry properties of the material. However, as fibers are not perfectly aligned but rather dispersed around the preferred directions, several works propose to take into account the fibers dispersion through different methodologies [160, 161]. Reviews of constitutive models for arteries motivated by phenomenological considerations can

be found in [162, 163, 164]. The construction of anisotropic polyconvex stored energy functions has been carried out in [165, 166, 167] for nearly incompressible materials and applied for large-scale simulation in, *e.g.*, [168, 169, 170, 171, 172]. In particular, the widely used constitutive model proposed in [104] was shown to be polyconvex in [167] under mild assumptions. A list of polyconvex models for nearly incompressible and compressible hyperelastic media can be found in the textbook [173]. Like most soft biological tissues, arterial walls are modeled as nearly incompressible and show different behaviors for isochoric or volumetric states of deformations [104]. One approach to take into account this feature is to decouple the deformation gradient into isochoric and volumetric contributions, as proposed in [174]. In this context, a multiplicative decomposition is introduced:

$$[F] = J^{-1/3}[\overline{F}]\,, \quad J = \det([F])\,, \tag{5.1}$$

such that $\det([\overline{F}]) = 1$. The isochoric right Cauchy-Green tensor $[\overline{C}]$ defined as $[\overline{C}] = [\overline{F}]^T[\overline{F}]$ can also be written as $[\overline{C}] = J^{-2/3}[C]$. In the following, we let $\mathbf{x} \mapsto \mathbf{a}_1(\mathbf{x})$ and $\mathbf{x} \mapsto \mathbf{a}_2(\mathbf{x})$ be the non-orthogonal preferred directions schematically identified with the directions of the two families of aligned fibers. The construction of suitable stored energy function is based on the introduction the structural tensors $\mathbf{x} \mapsto [M_\ell(\mathbf{x})]$ for $\ell = 1, 2$, such that

$$[M_\ell(\mathbf{x})] = [Q][M_\ell(\mathbf{x})][Q]^T\,, \quad \forall [Q] \in \mathscr{G}_{\mathbf{a}_\ell(\mathbf{x})}\,, \quad \forall \mathbf{x} \in \mathscr{B}\,, \tag{5.2}$$

where $\mathscr{G}_{\mathbf{c}}$ is the symmetry group defined as $\mathscr{G}_{\mathbf{c}} = \{[Q] \in \mathrm{SO}(3) \,:\, [Q]\mathbf{c} = \mathbf{c}\}$ for some given $\mathbf{c} \in \mathbb{R}^3$. Herein, we consider the prototypical stored energy function given by [70, 104, 167]

$$\begin{aligned} w(\mathbf{x}, [F]) = \mu_1(\mathbf{x})\frac{\|[F]\|_F^2}{(\det([F]))^{2/3}} + \mu_2(\mathbf{x})\frac{\|\mathrm{Cof}([F])\|_F^3}{(\det([F]))^2} + \mu_3(\mathbf{x})h(\det([F])) \\ + \frac{\mu_4(\mathbf{x})}{\beta_4}\Big(\exp\left(\beta_4\langle\|[F]\mathbf{a}_1(\mathbf{x})\|^2 - 1\rangle_m^2\right) + \exp\left(\beta_4\langle\|[F]\mathbf{a}_2(\mathbf{x})\|^2 - 1\rangle_m^2\right)\Big)\,, \end{aligned} \tag{5.3}$$

in which $\langle g\rangle_m = \max(0, g)$ represents the Macauley bracket and the function h writes

$$h(\delta) = \delta^{\beta_3} + \delta^{-\beta_3}\,, \quad \forall\, \delta > 0\,. \tag{5.4}$$

The first three terms correspond to a isotropic nearly incompressible Mooney-Rivlin like contribution [70], while the exponential terms represent locally anisotropic contributions associated to the preferred directions $\mathbf{x} \mapsto \mathbf{a}_1(\mathbf{x})$ and $\mathbf{x} \mapsto \mathbf{a}_2(\mathbf{x})$ [104]. It is worth pointing out that we do not resort to the volumetric-isochoric decomposition for the anisotropic terms as it leads to unphysical behaviors. In addition, the Macauley bracket ensures that the anisotropic terms do not contribute to the constitutive equations whenever the fibers are under compression. Hence, the material is locally isotropic if it undergoes compression along both preferred directions at a given location $\mathbf{x}$ in $\mathscr{B}$. In what follows, it is assumed that the model parameters are uniformly bounded by below, *i.e.*,

$$\mu_j(\mathbf{x}) \geqslant \mu_j^{\min} > 0\,, \quad \forall \mathbf{x} \in \mathscr{B}\,, \tag{5.5}$$

and that

$$\beta_3 > 2\,, \quad \beta_4 > 0\,. \tag{5.6}$$

It can then be shown that the stored energy function satisfies the following fundamental properties.

(i) *Polyconvexity.* For all $\mathbf{x} \in \mathscr{B}$, there exists a convex function $w^\star$ such that

$$w(\mathbf{x}, [F]) = w^\star(\mathbf{x}, [F], \mathrm{Cof}([F]), \det([F]))\,. \tag{5.7}$$

The proof follows from the polyconvexity of the functions [165, 166, 167]

$$[F] \mapsto \|(\det([F]))^{1/3}[F]\|_F^\alpha\,, \quad [F] \mapsto \|(\det([F]))^{-2/3}\mathrm{Cof}([F])\|_F^\gamma\,, \tag{5.8}$$

$$[F] \mapsto \exp(\beta_4\langle\|[F]\mathbf{a}_\ell(\mathbf{x})\|^2 - 1\rangle_m^2)\,, \tag{5.9}$$

and the convexity of the function $h(\delta) = \delta^{\beta_3} + \delta^{-\beta_3}$ for $\alpha \geqslant 3/2$, $\gamma \geqslant 3$, $\beta_3 > 2$ and $\beta_4 > 0$. The reader is referred to [70] and [167] for more details about the polyconvexity of isochoric and exponential functions, respectively. The model parameters being uniformly bounded from below (see Eq. (5.5)) and the exponents satisfying Eq. (5.6), it can be deduced that the stored energy function is polyconvex. Note that this property implies ellipticity (see Eq. (1.27)).

(ii) For all $\mathbf{x} \in \mathscr{B}$, $[F] \in \mathbb{M}^3$, there exists constants $c_0 > 0$, $c_1 \in \mathbb{R}$, $3/2 < p < 2$ and $3/2 < q < 3$ such that

$$w^\star(\mathbf{x}, [F], [H], \delta) \geqslant c_0\,(\|[F]\|_F^p + \|[H]\|_F^q + \delta^{\beta_3}) - c_1\,, \tag{5.10}$$

where the parameters p and q are given by

$$\frac{3}{2} < p = \frac{6\beta_3}{3\beta_3 + 2} < 2\,, \quad \frac{3}{2} < q = \frac{3\beta_3}{\beta_3 + 2} < 3\,. \tag{5.11}$$

and the constants c_0 and c_1 take the form

$$c_0 = \min\left\{\mu_1^{\min}\frac{3\beta_3+2}{3\beta_3}, \mu_3^{\min}\eta_1\frac{3\beta_3+2}{2}, \mu_2^{\min}\frac{\beta_3+2}{\beta_3}, \mu_3^{\min}\eta_2\frac{\beta_3+2}{2}, \mu_3^{\min}\eta_3\right\}. \tag{5.12}$$

and $c_1 = 0$, for any real scalars η_1, η_2 and η_3 such that $\eta_1 + \eta_2 + \eta_3 = 1$. This property can be derived following the methodology proposed in [70] which relies on Young's inequality. It implies that the stored energy function satisfies uniform growth conditions, also referred to as uniform coercivity in the sequel of this chapter. Note that Eq. (5.10) is stronger than the coercivity property given by Eq. (1.30).

Following [65, 70], these properties imply that there exists minimizers to the energy functional in the space

$$\mathcal{X}^{1,p} = \{\boldsymbol{\varphi} \in W^{1,p}(\mathscr{B}, \mathbb{R}^3) : \pi(\boldsymbol{\varphi}) < +\infty\,, \boldsymbol{\varphi}|_{\Gamma_D} = \boldsymbol{\varphi}_d\}\,, \tag{5.13}$$

where $\boldsymbol{\varphi}_d : \Gamma_D \to \mathbb{R}^3$ correspond to the essential boundary conditions. We end this section by analyzing the behavior at small strains of the hyperelastic medium characterized by the above stored energy function. Let $[\check{S}]$ be the second Piola-Kirchhoff stress tensor written in terms of the Green-Lagrange deformation tensor $[E]$ given by

$$[E] = \frac{1}{2}([F]^T[F] - [I_3])\,, \quad \forall [F] \in \mathbb{M}^3_+\,. \tag{5.14}$$

Using the definition of the stored energy function given by Eq. (5.3), it can be deduced that the linearized Piola-Kirchhoff stress tensor writes

$$\begin{aligned}[\check{S}(\mathbf{x}, [E])] =& \big(2\mu_3(\mathbf{x})\beta_3^2 - \frac{4}{3}\mu_1(\mathbf{x}) - 2\mu_3(\mathbf{x})3^{1/2}\big)\mathrm{Tr}([E])[I_3] \\ &+ \big(4\mu_1(\mathbf{x}) + 6\sqrt{3}\mu_2(\mathbf{x})\big)[E] + 8\mu_4(\mathbf{x})\sum_{\ell=1}^{2}\langle\mathrm{Tr}([E_\varphi(\mathbf{x})][M_\ell(\mathbf{x})])\rangle_m[M_\ell(\mathbf{x})] + o(\|[E]\|)\,.\end{aligned} \tag{5.15}$$

By letting $\mathbf{x} \mapsto [\![A(\mathbf{x})]\!]$ be the elasticity tensor at small strains defined such that $[\breve{S}(\mathbf{x}, [E])] = [\![A(\mathbf{x})]\!] : [E] + o(\|[E]\|)$, it can be deduced that

$$[\![A(\mathbf{x})]\!] = [\![A_{\rm iso}(\mathbf{x})]\!] + 8\mu_4(\mathbf{x}) \sum_{\ell=1}^{2} \mathbb{1}_{\mathcal{S}_\ell}([E])[M_\ell(\mathbf{x})] \otimes [M_\ell(\mathbf{x})]\,, \tag{5.16}$$

where $\mathcal{S}_\ell$ denotes the set of deformation tensors $[E]$ such that $\mathrm{Tr}([E][M_\ell(\mathbf{x})]) > 0$, and $\mathbf{x} \mapsto [\![A_{\rm iso}(\mathbf{x})]\!]$ denotes an isotropic contribution of the form

$$[\![A_{\rm iso}(\mathbf{x})]\!] = 6\mu_3(\mathbf{x})\beta_3^2 [\![E_1]\!] + (4\mu_1(\mathbf{x}) + 6\sqrt{3}\mu_2(\mathbf{x}))[\![E_2]\!] \tag{5.17}$$

in which $[\![E_1]\!]$ and $[\![E_2]\!]$ are the fourth-order mutually orthogonal projectors defined as

$$[\![E_1]\!] = \frac{1}{3}[I_3] \otimes [I_3]\,, \quad [\![E_2]\!] = [I_3] \boxtimes [I_3] - [\![E_1]\!]\,. \tag{5.18}$$

This shows that the hyperelastic material is isotropic at small strains, with bulk and shear moduli given by $\mathbf{x} \mapsto 2\mu_3(\mathbf{x})\beta_3^2$ and $\mathbf{x} \mapsto 2\mu_1(\mathbf{x}) + 3^{3/2}\mu_2(\mathbf{x})$, whenever it undergoes compression along to the two preferred directions $\mathbf{x} \mapsto \mathbf{a}_1(\mathbf{x})$ and $\mathbf{x} \mapsto \mathbf{a}_2(\mathbf{x})$. When a local stretch is prescribed along one preferred direction, say $\mathbf{a}_1(\mathbf{x})$, then the random elasticity tensor exhibits transverse isotropy with respect to $\mathbf{a}_1(\mathbf{x})$. Apart from these two situations, the elastic behavior at small strains turns out to be anisotropic.

5.3 Definition of a random field model

The functional form of the stored energy function for which a stochastic extension is sought has been presented in the previous section. We now let $\{\mathcal{W}_\epsilon(\mathbf{x}, [F]), (\mathbf{x}, [F]) \in \mathscr{B} \times \mathbb{M}^3_+\}$ be the random field corresponding to the stochastic stored energy function, defined on the probability space $(\Theta, \mathscr{T}, \mathbb{P})$, indexed by $\mathscr{B} \times \mathbb{M}^3_+$, and corresponding to the probabilistic modeling of the potential given by Eq. (5.3). In a first step, an algebraic decomposition of the stochastic stored energy function is introduced in order to enforce uniform growth conditions. Let $0 < \epsilon \ll 1$ be an arbitrary small regularizing parameter such that

$$\mathcal{W}_\epsilon(\mathbf{x}, [F]) = \frac{1}{1+\epsilon}(\mathcal{W}(\mathbf{x}, [F]) + \epsilon\, \mathbb{E}\{\mathcal{W}(\mathbf{x}, [F])\})\,, \quad \forall \mathbf{x} \in \mathscr{B}\,, \quad \forall [F] \in \mathbb{M}^3_+\,. \tag{5.19}$$

Let then $\{\mathbf{G}(\mathbf{x}), \mathbf{x} \in \mathscr{B}\}$ be a vector-valued random field such that $\mathbf{G}(\mathbf{x}) = (G_1(\mathbf{x}), \ldots, G_4(\mathbf{x}))$ corresponding to the probabilistic modeling of the parameter $\mathbf{x} \mapsto (\mu_1(\mathbf{x}), \ldots, \mu_4(\mathbf{x}))$ involved in Eq. (5.3). The random field $\{\mathcal{W}(\mathbf{x}, [F]), (\mathbf{x}, [F]) \in \mathscr{B} \times \mathbb{M}^3_+\}$ is then defined as

$$\begin{aligned} \mathcal{W}(\mathbf{x}, [F]) = {} & G_1(\mathbf{x}) \frac{\|[F]\|_F^2}{(\det([F]))^{2/3}} + G_2(\mathbf{x}) \frac{\|\mathrm{Cof}([F])\|_F^3}{(\det([F]))^2} + G_3(\mathbf{x}) h(\det([F])) \\ & + \frac{G_4(\mathbf{x})}{\beta_4} \Big(\exp\left(\beta_4 \langle \|[F]\mathbf{a}_1(\mathbf{x})\|^2 - 1 \rangle_m^2\right) + \exp\left(\beta_4 \langle \|[F]\mathbf{a}_2(\mathbf{x})\|^2 - 1 \rangle_m^2\right) \Big)\,, \end{aligned} \tag{5.20}$$

where $\beta_3 > 2$ and $\beta_4 > 0$. In addition, the following hypotheses are made regarding the random field $\{\mathbf{G}(\mathbf{x}), \mathbf{x} \in \mathbf{x} \in \mathscr{B}\}$. It is first assumed that for every $\mathbf{x} \in \mathscr{B}$, the random variables $G_j(\mathbf{x})$ are such that

$$G_j(\mathbf{x}) > 0\,, \quad 1 \leqslant j \leqslant 4\,, \tag{5.21}$$

almost surely. In addition, the mean value of the random field $\{\mathbf{G}(\mathbf{x}), \mathbf{x} \in \mathscr{B}\}$ is homogeneous over $\mathscr{B}$, *i.e.*,

$$\mathbb{E}\{\mathbf{G}(\mathbf{x})\} = \underline{\mathbf{g}}\,, \quad \forall \mathbf{x} \in \mathscr{B}\,, \tag{5.22}$$

with $g_j > 0$, $1 \leqslant j \leqslant 4$. Using the decomposition given by Eq. (5.19) and the definition of the random field in Eq. (5.20), one has

$$\begin{aligned}\mathcal{W}_\epsilon(\mathbf{x}, [F]) = G_{1\epsilon}(\mathbf{x}) \frac{\|[F]\|_F^2}{(\det([F]))^{2/3}} + G_{2\epsilon}(\mathbf{x}) \frac{\|\mathrm{Cof}([F])\|_F^3}{(\det([F]))^2} + G_{3\epsilon}(\mathbf{x}) h(\det([F])) \\ + \frac{G_{4\epsilon}(\mathbf{x})}{\beta_4} \Big(\exp\left(\beta_4 \langle \|[F]\mathbf{a}_1(\mathbf{x})\|^2 - 1 \rangle_m^2\right) + \exp\left(\beta_4 \langle \|[F]\mathbf{a}_2(\mathbf{x})\|^2 - 1 \rangle_m^2\right) \Big)\,,\end{aligned} \tag{5.23}$$

where the random variables $G_{j\epsilon}(\mathbf{x})$ are such that

$$G_{j\epsilon}(\mathbf{x}) = \frac{1}{1+\epsilon}(G_j(\mathbf{x}) + \epsilon\, \mathbb{E}\{G_j(\mathbf{x})\})\,, \quad 1 \leqslant j \leqslant 4\,. \tag{5.24}$$

Together with Eqs. (5.21)-(5.22), this implies that the entries of the random field $\{\mathbf{G}(\mathbf{x}), \mathbf{x} \in \mathscr{B}\}$ are uniformly bounded by below, *i.e.*,

$$G_{j\epsilon}(\mathbf{x}) > \frac{\epsilon \underline{g}_j}{1+\epsilon} = \mu_j^{\min}\,, \quad 1 \leqslant j \leqslant 4\,. \tag{5.25}$$

This implies that the random potential is uniformly bounded from below, *i.e.*,

$$\mathcal{W}_\epsilon(\mathbf{x}, [F]) \geqslant \frac{\epsilon}{1+\epsilon} \mathbb{E}\{\mathcal{W}(\mathbf{x}, [F])\}\,. \tag{5.26}$$

Let $\{[\![\mathbf{A}_\epsilon(\mathbf{x})]\!], \mathbf{x} \in \mathscr{B}\}$ be the random elasticity tensor at small strains associated to the stochastic potential defined by Eqs. (5.19)-(5.23). It can be deduced that the random elasticity tensor takes the form

$$[\![\mathbf{A}_\epsilon(\mathbf{x})]\!] = \frac{1}{1+\epsilon}([\![\mathbf{A}(\mathbf{x})]\!] + \epsilon\, \mathbb{E}\{[\![\mathbf{A}(\mathbf{x})]\!]\})\,, \quad \forall \mathbf{x} \in \mathscr{B}\,, \tag{5.27}$$

with $\{[\![\mathbf{A}(\mathbf{x})]\!], \mathbf{x} \in \mathscr{B}\}$ the random elasticity tensor given by

$$[\![\mathbf{A}(\mathbf{x})]\!] = [\![\mathbf{A}^{\mathrm{iso}}(\mathbf{x})]\!] + 8G_4(\mathbf{x}) \sum_{\ell=1}^{2} \mathbb{1}_{\mathcal{S}_\ell}([E_\varphi(\mathbf{x})])[M_\ell(\mathbf{x})] \otimes [M_\ell(\mathbf{x})]\,, \tag{5.28}$$

in which $\mathcal{S}_\ell$ denotes the set of deformation tensors $[E]$ such that $\mathrm{Tr}([E][M_\ell(\mathbf{x})]) > 0$ and the isotropic contribution writes

$$[\![\mathbf{A}^{\mathrm{iso}}(\mathbf{x})]\!] = 3C_1(\mathbf{x})[\![E_1]\!] + 2C_2(\mathbf{x})[\![E_2]\!]\,, \tag{5.29}$$

where $\{C_1(\mathbf{x}), \mathbf{x} \in \mathscr{B}\}$ and $\{C_2(\mathbf{x}), \mathbf{x} \in \mathscr{B}\}$ are the random bulk and shear moduli associated with the isotropic contribution of the random elasticity tensor, that is

$$C_1(\mathbf{x}) = 2\beta_3^2 G_3(\mathbf{x})\,, \quad C_2(\mathbf{x}) = 2G_1(\mathbf{x}) + 3\sqrt{3}G_2(\mathbf{x})\,, \quad \forall \mathbf{x} \in \mathscr{B}\,. \tag{5.30}$$

The above consistency relations at small strains allow for writing the random variables $G_3(\mathbf{x})$ and $G_2(\mathbf{x})$ in terms of the random bulk and shear moduli as follows

$$G_3(\mathbf{x}) = \frac{C_1(\mathbf{x})}{2\beta_3^2}\,, \quad G_2(\mathbf{x}) = 3^{-3/2}(C_2(\mathbf{x}) - 2G_1(\mathbf{x}))\,. \tag{5.31}$$

These relations allow a more convenient representation of the stochastic stored energy function to be introduced. Towards this aim, we introduce a random variable $U(\mathbf{x})$ such that

$$2G_1(\mathbf{x}) = C_2(\mathbf{x})U(\mathbf{x})\,, \tag{5.32}$$

and normalized in the sense that it takes its value in $(0,1)$, so that the random variable $G_2(\mathbf{x})$ can equivalently be written as

$$G_2(\mathbf{x}) = 3^{-3/2}C_2(\mathbf{x})(1-U(\mathbf{x}))\,. \tag{5.33}$$

Two strategies can be pursued at this stage.

- In a first approach, the stochastic stored energy function is considered as a function of the random field $\{\mathbf{G}(\mathbf{x}), \mathbf{x}\in\mathscr{B}\}$. The assumptions raised by the mathematical constraints do not introduce any cross-related information among the variables, leading to statistically independent random fields $\{G_i(\mathbf{x}), \mathbf{x}\in\mathscr{B}\}$ and $\{G_j(\mathbf{x}), \mathbf{x}\in\mathscr{B}\}$, $i\neq j$.
- In a second approach, the consistency relations with linearized elasticity given by Eq. (5.30) are taken into account and the stochastic stored energy function is parameterized by the random fields $\{C_i(\mathbf{x}), \mathbf{x}\in\mathscr{B}\}$, $i=1,2$, $\{U(\mathbf{x}), \mathbf{x}\in\mathscr{B}\}$ and $\{G_4(\mathbf{x}), \mathbf{x}\in\mathscr{B}\}$. In this case, the random fields $\{G_1(\mathbf{x}), \mathbf{x}\in\mathscr{B}\}$, $\{G_2(\mathbf{x}), \mathbf{x}\in\mathscr{B}\}$ and $\{G_3(\mathbf{x}), \mathbf{x}\in\mathscr{B}\}$ are defined by Eqs. (5.32) and (5.33) which generate statistical dependencies.

The first strategy turns out to be easier to handle in terms of both technical derivations and sampling issues. The second choice raises, by contrast, more complex calculations but offers the benefit of relying, in part, on information at small strains. This property may be found useful, especially for identification purposes, and motivates the selection of this approach.

Remark 5.3.1. *The selection of $G_2(\mathbf{x})$ as an independent variable in the consistency relations is arbitrary and turns out to be irrelevant, since similar expressions would be obtained by selecting $G_1(\mathbf{x})$ in lieu of $G_2(\mathbf{x})$. More precisely, one shall first extract $G_1(\mathbf{x})$ as*

$$G_1(\mathbf{x}) = \frac{1}{2}(C_2(\mathbf{x}) - 3^{3/2}G_2(\mathbf{x}))\,, \tag{5.34}$$

and then introduce the random variable $V(\mathbf{x})$ such that $C_2(\mathbf{x})V(\mathbf{x}) = 3^{3/2}G_2(\mathbf{x})$, so that

$$2G_1(\mathbf{x}) = C_2(\mathbf{x})(1-V(\mathbf{x}))\,. \tag{5.35}$$

The similitude in the expressions is obtained by comparing Eq. (5.35) with Eq. (5.33) and by letting $V(\mathbf{x}) = 1-U(\mathbf{x})$.

Let $\{\mathbf{P}(\mathbf{x}) = (C_1(\mathbf{x}), C_2(\mathbf{x}), U(\mathbf{x}), G_4(\mathbf{x})), \mathbf{x}\in\mathscr{B}\}$ be the vector-valued random field of model parameters. Following the classical approach to the modeling of non-Gaussian random processes, the random field is defined through the point-wise memoryless transformation

$$\mathbf{P}(\mathbf{x}) = \mathscr{H}(\mathbf{\Xi}(\mathbf{x}))\,, \quad \forall \mathbf{x}\in\mathscr{B}\,, \tag{5.36}$$

where $\{\mathbf{\Xi}(\mathbf{x}) = (\Xi_1(\mathbf{x}),\ldots,\Xi_4(\mathbf{x})), \mathbf{x}\in\mathbb{R}^3\}$ is a second-order centered Gaussian random field defined by the covariance function (which may be inferred either from measurements or expertise)

$$[R_{\mathbf{\Xi}}(\mathbf{x},\mathbf{y})] = \mathbb{E}\{\mathbf{\Xi}(\mathbf{x})\otimes\mathbf{\Xi}(\mathbf{y})\} = \mathrm{diag}(R_1(\mathbf{x},\mathbf{y}),\ldots,R_4(\mathbf{x},\mathbf{y}))\,, \tag{5.37}$$

where $[R_{\boldsymbol{\Xi}}(\mathbf{x},\mathbf{y})] = [I_3]$ and $(\mathbf{x},\mathbf{y}) \mapsto R_i(\mathbf{x},\mathbf{y})$ denotes the correlation function of the real-valued Gaussian random field $\{\Xi_i(\mathbf{x}), \mathbf{x} \in \mathbb{R}^3\}$. The definition of the covariance function Eq. (5.37) implies that the random fields $\{\Xi_i(\mathbf{x}), \mathbf{x} \in \mathscr{B}\}$ and $\{\Xi_j(\mathbf{x}), \mathbf{x} \in \mathbb{R}^2\}$, $i \neq j$, are statistically independent from one another. The nonlinear transformation $\mathscr{H}$ is obtained by constructing the family of first-order marginal probability density functions $\{\mathbf{p} \mapsto f_{\mathbf{P}(\mathbf{x})}(\mathbf{p};\mathbf{x})\}_{\mathbf{x}\in\mathscr{B}}$ of the random field $\{\mathbf{P}(\mathbf{x}), \mathbf{x} \in \mathscr{B}\}$. For simplicity, the first-order marginals are chosen as independent of the location $\mathbf{x}$. Hence, we are concerned with the construction of the probability density function $\mathbf{p} \mapsto f_{\mathbf{P}(\mathbf{x})}(\mathbf{p})$ of the random variable $\mathbf{P}(\mathbf{x})$, for an arbitrary location $\mathbf{x}$ in $\mathscr{B}$. Based on the previous sections, minimal requirements require that

$$C_1(\mathbf{x}) > 0\,, \quad C_2(\mathbf{x}) > 0\,, \quad G_4(\mathbf{x}) > 0\,, \tag{5.38}$$

and

$$0 < U(\mathbf{x}) < 1\,, \tag{5.39}$$

for all $\mathbf{x}$ in $\mathscr{B}$, almost surely. Following the same methodology as in the previous chapters, we consider the following constraints:

$$\mathbb{E}\{\log(P_j(\mathbf{x}))\} = \varpi_j\,, \quad |\varpi_j| < +\infty\,, \quad j = 1,2, \tag{5.40a}$$
$$\mathbb{E}\{\log(P_3(\mathbf{x}))\} = \zeta_1\,, \quad |\zeta_1| < +\infty\,, \tag{5.40b}$$
$$\mathbb{E}\{\log(1-P_3(\mathbf{x}))\} = \zeta_2\,, \quad |\zeta_2| < +\infty\,, \tag{5.40c}$$
$$\mathbb{E}\{\log(P_4(\mathbf{x}))\} = \varsigma_4\,, \quad |\varsigma_4| < +\infty\,, \tag{5.40d}$$

where it is recalled that $P_1(\mathbf{x}) = C_1(\mathbf{x})$, $P_2(\mathbf{x}) = C_2(\mathbf{x})$, $P_3(\mathbf{x}) = U(\mathbf{x})$ and $P_4(\mathbf{x}) = G_4(\mathbf{x})$ by convention. The above constraints are supplemented with the mean values of the random variables $P_1(\mathbf{x})$, $P_2(\mathbf{x})$ and $P_4(\mathbf{x})$, that is

$$\mathbb{E}\{P_j(\mathbf{x})\} = \underline{c}_j\,, \quad j = 1,2\,, \tag{5.41a}$$
$$\mathbb{E}\{P_4(\mathbf{x})\} = \underline{g}_4\,. \tag{5.41b}$$

It should be noted that the properties $G_1(\mathbf{x}) > 0$ and $G_2(\mathbf{x}) > 0$ readily follow, by construction (see Eqs. (5.32)-(5.33)). For $1 \leqslant i \leqslant 4$, let $(\lambda_i^{(1)}, \lambda_i^{(2)})$ be the Lagrange multipliers with the constraints on the random variable $P_i(\mathbf{x})$, such that $f_{\mathbf{P}(\mathbf{x})}$ is integrable over $\mathbb{R}^4$. In this setting, the MaxEnt-based probability density function $\mathbf{p} \mapsto f_{\mathbf{P}(\mathbf{x})}(\mathbf{p})$ is given by

$$f_{\mathbf{P}(\mathbf{x})}(\mathbf{p}) = \mathbb{1}_{\mathcal{S}_{\mathbf{P}}}(\mathbf{p})\, k_0\, \exp(-\phi(\mathbf{p}))\,, \tag{5.42}$$

where the potential function $\mathbf{p} \mapsto \phi(\mathbf{p})$ writes

$$\begin{aligned}\phi(\mathbf{p}) = {} & \lambda_1^{(1)} p_1 + \lambda_2^{(1)} \log(p_1) + \lambda_1^{(2)} p_2 + \lambda_2^{(2)} \log(p_2) \\ & + \lambda_1^{(3)} \log(p_3) + \lambda_2^{(3)} \log(1-p_3) + \lambda_1^{(4)} p_4 + \lambda_2^{(4)} \log(p_4)\,.\end{aligned} \tag{5.43}$$

Since the indicator function $\mathcal{S}_{\mathbf{P}}$ is separable in the present case, Eqs. (5.42)–(5.43) show that the probability density function $\mathbf{p} \mapsto f_{\mathbf{P}(\mathbf{x})}(\mathbf{p})$ is also separable, so that the random variables $P_1(\mathbf{x}), \ldots, P_4(\mathbf{x})$ are statistically independent. Moreover, and upon performing a change of variable the Lagrange multipliers and the hyperparameters associated with labeled statistical distributions, it can be deduced that:

- For $j = 1$ and $j = 2$, the random variable $P_j(\mathbf{x})$ follows a Gamma distribution with shape and scale parameters defined by $\delta_{C_j}^{-2}$ and $\underline{c}_j \delta_{C_j}^2$, with $\underline{c}_j$ and δ_{C_j} the mean and coefficient of variation of $C_i(\mathbf{x})$.

- The random variable $U(\mathbf{x})$ is distributed according to a Beta distribution, with parameters (ρ_1, ρ_2). By letting δ_U be the coefficient of variation of the random variable U, one has:

$$\underline{u} = \mathbb{E}\{U\} = \frac{\rho_1}{\rho_1 + \rho_2}\,, \quad \delta_U^2 = \frac{\rho_2}{\rho_1(\rho_1 + \rho_2 + 1)}\,. \tag{5.44}$$

- The random parameter $G_4(\mathbf{x})$ also follows a Gamma distribution with shape and scale parameters given by $\delta_{G_4}^{-2}$ and $\underline{g}_4 \delta_{G_4}^2$.

The random variables $C_1(\mathbf{x})$, $C_2(\mathbf{x})$, $U(\mathbf{x})$ and $G_4(\mathbf{x})$ are then defined as nonlinear transformations of standard Gaussian fields, such that the target first-order marginal probability density functions are obtained, that is

$$C_j(\mathbf{x}) = \mathfrak{a}(\Xi_j(\mathbf{x}); k_j, \theta_j)\,, \quad k_j = \delta_{C_j}^{-2}\,, \quad \theta_j = \underline{c}_j \delta_{C_j}^{-2}\,, \quad j = 1, 2\,, \tag{5.45a}$$

$$U(\mathbf{x}) = \mathfrak{b}(\Xi_3(\mathbf{x}); \rho_1, \rho_2)\,, \tag{5.45b}$$

$$G_4(\mathbf{x}) = \mathfrak{a}(\Xi_4(\mathbf{x}); k_4, \theta_4)\,, \quad k_4 = \delta_{G_4}^{-2}\,, \quad \theta_4 = \underline{g}_4 \delta_{G_4}^2\,, \tag{5.45c}$$

where

$$\mathfrak{a}(u; k, \alpha) = \mathcal{F}^{-1}_{\Gamma(k,\alpha)}(\mathcal{F}_{\mathcal{N}}(u)) \tag{5.46}$$

and

$$\mathfrak{b}(u; \rho_1, \rho_2) = \mathcal{F}^{-1}_{\mathcal{B}(\rho_1,\rho_2)}(\mathcal{F}_{\mathcal{N}}(u)) \tag{5.47}$$

with $\mathcal{F}^{-1}_{\Gamma(k,\alpha)}$ the inverse cumulative distribution function (i.c.d.f) of the Gamma distribution, $\mathcal{F}^{-1}_{\mathcal{B}(\rho_1,\rho_2)}$ is the i.c.d.f. of the Beta distribution and $\mathcal{F}_{\mathcal{N}}$ is the cumulative distribution of the normal distribution.

The nonlinear transformation $\mathcal{H}$ introduced in Eq. (5.36) is thus completely defined by Eqs. (5.45a)–(5.45c), and the stochastic stored energy function is defined by combining Eqs. (5.23), (5.24), (5.31) and (5.33). By construction, the random fields $\{C_1(\mathbf{x}), \mathbf{x} \in \mathscr{B}\}$, $\{C_2(\mathbf{x}), \mathbf{x} \in \mathscr{B}\}$, $\{U(\mathbf{x}), \mathbf{x} \in \mathscr{B}\}$ and $\{G_4(\mathbf{x}), \mathbf{x} \in \mathscr{B}\}$ are statistically independent. However, the random fields $\{G_1(\mathbf{x}), \mathbf{x} \in \mathscr{B}\}$ and $\{G_2(\mathbf{x}), \mathbf{x} \in \mathscr{B}\}$ end up being dependent while $\{G_3(\mathbf{x}), \mathbf{x} \in \mathscr{B}\}$ and $\{G_4(\mathbf{x}), \mathbf{x} \in \mathscr{B}\}$ remain independent from all other random fields. It should be emphasized that the hyperparameters of the labeled probability distributions are spatially dependent if the right-hand sides in the constraints given by Eq. (5.40) are chosen as spatially dependent. In the next section, a sampling algorithm for the proposed random field model is presented.

5.4 Sampling the random field model on complex domains

Within the proposed framework, realizations of the stochastic strain energy function can be obtained by generating realizations of the Gaussian random field $\{\boldsymbol{\Xi}(\mathbf{x}), \mathbf{x} \in \mathscr{B}\}$. When the domain $\mathscr{B}$ is homotopic to a simple (or simplified) geometry, such as a sphere, covariance models (satisfying some symmetry or periodicity properties) for the Gaussian field can easily be constructed, motivated by experimental data or selected in suitable classes of covariance kernels. Standard sampling techniques, including direct or iterative factorization methods [175] and spectral approaches [176] can be applied in order to generate independent realizations of the random field.

In this work, we focus on the more intricate situation where the reference configuration $\mathscr{B}$ is not homotopic to a sphere and involves boundaries defined by arbitrary smooth manifolds. In order to handle this issue, and following [177], our approach relies on defining each random

field $\{\Xi_j(\mathbf{x}), \mathbf{x} \in \mathscr{B}\}$ as the solution (see [178, 179]) of the spatial stochastic partial differential equation (SPDE)

$$[\gamma^2(\mathbf{x}) - \langle \boldsymbol{\nabla}, [H(\mathbf{x})]\boldsymbol{\nabla}\rangle]^{\zeta/2}\Xi_j(\mathbf{x}) = \dot{\mathscr{W}}(\mathbf{x}), \quad \mathbf{x} \in \mathscr{B}, \tag{5.48}$$

where $\gamma(\mathbf{x}) > 0$ is parameter controlloing the correlation range, $[H(\mathbf{x})]$ is a so-called positive-definite diffusion matrix, $\zeta \in \mathbb{N}_*^+$ and $\{\mathscr{W}(\mathbf{x}), \mathbf{x} \in \mathscr{B}\}$ is the spatial normalized Gaussian white noise. In three-dimensional applications, the integer ζ satisfies the relation $\zeta = \nu + 3/2$, where $\nu > 0$ controls the smoothness of the solution. When the SPDE is analytically solved over $\mathbb{R}^3$, the complete class of Matérn covariance kernels (which include the widely used exponential or square-exponential kernels) can be recovered, and the solution field can be shown to be $[\nu - 1]$ differentiable. The definition of the diffusion field $\mathbf{x} \mapsto [H(\mathbf{x})]$ is of primary importance in the proposed methodology, since it allows an ad-hoc covariance structure to be defined, even though in a non-explicit form, on the complex geometry under consideration. In what follows, we let $\{\mathbf{x} \mapsto \hat{\mathbf{e}}_i(\mathbf{x})\}_{i=1}^3$ be a local orthonormal basis that can capture, for instance, the features of the considered geometry. The diffusion tensor is further decomposed as

$$[H(\mathbf{x})] = \sum_{i=1}^{3} \hat{\tau}_i \, \hat{\mathbf{e}}_i(\mathbf{x}) \otimes \hat{\mathbf{e}}_i(\mathbf{x}), \quad \forall \mathbf{x} \in \mathscr{B}, \tag{5.49}$$

where $\{\hat{\tau}_i\}_{i=1}^3$ is a set of strictly positive parameters controlling the magnitude of the local anisotropy. Illustrative two-dimensional examples can be found in [178, 179] for stationary and non-stationary cases, and a detailed application of this strategy to vascular vessels in presented below. Herein, the value $\nu = 1/2$ is selected (hence, $\zeta = 2$), so that a classical Galerkin method can be used to solve the weak formulation of the SPDE with homogeneous natural boundary conditions. More specifically, we let $\mathcal{B}_h$ be the domain occupied by a finite element mesh of the reference configuration, made of n_d nodes and such that $\mathscr{B}_h = \cup_{e=1}^{n_e} \mathscr{B}_e$ with n_e the number of finite elements. For notational convenience, no distinction will be made between the Gaussian field $\{\Xi_j(\mathbf{x}), \mathbf{x} \in \mathscr{B}\}$ and the stochastic weak solution $\{\Xi_j^h(\mathbf{x}), \mathbf{x} \in \mathscr{B}_h\}$ of the SPDE which takes the form

$$\Xi_j(\mathbf{x}) = \sum_{i=1}^{n_d} \eta_i \psi_i(\mathbf{x}), \tag{5.50}$$

where $\{\psi_i\}_{i=1}^{n_d}$ is the set of finite element shape functions consisting of piece-wise linear functions. It can then be shown that the weights $\eta_1, \ldots, \eta_{n_d}$ are distributed according to a Gaussian distribution such that the random vector $\boldsymbol{\eta} = (\eta_1, \ldots, \eta_{n_d})$ is centered and exhibits a covariance matrix denoted by $[Q]^{-1}$, where $[Q]$ is the precision matrix defined as

$$[Q] = ([M] + [K])^T [N]^{-1} ([M] + [K]). \tag{5.51}$$

In the above equation, the $(n_d \times n_d)$ matrices $[M]$, $[K]$ and $[N]$ are defined components-wise as

$$M_{ij} = \int_{\mathscr{B}} \gamma^2(\mathbf{x}) \psi_i(\mathbf{x}) \psi_j(\mathbf{x}) \, \mathrm{d}\mathbf{x}, \quad K_{ij} = \int_{\mathscr{B}} \langle \boldsymbol{\nabla}\psi_i(\mathbf{x}), [H(\mathbf{x})]\boldsymbol{\nabla}\psi_j(\mathbf{x})\rangle \, \mathrm{d}\mathbf{x}, \tag{5.52}$$

for $1 \leqslant i, j \leqslant n_d$, and

$$N_{ij} = \int_{\mathscr{B}} \psi_i(\mathbf{x}) \psi_j(\mathbf{x}) \, \mathrm{d}\mathbf{x}. \tag{5.53}$$

While the above matrices are sparse, it can be seen form Eq. (5.51) that the precision matrix $[Q]$ turns out to be full and consequently, the computation of its Cholesky factorization may

be expensive in practice. In order to circumvent this issue, one may alternatively consider the following sparse approximation

$$[\widehat{Q}] = ([M] + [K])^T [\widehat{N}]^{-1} ([M] + [K]) \,, \tag{5.54}$$

where $[\widehat{N}]$ is the diagonal matrix with entries $\widehat{N}_{ii} = \sum_{j=1}^{n_d} N_{ij}$, $1 \leqslant i \leqslant n_d$. This approximation is sometimes referred to as a lumped matrix in computational mechanics. Realizations of the Gaussian field $\{\Xi_j(\mathbf{x}), \mathbf{x} \in \mathscr{B}\}$ are then obtained by sampling the random vector $\boldsymbol{\eta}$ according to the centered Gaussian distribution with covariance matrix $[\widehat{Q}]^{-1}$. In this setting, the stochastic weak solution to the SPDE is a Gaussian Markov approximation which exhibits the same convergence rate as the solution obtained with the full precision matrix $[Q]$ [177].

A few comments regarding the pros and cons of the aforementioned method are relevant at this point. First of all, the stochastic solver of the SPDE involves a finite element mesh which may coincide with the mesh related to the nonlinear mechanical problem, hence allowing for substantial computational savings when complex geometries are considered. In contrast with classical methods where the Gaussian field is sampled at the $n_d \times n_g$ Gauss integration points (with n_g the number of integration points within each element), this approach generates samples at the n_d nodes of the finite element mesh. Moreover, such a sampling strategy does not involve the storage of the full covariance matrix and can thus accommodate very large and dense meshes. Since the precision matrix $[\widehat{Q}]$ is sparse, fast factorization techniques can also be employed while sampling the random vector $\boldsymbol{\eta}$. Regarding drawbacks, one may first notice that the analytical form of the covariance kernel is unknown for bounded domains and/or spatially-dependent parameter fields. Furthermore, and as reported in [177, 178, 179], variance fluctuations may be observed while sampling for bounded domains or when resorting on heterogeneous diffusion fields. In this case, the solution must be subsequently rescaled in order to ensure a zero mean and unit variance. Another widely used approach to handle this issue is to embed to finite element mesh into a larger domain. Finally, the sparse inverse approximation $[\widehat{N}]^{-1}$ of the matrix $[N]$ can be shown to be singular for piecewise quadratic interpolations in two- and three-dimensional applications, so that other non-singular sparse inverse approximation for $[N]^{-1}$ must be introduced in this case.

We end this section by providing a simple pseudo-code for generating samples of the random vector $\boldsymbol{\eta}$ and by considering the particular case of a stationary SPDE.

5.4.1 Case of a stationary stochastic partial derivative equation

Consider the SPDE with $\zeta = 2$ but no longer restricted to $\mathscr{B} \subset \mathbb{R}^3$. If in addition the parameter $\mathbf{x} \mapsto \gamma(\mathbf{x})$ and the diffusion tensor $\mathbf{x} \mapsto [H(\mathbf{x})]$ are constant over $\mathbb{R}^3$, say $\gamma(\mathbf{x}) = \gamma$ and $[H(\mathbf{x})] = [H]$ for all $\mathbf{x} \in \mathscr{B}$, then the SPDE writes

$$[\gamma - \langle \boldsymbol{\nabla}, [H] \boldsymbol{\nabla} \rangle] \, \Xi_j(\mathbf{x}) = \dot{\mathscr{W}}(\mathbf{x}) \,, \quad \mathbf{x} \in \mathbb{R}^3 \,, \tag{5.55}$$

where $\{\dot{\mathscr{W}}(\mathbf{x}), \mathbf{x} \in \mathbb{R}^3\}$ is a spatial white noise over $\mathbb{R}^3$ with spectral density $1/(2\pi)^3$. In this case, the solution of the stochastic partial derivative equation is stationary and its power spectral density writes

$$S_j(\boldsymbol{\omega}) = \frac{1}{(2\pi)^3} \frac{1}{\gamma^2 + \langle \boldsymbol{\omega}, [H] \boldsymbol{\omega} \rangle} . \tag{5.56}$$

The associated covariance function is then given by

$$R_j(\mathbf{x}, \mathbf{y}) = \frac{1}{8\pi\gamma\sqrt{\det([H])}} \exp\left(-\gamma \| [H]^{-1/2} (\mathbf{x} - \mathbf{y}) \| \right) , \tag{5.57}$$

for $\mathbf{x}$ and $\mathbf{y}$ in $\mathbb{R}^3$. It is readily seen that a unit variance can be obtained by setting

$$\gamma = \frac{1}{8\pi\sqrt{\det([H])}}\,. \tag{5.58}$$

Furthermore, if the diffusion tensor writes $[H] = \sum_{i=1}^{3} \tau_i \hat{\mathbf{e}}_i \otimes \hat{\mathbf{e}}_i$ where the basis $\{\hat{\mathbf{e}}_i\}_{i=1}^{3}$ is constant over $\mathbb{R}^3$, then

$$R_j(\mathbf{x},\mathbf{y}) = \frac{1}{8\pi\gamma\sqrt{\tau_1\tau_2\tau_3}} \exp\left(-\gamma \sum_{i=1}^{3} \left(\frac{(\hat{y}_i - \hat{x}_i)^2}{\tau_i}\right)^{1/2}\right), \tag{5.59}$$

where $\hat{x}_i = \langle \mathbf{x}, \hat{\mathbf{e}}_i \rangle$ and $\hat{y}_i = \langle \mathbf{y}, \hat{\mathbf{e}}_i \rangle$. When the covariance function is evaluated for any $\mathbf{x} = \overline{x}\hat{\mathbf{e}}_\ell$ and $\mathbf{y} = \overline{y}\hat{\mathbf{e}}_\ell$ with $\ell \in \{1,2,3\}$, one has

$$R_j(\overline{x}\,\hat{\mathbf{e}}_\ell, \overline{y}\,\hat{\mathbf{e}}_\ell) = \frac{1}{8\pi\gamma\sqrt{\tau_1\tau_2\tau_3}} \exp\left(-\frac{\gamma}{\sqrt{\tau_\ell}}|\overline{y} - \overline{x}|\right), \tag{5.60}$$

whence the quantity $\mathfrak{L}_\ell = \sqrt{\tau_\ell}/\gamma$ can be interpreted as the correlation length associated with the direction $\hat{\mathbf{e}}_\ell$.

Algorithm 5.4.1. *A simple algorithm for generating n_r realizations $\{\xi_k(\mathbf{x},\theta_j), \mathbf{x} \in \mathscr{B}\}$, $1 \leqslant j \leqslant n_r$, of the Gaussian field $\{\Xi_k(\mathbf{x}), \mathbf{x} \in \mathscr{B}\}$ can be constructed as follows. Let $[Z]$ be the matrix gathering n_r independent realizations $\mathbf{z}(\theta_1), \ldots, \mathbf{z}(\theta_{n_r})$ of a Gaussian random variable $\mathbf{Z} \sim \mathcal{N}(\mathbf{0}, [I_{n_d}])$ with values in $\mathbb{R}^{n_d}$ and given component-wise as $Z_{ij} = z_i(\theta_j)$ for $1 \leqslant i \leqslant n_d$ and $1 \leqslant j \leqslant n_r$. Similarly let B be the matrix gathering the n_d realizations of the Gaussian field $\{\Xi_k(\mathbf{x}), \mathbf{x} \in \mathscr{B}\}$ and such that*

$$B_{ij} = \xi_k(\mathbf{x}^{(i)}, \theta_j) \quad 1 \leqslant i \leqslant n_d\,, \quad 1 \leqslant j \leqslant n_r\,, \tag{5.61}$$

where $\mathbf{x}^{(i)}$ is the i-th node of the triangulation $\mathscr{B}_h$. The sparse precision matrix $[\widehat{Q}]$ being positive definite, it can be decomposed as $[\widehat{Q}] = [L]^T[L]$ where $[L]$ denote its Cholesky factorization. The matrix $[B]$ is then defined as the solution of the linear system of equations (see e.g [180])

$$[L][B] = [Z]\,. \tag{5.62}$$

5.5 Uncertainty quantification in mechanics of arterial walls

This section is concerned with uncertainty modeling and propagation for soft biological tissues with a specific emphasis on the mechanics of vascular vessels [104]. Soft biological tissues are known for exhibiting large uncertainties which can be due to various sources such as age, gender or diseases (see, *e.g.*, [181, 18] for experimental evidences). Although arterial walls are seen as a three-layer structure, with each layer being composed of an isotropic ground matrix reinforced by families of collagen fibers, we restrict our analysis to the modeling of the intermediate layer, namely the media. In this work, Monte Carlo simulations are used as the stochastic solver (see [2] for a broad survey on uncertainty propagation, as well as [182] for the development of accelerated Monte Carlo methods). The stochastic boundary value problems were solved with a parallel finite element solver and the reader is referred to the Annexes A–B for more details in this regard. The reminder of this section is organized as follows. First, in Section 5.5.1, the histology of arterial walls is briefly described in order to highlight the modeling issues. The particular case of a homogeneous media strip under tension is considered in Section 5.5.2. Forward simulations are performed in order to get an insight about the influence of the model hyperparameters on the variability of the stress response. In Section 5.5.3, heterogeneous media strips are considered to investigate the impact on the correlation structure. Finally, an application to an arterial wall defined by a patient-specific geometry is presented in Section 5.5.4.

5.5.1 Histology of arteries

We start by briefly introducing the histology of human arteries [183] and some terminologies that will be used throughout this chapter. More detailed exposures can be found in, *e.g.*, [104, 161, 184, 162]. Herein, we are concerned with the modeling of elastic arteries, such as the aorta, which are close to the heart and have a large diameter. They differ from muscular arteries which exhibit a viscoelastic behavior and can be found, for instance, in the brain. As shown in Fig. 5.1, the structure of a healthy elastic arterial wall is composed of three layers, namely the *intima*, *media*, and *adventitia* (also referred to as *tunica externa*). The *intima* is a thin layer mainly made of endothelial cells that form an interface between the arterial wall and the blood flow. This layer is mechanically irrelevant in the case of healthy elastic arteries, whereas it is relatively thick in muscular arteries. The middle layer, namely the *media*, is made of a complex network of muscle cells, elastin and collagen fibers. It is the primary constituent of elastic arteries due to its thickness and ability to resist to longitudinal and circumferential loads. The *adventitia* is the outermost layer which is made of thick bundles of collagen fibers. From a mechanical standpoint, the media and adventitia are generally seen as a ground matrix, represented by the elastin network, reinforced by families of collagen fibers with some given preferred directions. Recent experimental characterization of the fibers distributions can be found in, e.g., [185, 186, 187, 188, 189] and a volume-rending of optical section through an entire aortic wall is shown in the right panel of Fig. 5.1. It can be seen that arterial walls have a complex

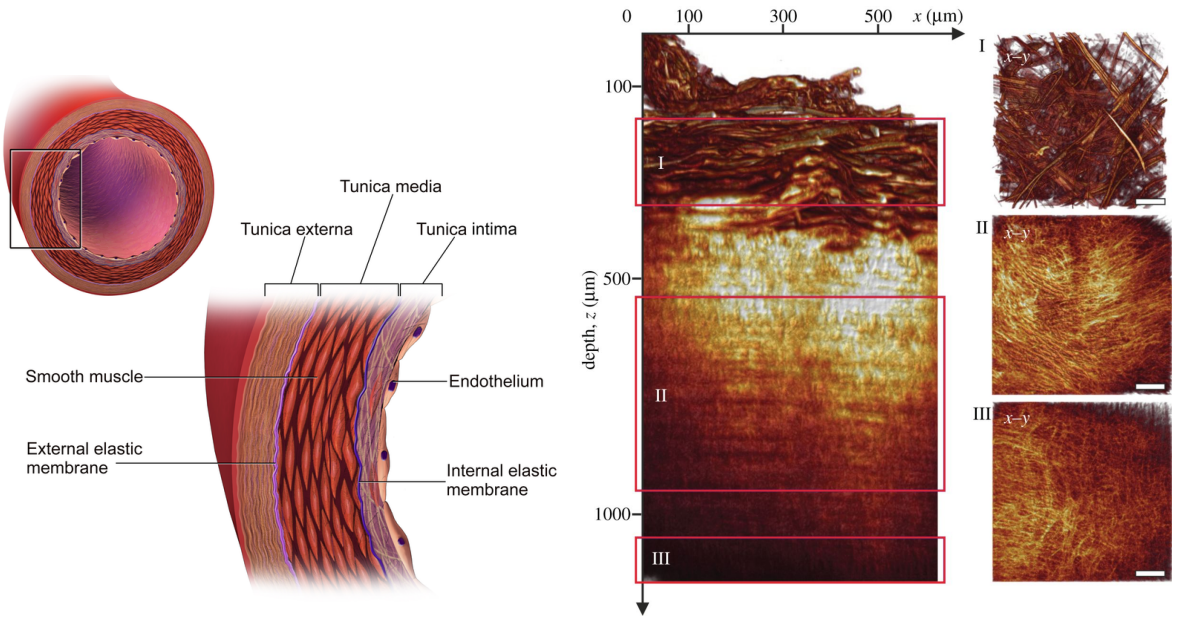

Figure 5.1 – Left panel: structure of a healthy elastic arterial wall [190]. Right panel: radial projection throughout the thickness of the arterial wall with closer views on the *adventitia*, *media* and *intima* [191].

microstructure with fibers dispersions varying with respect to the depth in the thickness, and in particular, the identification of the number of families of fibers is still an active research field. These soft biological tissues are very prone to uncertainties raised by various sources including age, gender and health state (see [181, 192] for experimental evidences). Stress responses in the longitudinal and circumferential directions are shown in Fig. 5.2 for thirteen samples of the adventitia, media and intima coming from different patients. For applications where the

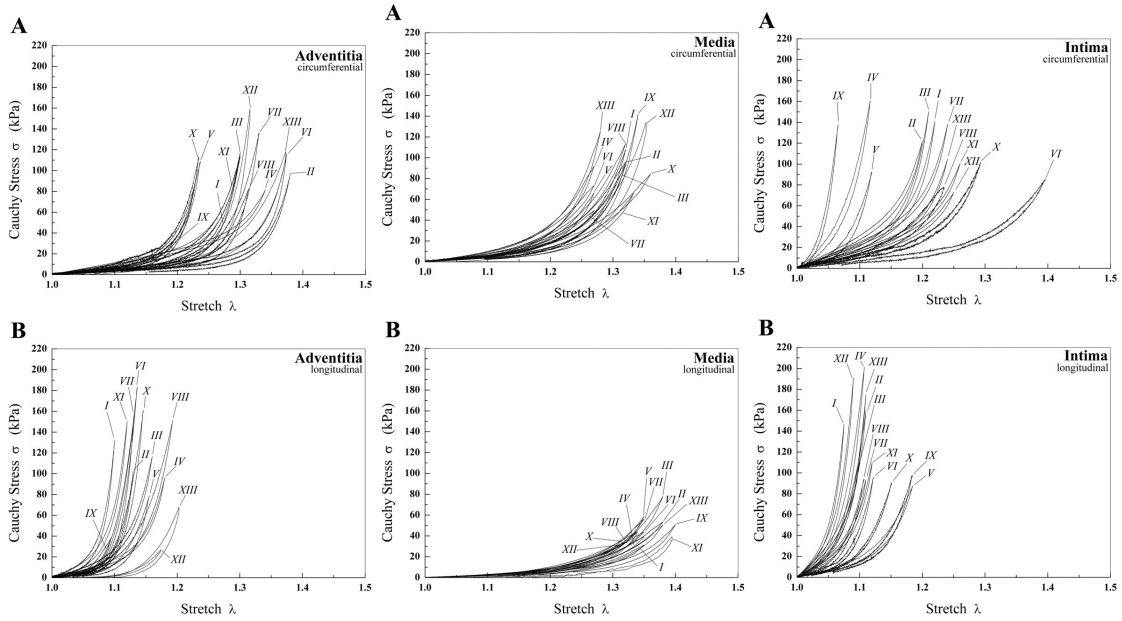

Figure 5.2 – Stress responses of uniaxial tensile tests for thirteen samples of *adventitia* (left), *media* (middle) and *intima* (right) [18].

constitutive model of the wall plays an important role (such as in the computational study of atherosclerosis evolution [193] and failure for vascular grafts, for which compliance mismatch was reported to generate postoperative complications [194, 195]; see [196] for a complementary discussion), such intrinsic variability must be taken into account in numerical simulations.

5.5.2 Case of homogeneous strips

In this first illustration, a homogeneous media strip undergoing a simple tensile test is considered. In this particular case, where only random variables are involved instead of random fields, the stochastic parameters are easily sampled by using standard algorithms for univariate probability distributions. It is assumed that the two preferred directions defining the anisotropic contributions in the stochastic stored energy function are defined as

$$\mathbf{a}_1 = \cos(\alpha)\mathbf{e}_1 + \sin(\alpha)\mathbf{e}_2\,, \quad \mathbf{a}_2 = \cos(\alpha)\mathbf{e}_1 - \sin(\alpha)\mathbf{e}_2\,, \tag{5.63}$$

where $\mathbf{e}_1$ and $\mathbf{e}_2$ span the median plane of the strip. The mean values of the random variables, the deterministic exponents β_3 and β_4 and the angle α are identified by solving a least-square optimization problem. The relative error between the mean Cauchy stress and the experimental data provided in [192] is minimized and a nearly incompressible solution is obtained by adding a classical penalty term in the objective function. The obtained mean parameters are given by $\underline{g}_1 = 4.1543$, $\underline{g}_2 = 2.5084$, $\underline{g}_3 = 9.7227$ and $\underline{g}_4 = 19.285$ in kPa. The values for the remaining deterministic parameters were obtained as $\beta_3 = 3.6537$, $\beta_4 = 500.02$ and $\alpha = 46.274$ (in degrees). By using the consistency relations with linearized elasticity, it is found that the mean values of the bulk and shear moduli of the isotropic elasticity tensor are given by $\underline{c}_1 = 259.59$ and $\underline{c}_2 = 21.343$ in kPa. Furthermore, note that the Lagrange multipliers associated with the random variable U must satisfy the relations

$$\rho_1 = \frac{2\underline{g}_1}{3^{3/2}\underline{g}_2}\rho_2\,, \quad \rho_2 = \frac{1-\delta_U^2}{\eta(1+\eta)\delta_U^2}\,, \tag{5.64}$$

where $0 < \delta_U < 1$ is the coefficient of variation of U, hence leaving ρ_2 as the only free hyper-parameter in the probability density function of U. In order to illustrate the influence of the statistical fluctuations of the random variables, we proceed as in the previous chapters and compute realizations of the random Cauchy stress by combining analytical derivations with Monte Carlo simulations. The confidence region at 90% is shown in Fig. 5.3 for $\delta_{C_1} = \delta_{G_4} = \delta_U = 0.1$ and increasing values of the coefficient of variation δ_{C_2}. In order to facilitate interpretation, the evolution of the confidence region when the coefficients of variation of all input random variables are set to the same value is also shown in Fig. 5.3 (right panel). In this case, all random variables exhibit larger fluctuations, hence making the variability much larger.

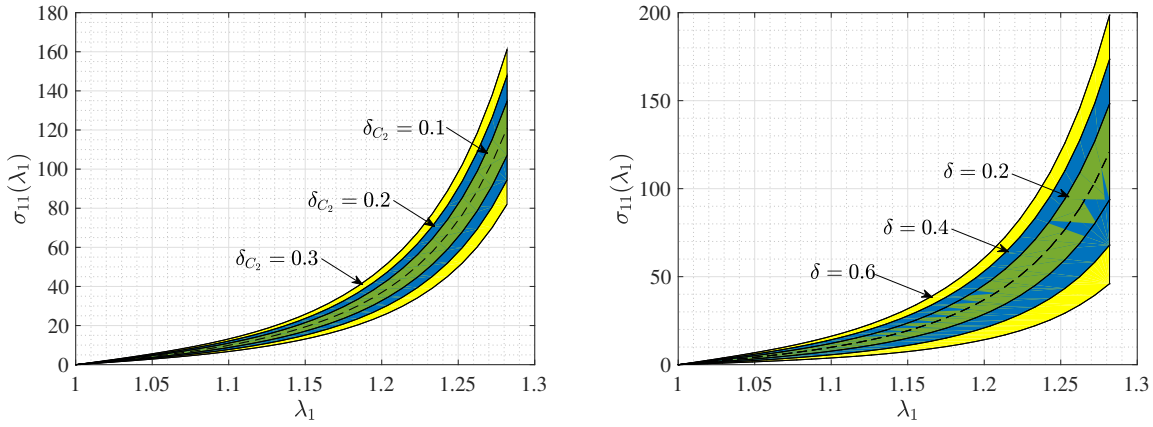

Figure 5.3 – Confidence regions (at a 90% probability level) of the Cauchy stress for a uniaxial tensile test along the circumferential direction of the strip. Left panel: $\delta_{C_1} = \delta_{G_4} = \delta_U = 0.1$, $\delta_{C_2} \in \{0.1, 0.2, 0.3\}$. Right panel: $\delta_{C_1} = \delta_{G_4} = \delta_U = \delta_{C_2} = \delta \in \{0.2, 0.4, 0.6\}$. The mean responses are represented in dashed lines.

These results provide an assessment about the capability of the stochastic model associated with the first-order marginal probability distribution to faithfully reproduce variability in the stress response and are in accordance with previous results derived for isotropic hyperelastic materials.

5.5.3 Case of heterogeneous strips

In this second illustration, numerical simulations of tensile tests on heterogeneous media strips are carried out. Following the computational framework discussed in [161], media strips of length $l_{\text{strip}} = 10$ mm, width $w_{\text{strip}} = 3$ mm and thickness $t_{\text{strip}} = 0.5$ mm are considered. A displacement is prescribed at the top end of the specimens, while the bottom is totally clamped. The mean parameters obtained in Section 5.5.2 are retained as the mean values of the random field $\{\mathbf{G}(\mathbf{x}), \mathbf{x} \in \mathscr{B}\}$, and the preferred directions are given by Eq. (5.63). The SPDE approach described in Section 5.4 is used for sampling purposes, and the diffusion tensor is chosen as homogeneous over $\mathscr{B}$. More precisely, the tensor $[H]$ is written as

$$[H] = \kappa[I_3] + \tau_1[M_1] + \tau_2[M_2]\,, \tag{5.65}$$

regardless of the Gaussian field under consideration, with $[M_\ell] = \mathbf{a}_\ell \otimes \mathbf{a}_\ell$ for $\ell = 1, 2$. The parameters κ, τ_1 and τ_2 involved in the diffusion tensor can be properly selected in order to adjust the anisotropy of the correlation structure inherited by the Gaussian random fields. The

same coefficient of variation δ is considered for all the random fields and the remaining parameters κ, τ_1 and τ_2 are chosen as $\kappa = 0.1$, $\tau_1 = \tau_2 = 10$. Realizations of the Cauchy stress along the loading direction are shown in Figs. 5.4 and 5.5 for $\gamma \in \{1, 10\}$ and $\delta \in \{0.1, 0.2\}$. These figures show how the stochastic fluctuations of the random parameters impact the random stress field. Moreover, it is seen that increasing the parameter γ reduces the correlation range of the random fields and the random stress field, for a given set of boundary conditions.

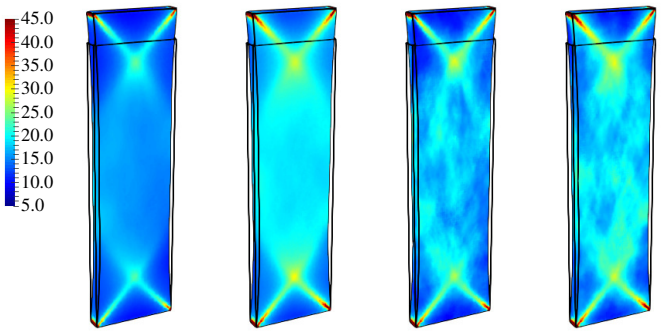

Figure 5.4 – Two realizations of the Cauchy stress [MPa] along the loading direction for $\delta = 10\%$, $\gamma = 1$ (left samples) and $\gamma = 10$ (right samples).

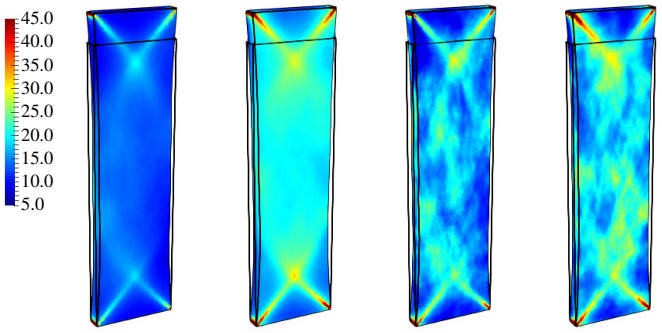

Figure 5.5 – Two realizations of the Cauchy stress [MPa] along the loading direction for $\delta = 20\%$, $\gamma = 1$ (left samples) or $\gamma = 10$ (right samples).

5.5.4 Case of a patient-specific arterial wall

In this last application, the case of an arterial wall composed by the media layer and defined by a patient-specific geometry is considered. The arterial wall is submitted to an inner pressure mimicking the blood pressure. Computational aspects related to the finite element implementation for such simulation can be found in, *e.g.*, [141, 109]. The geometry of the inner surface, referred to as the lumen, was extracted from the database [197] in the form of a STL file (ID:0098). The finite element mesh of the media layer was then generated following the methodology proposed in [198] which relies on the Vascular Modelling Toolkit [199] and the meshing software GMSH [200]. This resulting mesh is shown in Fig. 5.6 is approximatively 12 mm long and consists of

297 828 cells and 432 250 nodes, leading to a total of 1 296 750 degrees of freedom. As in Section 5.5.3, the mean stochastic stored energy function is obtained by using the parameters fitted in Section 5.5.2. The main ingredient of the methodology is the definition of the diffusion tensor $\mathbf{x} \mapsto [H(\mathbf{x})]$, which allows for sampling on the complex geometry defining the arterial wall. A methodology to achieve such a construction is introduced in the next section.

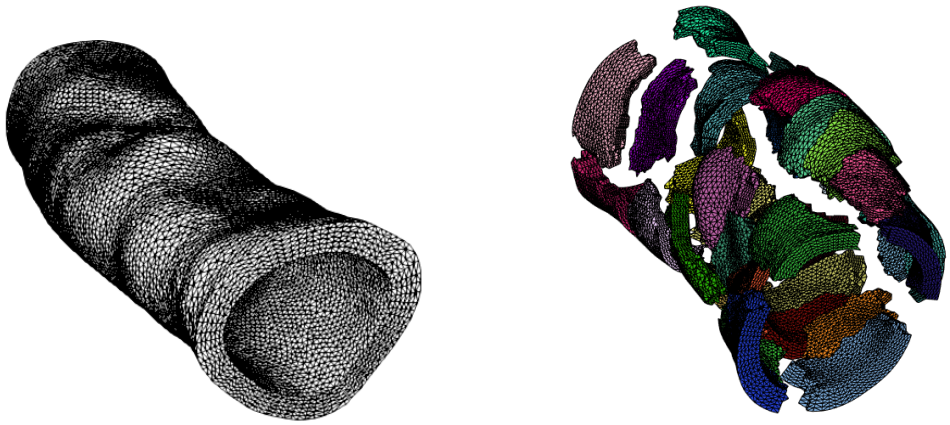

Figure 5.6 – Mesh of the patient-specific geometry in its reference configuration and its partition into 32 subdomains for the parallel finite element solver.

5.5.4.1 Definition of the diffusion field on the arterial wall

At every location $\mathbf{x}$ of the reference configuration $\mathscr{B}$, the definition of a local basis $\{\hat{\mathbf{e}}_i(\mathbf{x})\}_{i=1}^3$ and the preferred directions $\{\mathbf{a}_\ell(\mathbf{x})\}_{\ell=1}^2$ can be performed by having recourse to the Laplace-Dirichlet Rule-Based (LDBR) algorithm proposed in [201] for the myocardium and adapted for deterministic simulations on arteries in [172]. In this approach, two auxiliary Laplace boundary value problems are introduced in order to define local fields, denoted by $\mathbf{x} \mapsto \Psi_1(\mathbf{x})$ and $\mathbf{x} \mapsto \Psi_2(\mathbf{x})$, respectively, the gradient fields of which can be related to the aforementioned local basis and preferred directions. More precisely, the field $\mathbf{x} \mapsto \Psi_1(\mathbf{x})$ is defined as the solution of the following Laplace boundary value problem:

$$\begin{aligned} &\langle \boldsymbol{\nabla}, \boldsymbol{\nabla} \rangle \Psi_1(\mathbf{x}) = 0\,, \quad \mathbf{x} \in \mathscr{B}\,, \\ &\langle \boldsymbol{\nabla} \Psi_1(\mathbf{x}), \mathbf{n} \rangle = 0\,, \quad \mathbf{x} \in \Gamma_{\text{inner}} \cup \Gamma_{\text{outer}}\,, \end{aligned} \tag{5.66}$$

supplemented with the essential boundary conditions $\Psi_1(\mathbf{x}) = 0$ on Γ_{inlet} and $\Psi_1(\mathbf{x}) = 0$ on Γ_{outlet}. Similarly, Ψ_2 is seen as the solution of

$$\begin{aligned} &\langle \boldsymbol{\nabla}, \boldsymbol{\nabla} \rangle \Psi_2(\mathbf{x}) = 0\,, \quad \mathbf{x} \in \mathscr{B}\,, \\ &\langle \boldsymbol{\nabla} \Psi_2(\mathbf{x}), \mathbf{n} \rangle = 0\,, \quad \mathbf{x} \in \Gamma_{\text{inlet}} \cup \Gamma_{\text{outlet}}\,, \end{aligned} \tag{5.67}$$

with the essential conditions $\Psi_2(\mathbf{x}) = 0$ on Γ_{inner} and $\Psi_2(\mathbf{x}) = 0$ on Γ_{outer}. The above boundary value problems are solved with a standard finite element method using quadratic tetrahedra with 10 nodes as finite elements. The numerical solutions $\{\Psi_1^h(\mathbf{x}), \mathbf{x} \in \mathscr{B}\}$ and $\{\Psi_2^h(\mathbf{x}), \mathbf{x} \in \mathscr{B}\}$ are depicted in Fig. 5.7.

For a given $\mathbf{x}$ in $\mathscr{B}$, the local basis is next defined as

$$\hat{\mathbf{e}}_1(\mathbf{x}) = \frac{\boldsymbol{\nabla} \Psi_1^h(\mathbf{x})}{\|\boldsymbol{\nabla} \Psi_1^h(\mathbf{x})\|}\,, \quad \hat{\mathbf{e}}_2(\mathbf{x}) = \hat{\mathbf{e}}_1(\mathbf{x}) \times \hat{\mathbf{e}}_3(\mathbf{x})\,, \quad \hat{\mathbf{e}}_3(\mathbf{x}) = \frac{\boldsymbol{\nabla} \Psi_2^h(\mathbf{x})}{\|\boldsymbol{\nabla} \Psi_2(\mathbf{x})\|}\,, \tag{5.68}$$

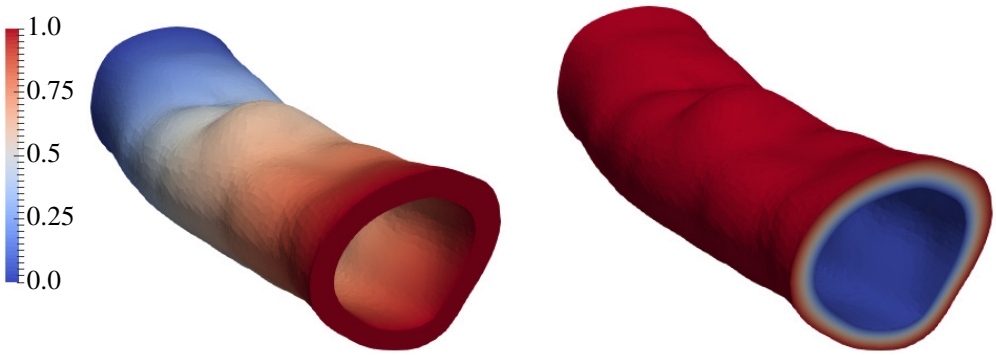

Figure 5.7 – Graph of the finite element solutions $\mathbf{x} \mapsto \Psi_1^h(\mathbf{x})$ and $\mathbf{x} \mapsto \Psi_2^h(\mathbf{x})$.

and the plots of the vector fields $\mathbf{x} \mapsto \hat{\mathbf{e}}_1(\mathbf{x})$ and $\mathbf{x} \mapsto \hat{\mathbf{e}}_2(\mathbf{x})$ thus defined are shown in Fig. 5.8. For any $\mathbf{x}$ in $\mathscr{B}$, the preferred directions (defining the local anisotropic contribution) are finally expressed as

$$\mathbf{a}_1(\mathbf{x}) = \cos(\alpha)\hat{\mathbf{e}}_1(\mathbf{x}) + \sin(\alpha)\hat{\mathbf{e}}_2(\mathbf{x})\,, \quad \mathbf{a}_2(\mathbf{x}) = \cos(\alpha)\hat{\mathbf{e}}_1(\mathbf{x}) - \sin(\alpha)\hat{\mathbf{e}}_2(\mathbf{x})\,. \tag{5.69}$$

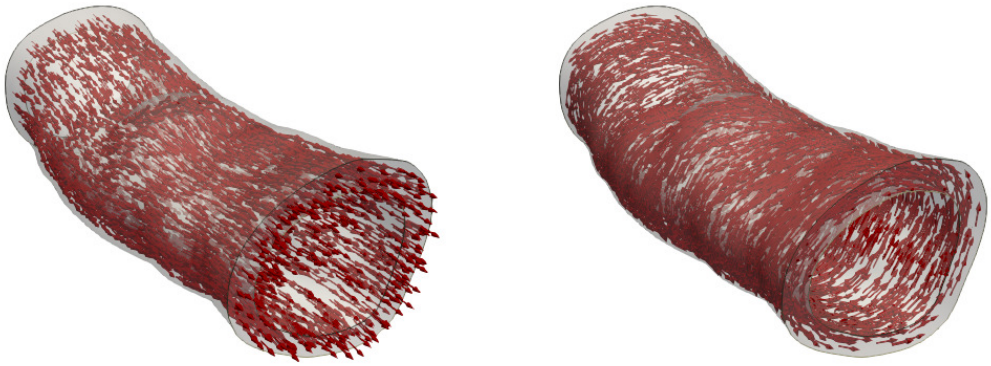

Figure 5.8 – Local directions $\mathbf{x} \mapsto \hat{\mathbf{e}}_1(\mathbf{x})$ (left) and $\mathbf{x} \mapsto \hat{\mathbf{e}}_2(\mathbf{x})$ (right) at uniformly distributed positions in the media.

5.5.4.2 Characterization of covariance kernels on manifolds

Based on the definition of the local basis addressed in the previous section, we now investigate through numerical experiments some covariance kernels that can be generated with the SPDE approach. Without loss of generality, the stochastic properties of interest are characterized by considering the Gaussian field $\{\Xi_1(\mathbf{x}), \mathbf{x} \in \mathscr{B}\}$. The field of diffusion tensor is first defined as

$$[H(\mathbf{x})] = \sum_{i=1}^{3} \hat{\tau}_i\, \hat{\mathbf{e}}_i(\mathbf{x}) \otimes \hat{\mathbf{e}}_i(\mathbf{x})\,, \quad \forall \mathbf{x} \in \mathscr{B}\,, \tag{5.70}$$

where $\hat{\tau}_1$, $\hat{\tau}_2$ and $\hat{\tau}_2$ are strictly positive parameters controlling the local anisotropy of the correlation structure. The plot of covariance function, estimated with $4,000$ independent realizations of the random field (and with respect to a given reference point on the outer surface), and one

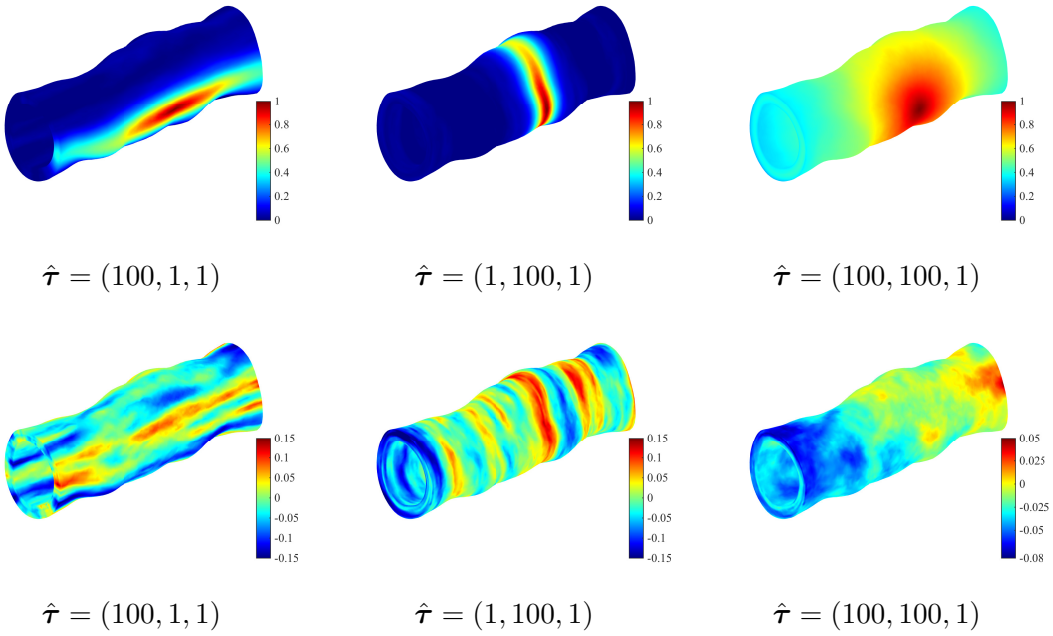

$\hat{\boldsymbol{\tau}} = (100, 1, 1)$ $\hat{\boldsymbol{\tau}} = (1, 100, 1)$ $\hat{\boldsymbol{\tau}} = (100, 100, 1)$

$\hat{\boldsymbol{\tau}} = (100, 1, 1)$ $\hat{\boldsymbol{\tau}} = (1, 100, 1)$ $\hat{\boldsymbol{\tau}} = (100, 100, 1)$

Figure 5.9 – Estimated covariance functions (top) and realizations (bottom) of the Gaussian field $\{\Xi_1(\mathbf{x}), \mathbf{x} \in \mathscr{B}\}$ for $\gamma = 3$.

realization of $\{\Xi_1(\mathbf{x}), \mathbf{x} \in \mathscr{B}\}$ are shown for $\gamma = 3$ and several values of $\hat{\boldsymbol{\tau}} = (\hat{\tau}_1, \hat{\tau}_2, \hat{\tau}_3)$ in Fig. 5.9.

It can be observed that increasing the parameter $\hat{\tau}_k$ allows for prescribing a locally anisotropic correlation structure oriented along the associated direction $\hat{\mathbf{e}}_k$, $1 \leqslant k \leqslant 3$. In particular, imposing $\hat{\tau}_1 \gg \hat{\tau}_2$ and $\hat{\tau}_1 \gg \hat{\tau}_3$ leads to a strong correlation along the longitudinal direction, and the associated realizations exhibit a typical signature of this correlation pattern. Similarly, selecting $\hat{\tau}_2 \gg \hat{\tau}_1$ and $\hat{\tau}_2 \gg \hat{\tau}_3$ leads to a longer correlation range along the circumferential direction. Finally, retaining $\hat{\tau}_1 = \hat{\tau}_2 \gg \hat{\tau}_3$ gives a locally isotropic correlation structure in the plane spanned by $(\hat{\mathbf{e}}_1(\mathbf{x}), \hat{\mathbf{e}}_2(\mathbf{x}))$. Further results involving the same directional configurations but shorter correlation ranges are also shown in Fig. 5.10.

Next, the diffusion tensor is chosen as

$$[H(\mathbf{x})] = \kappa[I_3] + \tau_1[M_1(\mathbf{x})] + \tau_2[M_2(\mathbf{x})]\,, \tag{5.71}$$

where $\kappa > 0$, $\tau_1 \geqslant 0$, $\tau_2 \geqslant 0$, and the structural tensors are defined with respect to the preferred directions given by Eq. (5.69) with $\alpha = 46.274$ in degrees. Correlation functions and realizations of the Gaussian field are shown in Fig. 5.11 for $\kappa = 0.1$, $\gamma = 1$ and some values of $\boldsymbol{\tau} = (\tau_1, \tau_2)$.

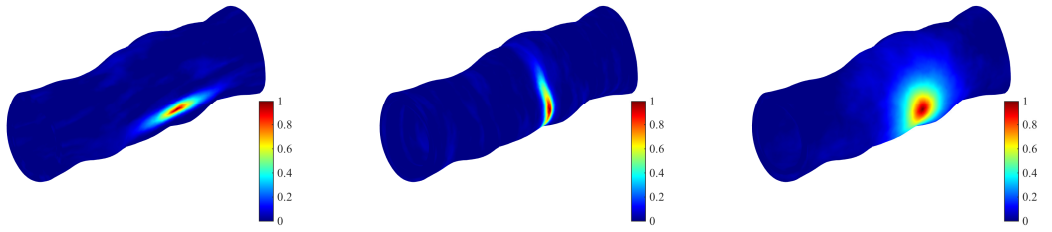

$\hat{\boldsymbol{\tau}} = (100, 1, 1)$ $\hat{\boldsymbol{\tau}} = (1, 100, 1)$ $\hat{\boldsymbol{\tau}} = (100, 100, 1)$

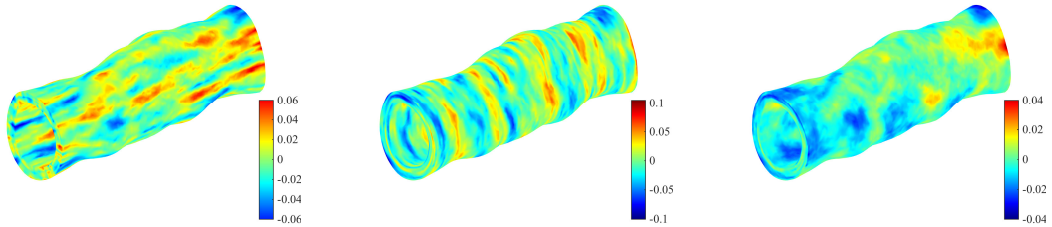

$\hat{\boldsymbol{\tau}} = (100, 1, 1)$ $\hat{\boldsymbol{\tau}} = (1, 100, 1)$ $\hat{\boldsymbol{\tau}} = (100, 100, 1)$

Figure 5.10 – Estimated covariance functions (top) and realizations (bottom) of the Gaussian field $\{\Xi_1(\mathbf{x}), \mathbf{x} \in \mathscr{B}\}$ for $\gamma = 10$.

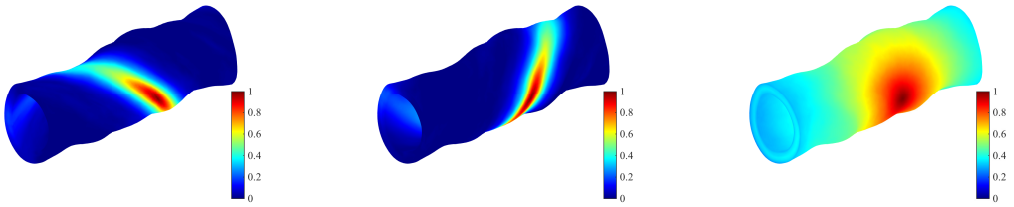

$\boldsymbol{\tau} = (10, 0)$ $\boldsymbol{\tau} = (0, 10)$ $\boldsymbol{\tau} = (10, 10)$

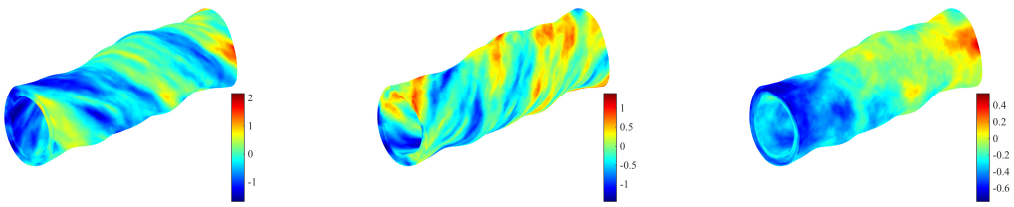

$\boldsymbol{\tau} = (10, 0)$ $\boldsymbol{\tau} = (0, 10)$ $\boldsymbol{\tau} = (10, 10)$

Figure 5.11 – Estimated covariance functions (top) and realizations (bottom) of the Gaussian field $\{\Xi_1(\mathbf{x}), \mathbf{x} \in \mathscr{B}\}$ for $\gamma = 1$ and $\kappa = 0.1$.

As expected, it is observed that selecting $\tau_i \gg \tau_j$ allows one to prescribe a signature of the anisotropy along the preferred direction $\mathbf{x} \mapsto \mathbf{a}_i(\mathbf{x})$. This feature is relevant to situations where the random field must account for subscale details. By contrast, the case $\tau_1 \approx \tau_2$ leads to a locally isotropic correlation structure in the plane spanned by $(\mathbf{a}_1(\mathbf{x}), \mathbf{a}_2(\mathbf{x}))$. We end this section by emphasizing that the random field $\{\mathbf{G}(\mathbf{x}), \mathbf{x} \in \mathscr{B}\}$ obtained the non linear transformations of the Gaussian fields inherits a correlation structure that exhibits the same features, as depicted in Fig. 5.12 for $\{G_1(\mathbf{x}), \mathbf{x} \in \mathscr{B}\}$.

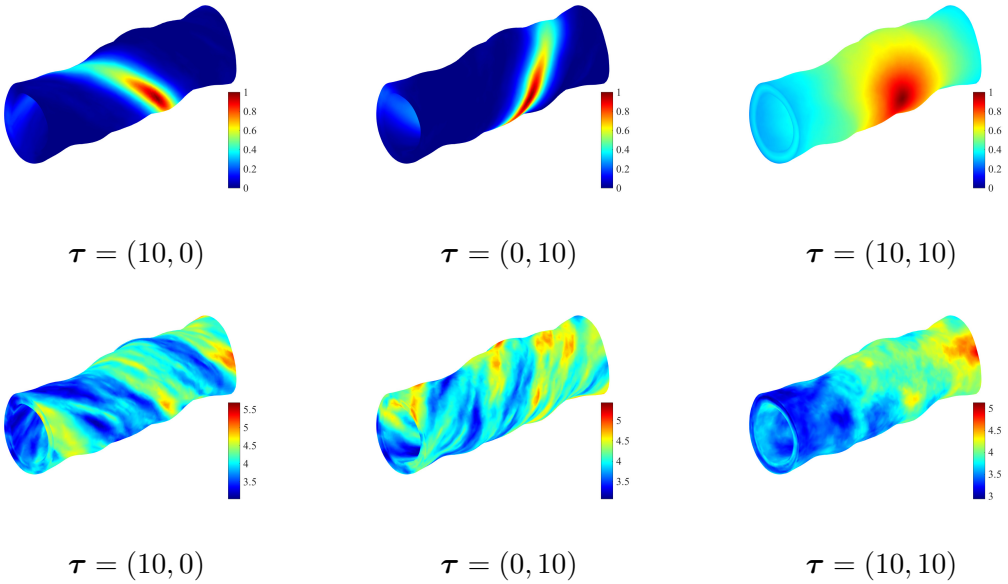

Figure 5.12 – Estimated covariance functions (top) and realizations (bottom) of the Gaussian field $\{G_1(\mathbf{x}), \mathbf{x} \in \mathscr{B}\}$ for $\gamma = 1$ and $\kappa = 0.1$.

5.5.4.3 Uncertainty propagation

In this final section, uncertainty propagation is performed by considering the random field model for anisotropic stored energy functions constructed in this work, as well as the sampling strategy presented in the previous sections. The patient-specific geometry is submitted to a 12 [kPa] pressure on its inner surface. The inlet surface is totally clamped while a sliding boundary condition is prescribed on the outlet surface. Alternative boundary conditions for such applications can be found in, *e.g.*, [171]. The diffusion tensor field is defined by Eq. (5.71) with $\kappa = 0.1$, $\gamma = 1$, $\tau_1 = \tau_2 = 10$ and $\alpha = 46.275$ [deg]. The coefficient of variation of the random fields are all set to 10%. Realizations of the Von Mises stress field (in terms of the Cauchy stress tensor) are shown, together with the response obtained with the nominal (mean) model in Figs. 5.13 and 5.14. It is seen that the fluctuations in the anisotropic stored energy functions can induce pronounced fluctuations in the Von Mises stress, especially when compared with the mean response, and may thus have a strong impact on any subsequent calculation. The localization patterns in the stress distribution turn out to be rather reproducible, given the influence of the deterministic geometry and preferred directions. The probability density function of the maximum Von Mises stress, computed from 500 independent realizations using the kernel estimation method, is finally shown in Fig. 5.15.

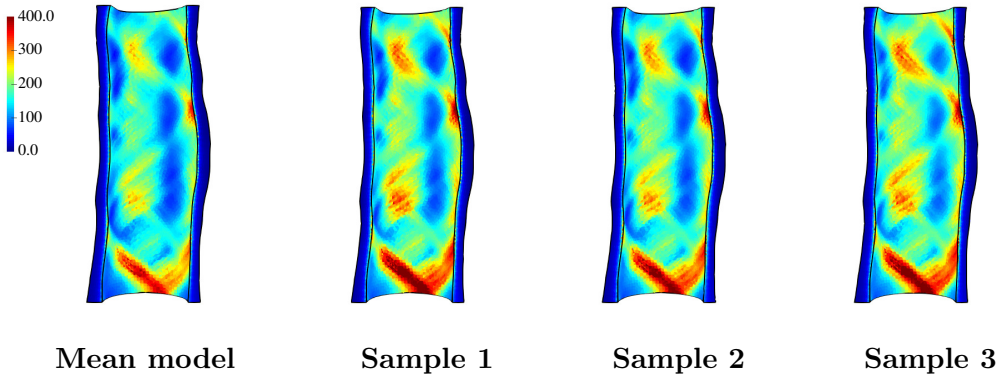

Figure 5.13 – Response associated with the mean model and three independent realizations of the Von Mises stress field (in kPa) on the inner surface of the media layer.

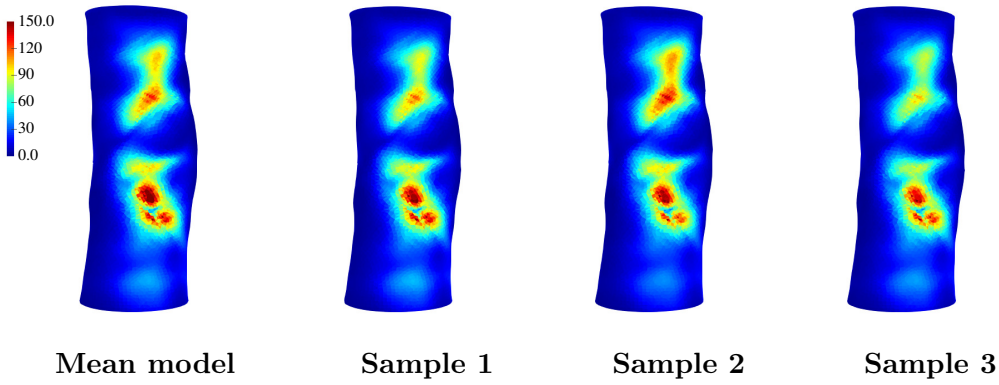

Figure 5.14 – Response associated with the mean model and three independent realizations of the Von Mises stress field (in kPa) on the outer surface of the media layer.

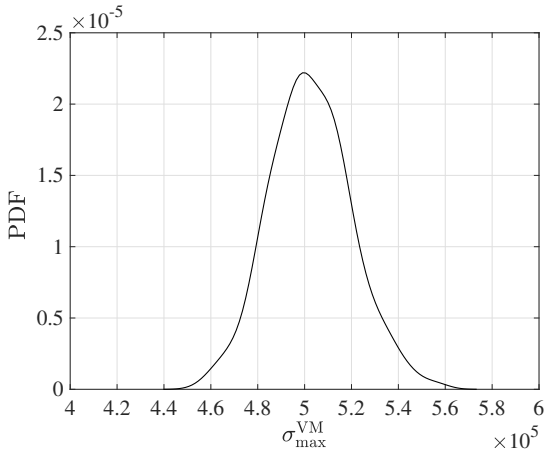

Figure 5.15 – Plot of the probability density function of the maximum Von Mises stress (in Pa).

5.6 Conclusion

In this chapter, a random field model for a prototypical anisotropic stored energy function was constructed [48]. An efficient and robust computational methodology for sampling the stochastic stored energy function on complex geometries was then presented and studied. In particular, the capability of the stochastic model to produce anisotropic correlation kernels and realizations with specific signatures on non-convex geometry was demonstrated. The proposed framework was finally applied to estimate the distribution of the Von Mises stress on a patient-specific geometry.

Chapter 6

A Unified Random Field Model of Elasticity Tensors

Contents

6.1 Introduction

This last chapter is focused on the construction of a unified approach for modeling a class of elasticity tensor random fields with values in any symmetry classes. Over the past three decades, this has been mostly achieved, in linear elasticity, by resorting to polynomial chaos expansions (see [32] and the references therein for a recent survey) and algebraic decompositions of random fields—mostly for isotropic media. The latter type of approaches includes the selection or construction of models in the class of all admissible second-order stochastic representations, where admissibility typically refers to the fulfillment (with probability one) of all the basic properties raised by the mathematical analysis of the stochastic boundary value problem [20, 202]. In three-dimensional linear elasticity, such properties include, for instance, the positive-definiteness of the tensor-valued elasticity coefficient [53]. A contribution involving *a priori* model selection can be found, for instance, in [203] for isotropic materials, while construction methodologies building upon information theory [83, 84] and the maximization of Shannon's entropy were proposed in, *e.g.*, [20, 22, 23, 24, 28, 30, 31, 33]. Such information-theoretic models define admissible subsets of the set of all second-order elasticity random fields [36]. They enable, in particular, fast numerical simulations for physics-based uncertainty propagation and involve low-dimensional hyperparameters, which allows for an identification solving (underdetermined) statistical inverse problems. It should be noticed that a recent theoretical work addressing the modeling (through spectral expansions) of the complete set of elasticity tensors for all symmetry classes can be found in [35].

From a modeling standpoint, a key issue is the representation of anisotropy and the evolution of the latter as the elasticity tensor becomes random. Depending on the retained framework, the sought quantity of interest and computational resources, one may consider random fields of

elasticity tensors with fluctuations in a given symmetry class (see [22] for the isotropic case, for instance) or in the triclinic class (see [204] for a micromechanics-based discussion). The latter (triclinic) case was first addressed in [20], making use of earlier derivations proposed in [86] for structural dynamics. The model relies on a random matrix formulation that induces triclinic fluctuations and does not allow other symmetry classes to be considered, due the eigenvalue repulsion phenomenon [26]. Similar ideas were then pursued in [28, 29], in which a decomposition onto an *ad hoc* tensor basis was used to circumvent this limitation. This approach involves an exponential map that allows one to relax the algebraic constraints generated by the positive-definiteness and symmetry properties of the tensor (in practice, these constraints can raise critical sampling issues for weak symmetries). Additionally, this construction enables efficient random field sampling through the integration of a family of stochastic differential equations. Below, we show that these two constructions can, indeed, be unified in a rather simple form.

This chapter is organized as follows. Section 6.2 is concerned with the construction of the stochastic representation. The methodology is first introduced in Section 6.2.1, and technical developments are then discussed in Sections 6.2.2–6.2.5. Numerical examples are provided in Section 6.3. Closed-form expressions for the symmetry classes that are not specifically addressed throughout the chapter are finally gathered in Section 6.4.

6.2 Construction of the non-Gaussian random field model

6.2.1 Overview of the methodology

Let $\mathscr{B}$ be the domain in $\mathbb{R}^3$ occupied by the body of interest in its reference configuration. Fourth-order elasticity tensors are represented using the standard modified Voigt notation [73]. Let then $\{[\mathbf{A}(\mathbf{x})], \mathbf{x} \in \mathscr{B}\}$ be the $\mathbb{S}$-valued random field, with $\mathbb{S} \subseteq \mathbb{S}^6_+$, corresponding to the modified Voigt notation of the random elasticity field $\{[\![\mathbf{A}(\mathbf{x})]\!], \mathbf{x} \in \mathscr{B}\}$. Regarding the material symmetry exhibited by the material, two practical situations can be considered as follows:

- When the symmetry class under consideration is defined by crystallographic orientations that are independent of the location $\mathbf{x}$ in $\mathscr{B}$, the symmetry properties hold in the global coordinate system and the state space $\mathbb{S}$ is equal to $\mathbb{S}^6_{\mathrm{sym}}$, where $\mathbb{S}^6_{\mathrm{sym}} \subset \mathbb{S}^6_+$ is the set of elasticity matrices defined as

$$\mathbb{S}^6_{\mathrm{sym}} = \{[A] \in \mathbb{S}^6_+ \,:\, [Q]^T[A][Q] = [A]\,, \forall\, [Q] \in \mathscr{G}_{\mathrm{sym}}\}\,, \tag{6.1}$$

  with $\mathscr{G}_{\mathrm{sym}} \subseteq \mathcal{S}\mathrm{O}(3)$.

- When the material involves crystallographic orientations that are spatially dependent, meaning that the symmetry properties are exhibited in a local coordinate system, the state space coincides with $\mathbb{S}^6_+$. At every location $\mathbf{x}$ in $\mathscr{B}$, the random elasticity matrix $[\mathbf{A}(\mathbf{x})]$ belongs to a set $\mathbb{S}^6_{\mathrm{sym}}(\mathbf{x})$ but for simplicity, the spatial dependency will be omitted in the sequel of this chapter. One example of such materials is wood, which typically exhibits orthotropy in local cylindrical coordinates: in this case, the unit vectors $\mathbf{a}$, $\mathbf{b}$ and $\mathbf{c}$ defining the three orientations are taken as $\mathbf{e}_r(\mathbf{x})$, $\mathbf{e}_\theta(\mathbf{x})$ and $\mathbf{e}_z(\mathbf{x})$ at the location $\mathbf{x}$, and the material appears as triclinic in the global coordinate system. Another example is given by spherical symmetry, in which the material is transversely isotropic with respect to the preferred direction $\mathbf{e}_r(\mathbf{x})$ at every location $\mathbf{x}$ of $\mathscr{B}$.

Let $\mathbf{x} \mapsto [\underline{A}(\mathbf{x})]$ be the mean function of the random elasticity tensor, that is $[\underline{A}(\mathbf{x})] = \mathbb{E}\{[\mathbf{A}(\mathbf{x})]\}$ for all $\mathbf{x}$ in $\mathscr{B}$. It is assumed that the mean field is uniformly bounded, meaning that there exist

constants $0 < \underline{k}_0 < \underline{k}_1$, independent of $\mathbf{x}$, such that

$$\underline{k}_0 \|\boldsymbol{\xi}\|^2 \leqslant \langle \boldsymbol{\xi}, [\underline{A}(\mathbf{x})]\boldsymbol{\xi} \rangle \leqslant \underline{k}_1 \|\boldsymbol{\xi}\|^2 \,, \quad \forall \boldsymbol{\xi} \in \mathbb{R}^6 \,. \tag{6.2}$$

In order to ensure the existence of a unique solution to the weak stochastic boundary value problem [20, 32], the random elasticity tensor must

(H1) take its values in $\mathbb{S}^6_+$ almost surely;

(H2) be such that the bilinear form in the associated weak form is continuous and elliptic;

(H3) be a second-order random variable, *i.e.*, $\mathbb{E}\{\|[\mathbf{A}(\mathbf{x})]\|_F^2\} < +\infty \,, \quad \mathbf{x} \in \mathscr{B}$.

Any admissible random field model must fulfill the above properties and (H1) makes Gaussian models non-admissible. It was shown in [20] that the last constraint (H3) requires the random elasticity tensor to be uniformly bounded, that is there exist $0 < \epsilon_0 < \epsilon_1$ such that

$$\epsilon_0 \|\boldsymbol{\xi}\|^2 \leqslant \langle \boldsymbol{\xi}, [\mathbf{A}(\mathbf{x})]\boldsymbol{\xi} \rangle \leqslant \epsilon_1 \|\boldsymbol{\xi}\|^2 \,, \quad \forall \boldsymbol{\xi} \in \mathbb{R}^6 \,, \tag{6.3}$$

almost surely, together with $\mathbb{E}\{\|[\mathbf{A}(\mathbf{x})]^{-1}\|_F^2\} < +\infty$. This can be achieved in various ways, by letting [205]

$$[\mathbf{A}(\mathbf{x})] = [A_0(\mathbf{x})] + ([\underline{A}(\mathbf{x})] - [A_0(\mathbf{x})])^{1/2} [\mathbf{M}(\mathbf{x})] ([\underline{A}(\mathbf{x})] - [A_0(\mathbf{x})])^{1/2} \,, \quad \forall \mathbf{x} \in \mathscr{B} \,, \tag{6.4}$$

where $\mathbf{x} \mapsto [A_0(\mathbf{x})]$ is a deterministic, symmetric positive-definite lower bound, *i.e.*,

$$\langle \boldsymbol{\xi}, [\mathbf{A}(\mathbf{x})]\boldsymbol{\xi} \rangle \geqslant \langle \boldsymbol{\xi}, [A_0(\mathbf{x})]\boldsymbol{\xi} \rangle > 0 \,, \quad \forall \boldsymbol{\xi} \in \mathbb{R}^6 \,, \tag{6.5}$$

almost surely, the definition of which may be inferred, for instance, from micromechanical considerations [28, 204, 25]. This construction involves an additional random field $\{[\mathbf{M}(\mathbf{x})], \mathbf{x} \in \mathscr{B}\}$ with values in $\mathbb{S}^6_{\text{sym}}$ and such that

$$\mathbb{E}\{[\mathbf{M}(\mathbf{x})]\} = [I_6] \,, \quad \forall \mathbf{x} \in \mathscr{B} \,. \tag{6.6}$$

In the following, we shall consider

$$[A_0(\mathbf{x})] = \frac{\epsilon}{1+\epsilon} [\underline{A}(\mathbf{x})] \,, \quad \forall \mathbf{x} \in \mathscr{B} \,, \tag{6.7}$$

with $\epsilon > 0$ an arbitrary small constant. In this setting, it can be deduced that the random matrix $[\mathbf{A}(\mathbf{x})]$ writes

$$[\mathbf{A}(\mathbf{x})] = \frac{1}{1+\epsilon} [\underline{A}(\mathbf{x})]^{1/2} \Big(\epsilon [I_6] + [\mathbf{M}(\mathbf{x})] \Big) [\underline{A}(\mathbf{x})]^{1/2} \,, \quad \forall \mathbf{x} \in \mathscr{B} \,, \tag{6.8}$$

and in virtue of the assumption given by Eq. (6.2), the ellipticity constant ϵ_0 is given by

$$\epsilon_0 = \frac{\epsilon \, \underline{k}_0}{1+\epsilon} \,. \tag{6.9}$$

The non-Gaussian random field $\{[\mathbf{M}(\mathbf{x})], \mathbf{x} \in \mathscr{B}\}$ is then defined as a pointwise nonlinear transformation, namely

$$[\mathbf{M}(\mathbf{x})] = \mathcal{H}(\mathbf{x}, \boldsymbol{\Xi}(\mathbf{x})) \,, \quad \forall \mathbf{x} \in \mathscr{B} \,, \tag{6.10}$$

where $\{\boldsymbol{\Xi}(\mathbf{x}) = (\Xi_1(\mathbf{x}), \ldots, \Xi_n(\mathbf{x})), \mathbf{x} \in \mathbb{R}^3\}$ is a second-order centered Gaussian random field with values in $\mathbb{R}^n$ and $\mathcal{H}$ is same spatially dependent in order to cover potentially nonstationnary cases. As it will be seen in the following developments, the integer n corresponds to the dimension of the matrix set $\mathbb{S}^6_{\text{sym}}$. The Gaussian field $\{\boldsymbol{\Xi}(\mathbf{x}), \mathbf{x} \in \mathbb{R}^3\}$ is defined by its normalized correlation function $(\mathbf{x}, \mathbf{y}) \mapsto [R(\mathbf{x}, \mathbf{y})]$ such that

$$[R(\mathbf{x}, \mathbf{y})] = \text{diag}(R_1(\mathbf{x}, \mathbf{y}), \ldots, R_n(\mathbf{x}, \mathbf{y})) \,, \quad \forall (\mathbf{x}, \mathbf{y}) \in \mathbb{R}^3 \times \mathbb{R}^3 \,, \tag{6.11}$$

with

$$R_k(\mathbf{x}, \mathbf{y}) = \mathbb{E}\{\Xi_k(\mathbf{x})\Xi_k(\mathbf{y})\} \,, \quad \forall (\mathbf{x}, \mathbf{y}) \in \mathbb{R}^3 \times \mathbb{R}^3 \,, \quad 1 \leqslant k \leqslant n \,, \tag{6.12}$$

and $[R(\mathbf{x}, \mathbf{x})] = [I_n]$. The random fields $\{\Xi_i(\mathbf{x}), \mathbf{x} \in \mathbb{R}^3\}$ and $\{\Xi_j(\mathbf{x}), \mathbf{x} \in \mathbb{R}^3\}$, $1 \leqslant i < j \leqslant n$, are statistically independent by construction.

6.2.2 Tensor decomposition of the elasticity field

Following [29, 28], the random matrix $[\mathbf{M}(\mathbf{x})]$ is decomposed onto the second-order representation of the (potentially spatially dependent) Walpole basis $\mathcal{B}_{\mathbf{x}} = \{[E_i(\mathbf{x})]\}_{i=1}^n$ [71]:

$$[\mathbf{M}(\mathbf{x})] = \sum_{i=1}^{n} M_i(\mathbf{x})[E_i(\mathbf{x})] \,, \tag{6.13}$$

where $\{M_i(\mathbf{x}), \mathbf{x} \in \mathscr{B}\}$, $1 \leqslant i \leqslant n$, are scalar-valued random fields. Let $\mathbf{M}(\mathbf{x})$ be the random vector gathering the random coefficients, *i.e.*, $\mathbf{M}(\mathbf{x}) = (M_1(\mathbf{x}), \ldots, M_n(\mathbf{x}))$. This random vector takes its values in the subset $\mathcal{S}_{\mathbf{x}}$ of $\mathbb{R}^n$ such that

$$\mathcal{S}_{\mathbf{x}} = \left\{ \mathbf{m} \in \mathbb{R}^n \,:\, \sum_{i=1}^{n} m_i[E_i(\mathbf{x})] \in \mathbb{S}^6_+ \right\} . \tag{6.14}$$

In the sequel of this work, the decomposition given by Eq. (6.13) is denoted by using the symbolic representation

$$[\mathbf{M}(\mathbf{x})] = \left\{ [\mathbf{N}_1(\mathbf{x})], \ldots, [\mathbf{N}_p(\mathbf{x})], M_{q+1}(\mathbf{x}), \ldots M_n(\mathbf{x}) \right\} , \tag{6.15}$$

where $\{[\mathbf{N}_i(\mathbf{x})]\}_{i=1}^p$ is a set of p random matrices with values in $\mathbb{S}^+_r$, the entries of which are made up of the $q = p \times r(r+1)/2$ coordinates of $[\mathbf{M}(\mathbf{x})]$ onto $\mathcal{B}_{\mathbf{x}}$. The values of n, p and r are listed in Tab. (6.1) for all symmetry classes of practical interest (monoclinic systems are not explicitly considered hereinafter, due to their restricted applicability). Note that for the isotropic

Symmetry class	n	p	r
Isotropy	2	0	–
Cubic	3	0	–
Transverse isotropy	5	1	2
Tetragonal	6	1	2
Trigonal	6	2	2
Orthotropy	9	1	3
Triclinic	21	1	6

Table 6.1 – Values of n, p and r for selected symmetry classes (reduced parameterizations are used for tetragonal and trigonal classes).

and cubic symmetries, $p = 0$, and the decomposition does not involve any random matrix. For a given symmetry class, the identity matrix $[I_6]$ is given by

$$[I_6] = \{\underbrace{[I_r], \ldots, [I_r]}_{p \text{ times}}, \underbrace{1, \ldots, 1}_{(n-N) \text{ times}}\}\,. \tag{6.16}$$

The symbolic representation by Eq. (6.15) reflects the particular underlying structure of the tensor (sub)algebras, and allows for simple calculations within $\mathbb{S}^6_{\text{sym}}$. For instance, it can be shown that the inverse $[\mathbf{M}(\mathbf{x})]^{-1}$ writes

$$[\mathbf{M}(\mathbf{x})]^{-1} = \left\{[\mathbf{N}_1(\mathbf{x})]^{-1}, \ldots, [\mathbf{N}_p(\mathbf{x})]^{-1}, M_{q+1}^{-1}(\mathbf{x}), \ldots, M_n^{-1}(\mathbf{x})\right\}, \tag{6.17}$$

and that any polynomial transformation $f([\mathbf{M}(\mathbf{x})])$ of the random matrix $[\mathbf{M}(\mathbf{x})]$ is given by

$$f([\mathbf{M}(\mathbf{x})]) = \left\{f([\mathbf{N}_1(\mathbf{x})]), \ldots, f([\mathbf{N}_p(\mathbf{x})]), f(M_{q+1}(\mathbf{x})), \ldots, f(M_n(\mathbf{x}))\right\}. \tag{6.18}$$

In addition, the random matrix $[\mathbf{M}(\mathbf{x})]$ is positive-definite a.s. if and only if the random matrices $[\mathbf{N}_1(\mathbf{x})], \ldots, [\mathbf{N}_p(\mathbf{x})]$ are positive definite and the random variables $M_{q+1}(\mathbf{x}), \ldots, M_n(\mathbf{x})$ strictly positive almost surely. It should be emphasized that while $[\mathbf{M}(\mathbf{x})]$ takes its values in $\mathbb{S}$, all the random matrices take their values in $\mathbb{S}^r_+$. These properties will be used in the sequel to construct the probabilistic model of the elementary elements in the symbolic representation, as well as to derive closed-form expressions for some model parameters. As an illustration, in the case of transverse isotropy, one has $n = 5$, $p = 1$ and $r = 2$, so that the random matrix $[\mathbf{M}(\mathbf{x})]$ can be written as

$$[\mathbf{M}(\mathbf{x})] = \left\{\underbrace{\begin{bmatrix} M_1(\mathbf{x}) & M_3(\mathbf{x}) \\ M_3(\mathbf{x}) & M_2(\mathbf{x}) \end{bmatrix}}_{[\mathbf{N}_1(\mathbf{x})]}, M_4(\mathbf{x}), M_5(\mathbf{x})\right\}. \tag{6.19}$$

The random matrix $[\mathbf{M}(\mathbf{x})]$ is positive-definite if and only if $\langle \mathbf{v}, [\mathbf{N}_1(\mathbf{x})]\mathbf{v}\rangle > 0$ for all $\mathbf{v} \in \mathbb{R}^2$, $M_4(\mathbf{x}) > 0$ and $M_5(\mathbf{x}) > 0$, almost surely.

The mapping $\mathcal{H}$ can be constructed by imposing that the family of first-order marginal probability density functions of $\{[\mathbf{M}(\mathbf{x})], \mathbf{x} \in \mathscr{B}\}$ coincides with a target family, obtained through the MaxEnt principle. Here, the entropy of a probability density function f (with support $\mathbb{S}$) is defined as

$$\mathscr{E}\{f\} = -\int_{\mathbb{S}} f([M]) \log(f([M]))\, \mathrm{d}[M]\,, \tag{6.20}$$

where $\mathrm{d}[M] = 2^{15/2} \prod_{i \leqslant j} \mathrm{d}M_{ij}$ is the measure in $\mathbb{S}^6$ [206] and $\mathrm{d}M_{ij}$ is the Lebesgue measure in $\mathbb{R}$. In view of invoking the MaxEnt principle, we consider the constraints

$$\mathbb{E}\{[\mathbf{M}(\mathbf{x})]\} = [I_6]\,, \tag{6.21}$$

and

$$\mathbb{E}\{\log(\det([\mathbf{M}(\mathbf{x})]))\} = \varsigma(\mathbf{x})\,, \quad |\varsigma(\mathbf{x})| < +\infty\,. \tag{6.22}$$

The first mean constraint follows from the normalization given by Eq. (6.6), while Eq. (6.22) ensures that $[\mathbf{M}(\mathbf{x})]$, as well as its inverse $[\mathbf{M}(\mathbf{x})]^{-1}$ are second-order random variables, and that $[\mathbf{M}(\mathbf{x})]$ is positive-definite, almost surely [20]. In previous works [29, 28], the above constraints were handled by resorting to an exponential mapping. One advantage of this approach was to

relax the constraints related to the sampling $\mathcal{S}_{\mathbf{x}}$, hence allowing for the recourse to generation algorithms based on stochastic differential equations. Herein, we pursue a different approach and show that the probability density functions of the random matrices $[\mathbf{N}_1(\mathbf{x})], \ldots, [N_p(\mathbf{x})]$ and random variables $M_{q+1}(\mathbf{x}), \ldots, M_n(\mathbf{x})$ correspond to labeled probability distributions. First, we note that Eqs. (6.15) and Eq. (6.21) readily imply that

$$\mathbb{E}\{[\mathbf{N}_i(\mathbf{x})]\} = [I_r]\,, \quad 1 \leqslant i \leqslant p\,, \tag{6.23}$$

and

$$\mathbb{E}\{M_k(\mathbf{x})\} = 1\,, \quad q+1 \leqslant k \leqslant n\,. \tag{6.24}$$

Furthermore, by applying Jensen's inequality, one has

$$\mathbb{E}\{\log(\det(\sum_{i=1}^{n} M_i(\mathbf{x})[E_i(\mathbf{x})]))\} \leqslant \log(\det([I_6])) = 0\,, \tag{6.25}$$

where the concavity of the mapping $[X] \mapsto \log(\det([X]))$ for $[X] \in \mathbb{S}^6_+$ has been used. Upon using the aforementioned symbolic representation, one has

$$\log(\det(\sum_{i=1}^{n} M_i(\mathbf{x})[E_i(\mathbf{x})])) = \sum_{j=1}^{p} \alpha_j \log(\det([\mathbf{N}_j(\mathbf{x})])) + \sum_{k=q+1}^{n} \beta_{k-q} \log(M_k(\mathbf{x}))\,, \tag{6.26}$$

where $\{\alpha_j\}_{j=1}^{p}$ and $\{\beta_k\}_{k=1}^{n-q}$ are two sets of positive integers. The proof of Eq. (6.26) is given below.

Proof. Invoking the symbolic representation given by Eq. (6.15), one has

$$\log(\det([\mathbf{M}(\mathbf{x})])) = \mathrm{Tr}\left(\{\log([\mathbf{N}_1(\mathbf{x})]), \ldots, \log([\mathbf{N}_p(\mathbf{x})]), \log(M_{q+1}(\mathbf{x})), \ldots, \log(M_n(\mathbf{x}))\}\right)\,, \tag{6.27}$$

for any symmetry class. Next, consider a symmetry class (r is then fixed in the sequel) and let $[\mathbf{T}_j(\mathbf{x})] = \log([\mathbf{N}_j(\mathbf{x})])$ and $T_k(\mathbf{x}) = \log(M_k(\mathbf{x}))$. Hence, it is seen that

$$\begin{aligned} \log(\det([\mathbf{M}(\mathbf{x})])) &= \mathrm{Tr}\left(\{[\mathbf{T}_1(\mathbf{x})], \ldots, [\mathbf{T}_p(\mathbf{x})], T_{q+1}(\mathbf{x}), \ldots, T_n(\mathbf{x})\}\right) \\ &= \sum_{j=1}^{p} \sum_{i=1}^{r(r+1)/2} T_i^{(j)}(\mathbf{x}) \mathrm{Tr}([E_{\mathcal{I}_r(i,j)}(\mathbf{x})]) + \sum_{k=q+1}^{n} T_k(\mathbf{x}) \mathrm{Tr}([E_k(\mathbf{x})])\,, \end{aligned} \tag{6.28}$$

with

$$[\mathbf{T}_j(\mathbf{x})] = \begin{bmatrix} T_1^{(j)}(\mathbf{x}) & T_3^{(j)}(\mathbf{x}) \\ T_3^{(j)}(\mathbf{x}) & T_2^{(j)}(\mathbf{x}) \end{bmatrix}\,, \tag{6.29}$$

if $r = 2$ and

$$[\mathbf{T}_j(\mathbf{x})] = \begin{bmatrix} T_1^{(j)}(\mathbf{x}) & T_4^{(j)}(\mathbf{x}) & T_6^{(j)}(\mathbf{x}) \\ T_4^{(j)}(\mathbf{x}) & T_2^{(j)}(\mathbf{x}) & T_5^{(j)}(\mathbf{x}) \\ T_6^{(j)}(\mathbf{x}) & T_5^{(j)}(\mathbf{x}) & T_3^{(j)}(\mathbf{x}) \end{bmatrix} \tag{6.30}$$

if $r = 3$ (note that the case $r = 6$ corresponding to the triclinic case is not considered here, since it does not introduce a split between matrix-valued and scalar-valued random fields), and $\mathcal{I}_r(i,j) = (j-1)r(r+1)/2 + i$. Noticing that $\mathrm{Tr}([E_{\mathcal{I}_r(i,j)}(\mathbf{x})]) = 0$ for $\mathcal{I}_r(i,j) > r$, it follows that

$$\log(\det([\mathbf{M}(\mathbf{x})])) = \sum_{j=1}^{p} \alpha_j \sum_{i=1}^{r} T_i^{(j)}(\mathbf{x}) + \sum_{k=q+1}^{n} T_k(\mathbf{x}) \mathrm{Tr}([E_k(\mathbf{x})])\,, \tag{6.31}$$

where $\alpha_j = \mathrm{Tr}([E_{\mathcal{I}_r(i,j)}(\mathbf{x})]) > 0$. Since $\sum_{i=1}^{r} T_i^{(j)}(\mathbf{x}) = \mathrm{Tr}([\mathbf{T}_j(\mathbf{x})])$ (by construction), it can be deduced that

$$\log(\det(\sum_{i=1}^{n} M_i(\mathbf{x})[E_i(\mathbf{x})])) = \sum_{j=1}^{p} \alpha_j \log(\det([\mathbf{N}_j(\mathbf{x})])) + \sum_{k=q+1}^{n} \beta_{k-q} \log(M_k(\mathbf{x}))\,, \tag{6.32}$$

with $\beta_{k-q} = \mathrm{Tr}([E_k(\mathbf{x})])$ for $q+1 \leqslant k \leqslant n$. □

As mentioned previously, the first sum in the right-hand side of Eq. 6.26 vanishes for isotropic and cubic symmetries. On the other hand, the second sum disappears for the triclinic case. Applying Jensen's inequality again, it is deduced that

$$\mathbb{E}\{\log(\det([\mathbf{N}_i(\mathbf{x})]))\} \leqslant 0\,, \quad 1 \leqslant j \leqslant p\,, \tag{6.33}$$

and

$$\mathbb{E}\{\log(M_k(\mathbf{x}))\} \leqslant 0\,, \quad q+1 \leqslant k \leqslant n\,. \tag{6.34}$$

As a result, the second constraint given by Eq. (6.22) can be rewritten as

$$\mathbb{E}\{\log(\det([\mathbf{N}_j(\mathbf{x})]))\} = \nu_j^m(\mathbf{x})\,, \quad |\nu_j^m(\mathbf{x})| < +\infty\,, \quad 1 \leqslant j \leqslant p\,, \tag{6.35}$$

and

$$\mathbb{E}\{\log(M_k(\mathbf{x}))\} = \nu_k^s(\mathbf{x})\,, \quad |\nu_k^s(\mathbf{x})| < +\infty\,, \quad q+1 \leqslant k \leqslant n\,. \tag{6.36}$$

It follows that the constraints on the random matrices $[\mathbf{N}_1(\mathbf{x})], \ldots, [\mathbf{N}_p(\mathbf{x})]$ and the random variables $M_{q+1}(\mathbf{x}), \ldots, M_n(\mathbf{x})$ can be decoupled and considered separately in the construction of a probabilistic model.

6.2.3 Stochastic representation of the matrix-valued random fields

We first address the construction of the marginal probability density function $[N] \mapsto f_{[\mathbf{N}_i(\mathbf{x})]}([N])$ of the random matrix $[\mathbf{N}_i(\mathbf{x})]$, $1 \leqslant i \leqslant p$ ($\mathbf{x}$ being fixed). It was shown in [86] that under the constraints given by Eqs. (6.23) and (6.34), the probability density function of $[\mathbf{N}_i(\mathbf{x})]$ maximizing the entropy is given by

$$f_{[\mathbf{N}_i(\mathbf{x})]}([N]) = \mathbb{1}_{\mathbb{S}_+^r}([N]) \times k_0 \times \det([N])^{\chi_r} \times \exp\left(-\frac{(r+1)}{2\delta_{[\mathbf{N}_i(\mathbf{x})]}^2}\mathrm{Tr}([N])\right)\,, \tag{6.37}$$

where $\delta_{[\mathbf{N}_i(\mathbf{x})]}$ is the dispersion parameter of $[\mathbf{N}_i(\mathbf{x})]$ and with

$$\chi_r = \frac{(r+1)(1-\delta_{[\mathbf{N}_i(\mathbf{x})]}^2)}{2\delta_{[\mathbf{N}_i(\mathbf{x})]}^2}\,. \tag{6.38}$$

Additionally, the random matrix $[\mathbf{N}_i(\mathbf{x})]$ being symmetric and positive-definite, it admits the decomposition

$$[\mathbf{N}_i(\mathbf{x})] = [\mathbf{H}_i(\mathbf{x})]^T[\mathbf{H}_i(\mathbf{x})]\,, \tag{6.39}$$

where $[\mathbf{H}_i(\mathbf{x})]$ is the upper-triangular random matrix defined as [20]

$$[\mathbf{H}_i(\mathbf{x})]_{k\ell} = \frac{\delta_{[\mathbf{N}_i(\mathbf{x})]}}{\sqrt{r+1}} U_{k\ell}^{(i)}(\mathbf{x})\,, \quad 1 \leqslant k < \ell \leqslant r\,, \tag{6.40}$$

and

$$[\mathbf{H}_i(\mathbf{x})]_{\ell\ell} = \frac{\delta_{[\mathbf{N}_i(\mathbf{x})]}}{\sqrt{r+1}}\sqrt{2\mathfrak{a}(U^{(i)}_{\ell\ell}(\mathbf{x}), \gamma^{(i)}_{\ell}(\mathbf{x}), 1)}\,, \quad 1 \leqslant \ell \leqslant r\,, \tag{6.41}$$

where $\{\{U^{(i)}_{k\ell}(\mathbf{x}), \mathbf{x} \in \mathbb{R}^3\}\}_{1\leqslant k\leqslant \ell\leqslant r}$ is a collection of $r(r+1)/2$ independent standard normal random fields, the parameter $\gamma^{(i)}_{\ell}(\mathbf{x})$ is given by

$$\gamma^{(i)}_{\ell}(\mathbf{x}) = \frac{r+1}{2\delta^2_{[\mathbf{N}_i(\mathbf{x})]}} + \frac{1-\ell}{2}\,, \tag{6.42}$$

and the nonlinear transformation $\mathfrak{a}$ is defined by Eq. (5.46). In accordance with the symbolic representation given by Eq. (6.15), we let $\{\boldsymbol{\Xi}(\mathbf{x}), \mathbf{x} \in \mathbb{R}^3\}$ be the random field which is decomposed as

$$\boldsymbol{\Xi}(\mathbf{x}) = (\boldsymbol{\Xi}^{(1)}(\mathbf{x}), \ldots, \boldsymbol{\Xi}^{(p)}(\mathbf{x}), \Xi_{q+1}(\mathbf{x}), \ldots, \Xi_n(\mathbf{x}))\,, \tag{6.43}$$

where each random field $\{\boldsymbol{\Xi}^{(j)}(\mathbf{x}), \mathbf{x} \in \mathbb{R}^3\}$, $1 \leqslant j \leqslant p$, is a Gaussian random vector of length $r(r+1)/2$. By letting $\alpha(i,k,\ell)$ be the positive integer defined as

$$\alpha(i,k,\ell) = k + \frac{1}{2}(r(r+1)(j-1) + \ell(\ell-1))\,, \tag{6.44}$$

the random matrix $[\mathbf{H}_i(\mathbf{x})]$ can be rewritten as

$$[\mathbf{H}_i(\mathbf{x})]_{k\ell} = \frac{\delta_{[\mathbf{N}_i(\mathbf{x})]}}{\sqrt{r+1}}\Xi^{(i)}_{\alpha(i,k,\ell)}(\mathbf{x})\,, \quad 1 \leqslant k < \ell \leqslant r\,, \tag{6.45}$$

and

$$[\mathbf{H}_i(\mathbf{x})]_{\ell\ell} = \frac{\delta_{[\mathbf{N}_i(\mathbf{x})]}}{\sqrt{r+1}}\sqrt{2\mathfrak{a}(\Xi_{\alpha(i,\ell,\ell)}(\mathbf{x}), \gamma^{(i)}_{\ell}(\mathbf{x}), 1)}\,, \quad 1 \leqslant \ell \leqslant r\,. \tag{6.46}$$

In accordance with Eq. (6.15), the Gaussian random field $\{\boldsymbol{\Xi}(\mathbf{x}), \mathbf{x} \in \mathscr{B}\}$ is formerly written as

$$\boldsymbol{\Xi}(\mathbf{x}) = (\boldsymbol{\Xi}^{(1)}(\mathbf{x}), \ldots, \boldsymbol{\Xi}^{(p)}(\mathbf{x}), \Xi_{q+1}(\mathbf{x}), \ldots, \Xi_n(\mathbf{x}))\,, \tag{6.47}$$

where each random field $\{\boldsymbol{\Xi}^{(i)}(\mathbf{x}), \mathbf{x} \in \mathscr{B}\}$, $1 \leqslant i \leqslant p$, is a Gaussian random vector of length $r(r+1)/2$. The above construction then defines a pointwise nonlinear between $\{\boldsymbol{\Xi}(\mathbf{x}), \mathbf{x} \in \mathbb{R}^3\}$ and $\{[\mathbf{N}_i(\mathbf{x})], \mathbf{x} \in \mathscr{B}\}$, $1 \leqslant i \leqslant p$.

6.2.4 Stochastic representation of the scalar-valued random fields

Let us now address the case of the remaining coordinates $\{M_k(\mathbf{x})\}_{k=q+1}^n$, which are assumed to satisfy the constraints defined by Eqs. (6.24) and (6.36). For these random variables, applying the MaxEnt principle leads to

$$f_{M_k(\mathbf{x})}(m) = \mathbb{1}_{(0,\infty)}(m) \times k_0 \times m^{\delta^{-2}_{M_k(\mathbf{x})}-1} \times \exp\left(-\frac{m}{\delta^2_{M_k(\mathbf{x})}}\right)\,, \tag{6.48}$$

where $\delta_{M_k(\mathbf{x})}$ is the coefficient of variation of $M_k(\mathbf{x})$. As a consequence, each random field $\{M_k(\mathbf{x}), \mathbf{x} \in \mathscr{B}\}$, $q+1 \leqslant k \leqslant n$, can be defined by the pointwise mapping

$$M_k(\mathbf{x}) = \mathfrak{a}(\Xi_k(\mathbf{x}); \delta^{-2}_{M_k(\mathbf{x})}, \delta^2_{M_k(\mathbf{x})})\,, \quad \forall \mathbf{x} \in \mathscr{B}\,, \tag{6.49}$$

where $\mathfrak{a}$ is defined by Eq. (5.46). This construction defines a pointwise mapping between $\{\Xi_k(\mathbf{x}), \mathbf{x} \in \mathscr{B}\}$ and $\{M_k(\mathbf{x}), \mathbf{x} \in \mathscr{B}\}$, $q+1 \leqslant k \leqslant n$.

6.2.5 Putting things together

The nonlinear mapping $\mathcal{H}$ is completely defined by combining Eqs. (6.39), (6.45)–(6.46) and (6.49) with Eq. (6.13), or equivalently (6.15). This enables, in particular, a fast and robust sampling of the random fields $\{[\mathbf{M}(\mathbf{x})], \mathbf{x} \in \mathscr{B}\}$ and $\{[\mathbf{A}(\mathbf{x})], \mathbf{x} \in \mathscr{B}\}$. A sketch of the associated sampling algorithm is provided below.

(I) Select:

(i) the symmetry class of interest, and deduce the values of n, p, r and the tensor basis $\mathcal{B}_{\mathbf{x}}$;

(ii) the dispersion fields $\mathbf{x} \mapsto \delta_{[\mathbf{N}_j(\mathbf{x})]}$ and $\mathbf{x} \mapsto \delta_{M_k(\mathbf{x})}$ for $1 \leqslant j \leqslant p$ and $q+1 \leqslant k \leqslant n$ (note that they can be chosen as homogeneous for simplicity);

(iii) and an autocorrelation function $(\mathbf{x}, \mathbf{y}) \mapsto [R(\mathbf{x}, \mathbf{y})]$ for the Gaussian random field $\{\mathbf{\Xi}(\mathbf{x}), \mathbf{x} \in \mathscr{B}\}$;

(II) Monte Carlo simulations:

(i) generate one realization of the Gaussian fields $\{\Xi_k(\mathbf{x}), \mathbf{x} \in \mathscr{B}\}$, $1 \leqslant k \leqslant n$;

(ii) if $p \neq 0$, then for $1 \leqslant j \leqslant p$, deduce the realization of the fields $\{[\mathbf{N}_i(\mathbf{x})], \mathbf{x} \in \mathscr{B}\}$ using Eqs. (6.45)–(6.46) with Eq. (6.39);

(iii) for $q+1 \leqslant k \leqslant n$, deduce the realization of the fields $\{M_k(\mathbf{x}), \mathbf{x} \in \mathscr{B}\}$ using Eq. (6.49);

(iv) deduce the realizations of $[\mathbf{M}(\mathbf{x})]$ and $[\mathbf{A}(\mathbf{x})]$ using Eqs. (6.13) and (6.4).

It should be noted that the choice of the covariance function $(\mathbf{x}, \mathbf{y}) \mapsto [R(\mathbf{x}, \mathbf{y})]$ is a of primary importance from a modeling standpoint, since it governs fundamental properties of $\{\mathbf{\Xi}(\mathbf{x}), \mathbf{x} \in \mathscr{B}\}$ and $\{[\mathbf{M}(\mathbf{x})], \mathbf{x} \in \mathscr{B}\}$. In particular, if $(\mathbf{x}, \mathbf{y}) \mapsto [R(\mathbf{x}, \mathbf{y})]$ is such that the Gaussian field $\{\mathbf{\Xi}(\mathbf{x}), \mathbf{x} \in \mathscr{B}\}$ has continuous sample paths, then $\{[\mathbf{M}(\mathbf{x})], \mathbf{x} \in \mathscr{B}\}$ also has a continuous version.

Furthermore, the dispersion parameter of the random field $\{[\mathbf{M}(\mathbf{x})], \mathbf{x} \in \mathscr{B}\}$ can readily be related to the dispersion parameters of the underlying random fields. More precisely, it can be shown that

$$\delta^2_{[\mathbf{M}(\mathbf{x})]} = \frac{1}{6}\left(r \sum_{j=1}^{p} \alpha_j \delta^2_{[\mathbf{N}_j(\mathbf{x})]} + \sum_{k=q+1}^{n} \beta_{k-q} \delta^2_{M_k(\mathbf{x})} \right) . \tag{6.50}$$

Proof. Let $[\mathbf{D}(\mathbf{x})]$ be the random matrix defined as $[\mathbf{D}(\mathbf{x})] = [\mathbf{M}(\mathbf{x})] - [I_3]$. Using the symbolic representations of the random matrix $[\mathbf{M}(\mathbf{x})]$ and the identity matrix $[I_3]$ given by Eqs. (6.15) and (6.16), one has

$$[\mathbf{D}(\mathbf{x})] = \{[\mathbf{F}_1(\mathbf{x})], \ldots, [\mathbf{F}_p(\mathbf{x})], F_{q+1}(\mathbf{x}), \ldots, F_n(\mathbf{x})\} , \tag{6.51}$$

where the random matrix $[\mathbf{F}_j(\mathbf{x})]$ is given by $[\mathbf{F}_j(\mathbf{x})] = [\mathbf{N}_j(\mathbf{x})] - [I_r]$ and $F_k(\mathbf{x}) = M_k(\mathbf{x}) - 1$. It follows that $\|[\mathbf{M}(\mathbf{x})] - [I_6]\|_F^2 = \mathrm{Tr}([\mathbf{D}(\mathbf{x})]^T[\mathbf{D}(\mathbf{x})])$ can be written as

$$\|[\mathbf{M}(\mathbf{x})] - [I_6]\|_F^2 = \mathrm{Tr}\left\{[\mathbf{F}_1(\mathbf{x})]^T[\mathbf{F}_1(\mathbf{x})], \ldots, [\mathbf{F}_p(\mathbf{x})]^T[\mathbf{F}_p(\mathbf{x})], F^2_{q+1}(\mathbf{x}), \ldots, F^2_n(\mathbf{x})\right\} . \tag{6.52}$$

Let then $[\mathbf{G}_j(\mathbf{x})]$ be the random matrix such that $[\mathbf{G}_j(\mathbf{x})] = [\mathbf{F}_j(\mathbf{x})]^T[\mathbf{F}_j(\mathbf{x})]$, with

$$[\mathbf{G}_j(\mathbf{x})] = \begin{bmatrix} G_1^{(j)}(\mathbf{x}) & G_3^{(j)}(\mathbf{x}) \\ G_3^{(j)}(\mathbf{x}) & G_2^{(j)}(\mathbf{x}) \end{bmatrix} , \tag{6.53}$$

if $r = 2$ and

$$[\mathbf{G}_j(\mathbf{x})] = \begin{bmatrix} G_1^{(j)}(\mathbf{x}) & G_4^{(j)}(\mathbf{x}) & G_6^{(j)}(\mathbf{x}) \\ G_4^{(j)}(\mathbf{x}) & G_2^{(j)}(\mathbf{x}) & G_5^{(j)}(\mathbf{x}) \\ G_6^{(j)}(\mathbf{x}) & G_5^{(j)}(\mathbf{x}) & G_3^{(j)}(\mathbf{x}) \end{bmatrix} \tag{6.54}$$

for $r = 3$. Proceeding as in Eqs. (6.31)-(6.32), it can be deduced that

$$\begin{aligned} \|[\mathbf{M}(\mathbf{x})] - [I_6]\|_F^2 &= \sum_{j=1}^{p}\sum_{i=1}^{r} G_i^{(j)}(\mathbf{x})\mathrm{Tr}([E_{\mathcal{I}_r(i,j)}(\mathbf{x})]) + \sum_{k=q+1}^{n} D_k^2(\mathbf{x})\mathrm{Tr}([E_k(\mathbf{x})]) \\ &= \sum_{j=1}^{p}\alpha_j \sum_{i=1}^{r} G_i^{(j)}(\mathbf{x}) + \sum_{k=q+1}^{n} D_k^2(\mathbf{x})\mathrm{Tr}([E_k(\mathbf{x})]) \\ &= \sum_{j=1}^{p}\alpha_j \sum_{i=1}^{r}\sum_{\ell=1}^{r} [\mathbf{F}_j(\mathbf{x})]_{i\ell}[\mathbf{F}_j(\mathbf{x})]_{i\ell} + \sum_{k=q+1}^{n} D_k^2(\mathbf{x})\mathrm{Tr}([E_k(\mathbf{x})]) \\ &= \sum_{j=1}^{p}\|[\mathbf{F}_j(\mathbf{x})]\|_F^2 + \sum_{k=q+1}^{n} D_k^2(\mathbf{x})\mathrm{Tr}([E_k(\mathbf{x})]) \\ &= \sum_{j=1}^{p}\alpha_j\|[\mathbf{N}_j(\mathbf{x})] - [I_r]\|_F^2 + \sum_{k=q+1}^{n}\beta_{k-q}(M_k(\mathbf{x}) - 1)^2 \,. \end{aligned} \tag{6.55}$$

By taking the mathematical expectation on both sides in the above equation, it can be deduced that

$$\mathbb{E}\{\|[\mathbf{M}(\mathbf{x})] - [I_6]\|_F^2\} = \sum_{j=1}^{p}\alpha_j\|[I_r]\|_F^2\delta_{[\mathbf{N}_j(\mathbf{x})]}^2 + \sum_{k=q+1}^{n}\beta_{k-q}\delta_{M_k(\mathbf{x})}^2 \,, \tag{6.56}$$

and thus, the dispersion parameter $\delta_{[\mathbf{M}(\mathbf{x})]}$ of the random matrix $[\mathbf{M}(\mathbf{x})]$ is given by Eq. (6.50). □

Remark 6.2.1. *While previous information-theoretic approaches for random fields have involved similar constraints (which are related, in part, to the well-posedness of the stochastic boundary value problem) in the definition of the family of first-order marginal distributions, the proposed framework takes advantage of the structure of the tensor set to properly define the matrix-valued and scalar-valued random fields (defining the matrix-valued random field of elasticity tensor with the target symmetry class) through memoryless transformations. This is notably in contrast with the formulation constructed in [28, 31], based on the use of an exponential map, where the sampling strategy requires solving a family of Itô stochastic differential equations (ISDE) indexed in space. The latter method is general and can accommodate arbitrary first-order marginal distributions, but it requires the selection of an appropriate integration scheme [30] and the generation of as many realizations of "n" Gaussian random fields as necessary to reach the stationary solution at every single point of the domain. Although the proposed formulation still necessitates the computation of inverse transformations, it allows for substantial computational savings. In addition, it turns out to be very easy to implement and does not involve any approximation in the calculation of the Lagrange multipliers, since closed-form expressions can be obtained for these hyperparameters.*

6.3 Numerical examples

In order to illustrate some of the capabilities of the proposed model, two examples involving weak symmetries and fields indexed by non-polyhedral geometries are provided below. The generation

of the underlying Gaussian random fields is carried out by resorting on the SPDE approach presented in Section 5.4 and the diffusion field will be denoted $\mathbf{x} \mapsto [D(\mathbf{x})]$ in the rest of this chapter.

6.3.1 Application to spherical transverse isotropy

In this first example, we consider the case of spherical transverse isotropy. This implies that for any $\mathbf{x} \in \mathscr{B}$, the elasticity tensor exhibits transverse isotropy with respect to the unit normal $\mathbf{n}(\mathbf{x}) = \mathbf{e}_r(\mathbf{x})$, with $\mathbf{e}_r(\mathbf{x})$ the radial basis vector at the location $\mathbf{x}$. This model was notably shown to be relevant to the modeling of random interphase properties in nanocomposites with spherical fillers [207], for example. Let $[P(\mathbf{x})]$ and $[Q(\mathbf{x})]$ be the second-order tensors defined as

$$[P(\mathbf{x})] = \mathbf{n}(\mathbf{x}) \otimes \mathbf{n}(\mathbf{x}) \,, \quad [Q(\mathbf{x})] = [I_3] - [P(\mathbf{x})] \,. \tag{6.57}$$

The local tensor basis is then defined by the second-order tensor representation of the following tensor basis [71]:

$$\begin{aligned}
&[\![E_1(\mathbf{x})]\!] = [P(\mathbf{x})] \otimes [P(\mathbf{x})] \,, \quad [\![E_2(\mathbf{x})]\!] = \frac{1}{2}([Q(\mathbf{x})] \otimes [Q(\mathbf{x})]) \,, \\
&[\![E_3(\mathbf{x})]\!] = \frac{1}{\sqrt{2}}([P(\mathbf{x})] \otimes [Q(\mathbf{x})] + [Q(\mathbf{x})] \otimes [P(\mathbf{x})]) \,, \\
&[\![E_4(\mathbf{x})]\!] = [Q(\mathbf{x})] \boxtimes [Q(\mathbf{x})] - \frac{1}{2}([Q(\mathbf{x})] \otimes [Q(\mathbf{x})]) \,, \\
&[\![E_5(\mathbf{x})]\!] = [P(\mathbf{x})] \boxtimes [Q(\mathbf{x})] + [Q(\mathbf{x})] \boxtimes [P(\mathbf{x})] \,.
\end{aligned} \tag{6.58}$$

Using Voigt's modified notation, the random matrix $[\mathbf{M}(\mathbf{x})]$ can be decomposed as

$$[\mathbf{M}(\mathbf{x})] = \sum_{i=1}^{5} M_i(\mathbf{x})[E_i(\mathbf{x})] = \{[\mathbf{N}_1(\mathbf{x})], M_4(\mathbf{x}), M_5(\mathbf{x})\} \,, \tag{6.59}$$

where the random matrix $[\mathbf{N}_1(\mathbf{x})]$ is given by

$$[\mathbf{N}_1(\mathbf{x})] = \begin{bmatrix} M_1(\mathbf{x}) & M_3(\mathbf{x}) \\ M_3(\mathbf{x}) & M_2(\mathbf{x}) \end{bmatrix} = [\mathbf{H}_1(\mathbf{x})]^T [\mathbf{H}_1(\mathbf{x})] \,, \tag{6.60}$$

with

$$[\mathbf{H}_1(\mathbf{x})] = \frac{\delta_{[\mathbf{N}_1(\mathbf{x})]}}{\sqrt{3}} \begin{bmatrix} \sqrt{2\mathbb{o}(\Xi_1(\mathbf{x}), \gamma_1(\mathbf{x}), 1)} & \Xi_3(\mathbf{x}) \\ 0 & \sqrt{2\mathbb{o}(\Xi_2(\mathbf{x}), \gamma_2(\mathbf{x}), 1)} \end{bmatrix} . \tag{6.61}$$

In addition, it is found that the dispersion parameter $\delta_{[\mathbf{M}(\mathbf{x})]}$ writes

$$\delta_{[\mathbf{M}(\mathbf{x})]} = \left\{ \frac{1}{3} \left(\delta^2_{[\mathbf{N}_1(\mathbf{x})]} + \delta^2_{M_4(\mathbf{x})} + \delta^2_{M_5(\mathbf{x})} \right) \right\}^{1/2} . \tag{6.62}$$

We consider sampling the random field inside the unit sphere $\mathscr{B} = \{\mathbf{x} \in \mathbb{R}^3 \,:\, \|\mathbf{x}\| \leqslant 1\}$, and the field of diffusion tensor $\mathbf{x} \mapsto [D(\mathbf{x})]$ is taken, for illustration purposes as

$$[D(\mathbf{x})] = [I_3] + \lambda_\theta \mathbf{e}_\theta(\mathbf{x}) \otimes \mathbf{e}_\theta(\mathbf{x}) \,, \tag{6.63}$$

where the parameter $\lambda_\theta \geqslant 0$ controls the correlation range along $\mathbf{e}_\theta$. From a computational standpoint, the Markov approximation is constructed with $q = 23\,623$ nodes. Examples of covariance

kernels obtained for two values of the diffusion tensor are shown in Fig. 6.1. More precisely, the left panel display an isotropic kernel, while the right panel shows a strongly anisotropic covariance structure where the correlation along $\mathbf{e}_\theta$ is more pronounced. One realization of the first Gaussian random field $\{\Xi_1(\mathbf{x}), \mathbf{x} \in \mathscr{B}\}$ and the associated realizations of the first component $\{M_1(\mathbf{x}), \mathbf{x} \in \mathscr{B}\}$ and $\{M_{11}(\mathbf{x}), \mathbf{x} \in \mathscr{B}\}$ are shown for the isotropic case in Fig. 6.2, while similar results for the anisotropic kernel are depicted in Fig. 6.3.

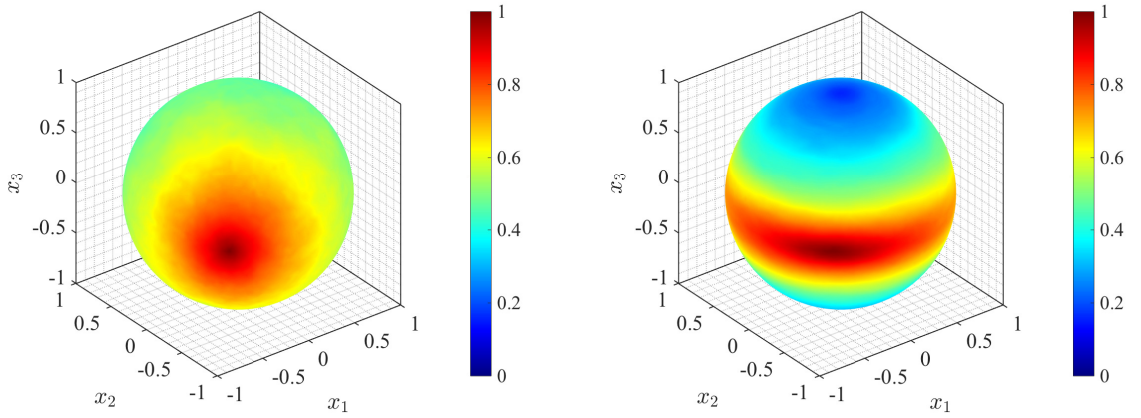

Figure 6.1 – The left panel displays the graph of the correlation function $\mathbf{y} \mapsto R_1(\mathbf{x}_0, \mathbf{y})$, estimated with 1 000 independent realizations for $\gamma(\mathbf{x}) = 2$ and $\lambda_\theta = 0$, *i.e.* $[D(\mathbf{x})] = [I_3]$. The right panel displays the estimated correlation function $\gamma(\mathbf{x}) = 4$ and $\lambda_\theta = 50$, which corresponds to a strongly anisotropic correlation structure. The reference point $\mathbf{x}_0$ is arbitrarily chosen on the outer surface of the sphere.

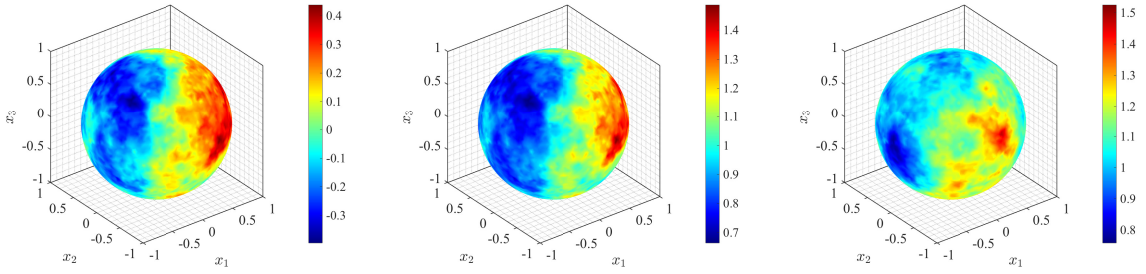

Figure 6.2 – Illustrative results for $\gamma(\mathbf{x}) = 2$ and $\lambda_\theta = 0$. One realization of $\{\Xi_1(\mathbf{x}), \mathbf{x} \in \mathscr{B}\}$ and the associated realizations of $\{M_1(\mathbf{x}), \mathbf{x} \in \mathscr{B}\}$ and $\{M_{11}(\mathbf{x}), \mathbf{x} \in \mathscr{B}\}$ are shown in the left, middle and right panels, respectively.

A comparison between these figures shows that the diffusion $\mathbf{x} \mapsto [D(\mathbf{x})]$ strongly affects the local geometry of the elasticity field. From a modeling standpoint, the field of diffusion tensor is a key parameter that may be appropriately defined in order to reproduce morphological features raised by fine scale information (such as the local orientation of polymer chains or fibers, for instance). Finally, an illustration with increasing levels of fluctuation is shown for the scalar random field $\{M_4(\mathbf{x}), \mathbf{x} \in \mathscr{B}\}$ in Fig. 6.4 (the same realization of the Gaussian field $\{\boldsymbol{\Xi}(\mathbf{x}), \mathbf{x} \in \mathscr{B}\}$ was used for the subfigures).

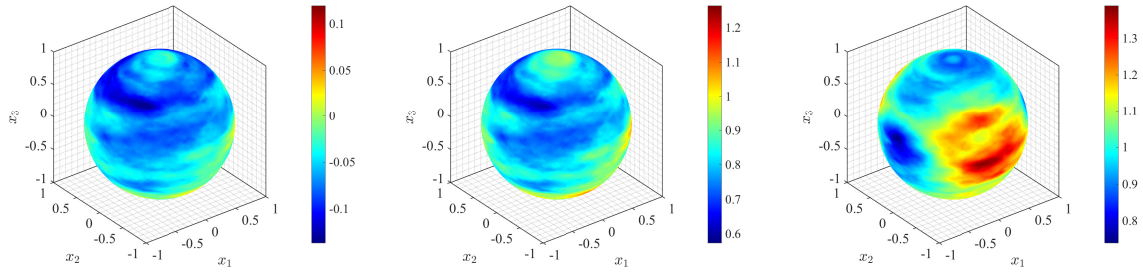

Figure 6.3 – Illustrative results for $\gamma(\mathbf{x}) = 4$ and $\lambda_\theta = 50$. One realization of $\{\Xi_1(\mathbf{x}), \mathbf{x} \in \mathscr{B}\}$ and the associated realizations of $\{M_1(\mathbf{x}), \mathbf{x} \in \mathscr{B}\}$ and $\{M_{11}(\mathbf{x}), \mathbf{x} \in \mathscr{B}\}$ are shown in the left, middle and right panels, respectively.

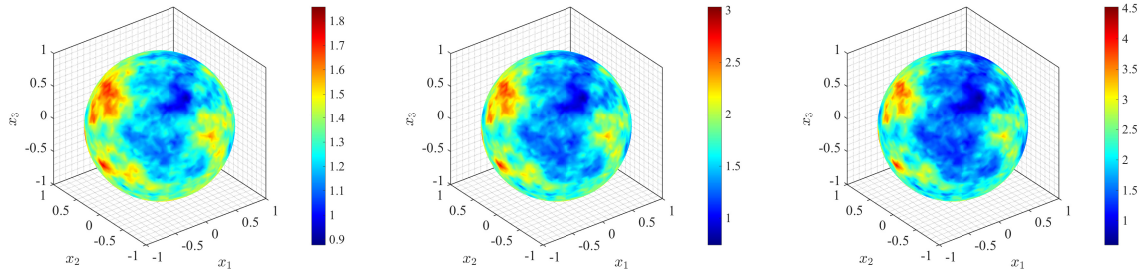

Figure 6.4 – Illustrative results for $\gamma(\mathbf{x}) = 2$ and $\lambda_\theta = 0$. One realization of $\{M_4(\mathbf{x}), \mathbf{x} \in \mathscr{B}\}$ is shown for $\delta = 0.2$ (left), $\delta = 0.4$ (middle) and $\delta = 0.6$ (right).

6.3.2 Application to cylindrical (or polar) orthotropy

In this second application, we consider the case of cylindrical orthotropy, with

$$\mathscr{B} = \{\mathbf{x} \in \mathbb{R}^3 \,:\, x_1^2 + x_2^2 \leqslant 1\,, \quad 0 \leqslant x_3 \leqslant 3\}\,. \tag{6.64}$$

The material is then assumed to exhibit local orthotropy at the location $\mathbf{x}$, where the crystallographic directions are defined by the unit mutually orthogonal vectors $\mathbf{a}(\mathbf{x})$, $\mathbf{b}(\mathbf{x})$ and $\mathbf{c}(\mathbf{x})$. This field of orientation vectors may by chosen as constant and coincident with the global coordinate system to model orthotropic laminates, or spatially dependent to model symmetries in the local coordinate system. Here, we address the second situation and define $\mathbf{a}(\mathbf{x}) = \mathbf{e}_r(\mathbf{x})$, $\mathbf{b}(\mathbf{x}) = \mathbf{e}_\theta(\mathbf{x})$ and $\mathbf{c}(\mathbf{x}) = \mathbf{e}_z(\mathbf{x})$ so that $(\mathbf{x}, \mathbf{e}_r(\mathbf{x}), \mathbf{e}_\theta(\mathbf{x}), \mathbf{e}_z(\mathbf{x}))$ corresponds to the local cylindrical coordinate system at location $\mathbf{x}$. This model is, in particular, relevant to the modeling of spatially dependent wood properties. The associated tensor basis is given by [71]:

$$\begin{aligned}
&[\![E_1]\!] = \mathbf{a}\otimes\mathbf{a}\otimes\mathbf{a}\otimes\mathbf{a}\,, \quad [\![E_2]\!] = \mathbf{b}\otimes\mathbf{b}\otimes\mathbf{b}\otimes\mathbf{b}\,, \quad [\![E_3]\!] = \mathbf{c}\otimes\mathbf{c}\otimes\mathbf{c}\otimes\mathbf{c}\,,\\
&[\![E_4]\!] = \mathbf{a}\otimes\mathbf{a}\otimes\mathbf{b}\otimes\mathbf{b}\,, \quad [\![E_5]\!] = \mathbf{b}\otimes\mathbf{b}\otimes\mathbf{c}\otimes\mathbf{c} + \mathbf{c}\otimes\mathbf{c}\otimes\mathbf{b}\otimes\mathbf{b}\,,\\
&[\![E_6]\!] = \mathbf{a}\otimes\mathbf{a}\otimes\mathbf{c}\otimes\mathbf{c} + \mathbf{c}\otimes\mathbf{c}\otimes\mathbf{a}\otimes\mathbf{a}\,, \quad [\![E_7]\!] = (\mathbf{a}\otimes\mathbf{b} + \mathbf{b}\otimes\mathbf{a})\otimes(\mathbf{a}\otimes\mathbf{b} + \mathbf{b}\otimes\mathbf{a})/2\,,\\
&[\![E_8]\!] = (\mathbf{b}\otimes\mathbf{c} + \mathbf{c}\otimes\mathbf{b})\otimes(\mathbf{b}\otimes\mathbf{c} + \mathbf{c}\otimes\mathbf{b})/2\,, \quad [\![E_9]\!] = (\mathbf{a}\otimes\mathbf{c} + \mathbf{c}\otimes\mathbf{a})\otimes(\mathbf{a}\otimes\mathbf{c} + \mathbf{c}\otimes\mathbf{a})/2\,,
\end{aligned} \tag{6.65}$$

where the spatial dependence of the quantities in the right-hand side has been omitted for notational convenience. The random field of elasticity tensor is written as

$$[\mathbf{M}(\mathbf{x})] = \sum_{i=1}^{9} M_i(\mathbf{x})[E_i(\mathbf{x})] = \left\{ \begin{bmatrix} M_1(\mathbf{x}) & M_4(\mathbf{x}) & M_6(\mathbf{x}) \\ M_4(\mathbf{x}) & M_2(\mathbf{x}) & M_5(\mathbf{x}) \\ M_6(\mathbf{x}) & M_5(\mathbf{x}) & M_3(\mathbf{x}) \end{bmatrix}, M_7(\mathbf{x}), M_8(\mathbf{x}), M_9(\mathbf{x}) \right\}. \tag{6.66}$$

Hence, the random matrix $[\mathbf{N}_1(\mathbf{x})]$ writes

$$[\mathbf{N}_1(\mathbf{x})] = \begin{bmatrix} M_1(\mathbf{x}) & M_4(\mathbf{x}) & M_6(\mathbf{x}) \\ M_4(\mathbf{x}) & M_2(\mathbf{x}) & M_5(\mathbf{x}) \\ M_6(\mathbf{x}) & M_5(\mathbf{x}) & M_3(\mathbf{x}) \end{bmatrix} , \tag{6.67}$$

and the dispersion parameter $\delta_{[\mathbf{M}(\mathbf{x})]}$ is found to be such that

$$\delta_{[\mathbf{M}(\mathbf{x})]} = \left\{ \frac{1}{6} \left(3\delta^2_{[\mathbf{N}_1(\mathbf{x})]} + \delta^2_{M_7(\mathbf{x})} + \delta^2_{M_8(\mathbf{x})} + \delta^2_{M_9(\mathbf{x})} \right) \right\}^{1/2} . \tag{6.68}$$

The diffusion tensor $\mathbf{x} \mapsto [D(\mathbf{x})]$ is chosen as

$$[D(\mathbf{x})] = [I_3] + \lambda_\theta \, \mathbf{e}_\theta(\mathbf{x}) \otimes \mathbf{e}_\theta(\mathbf{x}) + \lambda_z \, \mathbf{e}_z(\mathbf{x}) \otimes \mathbf{e}_z(\mathbf{x}) \, , \tag{6.69}$$

where the parameters $\lambda_\theta \geqslant 0$ and $\lambda_z \geqslant 0$ can be adjusted in order to target some correlation ranges along the associated directions. The Markov approximation is constructed with $16,460$ nodes. We consider an isotropic covariance kernel (defined with $\lambda_\theta = \lambda_z = 0$), as well as two anisotropic cases where a predominant correlation is locally imposed along $\mathbf{e}_\theta$ or $\mathbf{e}_z$ as depicted in Fig. 6.5. One realization of the random field $\{\Xi_1(\mathbf{x}), \mathbf{x} \in \mathscr{B}\}$ and the associated realizations $\{M_1(\mathbf{x}), \mathbf{x} \in \mathscr{B}\}$ and $\{M_{11}(\mathbf{x}), \mathbf{x} \in \mathscr{B}\}$ are shown for the isotropic case in Fig. 6.6. As expected, it is seen that the realizations do not exhibit any noticeable feature in terms of orientation. Similar results for the two anisotropic configurations are shown in Figs. 6.7–6.8. In contrast to the isotropic case, it is observed that the realizations can exhibit specific features that may be found representative of subscale details, such as local fiber orientation.

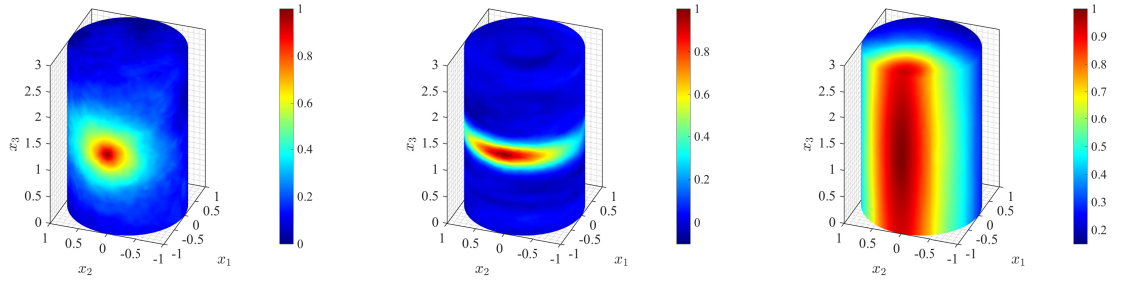

Figure 6.5 – This figure shows the graph of the correlation function $\mathbf{y} \mapsto R_1(\mathbf{x}_0, \mathbf{y})$, estimated with $1,000$ independent realizations, for $(\gamma(\mathbf{x}), \lambda_\theta, \lambda_z) = (2, 0, 0)$ (left panel), $(10, 50, 0.1)$ (middle panel) and $(2, 0, 50)$ (right panel). The reference point $\mathbf{x}_0$ is chosen on the outer surface of the cylinder.

Since the covariance kernel $(\mathbf{x}, \mathbf{y}) \mapsto [R(\mathbf{x}, \mathbf{y})]$ inherited from the choices of κ and $[D]$ is unknown a priori for spatially dependent coefficients, we investigate below, through numerical experiments, the shape of the the covariance kernel $(\mathbf{x}, \mathbf{y}) \mapsto R_1(\mathbf{x}, \mathbf{y})$. For this purpose, we consider three configurations related to directions of interest, namely:

- the radial direction, for which we select $\mathbf{x} = (0, 0, 0)$, $\mathbf{y} = (u, 0, 0)$ or $(0, u, 0)$ with $u \in [-1, 1]$, and let $R_1(\mathbf{x}, \mathbf{y}) = \rho_1(u)$;
- the orthoradial direction, which is explored using $\mathbf{x} = (r_i, 0, 0)$ and $\mathbf{y} = (r_i \cos(\theta), r_i \sin(\theta), 0)$, with $r_i \in \{0.5, 0.75, 1.0\}$ and $\theta \in [-\pi, \pi]$; here, we let $R_1(\mathbf{x}, \mathbf{y}) =: \rho_1(r_i\theta)$, where $r_i\theta$ measures the arc length at $r = r_i$;

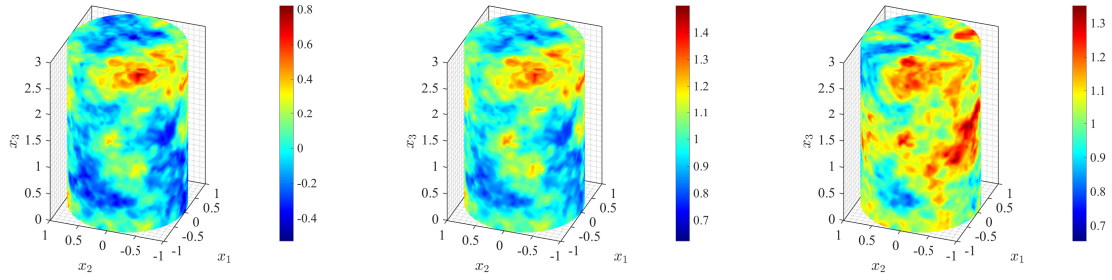

Figure 6.6 – Illustrative results for $\gamma(\mathbf{x}) = 2$ and $\lambda_\theta = \lambda_z = 0$. One realization of $\{\Xi_1(\mathbf{x}), \mathbf{x} \in \mathscr{B}\}$ and the associated realizations of $\{M_1(\mathbf{x}), \mathbf{x} \in \mathscr{B}\}$ and $\{M_{11}(\mathbf{x}), \mathbf{x} \in \mathscr{B}\}$ are shown in the left, middle and right panels, respectively.

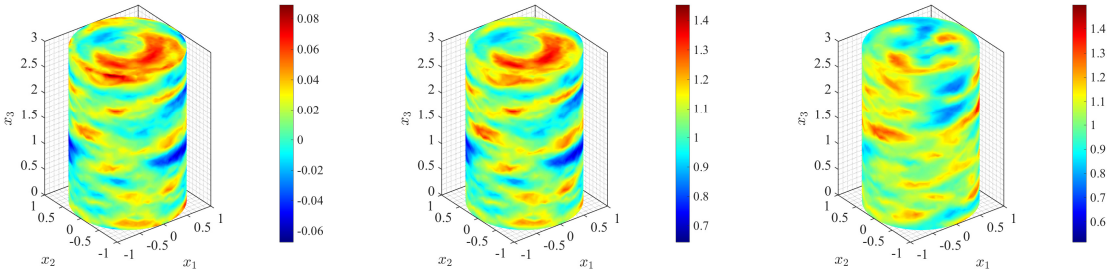

Figure 6.7 – Illustrative results for $\gamma(\mathbf{x}) = 10$ and $\lambda_\theta = 50$ and $\lambda_z = 0.1$. One realization of $\{\Xi_1(\mathbf{x}), \mathbf{x} \in \mathscr{B}\}$ and the associated realizations of $\{M_1(\mathbf{x}), \mathbf{x} \in \mathscr{B}\}$ and $\{M_{11}(\mathbf{x}), \mathbf{x} \in \mathscr{B}\}$ are shown in the left, middle and right panels, respectively.

- the longitudinal direction, where $\mathbf{x} = (u, v, 1.5)$, $\mathbf{y} = (u, v, z)$, $u \in \{-1, 0, 1\}$, $v \in \{-1, 0, 1\}$ and $z = [1, 2]$; we then define $R_1(\mathbf{x}, \mathbf{y}) = \rho_1(z)$.

The covariance functions estimated with 20 000 independent realizations are shown for these three configurations in Fig. 6.9. It can be observed in this figure that the covariance function (expressed in appropriate coordinates) exhibits some invariance properties along preferred directions. These properties are induced by the particular definition $\mathbf{x} \mapsto [D(\mathbf{x})]$, which is chosen in accordance with the geometric symmetries in this application. While this may suggest stationarity, it is worth pointing out that the solution is not stationary for the translation in $\mathbb{R}^3$.

6.4 Closed-form expressions

In this final section, the tensor bases and the expressions of the dispersion parameter are provided for the symmetry classes that were not considered to exemplify the framework (recall that the modified Voigt notation has been used for fourth-order tensors). As indicated previously, the monoclinic system is not considered either due to limited applicability. In the following, the nonlinear transformation $\mathfrak{a}$ of standard Gaussian fields is defined by Eq. (5.46).

6.4.1 Isotropy

In the case of isotropy, the random elasticity tensor writes $[\![\mathbf{C}(\mathbf{x})]\!] = 3C_1(\mathbf{x})[\![E_1]\!] + 2C_2(\mathbf{x})[\![E_2]\!]$ where

$$[\![E_1]\!] = \frac{1}{3}[I_3] \otimes [I_3]\,, \quad [\![E_2]\!] = [I_3] \boxtimes [I_3] - [\![E_1]\!]\,, \tag{6.70}$$

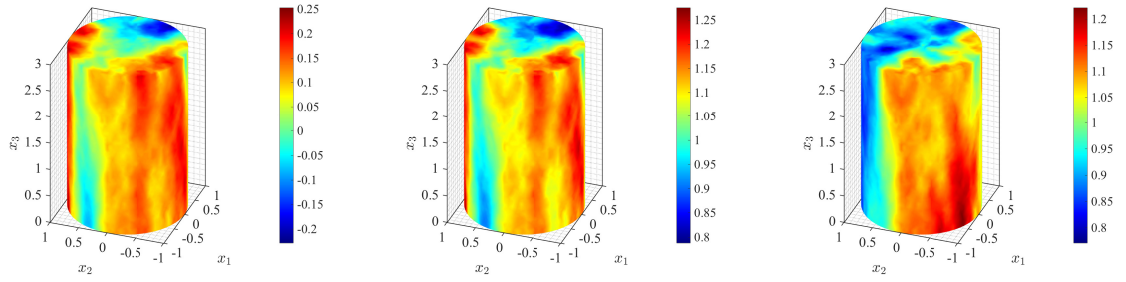

Figure 6.8 – Illustrative results for $\gamma(\mathbf{x}) = 20$ and $\lambda_\theta = 0$ and $\lambda_z = 50$. One realization of $\{\Xi_1(\mathbf{x}), \mathbf{x} \in \mathscr{B}\}$ and the associated realizations of $\{M_1(\mathbf{x}), \mathbf{x} \in \mathscr{B}\}$ and $\{M_{11}(\mathbf{x}), \mathbf{x} \in \mathscr{B}\}$ are shown in the left, middle and right panels, respectively.

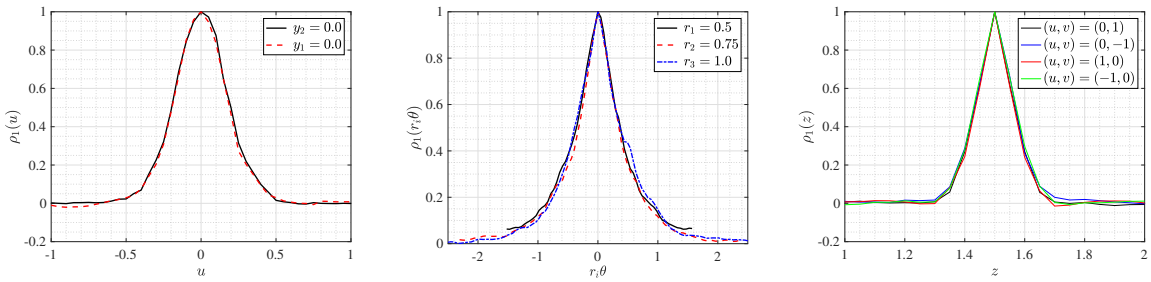

Figure 6.9 – Illustrative results for $\gamma(\mathbf{x}) = 20$ and $\lambda_\theta = 50$ and $\lambda_z = 0.1$. These figures show the estimated covariance kernels in the selected radial, orthoradial and longitudinal directions.

and the dispersion parameter reads as

$$\delta^2_{[\mathbf{M}(\mathbf{x})]} = \frac{1}{6}\left(\delta^2_{M_1(\mathbf{x})} + 5\delta^2_{M_2(\mathbf{x})}\right). \tag{6.71}$$

The random matrix $[\mathbf{M}(\mathbf{x})]$ then writes $[\mathbf{M}(\mathbf{x})] = M_1(\mathbf{x})[E_1] + M_2(\mathbf{x})[E_2]$ where the random variables $M_1(\mathbf{x})$ and $M_2(\mathbf{x})$ are defined as

$$M_k(\mathbf{x}) = \mathbb{o}(\Xi_k(\mathbf{x}), \delta^{-2}_{M_k(\mathbf{x})}, \delta^2_{M_k(\mathbf{x})}), \quad 1 \leqslant k \leqslant 2, \tag{6.72}$$

with $\{\Xi_k(\mathbf{x}), \mathbf{x} \in \mathscr{B}\}$ a normalized Gaussian random field.

6.4.2 Cubic symmetry

Let $(\mathbf{a}(\mathbf{x}), \mathbf{b}(\mathbf{x}), \mathbf{c}(\mathbf{x}))$ define the crystallographic system at the location $\mathbf{x}$ in $\mathscr{B}$. The tensor basis is then defined as

$$[\![E_1]\!] = \frac{1}{3}[I_3] \otimes [I_3], \quad [\![E_2]\!] = [I_3] \boxtimes [I_3] - [\![E_0(\mathbf{x})]\!], \quad [\![E_3(\mathbf{x})]\!] = [\![E_0(\mathbf{x})]\!] - [\![E_1]\!], \tag{6.73}$$

with

$$[\![E_0(\mathbf{x})]\!] = \mathbf{a}(\mathbf{x})\otimes\mathbf{a}(\mathbf{x})\otimes\mathbf{a}(\mathbf{x})\otimes\mathbf{a}(\mathbf{x}) + \mathbf{b}(\mathbf{x})\otimes\mathbf{b}(\mathbf{x})\otimes\mathbf{b}(\mathbf{x})\otimes\mathbf{b}(\mathbf{x}) + \mathbf{c}(\mathbf{x})\otimes\mathbf{c}(\mathbf{x})\otimes\mathbf{c}(\mathbf{x})\otimes\mathbf{c}(\mathbf{x}). \tag{6.74}$$

The dispersion parameter is given by

$$\delta^2_{[\mathbf{M}(\mathbf{x})]} = \frac{1}{6}\left(\delta^2_{M_1(\mathbf{x})} + 3\delta^2_{M_2(\mathbf{x})} + 2\delta^2_{M_3(\mathbf{x})}\right). \tag{6.75}$$

The random matrix $[\mathbf{M}(\mathbf{x})]$ is then decomposed as $[\mathbf{M}(\mathbf{x})] = \sum_{i=1}^{3} M_i(\mathbf{x})[E_i(\mathbf{x})]$, with

$$M_k(\mathbf{x}) = \mathbb{o}(\Xi_k(\mathbf{x}), \delta^{-2}_{M_k(\mathbf{x})}, \delta^2_{M_k(\mathbf{x})}), \quad 1 \leqslant k \leqslant 3. \tag{6.76}$$

6.4.3 Tetragonal symmetry

Let $\mathbf{n}(\mathbf{x})$ be the unit vector defining the preferred direction of the system, and let $\mathbf{a}(\mathbf{x})$ and $\mathbf{b}(\mathbf{x})$ be two unit vectors in $\mathbb{R}^3$ such that $(\mathbf{a}(\mathbf{x}), \mathbf{b}(\mathbf{x}), \mathbf{c}(\mathbf{x}))$ are mutually orthogonal at the location $\mathbf{x}$. Moreover, let $[P(\mathbf{x})]$ and $[Q(\mathbf{x})]$ be two tensors defined as

$$[P(\mathbf{x})] = \mathbf{n}(\mathbf{x}) \otimes \mathbf{n}(\mathbf{x}) \,, \quad [Q(\mathbf{x})] = [I_3] - [P(\mathbf{x})] \,. \tag{6.77}$$

The basis is given by

$$\begin{aligned}
&[\![E_1(\mathbf{x})]\!] = [P(\mathbf{x})] \otimes [P(\mathbf{x})] \,, \quad [\![E_2(\mathbf{x})]\!] = [Q(\mathbf{x})] \otimes [Q(\mathbf{x})]/\sqrt{2} \,, \\
&[\![E_3(\mathbf{x})]\!] = ([P(\mathbf{x})] \otimes [Q(\mathbf{x})] + [Q(\mathbf{x})] \otimes [P(\mathbf{x})])/\sqrt{2} \,, \\
&[\![E_4(\mathbf{x})]\!] = (\mathbf{a}(\mathbf{x}) \otimes \mathbf{b}(\mathbf{x}) + \mathbf{b}(\mathbf{x}) \otimes \mathbf{a}(\mathbf{x})) \otimes (\mathbf{a}(\mathbf{x}) \otimes \mathbf{b}(\mathbf{x}) + \mathbf{b}(\mathbf{x}) \otimes \mathbf{a}(\mathbf{x}))/2 \,, \\
&[\![E_5(\mathbf{x})]\!] = (\mathbf{a}(\mathbf{x}) \otimes \mathbf{a}(\mathbf{x}) - \mathbf{b}(\mathbf{x}) \otimes \mathbf{b}(\mathbf{x})) \otimes (\mathbf{a}(\mathbf{x}) \otimes \mathbf{a}(\mathbf{x}) - \mathbf{b}(\mathbf{x}) \otimes \mathbf{b}(\mathbf{x}))/2 \,, \\
&[\![E_6(\mathbf{x})]\!] = [P(\mathbf{x})] \boxtimes [Q(\mathbf{x})] + [Q(\mathbf{x})] \boxtimes [P(\mathbf{x})] \,.
\end{aligned} \tag{6.78}$$

Furthermore, the dispersion parameter writes

$$\delta^2_{[\mathbf{M}(\mathbf{x})]} = \frac{1}{6} \left(2\delta^2_{[\mathbf{N}_1(\mathbf{x})]} + \delta^2_{M_4(\mathbf{x})} + \delta^2_{M_5(\mathbf{x})} + 2\delta^2_{M_6(\mathbf{x})} \right) . \tag{6.79}$$

For this symmetry class, the random matrix $[\mathbf{M}(\mathbf{x})]$ then writes $[\mathbf{M}(\mathbf{x})] = \sum_{i=1}^{6} M_i(\mathbf{x})[E_i(\mathbf{x})]$, and the symbolic representation takes the form $[\mathbf{M}(\mathbf{x})] = \{[\mathbf{N}_1(\mathbf{x})], N_4(\mathbf{x}), N_5(\mathbf{x}), N_6(\mathbf{x})\}$, where

$$[\mathbf{N}_1(\mathbf{x})] = \begin{bmatrix} M_1(\mathbf{x}) & M_3(\mathbf{x}) \\ M_3(\mathbf{x}) & M_2(\mathbf{x}) \end{bmatrix} . \tag{6.80}$$

The latter is decomposed as $[\mathbf{N}_1(\mathbf{x})] = [\mathbf{H}_1(\mathbf{x})]^T [\mathbf{H}_1(\mathbf{x})]$ with

$$[\mathbf{H}_1(\mathbf{x})] = \frac{\delta_{[\mathbf{N}_1(\mathbf{x})]}}{\sqrt{3}} \begin{bmatrix} \sqrt{2\mathbb{o}(\Xi_1(\mathbf{x}), \gamma_1(\mathbf{x}), 1)} & \Xi_3(\mathbf{x}) \\ 0 & \sqrt{2\mathbb{o}(\Xi_2(\mathbf{x}), \gamma_2(\mathbf{x}), 1)} \end{bmatrix} , \tag{6.81}$$

in which $\gamma_1(\mathbf{x}) = 3/(2\delta^2_{[\mathbf{N}_1(\mathbf{x})]})$ and $\gamma_2(\mathbf{x}) = 3/(2\delta^2_{[\mathbf{N}_1(\mathbf{x})]}) - 1/2$. The remaining random variables $M_k(\mathbf{x})$, $4 \leqslant k \leqslant 6$ are defined as

$$M_k(\mathbf{x}) = \mathbb{o}(\Xi_k(\mathbf{x}), \delta^{-2}_{M_k(\mathbf{x})}, \delta^2_{M_k(\mathbf{x})}) \,. \tag{6.82}$$

6.4.4 Trigonal symmetry

Let $\mathbf{n}(\mathbf{x})$ be the unit vector orthogonal to the plan spanned by the unit vectors $\mathbf{a}(\mathbf{x})$ and $\mathbf{b}(\mathbf{x})$, and assume that an angle of $2\pi/3$ is left between these two vectors in that plane, at the location $\mathbf{x}$. Let us introduce the following tensors:

$$\begin{aligned}
&[P(\mathbf{x})] = \mathbf{n}(\mathbf{x}) \otimes \mathbf{n}(\mathbf{x}) \,, \quad [Q(\mathbf{x})] = [I_3] - [P(\mathbf{x})] \,, \\
&[S(\mathbf{x})] = \sqrt{2/3}(\mathbf{a}(\mathbf{x}) \otimes \mathbf{a}(\mathbf{x}) + \mathbf{a}(\mathbf{x}) \otimes \mathbf{b}(\mathbf{x}) + \mathbf{b}(\mathbf{x}) \otimes \mathbf{a}(\mathbf{x})) \,, \\
&[T(\mathbf{x})] = \sqrt{2/3}(\mathbf{b}(\mathbf{x}) \otimes \mathbf{b}(\mathbf{x}) + \mathbf{a}(\mathbf{x}) \otimes \mathbf{b}(\mathbf{x}) + \mathbf{b}(\mathbf{x}) \otimes \mathbf{a}(\mathbf{x})) \,, \\
&[U(\mathbf{x})] = (\mathbf{n}(\mathbf{x}) \otimes \mathbf{a}(\mathbf{x}) + \mathbf{a}(\mathbf{x}) \otimes \mathbf{n}(\mathbf{x}))/\sqrt{2} \,, \quad [V(\mathbf{x})] = -(\mathbf{n}(\mathbf{x}) \otimes \mathbf{b}(\mathbf{x}) + \mathbf{b}(\mathbf{x}) \otimes \mathbf{n}(\mathbf{x}))/\sqrt{2} \,, \\
&[W(\mathbf{x})] = (4/3)([S(\mathbf{x})] \otimes [U(\mathbf{x})] + [T(\mathbf{x})] \otimes [V(\mathbf{x})] - (1/2)[T(\mathbf{x})] \otimes [U(\mathbf{x})] - (1/2)[S(\mathbf{x})] \otimes [V(\mathbf{x})]) \,, \\
&[Z(\mathbf{x})] = (4/3)([U(\mathbf{x})] \otimes [S(\mathbf{x})] + [V(\mathbf{x})] \otimes [T(\mathbf{x})] - (1/2)[U(\mathbf{x})] \otimes [T(\mathbf{x})] - (1/2)[V(\mathbf{x})] \otimes [S(\mathbf{x})]) \,.
\end{aligned} \tag{6.83}$$

The basis is then defined by the following tensors:

$$\delta^2_{[\mathbf{M}(\mathbf{x})]} = \frac{1}{3}\left(\delta^2_{[\mathbf{N}_1(\mathbf{x})]} + 2\delta^2_{[\mathbf{N}_2(\mathbf{x})]}\right) . \tag{6.84}$$

The random matrix $[\mathbf{M}(\mathbf{x})]$ reads as $[\mathbf{M}(\mathbf{x})] = \sum_{i=1}^{6} M_i(\mathbf{x})[E_i(\mathbf{x})]$ or using the symbolic representation $[\mathbf{M}(\mathbf{x})] = \{[\mathbf{N}_1(\mathbf{x})], [\mathbf{N}_2(\mathbf{x})]\}$, with

$$[\mathbf{N}_1(\mathbf{x})] = \begin{bmatrix} M_1(\mathbf{x}) & M_3(\mathbf{x}) \\ M_3(\mathbf{x}) & M_2(\mathbf{x}) \end{bmatrix} , \quad [\mathbf{N}_2(\mathbf{x})] = \begin{bmatrix} M_4(\mathbf{x}) & M_6(\mathbf{x}) \\ M_6(\mathbf{x}) & M_5(\mathbf{x}) \end{bmatrix} . \tag{6.85}$$

Each of the above matrix are decomposed as $[\mathbf{N}_j(\mathbf{x})] = [\mathbf{H}_j(\mathbf{x})]^T[\mathbf{H}_j(\mathbf{x})]$ where

$$[\mathbf{H}_1(\mathbf{x})] = \frac{\delta_{[\mathbf{N}_1(\mathbf{x})]}}{\sqrt{3}} \begin{bmatrix} \sqrt{2\mathbb{Q}(\Xi_1(\mathbf{x}), \gamma_1^{(1)}(\mathbf{x}), 1)} & \Xi_3(\mathbf{x}) \\ 0 & \sqrt{2\mathbb{Q}(\Xi_2(\mathbf{x}), \gamma_2^{(1)}(\mathbf{x}), 1)} \end{bmatrix} , \tag{6.86}$$

and

$$[\mathbf{H}_2(\mathbf{x})] = \frac{\delta_{[\mathbf{N}_2(\mathbf{x})]}}{\sqrt{3}} \begin{bmatrix} \sqrt{2\mathbb{Q}(\Xi_4(\mathbf{x}), \gamma_1^{(2)}(\mathbf{x}), 1)} & \Xi_6(\mathbf{x}) \\ 0 & \sqrt{2\mathbb{Q}(\Xi_5(\mathbf{x}), \gamma_2^{(2)}(\mathbf{x}), 1)} \end{bmatrix} , \tag{6.87}$$

in which $\gamma_\ell^{(j)}(\mathbf{x}) = 3/(2\delta^2_{[\mathbf{N}_j(\mathbf{x})]}) + (1-\ell)/2$, for $1 \leqslant j, \ell \leqslant 2$.

6.5 Conclusion

In this chapter, a unified approach to the modeling and simulation of (non-Gaussian) random fields of elasticity tensors was proposed [34]. The information-theoretic stochastic representation builds upon the so-called Walpole tensor decomposition, which allows the probabilistic model to be constructed using independent matrix-valued and scalar-valued random fields. In contrast to alternative approaches proposed elsewhere, the model can be sampled through a memoryless transformation, hence providing substantial computational savings. Two applications involving weak symmetries and spherical and cylindrical geometries were finally given in order to exemplify some modeling capabilities of the framework. In particular, it was shown that an appropriate parametrization of the underlying Gaussian fields (through the diffusion field) allows specific features (such as those related to subscale details, including morphological anisotropy) to be prescribed on the sample paths of the random field of elasticity tensor. The model and generator are readily applicable, for instance, to the modeling of composite laminates and wood species, as well as to the representation of, *e.g.*, bone properties (which may be modeled as a transversely isotropic material) in computational biomechanics.

Conclusion and Perspectives

General conclusion

In this thesis, we have addressed the construction, identification and simulation of stochastic nonlinear constitutive models. The proper randomization of homogeneous, isotropic Ogden-type stored energy functions was first tackled in the case of compressible and incompressible hyperelastic media. This problem was approached within the framework of information theory. More precisely, the principle of maximum entropy was invoked to impose constraints related to the mathematical analysis of weak formulations in finite elasticity. The obtained stochastic Ogden potentials are, in particular, polyconvex and coercive almost surely, which makes the associated stochastic nonlinear boundary value problem well posed. They can thus be used to perform uncertainty propagation through nonlinear models, using an appropriate randomization around a nominal model, or to regularize underdetermined statistical inverse problems. They can also be used as prior models in a Bayesian formulation to model identification. Two probabilistic models were derived to offer various levels of modeling flexibility, and explicit results for Neo-Hookean and Mooney-Rivlin materials were provided. The relevance of the newly constructed potentials to reproduce experimental variability was then assessed on several databases for soft biological tissues, available elsewhere. A simple identification procedure was specifically devised, and it was shown that the stochastic Ogden stored energy functions enable the accurate modeling of stochastic hyperelastic responses for a variety of materials, over a wide range of strain rates.

The construction of surrogate models for nonlinear multiscale solution maps was subsequently presented, and two strategies were proposed. In a first approach, the homogenized potential was expanded in a polynomial series involving the macroscopic deformations. Extensive numerical benchmarks were conducted on various deterministic and random microstructures. It was shown that the polynomial approximant remains very accurate over the considered sets of deformations, regardless of the underlying microstructural anisotropy. These results are found in accordance with other theoretical analyses developed elsewhere. In a second approach, the definition of closest approximations into predefined sets of stored energy functions was proposed. While this strategy induces a non-vanishing residual between the surrogate and the reference solution, it allows the multiscale information to be transferred back-and-forth between the microscopic and macroscopic scales at no additional cost. These two approaches were then gauged against each other and compared to the FE^2 method, and the projection-based approximant was shown to still deliver very satisfactory results for the localization and magnitude of the peak Von Mises stress.

In a third stage of development, the modeling and robust simulation of spatially varying, anisotropic stored energy functions were considered. Here, a prototypical anisotropic potential was selected and involves structural tensors associated with the class of transversely isotropic

behaviors. As with the homogeneous case, the maximum entropy principle was invoked and used to construct the system of first-order marginal probability distributions of the non-Gaussian field, accounting for constraints related to the stochastic nonlinear boundary value problem. A methodology allowing the random field model to be sampled on non-convex domains was further proposed and applied for modeling stochasticity in arterial walls. In particular, the capability of the proposed computational framework to generate very different correlation kernels on a real, patient-specific geometry was demonstrated. The forward propagation of the uncertainties hence generated was finally achieved to estimate the probability density function of the maximum Von Mises stress in the vascular vessel.

In the last part of this work, a probabilistic model unifying previous information-theoretic formulations for random fields of elasticity tensors was presented. The random field model allows fluctuations in all classes of material symmetries (ranging from isotropy to fully anisotropic media) to be generated and involves a low-dimensional, physically-based parametrization. The associated random generator turns out to be robust and simple. Numerical illustrations were finally performed in the case of materials exhibiting spherical isotropy and cylindrical orthotropy on curved geometries.

Perspectives

In addition to technical refinements that could be proposed here and there, some future research directions can be identified as follows.

- First, it would be very interesting to complement the probabilistic modeling effort with developments related to the identification and validation of the stochastic models, using experimental data.
- Second, introducing time-dependency in the proposed stochastic formulations is a very natural extension that would broaden the scope of applications for some soft biological tissues, such as brain tissues.
- Third, investigating the construction and assessing the accuracy of approximants for three-dimensional, highly nonlinear multiscale solution maps are necessary steps toward the integration of homogenization-based surrogates.

Appendix A

Stress and Tangent Tensors

In this annex, closed-form expressions of the second Piola-Kirchhoff stress tensor $\{[\mathbf{S}_\epsilon(\mathbf{x})], \mathbf{x} \in \mathscr{B}\}$ and fourth-order tangent modulus $\{[\![\mathbf{L}_\epsilon(\mathbf{x})]\!], \mathbf{x} \in \mathscr{B}\}$ are given for the stochastic stored energy function defined by Eq. (5.23). Note first that the latter can be decomposed into volumetric and isochoric contributions as follows:

$$\mathcal{W}_\epsilon(\mathbf{x}, [C]) = \overline{\mathcal{W}}_\epsilon(\mathbf{x}, [\overline{C}]) + \sum_{\ell=1}^{2} \frac{G_{4\epsilon}(\mathbf{x})}{\beta_4} \exp\left(\beta_4 \langle \|[F]\mathbf{a}_\ell(\mathbf{x})\|_2^2 - 1\rangle_m^2\right) + G_{3\epsilon}(\mathbf{x}) h(J)\,, \tag{A.1}$$

with $J = \sqrt{\det([C])}$, $h(J) = J^{\beta_3} + J^{-\beta_3}$ and

$$\overline{\mathcal{W}}_\epsilon(\mathbf{x}, [\overline{C}]) = G_{1\epsilon}(\mathbf{x}) \mathrm{Tr}([\overline{C}]) + G_{2\epsilon}(\mathbf{x}) (\mathrm{Tr}(\mathrm{Cof}([\overline{C}])))^{3/2}\,. \tag{A.2}$$

Using the definition of the second Piola-Kirchhoff stress tensor (see Eq. (1.14)), it follows that

$$[\mathbf{S}_\epsilon(\mathbf{x}, [C])] = [\mathbf{S}_\epsilon^{\mathrm{isc}}(\mathbf{x}, [C])] + G_{3\epsilon}(\mathbf{x}) J h'(J) [C]^{-1} \tag{A.3}$$

where the random isochoric stress tensor writes

$$\begin{aligned}[\mathbf{S}_\epsilon^{\mathrm{isc}}(\mathbf{x}, [C])] = {} & J^{-2/3} \left([I_3] \boxtimes [I_3] - \frac{1}{3} [C]^{-1} \otimes [C] \right) : [\overline{\mathbf{S}}_\epsilon(\mathbf{x}, [\overline{C}])] \\ & + \sum_{\ell=1}^{2} 4 G_{4\epsilon}(\mathbf{x}) \langle \mathrm{Tr}([C][M_\ell(\mathbf{x})]) - 1 \rangle_m \exp\left(\beta_4 \langle \mathrm{Tr}([C][M_\ell(\mathbf{x})] - 1\rangle_m^2\right) [M_\ell(\mathbf{x})]\,,\end{aligned} \tag{A.4}$$

where $([A] \boxtimes [B])_{ijkl} = (A_{ik}B_{jl} + A_{il}B_{jk})/2$ for $1 \leqslant i, j, k, l \leqslant 3$ and

$$\overline{\mathbf{S}}_\epsilon(\mathbf{x}, [\overline{C}])_{ij} = 2 \frac{\partial \overline{\mathcal{W}}_\epsilon(\mathbf{x}, [\overline{C}])}{\partial \overline{C}_{ij}}\,, \quad 1 \leqslant i, j \leqslant 3\,, \tag{A.5}$$

Let then $\{[\![\mathbf{L}_\epsilon(\mathbf{x}, [C])]\!], (\mathbf{x}, [C]) \in \mathscr{B} \times \mathbb{S}_+^3\}$ be the fourth-order elasticity tensor defined as

$$\mathbf{L}_\epsilon(\mathbf{x}, [C])_{ijkl} = 4 \frac{\partial^2 \mathcal{W}_\epsilon(\mathbf{x}, [C])}{\partial C_{ij} \partial C_{kl}}\,, \quad 1 \leqslant i, j, k, l \leqslant 3\,. \tag{A.6}$$

From Eq. (A.3), it is deduced that $[\![\mathbf{L}_\epsilon(\mathbf{x}, [C])]\!]$ can be decomposed as

$$[\![\mathbf{L}_\epsilon(\mathbf{x}, [C])]\!] = [\![\mathbf{L}_\epsilon^{\mathrm{isc}}(\mathbf{x}, [C])]\!] + [\![\mathbf{L}_\epsilon^{\mathrm{vol}}(\mathbf{x}, [C])]\!] + [\![\mathbf{L}_\epsilon^{\mathrm{ani}}(\mathbf{x}, [C])]\!]\,, \tag{A.7}$$

where the isochoric contribution writes

$$\begin{aligned}[\![\mathbf{L}_\epsilon^{\mathrm{isc}}(\mathbf{x},[C])]\!] = J^{-4/3}\Big([I_3]\boxtimes[I_3]-\frac{1}{3}[C]^{-1}\otimes[C]\Big) : [\![\overline{\mathbf{L}}_\epsilon(\mathbf{x},[\overline{C}])]\!] : \Big([I_3]\boxtimes[I_3]-\frac{1}{3}[C]\otimes[C]^{-1}\Big)\\ -\frac{2}{3}\left([\mathbf{S}_\epsilon^{\mathrm{isc}}(\mathbf{x},[C])]\otimes[C]^{-1}+[C]^{-1}\otimes[\mathbf{S}_\epsilon^{\mathrm{isc}}(\mathbf{x},[C])]\right)\\ +\frac{2}{3}J^{-2/3}\mathrm{Tr}([C][\overline{\mathbf{S}}_\epsilon(\mathbf{x},[\overline{C}])])\Big([C]^{-1}\boxtimes[C]^{-1}-\frac{1}{3}[C]^{-1}\otimes[C]^{-1}\Big)\,,\end{aligned} \tag{A.8}$$

the volumetric contribution reads as

$$[\![\mathbf{L}_\epsilon^{\mathrm{vol}}(\mathbf{x},[C])]\!] = G_{3\epsilon}(\mathbf{x})J\left(h'(J)+Jh''(J)\right)[C]^{-1}\otimes[C]^{-1}-2G_{3\epsilon}(\mathbf{x})Jh'(J)[C]^{-1}\boxtimes[C]^{-1}\,, \tag{A.9}$$

and the anisotropic elasticity tensor is given by

$$\begin{aligned}[\![\mathbf{L}_\epsilon^{\mathrm{ani}}(\mathbf{x},[C])]\!] = \sum_{\ell=1}^{2} 8G_{4\epsilon}(\mathbf{x})\mathbb{1}_{\mathrm{Tr}([C][M_\ell(\mathbf{x})])>1}([C])\exp(\beta_4\langle\mathrm{Tr}([C][M_\ell(\mathbf{x})])-1\rangle_m^2)[M_\ell(\mathbf{x})]\otimes[M_\ell(\mathbf{x})]\\ +\sum_{\ell=1}^{2}16G_{4\epsilon}(\mathbf{x})\beta_4\langle\mathrm{Tr}([C][M_\ell(\mathbf{x})])-1\rangle_m\exp(\beta_4\langle\mathrm{Tr}([C][M_\ell(\mathbf{x})])-1\rangle_m^2)[M_\ell(\mathbf{x})]\otimes[M_\ell(\mathbf{x})]\,.\end{aligned} \tag{A.10}$$

For all $\mathbf{x}\in\mathscr{B}$ and $[C]\in\mathbb{S}_+^3$, the random tensor $[\![\overline{\mathbf{L}}(\mathbf{x},[\overline{C}])]\!]$ involved in Eq. (A.8) is defined as

$$\overline{\mathbf{L}}_\epsilon(\mathbf{x},[\overline{C}])_{ijkl} = 4\frac{\partial^2\overline{\mathcal{W}}_\epsilon(\mathbf{x},[\overline{C}])}{\partial\overline{C}_{ij}\partial\overline{C}_{k\ell}}\,,\quad 1\leqslant i,j,k,l\leqslant 3\,. \tag{A.11}$$

Recalling that in the above equations the random field $\{\mathbf{G}_\epsilon(\mathbf{x}),\mathbf{x}\in\mathscr{B}\}$ is defined componentwise by Eq. (5.24), realizations of the stress and elasticity tensor can be decomposed in view of solving the stochastic boundary value problems of interest.

Appendix B

Weak Formulation and Static Condensation

In this section, we describe the weak formulation that has been used for solving the nonlinear boundary value problems in chapter 5. The latter are solved with the finite element method and a total Lagrangian formulation [152, 153, 109]; see also [168, 171] for a discussion about advances techniques for the numerical modeling of arterial walls. In order to circumvent the well-known locking phenomenon raised by quasi-incompressibility, we have recourse to a three-field formulation with static condensation (mean dilation method) [208, 209, 210]. More precisely, a $\mathbb{P}_2 - \mathbb{P}_0 - \mathbb{P}_0$ discretization is used, and the displacement-based formulation is solved with a standard Newton-Raphson combined with load stepping scheme. A parallel finite element solver was implemented with Sandia C++ Trilinos packages [211, 212], and validated by using numerical benchmarks and the method of manufactured solution. We consider the boundary value problem defined in the reference configuration (see Eq. (1.9) in the deterministic setting) where the natural boundary condition is given by the deformation dependent load $\mathbf{h}(\mathbf{x}) = \mathcal{P}\det([F_\varphi(\mathbf{x})])[F_\varphi(\mathbf{x})]^{-T}\mathbf{n}(\mathbf{x})$, with $\mathcal{P} \leqslant 0$, for $\mathbf{x} \in \Gamma_N$. The weak formulation is then given by [109]: find $\boldsymbol{\varphi} \in \mathbf{H}^1(\mathscr{B}, \mathbb{R}^3)$ such that

$$a(\boldsymbol{\varphi}, \mathbf{v}) = \ell(\boldsymbol{\varphi}, \mathbf{v})\,, \quad \forall \mathbf{v} \in \mathbf{H}^1_0(\mathscr{B}, \mathbb{R}^3)\,, \tag{B.1}$$

where

$$a(\boldsymbol{\varphi}, \mathbf{v}) = \int_{\mathscr{B}} \left([\mathbf{S}^{\mathrm{isc}}_\epsilon(\mathbf{x}, [C_\varphi])] + \det([F_\varphi(\mathbf{x})])h'(\det([F_\varphi(\mathbf{x})]))[C_\varphi(\mathbf{x})]^{-1}\right) : [\delta E(\boldsymbol{\varphi}, \mathbf{v})]\,\mathrm{d}\mathbf{x}\,, \tag{B.2}$$

with $[\delta E(\boldsymbol{\varphi}, \mathbf{v})] = ([\nabla\boldsymbol{\varphi}(\mathbf{x})]^T[\nabla\mathbf{v}(\mathbf{x})] + [\nabla\mathbf{v}(\mathbf{x})]^T[\nabla\boldsymbol{\varphi}(\mathbf{x})])/2$ and

$$\ell(\boldsymbol{\varphi}, \mathbf{v}) = \int_{\Gamma_N} \langle \mathcal{P}\det([F_\varphi(\mathbf{x})])[F_\varphi(\mathbf{x})]^{-T}\mathbf{n}, \mathbf{v}\rangle_2\,\mathrm{d}a\,. \tag{B.3}$$

The three-field formulation [209, 210] consists in introducing two additional fields $\mathbf{x} \mapsto \overline{\Theta}(\mathbf{x})$ and $\mathbf{x} \mapsto \overline{p}(\mathbf{x})$ corresponding to the volume dilatation and hydrostatic pressure, respectively, and such that

$$\int_{\mathscr{B}} \left(\overline{\Theta}(\mathbf{x}) - \det([F_\varphi(\mathbf{x})])\right) q(\mathbf{x})\,\mathrm{d}\mathbf{x} = 0\,, \quad \forall q \in L^2(\mathscr{B}, \mathbb{R}^3)\,, \tag{B.4}$$

and

$$\int_{\mathscr{B}} \left(\overline{p}(\mathbf{x}) - G_{3\epsilon}(\mathbf{x})h'(\det([F_\varphi(\mathbf{x})]))\right) r(\mathbf{x})\,\mathrm{d}\mathbf{x} = 0\,, \quad \forall r \in L^2(\mathscr{B}, \mathbb{R}^3)\,. \tag{B.5}$$

In the following, we denote by $\mathscr{B}_h$ the triangulation of the reference configuration $\mathscr{B}$, such that $\mathscr{B}_h = \cup_{e=1}^{n_e}\mathscr{B}_e$. While the displacement field is assumed to be continuous over $\mathscr{B}$, the additional

scalar fields $\overline{\Theta}$ and $\overline{p}$ are chosen to be constant in each element $\mathscr{B}_e$ of the triangulation $\mathscr{B}_h$. This approach is referred to as static condensation or mean dilatation method [208] and leads to $\overline{\Theta}_e = \overline{\Theta}(\mathbf{x})\big|_{\mathscr{B}_e}$ and $\overline{p}_e = \overline{p}(\mathbf{x})|_{\mathscr{B}_e}$, with

$$\overline{\Theta}_e = \frac{1}{|\mathscr{B}_e|}\int_{\mathscr{B}_e} \det([F_\varphi(\mathbf{x})])\,\mathrm{d}\mathbf{x}\,, \quad \overline{p}_e = \frac{1}{|\mathscr{B}_e|}\int_{\mathscr{B}_e} G_{3\epsilon}(\mathbf{x}) h'(\overline{\Theta}_e)\,\mathrm{d}\mathbf{x}\,. \tag{B.6}$$

The three-field formulation then reduces to a standard displacement formulation, *i.e.*, the non-linear form a writes

$$a(\boldsymbol{\varphi},\mathbf{v}) = \sum_{e=1}^{n_e}\int_{\mathscr{B}_e} \left([\mathbf{S}^{\mathrm{isc}}_\epsilon(\mathbf{x},[C_\varphi])] + \det([F_\varphi(\mathbf{x})])\overline{p}_e[C_\varphi(\mathbf{x})]^{-1}\right) : [\delta E(\boldsymbol{\varphi},\mathbf{v})]\,\mathrm{d}\mathbf{x}\,, \tag{B.7}$$

Herein, the weak formulation is then solved with a standard Newton-Raphson, that is

$$\text{for } k \geqslant 0: \quad a'(\boldsymbol{\varphi}^{(k)},\mathbf{v}).(\Delta\boldsymbol{\varphi}^{(k+1)}) - \ell(\boldsymbol{\varphi}^{(k)},\mathbf{v}).(\Delta\boldsymbol{\varphi}^{(k+1)}) = \ell(\boldsymbol{\varphi},\mathbf{v}) - a(\boldsymbol{\varphi},\mathbf{v})\,, \tag{B.8}$$

where $a'(\boldsymbol{\varphi}^{(k)},\mathbf{v}).(\Delta\boldsymbol{\varphi}^{(k+1)})$ and $\ell(\boldsymbol{\varphi}^{(k)},\mathbf{v}).(\Delta\boldsymbol{\varphi}^{(k+1)})$ denote the Gateaux derivatives at $\boldsymbol{\varphi} = \boldsymbol{\varphi}^{(k)}$ with the increment $\Delta\boldsymbol{\varphi}^{(k+1)} = \boldsymbol{\varphi}^{(k+1)} - \boldsymbol{\varphi}^{(k)}$. Using the chain rule, it can first be deduced that

$$\begin{aligned}
a'(\boldsymbol{\varphi},\mathbf{v}).(\Delta\boldsymbol{\varphi}) &= \sum_{e=1}^{n_e}\int_{\mathscr{B}_e} [\delta E(\boldsymbol{\varphi},\mathbf{v})] : [\![\mathbf{L}^e_\epsilon(\mathbf{x},[C_\varphi])]\!] : [\delta E(\boldsymbol{\varphi},\Delta\boldsymbol{\varphi})]\,\mathrm{d}\mathbf{x} \\
&+ \sum_{e=1}^{n_e}\int_{\mathscr{B}_e} ([\mathbf{S}_\epsilon(\mathbf{x},[C_\varphi]) + \det([F_\varphi])\overline{p}_e[C_\varphi]^{-1}) : [\nabla\Delta\boldsymbol{\varphi}(\mathbf{x})]^T[\nabla\mathbf{v}(\mathbf{x})]\,\mathrm{d}\mathbf{x} \\
&+ \sum_{e=1}^{n_e}\frac{h''(\overline{\Theta}_e)}{|\mathscr{B}_e|^2}\int_{\mathscr{B}_e} J_\varphi[C_\varphi]^{-1} : [\delta E(\boldsymbol{\varphi},\mathbf{v})]\mathrm{d}\mathbf{x}\int_{\mathscr{B}_e} G_{3\epsilon}(\mathbf{x})\mathrm{d}\mathbf{x}\int_{\mathscr{B}_e} J_\varphi[C_\varphi]^{-1} : [\delta E(\boldsymbol{\varphi},\Delta\boldsymbol{\varphi})]\mathrm{d}\mathbf{x}\,,
\end{aligned} \tag{B.9}$$

with

$$[\![\mathbf{L}^e_\epsilon(\mathbf{x},[C_\varphi])]\!] = [\![\mathbf{L}^{\mathrm{isc}}_\epsilon(\mathbf{x},[C_\varphi])]\!] + J_\varphi\overline{p}_e([C_\varphi]^{-1}\otimes[C_\varphi]^{-1} - 2[C_\varphi]^{-1}\boxtimes[C_\varphi]^{-1}) + [\![\mathbf{L}^{\mathrm{ani}}_\epsilon(\mathbf{x},[C_\varphi])]\!] \tag{B.10}$$

and $J_\varphi(\mathbf{x}) = \det([F_\varphi(\mathbf{x})])$. The pressure load being deformation dependent, the linearization of the form $(\boldsymbol{\varphi},\mathbf{v}) \mapsto \ell(\boldsymbol{\varphi},\mathbf{v})$ is rather complicated. This issue can be circumvented by having recourse to a parameterization of the surface on which the pressure load is applied [141, 109], that is

$$\ell(\boldsymbol{\varphi},\mathbf{v}) = \sum_{e=1}^{n_{\Gamma_N}}\int_{\Gamma^{\boldsymbol{\xi}}_e} \mathcal{P}\langle\widehat{\mathbf{x}}_{,\xi_1}(\boldsymbol{\xi})\times\widehat{\mathbf{x}}_{,\xi_2}(\boldsymbol{\xi}),\mathbf{v}\rangle\,\mathrm{d}\xi_1\mathrm{d}\xi_2\,, \tag{B.11}$$

in which $\widehat{\mathbf{x}}(\boldsymbol{\xi}) = \boldsymbol{\varphi}(\mathbf{x})$ in $\mathscr{B}_e$. It can be deduced that the first Gateaux derivative writes

$$\ell'(\boldsymbol{\varphi},\mathbf{v}).(\Delta\boldsymbol{\varphi}) = \sum_{e=1}^{n_{\Gamma_N}}\int_{\Gamma^{\boldsymbol{\xi}}_e} \mathcal{P}\langle\Delta\boldsymbol{\varphi}_{,\xi_1}(\mathbf{x})\times\widehat{\mathbf{x}}_{,\xi_2}(\boldsymbol{\xi}) + \Delta\boldsymbol{\varphi}_{,\xi_2}(\mathbf{x})\times\widehat{\mathbf{x}}_{,\xi_1}(\boldsymbol{\xi}),\mathbf{v}\rangle\,\mathrm{d}\xi_1\mathrm{d}\xi_2\,. \tag{B.12}$$

Note that this leads to a non self-adjoint operator (and thus a non-symmetric tangent matrix within the Newton-Raphson algorithm) but this issue can be circumvented in some particular cases such as a closed boundary surface Γ_N or fixed contour $\partial\Gamma_N$ [141]. Closed-form expressions of the discretized matrices and vectors can be found in, *e.g.*, [141, 109].

Bibliography

[1] R. Ghanem and P. Spanos. *Stochastic finite elements: a Spectral Approach.* Springer, New-York, 1991.

[2] R. Ghanem, D. Higdon, and H. Owhadi. *Handbook of uncertainty quantification.* Springer, 2017.

[3] O. P. Le Maître and O. M. Knio. *Spectral Methods for Uncertainty Quantification with Applications to Computational Fluid Dynamics.* Springer-Verlag New York, 2010.

[4] T.J. Sullivan. *Introduction to uncertainty quantification*, volume 63. Springer, 2015.

[5] C. Soize. *Uncertainty Quantification: An Accelerated Course with Advanced Applications in Computational Engineering*, volume 47. Springer, 2017.

[6] K. Miller and K. Chinzei. Mechanical properties of brain tissue in tension. *Journal of biomechanics*, 35(4):483–490, 2002.

[7] K. Miller and K. Chinzei. Constitutive modelling of brain tissue: experiment and theory. *Journal of biomechanics*, 30(11):1115–1121, 1997.

[8] F. Velardi, F. Fraternali, and M. Angelillo. Anisotropic constitutive equations and experimental tensile behavior of brain tissue. *Biomechanics and modeling in mechanobiology*, 5(1):53–61, 2006.

[9] M. Hrapko, J.A.W. Van Dommelen, G.W.M. Peters, and J.S.H.M. Wismans. Characterisation of the mechanical behaviour of brain tissue in compression and shear. *Biorheology*, 45(6):663–676, 2008.

[10] B. Rashid, M. Destrade, and M.D. Gilchrist. Mechanical characterization of brain tissue in compression at dynamic strain rates. *Journal of the mechanical behavior of biomedical materials*, 10:23–38, 2012.

[11] B. Rashid, M.D. Gilchrist, and M. Destrade. Experimental characterisation of neural tissue at collision speeds. In *International Research Council on Biomechanics of Injury Conference (IRCOBI 2012)*. International Research Council on Biomechanics of Injury (IRCOBI), 2012.

[12] X. Jin, F. Zhu, H. Mao, M. Shen, and K.H. Yang. A comprehensive experimental study on material properties of human brain tissue. *Journal of Biomechanics*, 46(16):2795 – 2801, 2013.

[13] B. Rashid, M. Destrade, and M.D. Gilchrist. Mechanical characterization of brain tissue in simple shear at dynamic strain rates. *Journal of the mechanical behavior of biomedical materials*, 28:71–85, 2013.

[14] S. Umale, C. Deck, N. Bourdet, P. Dhumane, L. Soler, J. Marescaux, and R. Willinger. Experimental mechanical characterization of abdominal organs: liver, kidney & spleen. *Journal of the mechanical behavior of biomedical materials*, 17:22–33, 2013.

[15] B. Rashid, M. Destrade, and M.D. Gilchrist. Mechanical characterization of brain tissue in tension at dynamic strain rates. *Journal of the mechanical behavior of biomedical materials*, 33:43–54, 2014.

[16] I. Sakuma, Y. Nishimura, C. Chui, E. Kobayashi, H. Inada, X. Chen, and T. Hisada. In vitro measurement of mechanical properties of liver tissue under compression and elongation using a new test piece holding method with surgical glue. In *Surgery Simulation and Soft Tissue Modeling*, pages 284–292. Springer, 2003.

[17] C. Chui, E. Kobayashi, X. Chen, T. Hisada, and I. Sakuma. Combined compression and elongation experiments and non-linear modelling of liver tissue for surgical simulation. *Medical and Biological Engineering and Computing*, 42(6):787–798, 2004.

[18] G.A. Holzapfel, G. Sommer, C.T. Gasser, and P. Regitnig. Determination of layer-specific mechanical properties of human coronary arteries with nonatherosclerotic intimal thickening and related constitutive modeling. *American Journal of Physiology-Heart and Circulatory Physiology*, 289(5):H2048–H2058, 2005.

[19] A. Quarteroni, A. Manzoni, and C. Vergara. The cardiovascular system: mathematical modelling, numerical algorithms and clinical applications. *Acta Numerica*, 26:365–590, 2017.

[20] C. Soize. Non-gaussian positive-definite matrix-valued random fields for elliptic stochastic partial derivative operators. *Computer Methods in Applied Mechanics and Engineering*, 195:26–64, 2006.

[21] S. Das, R. Ghanem, and S. Finette. Polynomial chaos representation of spatio-temporal random field from experimental measurements. *Journal of Computational Physics*, 228:8726–8751, 2009.

[22] Q-A. Ta, D. Clouteau, and R. Cottereau. Modeling of random anisotropic elastic media and impact on wave propagation. *European Journal of Computational Mechanics/Revue Européenne de Mécanique Numérique*, 19(1-3):241–253, 2010.

[23] J. Guilleminot, A. Noshadravan, R. Ghanem, and C. Soize. A probabilistic model for bounded elasticity tensor random fields with application to polycrystalline microstructures. *Computer Methods in Applied Mechanics and Engineering*, 200:1637–1648, 2011.

[24] J. Guilleminot and C. Soize. Non-gaussian positive-definite matrix-valued random fields with constrained eigenvalues: application to random elasticity tensors with uncertain material symmetries. *International Journal for Numerical Methods in Engineering*, 88:1128–1151, 2011.

[25] J. Guilleminot and C. Soize. Generalized stochastic approach for constitutive equation in linear elasticity: A random matrix model. *International Journal for Numerical Methods in Engineering*, 90(5):613–635, 2012.

[26] J. Guilleminot and C. Soize. Stochastic modeling of anisotropy in multiscale analysis of heterogeneous materials: A comprehensive overview on random matrix approaches. *Mechanics of Materials*, 44:35–46, 2012.

[27] J. Guilleminot and C. Soize. Probabilistic modeling of apparent tensors in elastostatics: a maxent approach under material symmetry and stochastic boundedness constraints. *Probabilistic Engineering Mechanics*, 28:118–124, 2012.

[28] J. Guilleminot and C. Soize. Stochastic model and generator for random fields with symmetry properties: Application to the mesoscopic modeling of elastic random media. *SIAM Multiscale Modeling & Simulation*, 11:840–870, 2013.

[29] J. Guilleminot and C. Soize. On the statistical dependence for the components of random elasticity tensors exhibiting material symmetry properties. *Journal of Elasticity*, 111:109–130, 2013.

[30] J. Guilleminot and C. Soize. Isde-based generator for a class of non-gaussian vector-valued random fields in uncertainty quantification. *SIAM Journal on Scientific Computing*, 36:2763–2786, 2014.

[31] B. Staber and J. Guilleminot. Approximate solutions of lagrange multipliers for information-theoretic random field models. *SIAM/ASA Journal on Uncertainty Quantification*, 3:599–621, 2015.

[32] A. Nouy and C. Soize. Random field representations for stochastic elliptic boundary value problems and statistical inverse problems. *European Journal of Applied Mathematics*, 25(3):339–373, 2014.

[33] V. P. Tran, J. Guilleminot, S. Brisard, and K. Sab. Stochastic modeling of mesoscopic elasticity random field. *Mechanics of Materials*, 93:1–12, 2016.

[34] B. Staber and J. Guilleminot. Stochastic modeling and generation of random fields of elasticity tensors: A unified information-theoretic approach. *Comptes Rendus Mécanique*, 345(6):399–416, 2017.

[35] A. Malyarenko and M. Ostoja-Starzewski. A random field formulation of hooke's law in all elasticity classes. *Journal of Elasticity*, 127(2):269–302, 2017.

[36] J. Guilleminot and C. Soize. *Non-Gaussian Random Fields in Multiscale Mechanics of Heterogeneous Materials*, pages 1–9. Springer Berlin Heidelberg, Berlin, Heidelberg, 2017.

[37] A. Clément, C. Soize, and J. Yvonnet. Computational nonlinear stochastic homogenization using a non-concurrent multiscale approach for hyperelastic heterogeneous microstructures analysis. *International Journal for Numerical Methods in Engineering*, 91(8):799–824, 2012.

[38] A. Clément, C. Soize, and J. Yvonnet. Uncertainty quantification in computational stochastic multiscale analysis of nonlinear elastic materials. *Computer Methods in Applied Mechanics and Engineering*, 254:61–82, 2013.

[39] A. Eddhahak-Ouni, I. Masson, E. Allaire, and M. Zidi. Stochastic approach to estimate the arterial pressure. *European Journal of Mechanics-A/Solids*, 28(4):712–719, 2009.

[40] A. Eddhahak-Ouni, I. Masson, F. Mohand-Kaci, and M. Zidi. Influence of random uncertainties of anisotropic fibrous model parameters on arterial pressure estimation. *Applied Mathematics and Mechanics*, 34(5):529–540, 2013.

[41] J. Ma, S. Sahraee, P. Wriggers, and L. De Lorenzis. Stochastic multiscale homogenization analysis of heterogeneous materials under finite deformations with full uncertainty in the microstructure. *Computational Mechanics*, 55(5):819–835, 2015.

[42] L. Xiong, C-K. Chui, Y. Fu, C-L. Teo, and Y. Li. Modeling of human artery tissue with probabilistic approach. *Computers in biology and medicine*, 59:152–159, 2015.

[43] J. Biehler, M.W. Gee, and W.A. Wall. Towards efficient uncertainty quantification in complex and large-scale biomechanical problems based on a bayesian multi-fidelity scheme. *Biomechanics and modeling in mechanobiology*, 14(3):489–513, 2015.

[44] J. Biehler, S. Kehl, M.W. Gee, F. Schmies, J. Pelisek, A. Maier, C. Reeps, H-H. Eckstein, and W.A. Wall. Probabilistic noninvasive prediction of wall properties of abdominal aortic aneurysms using bayesian regression. *Biomechanics and modeling in mechanobiology*, 16(1):45–61, 2017.

[45] B. Staber and J. Guilleminot. Stochastic modeling of a class of stored energy functions for incompressible hyperelastic materials with uncertainties. *Comptes Rendus Mécanique*, 343(9):503–514, 2015.

[46] B Staber and J Guilleminot. Stochastic hyperelastic constitutive laws and identification procedure for soft biological tissues with intrinsic variability. *Journal of the mechanical behavior of biomedical materials*, 65:743–752, 2017.

[47] B. Staber and J. Guilleminot. Stochastic modeling of the ogden class of stored energy functions for hyperelastic materials: the compressible case. *ZAMM-Journal of Applied Mathematics and Mechanics/Zeitschrift für Angewandte Mathematik und Mechanik*, 97(3):273–295, 2017.

[48] B. Staber and J. Guilleminot. A random field model for anisotropic strain energy functions and its application for uncertainty quantification in vascular mechanics. *Computer Methods in Applied Mechanics and Engineering*, 333:94–113, 2018.

[49] L.A. Mihai, T.E. Woolley, and A. Goriely. Stochastic isotropic hyperelastic materials: constitutive calibration and model selection. *Proc. R. Soc. A*, 474(2211):20170858, 2018.

[50] I. Caylak, E. Penner, A. Dridger, and R. Mahnken. Stochastic hyperelastic modeling considering dependency of material parameters. *Computational Mechanics*, pages 1–13, 2018.

[51] C. Truesdell and W. Noll. *The Non-Linear Field Theories of Mechanics*. Springer, Berlin, third edition, 2004.

[52] J.E. Marsden and T.J.R Hughes. *Mathematical Foundations of Elasticity*. Dover, 1983.

[53] P.G. Ciarlet. *Mathematical Elasticity, vol. I: Three-Dimensional Elasticity.* Elsevier Science Publishers, North-Holland, Amsterdam, 1988.

[54] R.W. Ogden. *Non-Linear Elastic Deformations.* Dover Publications, Mineola, New York, 1997.

[55] G.A. Holzapfel. *Nonlinear Solid Mechanics - A Continuum Approach for Engineering.* John Wiley & Sons Ltd, The Atrium, Southern Gate, Chichester, England, 2000.

[56] W. Noll. On the continuity of the solid and fluid states. *Journal of Rational Mechanics and Analysis*, 4:3–81, 1955.

[57] W. Noll. A mathematical theory of the mechanical behavior of continuous media. *Archive for rational Mechanics and Analysis*, 2(1):197–226, 1958.

[58] M. Gurtin. *An introduction to continuum mechanics*, volume 158. Academic press, 1982.

[59] J. Boehler. *Applications of tensor functions in solid mechanics*, volume 292. Springer, 1987.

[60] Q-S. Zheng. Theory of representations for tensor functions–a unified invariant approach to constitutive equations. *Applied Mechanics Reviews*, 47(11):545–587, 1994.

[61] H. Brezis. *Functional analysis, Sobolev spaces and partial differential equations.* Springer Science & Business Media, 2010.

[62] B. Dacorogna. *Direct methods in the calculus of varations.* Springer, second edition, 1989.

[63] T. Roubíček. *Nonlinear partial differential equations with applications*, volume 153. Springer Science & Business Media, 2013.

[64] C. Morrey. Quasi-convexity and the lower semicontinuity of multiple integrals. *Pacific Journal of Mathematics*, 2(1):25–53, 1952.

[65] J.M. Ball. Convexity conditions and existence theorems in nonlinear elasticity. *Archive for Rational Mechanics and Analysis*, 3:337–403, 1977.

[66] S. Müller, T. Qi, and B.S. Yan. On a new class of elastic deformations not allowing for cavitation. *Ann. Inst. Henri Poincaré, Analyse Nonlinéaire*, 11(2):217–243, 1994.

[67] J.M. Ball. Some recent developments in nonlinear elasticity and its applications to materials science. In P.J. Aston, editor, *Nonlinear Mathematics and its Applications*, pages 93–119. Cambridge University Press, Cambridge, 2006.

[68] J.M. Ball. *Some Open Problems in Elasticity. Geometry, Dynamics and Mechanics: 60th Birthday volume for J.E. Marsden.* Springer, 2002.

[69] P.G. Ciarlet and G. Geymonat. Sur les lois de comportement en élasticité non-linéaire compressible. *Les Comptes Rendus de l'Académie des Sciences*, 295:423–426, 1982.

[70] P. Charrier, B. Dacorogna, B. Hanouzet, and P. Laborde. An existence theorem for slightly compressible materials in nonlinear elasticity. *SIAM Journal on Mathematical Analysis*, 19(1):70–85, 1988.

[71] L.J. Walpole. Fourth-rank tensors on the thirty-two crystal classes: Multiplication tables. *Proc. R. Soc. Lond. A*, 391:149–179, 1984.

[72] R. Dautray and J. L. Lions. *Mathematical Analysis and Numerical Methods for Science and Technology. Volume 2: Functional and variational methods.* Springer-Verlag New York, 2000.

[73] M.M. Mehrabadi and S.C. Cowin. Eigentensors of linear anisotropic elastic materials. *The Quarterly Journal of Mechanics and Applied Mathematics*, 43:15–41, 1990.

[74] J. Bernado and A. Smith. *Bayesian Theory.* Wiley, 2000.

[75] A. Gelman, J. Carlin, H. Stern, and D. Rubin. *Bayesian Data Analysis.* Chapman & Hall/CRC, 2003.

[76] R.W. Ogden. Large deformation isotropic elasticity - on the correlation of theory and experiment for compressible rubberlike solids. *Proc. R. Soc. Lond. A*, 326(1567):565–584, 1972.

[77] R.W. Ogden. Large deformation isotropic elasticity - on the correlation of theory and experiment for incompressible rubberlike solids. *Proc. R. Soc. Lond. A*, 328(1575):567–583, 1972.

[78] R.W. Ogden, G. Saccomandi, and I. Sgura. Fitting hyperelastic models to experimental data. *Comput. Mech.*, 34:484–502, 2004.

[79] P. Martins, J. R.M. Natal, and A.J.M. Ferreira. A comparative study of several material models for prediction of hyperelastic properties: Application to silicone-rubber and soft tissues. *Strain*, 42(3):135–147, 2006.

[80] G. Chagnon, M. Rebouah, and D. Favier. Hyperelastic energy densities for soft biological tissues: A review. *Journal of Elasticity*, pages 1–32, 2014.

[81] L.R.G. Treloar. Stress-strain data for vulcanised rubber under various types of deformation. *Transactions of the Faraday Society*, 40:59–70, 1944.

[82] M. Giaquinta, G. Modica, and J. Soucek. Cartesian currents and variational problems for mappings into spheres. *Annali della Scuola Normale Superiore di Pisa*, 16(3):393–485, 1989.

[83] E.T. Jaynes. Information theory and statistical mechanics i. *Physical Review*, 106(4):620–630, 1957.

[84] E.T. Jaynes. Information theory and stastitical mechanics ii. *Physical Review*, 108(2):171–190, 1957.

[85] C.E. Shannon. A mathematical theory of communication. *Bell System Technical Journal*, 27:379–423/623–659, 1948.

[86] C. Soize. A nonparametric model of random uncertainties for reduced matrix models in structural dynamics. *Probabilistic Engineering Mechanics*, 15(3):277–294, 2000.

[87] M. Abramowitz and I.A. Stegun. *Handbook of Mathematical Functions: With Formulas Graphs, And Mathematical Tables.* Dover, New-York, 1970.

[88] S. Kotz, N. Balakrishnan, and N. L. Johnson. *Continuous Multivariate Distributions. Volume 1: Models and Applications*. Wiley, second edition, 2000.

[89] L. Devroye. *Non-Uniform Random Variate Generation*. Springer-Verlag, New-York, 1986.

[90] S. Nadarajah and S. Kotz. On the product and ratio of gamma and beta random variables. *Allgemeines Statistisches Archiv*, 89(4):435–449, 2005.

[91] S. Das and R. Ghanem. A bounded random matrix approach for stochastic upscaling. *Multiscale Model. Simul*, 8(1):296–325, 2009.

[92] A.K. Gupta, L. Cardeño, and D.K. Nagar. Matrix variate kummer-dirichlet distributions. *Journal of Applied Mathematics*, 1(3):117–139, 2001.

[93] C. P. Robert and G. Casella. *Monte Carlo Statistical Methods*. Springer, New York, 2005.

[94] C. Soize. Construction of probability distributions in high dimension using the maximum entropy principle: Applications to stochastic processes, random fields and random matrices. *International Journal for Numerical Methods in Engineering*, 76:1583–1611, 2008.

[95] M.B. Gordy. Computationally convenient distributional assumptions for common-value auctions. *Computational Economics*, 12(1):61–78, 1998.

[96] D.K. Nagar and A.K. Gupta. Matrix-variate kummer-beta distribution. *Journal of the Australian Mathematical Society*, 73(1):11–26, 2002.

[97] P. Koev and A. Edelman. The efficient evaluation of the hypergeometric function of a matrix argument. *Math. Comp.*, 75:833–846, 2006.

[98] S. Madireddy, B. Sista, and K. Vemaganti. A bayesian approach to selecting hyperelastic constitutive models of soft tissue. *Computer Methods in Applied Mechanics and Engineering*, 291:102–122, 2015.

[99] P. Miles, M. Hays, R. Smith, and W. Oates. Bayesian uncertainty analysis of finite deformation viscoelasticity. *Mechanics of Materials*, 91:35–49, 2015.

[100] S. Madireddy, B. Sista, and K. Vemaganti. Bayesian calibration of hyperelastic constitutive models of soft tissue. *Journal of the mechanical behavior of biomedical materials*, 59:108–127, 2016.

[101] S. Mashayekhi, P. Miles, M.Y. Hussaini, and W.S. Oates. Fractional viscoelasticity in fractal and non-fractal media: Theory, experimental validation, and uncertainty analysis. *Journal of the Mechanics and Physics of Solids*, 111:134–156, 2018.

[102] E. Roan and K. Vemaganti. The nonlinear material properties of liver tissue determined from no-slip uniaxial compression experiments. *Journal of biomechanical engineering*, 129(3):450–456, 2007.

[103] C.J. Sparrey and T.M. Keaveny. Compression behavior of porcine spinal cord white matter. *Journal of biomechanics*, 44(6):1078–1082, 2011.

[104] G.A. Holzapfel, T.C. Gasser, and R.W. Ogden. A new constitutive framework for arterial wall mechanics and a comparative study of material models. *Journal of elasticity and the physical science of solids*, 61(1-3):1–48, 2000.

[105] M. Skoge, A. Donev, F. H. Stillinger, and S. Torquato. Packing Hyperspheres in High-Dimensional Euclidean Spaces. *Physical Review E*, 74:041127, 2006.

[106] R. Hill. On constitutive macro-variables for heterogeneous solids at finite strain. *Proceedings of the Royal Society of London A*, 326:131–147, 1972.

[107] R. Hill and J. R. Rice. Elastic potentials and the structures of inelastic constitutive laws. *Proceedings of the Royal Society of London A*, 25(3):448–461, 1973.

[108] C. Miehe, J. Schröder, and M. Becker. Computational homogenization analysis in finite elasticity: material and structural instabilities on the micro- and macro-scales of periodic composites and their interaction. *Computer Methods in Applied Mechanics and Engineering*, 191:4971–5005, 2002.

[109] P. Wriggers. *Nonlinear Finite Element Methods*. Springer, Verlag Berlin Heidelberg, 2008.

[110] G. Guennebaud and B. Jacob *et al.* Eigen v.3. http://eigen.tuxfamily.org, 2010.

[111] N. Wiener. The homogeneous chaos. *American Journal of Mathematics*, 60:897–936, 1938.

[112] R.H. Cameron and W.T. Martin. The orthogonal development of non-linear functionals in series of fourier-hermite functionals. *Annals of Mathematics*, 48(2):385–392, 1947.

[113] D. Xiu and G. Karniadakis. The wiener-askey polynomial chaos for stochastic differential equations. *SIAM Journal on Scientific Computing*, 24:619–644, 2002.

[114] P.J. Davis and P. Rabinowitz. *Methods of numerical integration*. Courier Corporation, 2007.

[115] F. Feyel and J.L. Chaboche. FE^2 multiscale approach for modelling the elastoviscoplastic behaviour of long fiber SiC/Ti composite materials. *Computer Methods in Applied Mechanics and Engineering*, 183:309–330, 2000.

[116] F. Feyel. A multilevel finit element method (FE^2) to describe the response of highly non-linear structures using generalized continua. *Computer Methods in Applied Mechanics and Engineering*, 192:3233–3244, 2003.

[117] M. Mosby and K. Matouš. Hierarchically parallel coupled finite strain multiscale solver for modeling heterogeneous layers. *International Journal for Numerical Methods in Engineering*, 102:748–765, 2015.

[118] Y. Efendiev, T. Hou, and V. Ginting. Multiscale finite element methods for nonlinear problems and their applications. *Communications in Mathematical Sciences*, 2(4):553–589, 2004.

[119] Y. Efendiev and T.Y. Hou. *Multiscale Finite Element Methods: Theory and Applications*. Springer-Verlag New York, 2009.

[120] E. Weinan and B. Engquist. The Heterogeneous Multiscale Methods. *Communications in Mathematical Sciences*, 1(1):87–132, 2003.

[121] E. Weinan, B. Engquist, X. Li, W. Ren, and E. Vanden-Eijnden. The heterogeneous multiscale method: A review. *Communications in Computational Physics*, 2(4):367–450, 2007.

[122] A. Abdulle and Y. Bai. Adaptive reduced basis finite element heterogeneous multiscale method. *Computer Methods in Applied Mechanics and Engineering*, 257:203 – 220, 2013.

[123] A. Abdulle, E. Weinan, B. Engquist, and E. Vanden-Eijnden. The heterogeneous multiscale method. *Acta Numerica*, 21:1–87, 2012.

[124] J. Yvonnet and Q.-C. He. The reduced model multiscale method (R3M) for the non-linear homogenization of hyperelastic media at finite strains. *Journal of Computational Physics*, 223:341–368, 2007.

[125] E. Monteiro, J. Yvonnet, and Q.-C. He. Computational homogenization for nonlinear conduction in heterogeneous materials using model reduction. *Computational Materials Science*, 42:704–712, 2008.

[126] J. Yvonnet, D. Gonzalez, and Q-C. He. Numerically explicit potentials for the homogenization of nonlinear elastic heterogeneous materials. *Computer Methods in Applied Mechanics and Engineering*, 298:2723–2737, 2009.

[127] B.A. Le, J. Yvonnet, and Q-C. He. Computational homogenization of nonlinear elastic materials using neural networks. *International Journal for Numerical Methods in Engineering*, 104:1061–1084, 2015.

[128] I. Temizer and P. Wriggers. An adaptive method for homogenization in orthotropic nonlinear elasticity. *Computer Methods in Applied Mechanics and Engineering*, 35-36:3409–3423, 2007.

[129] I. Temizer and T.I. Zohdi. A numerical method for homogenization in non-linear elasticity. *Computational Mechanics*, 40(2):281–298, 2007.

[130] F. Fritzen and T. Boehlke. Reduced basis homogenization of viscoelastic composites. *Composites Science and Technology*, 76:84–91, 2013.

[131] S. Bhattacharjee and K. Matouš. A nonlinear manifold-based reduced order model for multiscale analysis of heterogeneous hyperelastic materials. *Journal of Computational Physics*, 313:635 – 653, 2016.

[132] K. Matouš, M.D.G. Geers, V.G. Kouznetsova, and A. Gillman. A review of predictive nonlinear theories for multiscale modeling of heterogeneous materials. *Journal of Computational Physics*, 330:192–220, 2017.

[133] M.D.G. Geers, V.G. Kouznetsova, K. Matouš, and J. Yvonnet. Homogenization methods and multiscale modeling: Nonlinear problems. *Encyclopedia of Computational Mechanics Second Edition*, 2017.

[134] A. Clément, C. Soize, and J. Yvonnet. Une méthode multi-échelles pour l'homogénéisation de matériaux hétérogènes non linéaires. In *Proceedings of CSMA 2013*, 2013.

[135] A. Doostan and H. Owhadi. A non-adapted sparse approximation of PDEs with stochastic inputs. *Journal of Computational Physics*, 230(8):3015–3034, 2011.

[136] C. Miehe, J. Schröder, and J. Schotte. Computational homogenization analysis in finite plasticity simulation of texture development in polycrystalline materials. *Computer methods in applied mechanics and engineering*, 171(3-4):387–418, 1999.

[137] M. Petracca, L. Pelà, R. Rossi, S. Oller, G. Camata, and E. Spacone. Regularization of first order computational homogenization for multiscale analysis of masonry structures. *Computational mechanics*, 57(2):257–276, 2016.

[138] S. Müller. Homogenization of nonconvex integral functionals and cellular elastic materials. *Archive for Rational Mechanics and Analysis*, 99:189–212, 1997.

[139] G. Geymont, S. Müller, and N. Triantafyllidis. Homogenization of nonlinear elastic materials, microscopic bifurcation and macroscopic loss of rank-one convexity. *Archive for Rational Mechanics and Analysis*, 122:231–290, 1993.

[140] R. Avazmohammadi and P. Ponte-Castañeda. Macroscopic constitutive relations for elastomers reinforced with short aligned fibers: instabilities and post-bifurcation response. *Journal of Mechanics of Physics and Solids*, 2015.

[141] J. Bonet and R.D. Wood. Nonlinear continuum mechanics for finite element analysis, 1997.

[142] A. Quarteroni, R. Sacco, and F. Saleri. *Numerical mathematics*, volume 37. Springer Science & Business Media, 2010.

[143] M. Arnst and J-P. Ponthot. An overview of nonintrusive characterization, propagation, and sensitivity analysis of uncertainties in computational mechanics. *International Journal for Uncertainty Quantification*, 4(5):387–421, 2014.

[144] C. Soize and C. Desceliers. Computational aspects for constructing realizations of polynomial chaos in high dimensions. *SIAM Journal on Scientific Computing*, 32(5):2820–2831, 2010.

[145] G. Perrin, C. Soize, D. Duhamel, and C. Funfschilling. Identification of polynomial chaos representations in high dimension from a set of realizations. *SIAM Journal on Scientific Computing*, 34(6):A2917–A2945, 2012.

[146] O. Lopez-Parmis and P. Ponte-Castañeda. Second-order estimates for the macroscopic response and loss of ellipcity in porous rubbers at large deformations. *J. Elasticity*, 76:247–287, 2004.

[147] O. Lopez-Pamies and P. Ponte-Castañeda. On the overall behavior, microstructure evolution, and macroscopic stability in reinforced rubbers at large deformations: I?theory. *Journal of the Mechanics and Physics of Solids*, 54(4):807–830, 2006.

[148] O. Lopez-Pamies and P. Ponte-Castañeda. On the overall behavior, microstructure evolution, and macroscopic stability in reinforced rubbers at large deformations: Ii?application to cylindrical fibers. *Journal of the Mechanics and Physics of Solids*, 54(4):831–863, 2006.

[149] J. Moraleda, J. Segurado, and J. LLorca. Finite deformation of incompressible fiber-reinforced elastomers: a computational micromechanics approach. *Journal of the Mechanics and Physics of Solids*, 57(9):1596–1613, 2009.

[150] V. Bouchart, M. Brieu, N. Bhatnagar, and D. Kondo. A multiscale approach of nonlinear composites under finite deformation: Experimental characterization and numerical modeling. *International Journal of Solids and Structures*, 47(13):1737–1750, 2010.

[151] Z.F. Khisaeva and M. Ostoja-Starzewski. On the size of rve in finite elasticity of random composites. *Journal of elasticity*, 85(2):153, 2006.

[152] P.G. Ciarlet. The finite element method for elliptic problems. *Classics in applied mathematics*, 40:1–511, 2002.

[153] S. Brenner and R. Scott. *The mathematical theory of finite element methods*, volume 15. Springer Science & Business Media, 2007.

[154] B. Staber and J. Guilleminot. Functional approximation and projection of stored energy functions in computational homogenization of hyperelastic materials: A probabilistic perspective. *Computer Methods in Applied Mechanics and Engineering*, 313:1–27, 2017.

[155] A. Cohen, M.A. Davenport, and D. Leviatan. On the stability and accuracy of least squares approximations. *Foundations of computational mathematics*, 13(5):819–834, 2013.

[156] A. Chkifa, A. Cohen, R. DeVore, and C. Schwab. Sparse adaptive taylor approximation algorithms for parametric and stochastic elliptic pdes. *ESAIM: Mathematical Modelling and Numerical Analysis*, 47(1):253–280, 2013.

[157] A. Chkifa, A. Cohen, and C. Schwab. High-dimensional adaptive sparse polynomial interpolation and applications to parametric pdes. *Foundations of Computational Mathematics*, 14(4):601–633, 2014.

[158] A. Chkifa, A. Cohen, and C. Schwab. Breaking the curse of dimensionality in sparse polynomial approximation of parametric pdes. *Journal de Mathématiques Pures et Appliquées*, 103(2):400–428, 2015.

[159] A. Chkifa, A. Cohen, G. Migliorati, F. Nobile, and R. Tempone. Discrete least squares polynomial approximation with random evaluations- application to parametric and stochastic elliptic pdes. *ESAIM: Mathematical Modelling and Numerical Analysis*, 49(3):815–837, 2015.

[160] Y. Lanir. A structural theory for the homogeneous biaxial stress-strain relationships in flat collagenous tissues. *Journal of biomechanics*, 12(6):423–436, 1979.

[161] T.C. Gasser, R.W. Ogden, and G.A. Holzapfel. Hyperelastic modelling of arterial layers with distributed collagen fibre orientations. *Journal of the royal society interface*, 3(6):15–35, 2006.

[162] G.A. Holzapfel and R.W. Ogden. Constitutive modelling of arteries. *Proceedings of the Royal Society of London A: Mathematical, Physical and Engineering Sciences*, 466(2118):1551–1597, 2010.

[163] G.A. Holzapfel, J.A. Niestrawska, R.W. Ogden, A.J. Reinisch, and A.J. Schriefl. Modelling non-symmetric collagen fibre dispersion in arterial walls. *Journal of the Royal Society Interface*, 12(106):20150188, 2015.

[164] G.A. Holzapfel and R.W. Ogden. On fiber dispersion models: exclusion of compressed fibers and spurious model comparisons. *Journal of Elasticity*, 129(1-2):49–68, 2017.

[165] S. Hartmann and P. Neff. Polyconvexity of generalized polynomial-type hyperelastic strain energy functions for near-incompressibility. *International journal of solids and structures*, 40(11):2767–2791, 2003.

[166] J. Schröder and P. Neff. Invariant formulation of hyperelastic transverse isotropy based on polyconvex free energy functions. *International journal of solids and structures*, 40(2):401–445, 2003.

[167] D. Balzani, P. Neff, J. Schröder, and G.A. Holzapfel. A polyconvex framework for soft biological tissues. adjustment to experimental data. *International journal of solids and structures*, 43(20):6052–6070, 2006.

[168] D. Brands, A. Klawonn, O. Rheinbach, and J. Schröder. Modelling and convergence in arterial wall simulations using a parallel feti solution strategy. *Computer Methods in Biomechanics and Biomedical Engineering*, 11(5):569–583, 2008.

[169] D. Balzani, D. Brands, A. Klawonn, O. Rheinbach, and J. Schröder. On the mechanical modeling of anisotropic biological soft tissue and iterative parallel solution strategies. *Archive of Applied Mechanics*, 80(5):479–488, 2010.

[170] D. Balzani, D. Böse, D. Brands, R. Erbel, A. Klawonn, O. Rheinbach, and J. Schröder. Parallel simulation of patient-specific atherosclerotic arteries for the enhancement of intravascular ultrasound diagnostics. *Engineering Computations*, 29(8):888–906, 2012.

[171] S. Brinkhues, A. Klawonn, O. Rheinbach, and J. Schröder. Augmented lagrange methods for quasi-incompressible materials : Applications to soft biological tissue. *International journal for numerical methods in biomedical engineering*, 29(3):332–350, 2013.

[172] C. Augustin, G.A. Holzapfel, and O. Steinbach. Classical and all-floating feti methods for the simulation of arterial tissues. *International journal for numerical methods in engineering*, 99(4):290–312, 2014.

[173] J. Schröder and P. Neff. *Poly-, quasi- and rank-one convexity in applied mechanics*, volume 516. Springer Science & Business Media, 2010.

[174] P.J. Flory. Thermodynamic relations for high elastic materials. *Transactions of the Faraday Society*, 57:829–838, 1961.

[175] E. Chow and Y. Saad. Preconditioned krylov subspace methods for sampling multivariate gaussian distributions. *SIAM Journal on Scientific Computing*, 36(2):A588–A608, 2014.

[176] M. Shinozuka. Simulation of multivariate and multidimensional random processes. *The Journal of the Acoustical Society of America*, 49(1B):357–368, 1971.

[177] F. Lindgren, H. Rue, and J. Lindström. An explicit link between gaussian fields and gaussian markov random fields: the stochastic partial differential equation approach. *Journal of the Royal Statistical Society: Series B (Statistical Methodology)*, 73(4):423–498, 2011.

[178] G.A. Fuglstad, D. Simpson, F. Lindgren, and H. Rue. Does non-stationary spatial data always require non-stationary random fields? *Spatial Statistics*, 14:505–531, 2015.

[179] G-A. Fuglstad, F. Lindgren, D. Simpson, and H. Rue. Exploring a new class of non-stationary spatial gaussian random fields with varying local anisotropy. *Statistica Sinica*, pages 115–133, 2015.

[180] H. Rue and L. Held. *Gaussian Markov random fields: theory and applications*. CRC press, 2005.

[181] G.A. Holzapfel, G. Sommer, and P. Regitnig. Anisotropic mechanical properties of tissue components in human atherosclerotic plaques. *Journal of biomechanical engineering*, 126(5):657–665, 2004.

[182] P. Hauseux, J.S. Hale, and S. Bordas. Accelerating monte carlo estimation with derivatives of high-level finite element models. *Computer Methods in Applied Mechanics and Engineering*, 318:917–936, 2017.

[183] J.D. Humphrey. Mechanics of the arterial wall: Review and directions. *Critical reviews in biomedical engineering*, 23:1–162, 02 1995.

[184] G.A. Holzapfel and R.W. Ogden. *Mechanics of biological tissue*. Springer Science & Business Media, 2006.

[185] S. Ghazanfari, A. Driessen-Mol, G.J. Strijkers, F.M.W. Kanters, F.P.T. Baaijens, and C.V.C. Bouten. A comparative analysis of the collagen architecture in the carotid artery: second harmonic generation versus diffusion tensor imaging. *Biochemical and biophysical research communications*, 426(1):54–58, 2012.

[186] R. Rezakhaniha, A. Agianniotis, J.T.C. Schrauwen, A. Griffa, D. Sage, C.V.C Bouten, F.N. Van de Vosse, M. Unser, and N. Stergiopulos. Experimental investigation of collagen waviness and orientation in the arterial adventitia using confocal laser scanning microscopy. *Biomechanics and modeling in mechanobiology*, 11(3-4):461–473, 2012.

[187] S. Polzer, T.C. Gasser, K. Novak, V. Man, M. Tichy, P. Skacel, and J. Bursa. Structure-based constitutive model can accurately predict planar biaxial properties of aortic wall tissue. *Acta biomaterialia*, 14:133–145, 2015.

[188] P. Sáez, A. García, E. Peña, T.C. Gasser, and M.A. Martínez. Microstructural quantification of collagen fiber orientations and its integration in constitutive modeling of the porcine carotid artery. *Acta biomaterialia*, 33:183–193, 2016.

[189] L. Azinfar, M. Ravanfar, Y. Wang, K. Zhang, D. Duan, and G. Yao. High resolution imaging of the fibrous microstructure in bovine common carotid artery using optical polarization tractography. *Journal of biophotonics*, 10(2):231–241, 2017.

[190] Blausen.com staff. Medical gallery of Blausen Medical, http://blausen.com. Web Site, 2014.

[191] A.J. Schriefl, H. Wolinski, P. Regitnig, S.D. Kohlwein, and G.A. Holzapfel. An automated approach for three-dimensional quantification of fibrillar structures in optically cleared soft biological tissues. *Journal of The Royal Society Interface*, 10(80), 2013.

[192] G.A. Holzapfel. Determination of material models for arterial walls from uniaxial extension tests and histological structure. *Journal of theoretical biology*, 238(2):290–302, 2006.

[193] H.C. Stary. *An atlas of atherosclerosis progression and regression*. CRC Press, 1999.

[194] P.D. Ballyk, C. Walsh, J. Butany, and M. Ojha. Compliance mismatch may promote graft–artery intimal hyperplasia by altering suture-line stresses. *Journal of biomechanics*, 31(3):229–237, 1997.

[195] F. Nappi, A.R. Carotenuto, A. Cutolo, P. Fouret, C. Acar, J.C. Chachques, and M. Fraldi. Compliance mismatch and compressive wall stresses drive anomalous remodelling of pulmonary trunks reinforced with dacron grafts. *Journal of the mechanical behavior of biomedical materials*, 63:287–302, 2016.

[196] G.R. Joldes, K. Miller, A. Wittek, and B. Doyle. A simple, effective and clinically applicable method to compute abdominal aortic aneurysm wall stress. *Journal of the mechanical behavior of biomedical materials*, 58:139–148, 2016.

[197] Aneurisk-Team. AneuriskWeb project website, http://ecm2.mathcs.emory.edu/aneuriskweb. Web Site, 2012.

[198] E. Marchandise, C. Geuzaine, and J-F. Remacle. Cardiovascular and lung mesh generation based on centerlines. *International journal for numerical methods in biomedical engineering*, 29(6):665–682, 2013.

[199] L. Antiga, M. Piccinelli, L. Botti, B. Ene-Iordache, A. Remuzzi, and D. Steinman. An image-based modeling framework for patient-specific computational hemodynamics. *Medical & biological engineering & computing*, 46(11):1097, 2008.

[200] C. Geuzaine and J-F. Remacle. Gmsh: A 3-d finite element mesh generator with built-in pre-and post-processing facilities. *International journal for numerical methods in engineering*, 79(11):1309–1331, 2009.

[201] J.D. Bayer, R.C. Blake, G. Plank, and N.A. Trayanova. A novel rule-based algorithm for assigning myocardial fiber orientation to computational heart models. *Annals of biomedical engineering*, 40(10):2243–2254, 2012.

[202] M. Grigoriu. Probabilistic models for stochastic elliptic partial differential equations. *Journal of Computational Physics*, 229:8406–8429, 2010.

[203] M. Grigoriu. Microstructure models and material response by extreme value theory. *SIAM/ASA Journal on Uncertainty Quantification*, 4(1):190–217, 2016.

[204] M. Ostoja-Starzewski. *Microstructural Randomness and Scaling in Mechanics of Materials*. Chapman and Hall-CRC, 2008.

[205] C. Soize. Random matrix theory for modeling uncertainties in computational mechanics. *Computer methods in applied mechanics and engineering*, 194(12-16):1333–1366, 2005.

[206] R. Balian. Random matrices and information theory. *Il Nuovo Cimento B (1965-1970)*, 57(1):183–193, 1968.

[207] T-T. Le, J. Guilleminot, and C. Soize. Stochastic continuum modeling of random interphases from atomistic simulations. application to a polymer nanocomposite. *Computer Methods in Applied Mechanics and Engineering*, 303:430–449, 2016.

[208] J.C. Nagtegaal, D.M. Parks, and J.R. Rice. On numerically accurate finite element solutions in the fully plastic range. *Computer methods in applied mechanics and engineering*, 4(2):153–177, 1974.

[209] J.C. Simo, R.L. Taylor, and K.S. Pister. Variational and projection methods for the volume constraint in finite deformation elasto-plasticity. *Computer methods in applied mechanics and engineering*, 51(1-3):177–208, 1985.

[210] J.C. Simo and R.L. Taylor. Quasi-incompressible finite elasticity in principal stretches. continuum basis and numerical algorithms. *Computer methods in applied mechanics and engineering*, 85(3):273–310, 1991.

[211] M. Heroux, R. Bartlett, V. Howle, R. Hoekstra, J. Hu, T. Kolda, R. Lehoucq, K. Long, R. Pawlowski, E. Phipps, et al. An overview of the trilinos project. *ACM Transactions on Mathematical Software (TOMS)*, 31(3):397–423, 2005.

[212] M. Heroux and J.M. Willenbring. A new overview of the trilinos project. *Scientific Programming*, 20(2):83–88, 2012.